ISSN 1349-113X
JAXA-SP-12-008E
JAXA Special Publication

JAXA Special Publication

Proceedings of 10th International Workshop on Radiation Effects on Semiconductor Devices for Space Applications

March 2013

Japan Aerospace Exploration Agency

Proceedings of 10th International Workshop on Radiation Effects on Semiconductor Devices for Space Applications

Dec. 10 - Dec. 12, 2012

Japan Aerospace Exploration Agency (JAXA)
Japan Atomic Energy Agency (JAEA)

Contents

C-3 Heavy Ion Induced Charge Enhancement in 4H-SiC Schottky Barrier Diodes
Takahiro Makino, Manato Deki, Naoya Iwamoto, Shinobu Onoda, Norihiro Hoshino, Hidekazu Tsuchida, and Takeshi Ohshima

C-4 Microbeam Irradiation Effects on Transmission Diamond Detector
Wataru Kada, Takahiro Satoh, Naoto Iwamoto, Shinobu Onoda, Velko Grilj, Natko Skukan, Takahiro Makino, Masashi Koka, Milko Jakšić, Takeshi Ohshima, and Tomihiro Kamiya

C-P1 3-D Simulation of Angled Strike Heavy-Ion Induced Charge Collection in SiGe HBTs
Jinxin Zhang, Hongxia Guo, Qi Guo, Lin Wen, Jiangwei Cui, Xin Wang, Wei Deng

C-P2 LET Dependence of Gate Oxide Breakdown of SiC-MOS Capacitors due to Single Heavy Ion Irradiation
Manato Deki, Takahiro Makino, Takuro Tomita, Shuichi Hashimoto, Kazutoshi Kojima, and Takeshi Ohshima

C-P3 Radiation damage of Si1-yCy Source/Drain n-MOSFETs with different carbon concentrations
T. Nakashima, Y. Asai, M. Yoneoka, I. Tsunoda, T. Takakura, M.B. Gonzalez E. Simoen, C. Claeys and K. Yoshino

Session D

D-1 [Invite] Facilities and Radiation Test Methods
Ari Virtanen

D-2 Development of Ion Photon Emission Microscopy at JAEA
S. Onoda, H. Abe, T. Yamamoto, T. Ohshima, J. Isoya, T. Teraji and K. Watanabe

D-3 Large-Area Uniform Ion Beam Formed in the Nonlinear Beam Optics at the JAEA TIARA cyclotron
Yosuke Yuri, Takahiro Yuyama, Tomohisa Ishizaka, Ikuo Ishibori, and Susumu Okumura

D-4 PL/EL IMAGE ANALYSIS OF RADIATION DETERIORATION IN TRIPLE-JUNCTION SOLAR CELLS
Yuki Kobayashi, Mitsuru Imaizumi, Shirou Kawakita and Masato Takahashi

Session E

E-1 [Invite] Single-Event Effects in Microelectronics Induced by Through-Wafer Sub-Bandgap Two-Photon Absorption
Dale McMorrow, Stephen Buchner, Jeffrey Warner, Nicolas Roche, and Ani Khachatrian

E-2 Dual-PLL based on Temporal Redundancy for Radiation-Hardening
SinNyoung KIM, Akira TSUCHIYA, and Hidetoshi ONODERA

E-3 Relationship between soft error rate in SOI-SRAM and amount of generated charge by high energy ion probes
Masatoshi Hazama, Satoshi Abo, Naoyuki Masuda, Fujio Wakaya, Shinobu Onoda,Takahiro Makino, Toshio Hirao, Takeshi Oshima, Toshiaki Iwamatu, Hidekazu Oda, Mikio Tskai

E-4 Applicability of redundant pairs of SOI transistors for analog circuits
Akiko MAKIHARA, Koichi TANI, Tamotsu YOKOSE, Yoshihisa TSUCHIYA, Yoshio MIYAZAKI, Tadaaki MORIMURA, Hiroshi ABE, Hiroyuki SHINDOU, Tsukasa EBIHARA, Akifumi MARU, Koichi MORIKAWA, Satoshi KUBOYAMA, and Takashi TAMURA

E-5 Investigation of the SEE sensitivity of 90nm DICE based Flip-Flops using pulsed-laser testing methodology
H. Shindou, A. Maru, T. Ebihara, A. Makihara, S. Kuboyama and T. Tamura

E-P1 Suppression of Heavy-Ion induced Current in SOI Device
S. Ogura, T. Komiyama, Y. Takahashi, T. Makino, S. Onoda, T. Hirao and T. Oshima

E-P2 Experimental study on radiation tolerance of an SOI-PLL
Eijiro Hoshino, Daisuke Kobayashi, Takahiro Makino, Takeshi Ohshima, and Kazuyuki Hirose

E-P7 SEE Tests of the 4Gb and 8Gb Nand Flash
Pierre Xiao WANG, Pierre-Eric BERTHET, Lionel GOUYET, Alexandre ROUSSET, Benjamin VANDEVELDE

E-P9 Consideration of Single-Event Gate Rupture Mechanism in power MOSFET
S. Kuboyama, E. Mizuta, N. Ikeda, H. Abe, T. Ohshima, and T. Tamura

Session F

F-1 [Invite] State-of-the-Art Study on Mitigation Techniques of Single Event Effects in Terrestrial Applications
Eishi Ibe, Ken-ichi Shimbo, Tadanobu Toba, Hitoshi Taniguchi, Takumi Uezono

F-2 Validation of Sensitive Volume Size based on a Multi-Scale Monte Carlo Simulation in Neutron-Induced Soft Error Analyses
Shin-ichiro Abe and Yukinobu Watanabe

F-3 Measurement of Distance-dependent Multiple Upsets of Flip-Flops in 65nm CMOS Process
Jun FURUTA, Kazutoshi KOBAYASHI, and Hidetoshi ONODERA

F-4 Evaluation of SiC Power Diodes against Terrestrial Neutron-Induced Failure at Ground Level
Hiroaki Asai, Kenji Sugimoto, Isamu Nashiyama, Kensuke Shiba, Mieko Matsuda and Tadaaki Morimura

Session G

G-1 [Invite] Total Ionizing Dose and Displacement Damage Effects in Integrated Circuits: Recent Results and the Implications for Emerging Technology
Leif Scheick, Allan Johnston, Steven McClure, and Philippe Adell

G-2 [Invite] Verification of Enhanced Low Dose Rate Sensitivity(ELDRS) Accelerated Test Method
Marc Poizat, Michael Wind, Peter Beck, Marcin Latocha, Laurent Dusseau, Jerome Boch, Fréderic Saigné, Ali Zadeh

G-3 Built-In Self-Test Circuit for Total Ionizing Dose Radiation Effects in Analog-to-Digital Converters
Esko O. Mikkola, Viraj S. Pandit , Byoung Uk Kim, Andrew Levy

G-P1 Study of radiation damage caused by 23MeV protons on Multi-Pixel Photon Counters(MPPCs)

Zhengwei Li, Yupeng Xu, Congzhan Liu,Yudong Gu, Xu Zhou, Xuefeng Lu, Xuefang Li, Shuo Zhang, Zhenling Xu, Yifei Zhang and Jianlin zhao

G-P2 Difference of radiation tolerance with p- and n-type JFETs

K. Takakura, S. Sakiyama, I. Tsunoda, M. Yoneoka, T. Nakashima

Sponser Corporation

- Fuji Electric Co.,Ltd
- RYOEI TECHNICA CORPORATION
- NEC Corporation
- High-Reliability Engineering & Components Corporation (HIREC)

Plenary Talk

Overview of Radiation Single Event Effects Issues as Experienced at the European Space Agency/ESTEC.

Reno Harboe-Sørensen

former European Space Agency/ESTEC, The Netherlands
reno.harboe.sorensen@ziggo.nl

Keyword(s): Space environment, Radiation effects in components, SEE testing, Ion range in Si, Reference SEU Monitor, Technology Demonstration Monitor, Spacecraft Flight Anomalies.

Abstract

This overview paper will start with a short introduction of the space environment, with strong focus on issues directly relevant to radiation Single Event Effects (SEE) in components, the main subject of this paper. Radiation test facilities used for SEE testing will be described and testing constrains discussed. The background and use of the 'Reference SEU Monitor' system will be summarized, followed by recent PROBA-II/TDM orbital data. Finally some ESA spacecraft anomalies will conclude this overview paper

1. Introduction

Cosmic-Ray effects in microelectronic like Single Event Upset (SEU) and Single Event Latch-up (SEL) has been of major concern in satellite electronics since the '70 and continued over the years to be of increased concern. The reason for this is primarily increased sensitivity to upset events due to smaller feature sizes of modern semiconductor technologies. The same amount of charge deposit by a Cosmic-Ray particle can now cause Multiple Bit Upset (MBU) or even destructive effects in devices. So SEE hardness assurance ranging from ground testing to modeling and prediction has been the subject of intensive development over the years and much progress has been made in these areas. This paper will summarize some of the more interesting SEE disciplines as experienced over 30 year at the European Space Agency/ESTEC.

2. Space Environment

Prior to discussion of the mechanism of Single Event Effects it is useful to briefly recapitulate the nature of the space environment. Here the most important part of the cosmic ray environment is galactic cosmic rays which originate outside the solar system but are associated with the galaxy [1]. Cosmic rays are isotopic, highly energetic charged particles with energies ranging from KeV to GeV and beyond. Fluxes are generally few per cm² per seconds but vary with the solar cycle. These particles are either trapped by the Earth's magnetic field or passing through the solar system. They consist of electrons, protons and highly charged nuclei. The most numerous particles are protons with smaller populations of alpha particles (helium nuclei) and decreasing numbers of heavier nuclei. The cosmic ray environment has been very well documented and useful curves present the integral Linear Energy Transfer (LET) spectra for different orbits as part of the CREME suite of programs by Adams. As an example, the LET spectra shown in Fig. 1a, are applicable to low circular Earth orbit at 400 Km (close to the International Space Station orbit of 409/430 Km/Inclination 51,6º) which clearly show the protection by the Earth's magnetic field when changing the orbit inclinations from 30º to 90º. For a better understanding of the influence of the environment on a semiconductor device, a typical SEU cross-section (cm²/bit) curve has been superimposed as Fig. 1b (right scale). Note the saturated cross-section to be about 1E-6 cm²/bit and the LET threshold to be around 1MeV(mg/cm²).

Trapped radiation by the Earth's magnetic field consists of a very broad spectrum of energetic charged particles, in general known as the 'Van Allen radiation belts'. These radiation belts in an idealized dipole space layout, according to the AP8 and AE8 models [1], can be seen in Fig. 2. Based on Earth radii (horizontal axes), note the difference in satellite orbit altitudes between most Earth observations satellite (and ISS) at < 1000 Km (primarily seeing protons) compare to Geostationary satellites at 35.786 Km (about 6 Earth radii) primarily seeing electrons.

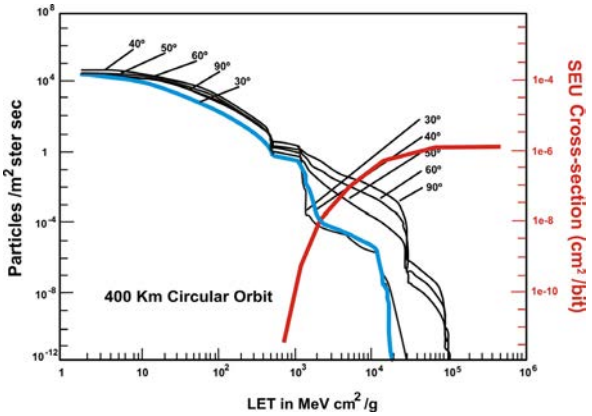

Fig. 1. a) - left, Integral spectra of flux versus Linear Energy Transfer. b) - right, Typical SEU device sensitivity.

Unfortunately the Earth's field is tilted by 11º in respect to the rotation axis and offset by approximately 500 Km towards the West Pacific, causing the radiation belt (protons and electrons) to go down to a low altitude over the South Atlantic (over Brazil). This anomaly is primarily a problem for low Earth orbiting satellites, since a proton rich zone, known as the South Atlantic Anomaly (SAA), causes additional problems when a satellite passes through. Examples of spacecraft SEE problems from the SAA will be shown later in the paper.

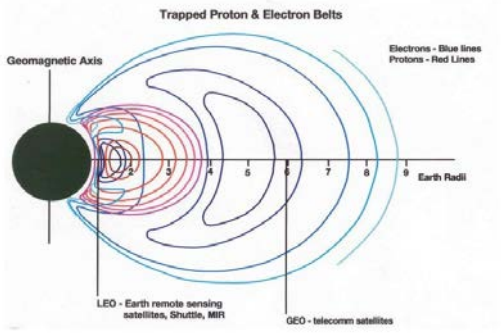

Fig. 2. Contours of trapped protons (inner belt) and trapped electrons (outer belt) versus Earth radii = 6371 Km.

Finally solar particle events, solar flares burst or Coronal Mass Ejection (CME), are large eruptions of plasma from the sun. These events tend to be proton rich, can lasts for days and causes significant disturbance in interplanetary space and the magnetosphere. Due to their high fluence, these types of event can cause significant or permanent damage to satellite systems such as Total Ionizing Dose (TID), Displacement Damage (DD) and both transient and permanent SEEs. Some examples of spacecraft SEE problems during solar particle events will also be discussed later in this paper.

3. Single Event Effects

So as briefly mentioned, the natural space radiation environment contains different energetic particles capable of causing significant damage to spacecraft components (Displacement Damage or Total Ionizing Dose damage) resulting in degraded component performances or failures. Single Event Effects often results in temporary loss of performance or catastrophic failures (if a device or system is not protected).

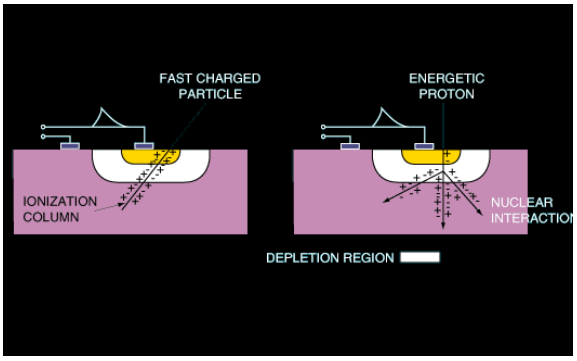

Fig. 3. Transient spike (or SEU) in a CMOS cell caused by an ion hit (left) or proton nuclear reaction (right).

In satellite systems, many different types of SEE have been experienced with Single Event Upset (SEU) or 'soft error' or 'bit-flip' as the most common event. An SEU is the change of state of a bistable element caused by the impact of an energetic heavy ion or proton. However, in simple transistor structures such as shown in Fig. 3, Single Event Transient (SET) spikes can be produced (as indicated) when a particle deposits sufficient charge in the sensitive region. In complex satellite systems, even spikes can be of concern if they have sufficient magnitude and duration, to reach and trigger latches or comparators [2]. In addition to SEU and SET, Multi Bit Upset (MBU), Multi Cell Upset (MCU) and Single Event Functional Interrupt (SEFI) are other non-destructive events commonly experienced. Of destructive events, Single Event Latch-up (SEL), Single Event Gate Rupture (SEGR) or Single Event Burn-out (SEB) are some of the more common events to be avoided.

4. European Component Irradiation Facilities

So in order to evaluate the radiation sensitivity of components, a great deal of ground simulation testing is carried out. Different irradiation sources and test sites are used, with Co-60 gamma being the most commonly used for TID testing, and low energy protons for displacement damage. Less well known are the irradiation sources and sites used for SEE testing. Several accelerator facilities have ions and proton energy suitable for SEE testing. Three of these facilities, all under ESA contract, will be described here, and examples of heavy ion and proton single event upset (SEU) data given.

Fig. 4. ECIF logo/ESA's Test Locations.

4.1 Proton Irradiation Facility (PIF).

The first external test facility to be part of European Component Irradiation Facility (ECIF) was the Proton Irradiation Facility (PIF) at Paul Scherrer Institut, Villigen, Switzerland. This facility under ESA contract

since 1992 was moved around to many different beam line locations over the years. Today, the PIF is convenient located in the PROSCAN area of PSI where a permanent modern set-up for component and material testing is installed. A very user friendly set-up allows experimenters to perform tests on their own following a short set-up and calibration exercise. Proton energies between 10 to 300 MeV are used most of the time [3].

4.2 Heavy ion Irradiation Facility (HIF).

Following an initial evaluation and assessment period in the early 90's, the second external test facility to be part of ECIF was the Heavy-ion Irradiation Facility (HIF) at the Centre de Recherches du Cyclotron, Université catholique de Louvain (UCL), Belgium. This facility became official part of the ECIF in 1996 but has seen quite a few upgrades since the opening. Interesting at the HIF is the two ion cocktails available, a high LET cocktail covering LETs between 1.7 and 55.9 MeV/(mg/cm²) with ion ranges in silicon of 80 to 43 microns and a high ion penetrating cocktail covering LETs between 1.2 and 32.4 MeV/(mg/cm²) with ion ranges in silicon of 266 to 92 microns.[4].

The second ion cocktail was developed since packaging and assembly technology changes in modern memory devices pushed heavy ion testing to take place from the back side of a device. Initial when comparing front and back side SEU test results as shown in Fig. 5, using the HIF high LET cocktail, it soon became clear that deeper ion penetration was required. As can be seen at low LET for Ne and Ar ions without tiling (maximum ion penetration) identical SEU results were obtained for front and back side testing. However, when tilting the back side tested device or going to higher LETs, Kr and Xe (less ion penetration), clear drops in SEU cross section sensitivity indicate incorrect testing [5]. Unfortunately the new high penetrating ion cocktail had Kr as the highest LET at 32.4 MeV/(mg/cm²) - not quite sufficient for a full device characterization. However, this issue was further evaluated and assessed at a new facility at the University of Jyväskylä, Finland.

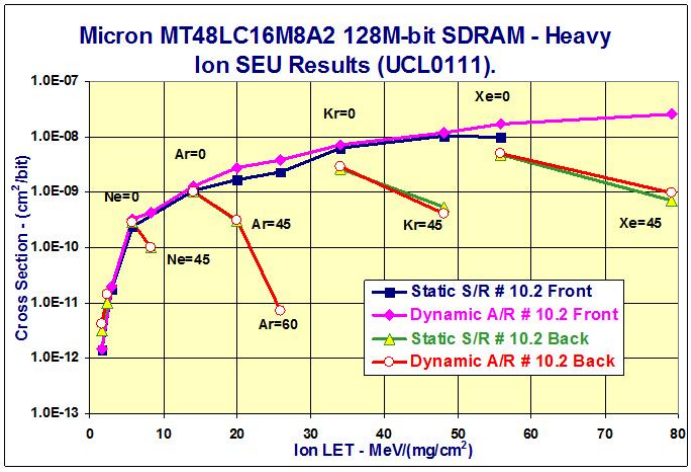

Fig. 5. Front and back-side irradiation SEU results from HIF.

4.3 RADiation Effects Facility (RADEF).

The increasing demand for radiation testing at accelerators attracted ESA and the space community to the RADiation Effects Facility (RADEF), University of Jyväskylä, Finland, some years back. Initial test campaigns showed capabilities at RADEF that were not present at the HIF. Ions initially available were assessed and complemented with new types. Higher ion energies resulting in much deeper ion penetration ranges allowed successful reverse side irradiation of thinned Integrated Circuits (ICs). This facility was officially commissioned in 2005 as the third external ESA facility under the ECIF [6].

Ion Cocktail M/Q=3.7	Energy MeV	Range µm Si	LET MeV(mg/cm²)
$^{15}N^{4+}$	139	202	1.9
$^{20}Ne^{6+}$	186	146	3.7
$^{30}Si^{8+}$	278	130	6.7
$^{40}Ar^{12+}$	372	118	10.1
$^{56}Fe^{15+}$	523	97	18.8
$^{82}Kr^{22+}$	768	94	30.4
$^{131}Xe^{35+}$	1217	89	55.0
JYFL – Ion Cocktail produced for ESA April 2005			

Table I. RADEF cocktail of ions – LET experimental values.

Since the opening in 2005, energy loss measurements of heavy ions in silicon took place at RADEF. Details of these test have been published in [7][8][9] whereas here, LET values as presented in Table I, has been updated from SRIM values to experimental values in silicon. See ECIF cocktail calculator at the RADEF www pages [9a].

5. Testing for SEE

The complexity of performing heavy ion SEE testing on advanced ICs often requires a dedicated test system capable of running the device under test (DUT) at its maximum speed, and with critical steps like initialization, read and write operations to take place during periods of no beam exposure [5]. Often the DUTs need to be prepared prior to test [10] with re-packaging of the die, removal of packaging material or thinning the die for back-side irradiating. Several different test modes are often required under different voltage and temperature conditions. Latch-up protection features and SEFI recovery concepts are needed as well as knowledge of the

DUT technology when performing the error analysis. Some of the problems related to DUT thinning will be further discussed below.

With RADEF ion penetration in silicon as listed in Table I, the goal for thinning devices is 50 micron but as earlier discovered, thickness non-uniformity represents a major problem [11]. All thinned devices used by ESA were checked for thickness variations by Interferometry. Examples of device thinning variations can be seen in Fig. 6, for a Samsung DDR-II die of 9.1 mm x 8.2mm. The center part is thinned to 35/45 micron with the corners to 75/85 micron. Obviously if we use a RADEF Xe-ion we could risk a SEU distribution as shown in Fig. 7 (for the lower/right quarter of the die). Here SEU (each spot) are assigned to their physical locations and we see no or only a few upsets in the corner part. Without this information, we probably had assuming a full tested die, and produced a wrong SEU cross section sensitivity. Now we at least can correct this sensitivity with the number of bits not tested or calculate the SEU cross section sensitivity based on upsets from the center part only [12]. However, now the second problem arises – what LET value shall we assign to this test. Here it is interesting to note that different stopping power codes give different LET values! For example, SRIM and LET Calculator codes produce LET values, for the RADEF ions, with a difference of 2% to 12% [7]. So in order to clarify this inconsistency, all 7 ions at RADEF were measured over the energy range of 1-10 MeV/u and new LET values established (see Table I). But what LET value should be assigned, the surface value of 55.0 MeV/(mg/cm²), the value at 30 micron of penetrating – 62.1 MeV/(mg/cm²) or the one after 60 micron of penetration 67.7 MeV/(mg/cm²) or just one value in the middle! By knowing all details around the test, several SEU cross sections sensitivities versus LET values could be correctly assigned – but only if details as addressed above are known [5][9][11].

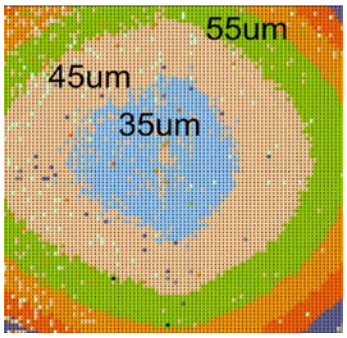

Fig. 6. Back-side thinned DDR-II memory – thickness in um.

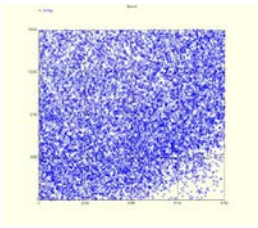

Fig. 7. SEU distribution of a ¼ of the die of Fig.6.

6. Reference SEU Monitor

Earlier attempts to compare SEU data from different test facilities often failed due to slightly different test set-ups and test conditions. Now, the same test system – referred to, as the "Reference SEU Monitor" can be used every time.

In summary, the Reference SEU Monitor system was presented as a simple and reliable beam monitoring system which could be used at the accelerator and accepted by both the SEE experimenter and beam provider in support of beam calibrations. This system, based on SEU in a well calibrated 4 Mbit SRAM as the detector element, was assembled and tested in 2005 in collaboration with HIREX Engineering [13]. With its simple control from a laptop or PC, monitoring of SEUs are directly compared with pre-calibrated SEU curves, previously obtained at heavy ion, proton and neutron facilities. The 'detector element' a 4 Mbit SRAM from Atmel (AT60142F), has a die area of 6.1 mm x 11.2 mm. The layout of the motherboard and the detector board can be seen in Fig. 9, with the 'detector element' having the lid taped on (for protection). Many experimenters have confirmed the need for such a reference system at the accelerator [14] and even beam provider now find the new version attractive. The new version of the Reference SEU Monitor is slightly improved with the 'detector element', the Atmel AT60142F SRAM, now in a hybrid configuration with 4 dies, see Fig. 10. This allows better beam profile and homogeneity checks, since the 4 dies now cover a much larger area, approximately 20 mm x 20 mm.

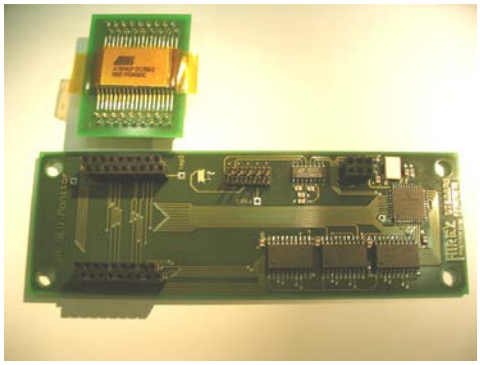

Fig. 9. "Reference SEU Monitor" system.

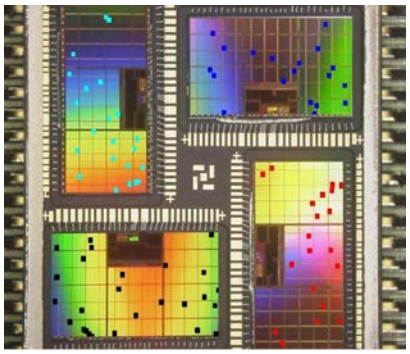

Fig. 10. SEU in the new detector element, the AT68166 MCM.

As detailed in an NSREC 2008 paper [14] this 'reference standard' appear to have helped many researchers and are even used routinely at many accelerators as part of the beam calibrations. However, as also outlined in [14] the ultimate goal would be to have a space 'reference standard'. This opportunity started in 2009 with the Technology Demonstration Module (TDM) to be flown on-board the ESA PROBA-II satellite.

7. Technology Demonstration Module

The TDM is a component radiation effects experiment focusing on SEEs in memory devices in order to address and study the difference between flight and ground events**.** The TDM consists of four different radiation effects experiments in order to study the in-flight performance of: 1) SEUs in the 'Reference SEU Monitor' (4 SRAM devices in the hybrid configuration), 2) Latch-up events in 4 different SRAM devices, 3) in-flight technology demonstration of 8 G-bit FLASH memories, and 4) measure of the local TID environment employing RADFET dosimeters. The flight unit of the TDM as shown in a folded out configuration in Fig. 11, has the 16 Mbit SRAM Multi-Chip Module operated in the same Static mode as in the Reference SEU Monitor system (right hand side board at the front).

Fig. 11. The TDM Flight Unit folded out.

The TDM was manufactured by QinetiQ (Belgium) under ESA contract. The TDM was integrated into the Advanced Data & Power Management System (ADPMS) as part of the ESA satellite PROBA-II (Project for On-Board Autonomy). PROBA-II was launched on November 2nd 2009 into sun-synchronous 800 Km polar orbit. The 265 gram TDM was switched-on on February 15th 2010 and has produced reliable radiation data since. Further details and a first set of TDM orbital data can be found in [11]. A second set of orbital data was published in [15] with further reporting under preparation. In Fig. 12, the total number of SEUs and SELs as observed in a month, April 2010, has been plotted on a world map. Here it is very clear that most SEEs are observed when passing through the South Atlantic Anomaly and therefore induced by protons. Very similar proton SEU plots were presented back in 1989 for the UoSAT-2 spacecraft also operating in a polar orbit of 700-800 Km [16][17].

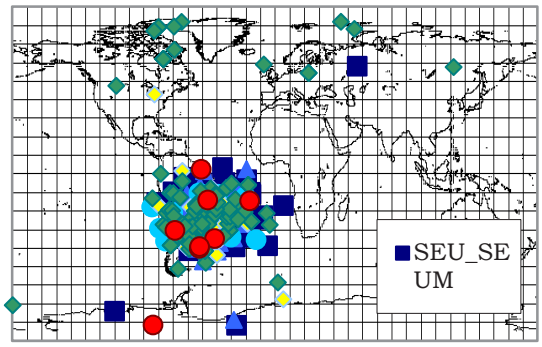

Fig. 12. Location of all TDM SEUs and SELs observed during the month of April 2010.

As part of the earlier TDM evaluation and assessment, Fig. 10, also shows the distribution of SEUs as observed in the AT68166 MCM for the first 1032 hours of analyzed flight data. The 90 SEUs recorded are randomly distribution across all four SRAMs with S1 seeing 23 SEUs, S2 seeing 27 SEUs, S3 seeing 21 SEUs and S4 seeing 19 SEUs. Later analysis revealed a very similar SEU/die distribution and the bit flips rate was established to be 57% changes going from 0 to 1 and 43% changes going from 1 to 0.

In summary, it is interesting to report that the orbital locations of SEU stayed the same for the other four SRAM types flown (the SEL experiment) with 88/89% of SEUs occurring in the SAA, 7/8% of SEUs occurring at the polar horns and 4/5% of SEUs occurring at < 60º north/south but outside the SAA. Very identical numbers can be reported for the SEU Monitor (SAA = 88.6%, >60º = 7.2% and <60º 4.2%). So despite different semiconductor types with some technology differences the % of SEUs appears to occur at the same orbital locations [14][15].

The four different SRAMs used for the latch-up experiment of the TDM, have very different heavy ion SEL sensitivities as shown in Fig. 13, tested at 40ºC. The most SEL sensitive device, the Brilliance Semiconductor's device, is not part of the TDM, but the tested type is the one mentioned in the following paragraph, flown on BIOPAN-5. Over the first 407 days of flight, one SEL occurred in the ISSI IS62 device over the SAA. For the Samsung device we observed a total of 3 SEL. One event was observed at high latitude > 60º north and two events occurred in the SAA. So far no SEL events occurred in the Alliance Semiconductor device where as the ISSI IS61 showed a total of 87 SEL. Grouping the location of these SEL events as for the SEUs, we see 79% SELs occurring in the SAA, 14% SELs at the polar horns and 7% SELs at < 60º north/south but outside the SAA.

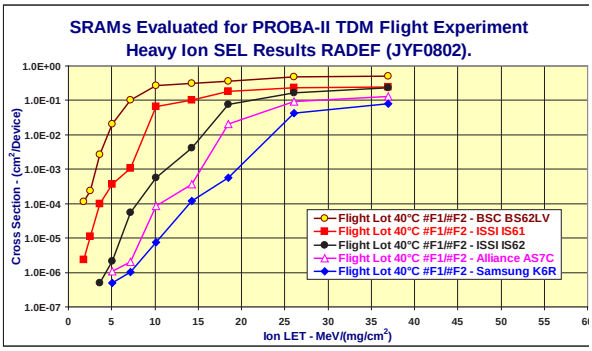

Fig. 13. SRAMs Latch-up sensitivities at 40 ºC.

Altogether, the presented flight data shows that all experiments are working well and that the TDM is running reliably. SEU and SEL rates appear to be

stable over the analyzed flight period and no indications of problems can be reported to the end of August 2011, however, the present analyzed SEU/SEL database is still too small for extensive conclusions.

8. SEE Spacecraft Anomalies

Spacecraft anomalies in general are not the type of PR any project like to see published. However, over the years, at a technical level, a lot have been learned from these failures. Here, I just like to summarize two ESA spacecraft event which probably helped many other projects, one proton SEL related event and transient SEU events in the same spacecraft.

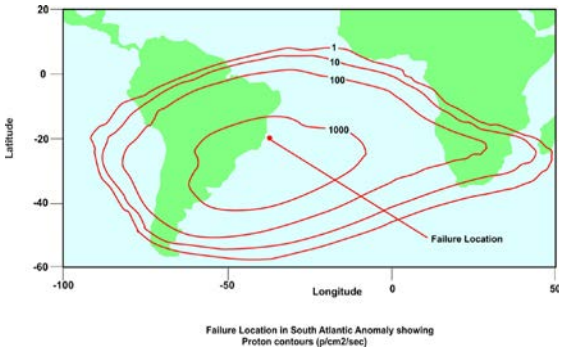

Fig. 14, ERS-1/PRARE Failure location, proton latch-up.

The first event goes back to July 1991 when ESAs Earth Resources Satellite (ERS-1) was launched into a 784 km sun-synchronous polar orbit. As part of the payload, one of the non-ESA instruments carried was the Precision Range and Range Rate Equipment (PRARE). After 5 days of operating this experiment shut down immediately following a transient over current condition and could not be restarted. This switch-off occurred during a pass over the South Atlantic, as shown in Fig. 14. During the first 5 days of operation a fair number of other anomalies were noted including SEUs and a slave processor reboot.

Ground testing took place at the PIF/PSI facility using 30/60 MeV protons and the engineering model of PRARE. Soon it became apparent that a NEC D4464G 64 Kbit CMOS SRAM memory was causing latch-up and the full orbital failure condition simulated. Additional heavy ion testing of 'flight spare devices' also revealed latch-up occurrences even at extreme low LETs [18]. As of today I still do not recall any other device to be more SEL sensitive, however, a very similar SEL event in May 2005 caused ESA's BIOPAN-5 on-board FOTON-2 (altitude 280/305 km) to fail at the location shown in Fig. 15. This time it was an 8 Mbit SRAM from Brilliance Semiconductors going into a latch-up condition during the 5th orbit. This device type, identical to the one tested in [14] has a SEL sensitivity similar to the NEC devise with a heavy ion SEL cross section threshold below 2.0 MeV/(mg/cm²), as shown in Fig. 13. For both events, no ground SEE testing of the flown/failed device type was carried out prior to flight!

Fig. 15, FOTON-2/BIOPAN-5 Latch-up location.

The second example of spacecraft anomalies is summarized for the Solar and Heliospheric Observatory (SOHO), ESAs solar satellite in a Halo orbit around the Lagrangian point L1 located 1.500.000 km from the Earth in the sunward direction. SOHO experienced a large number of SEEs, all of which were recoverable. Analysis of all SEEs experienced during the first five years of successful operation was report in 2002 [19]. Events were reported occurring in the various power supply units (PSUs), in the solid-state recorder (SSR) and in one of the instrument.

The most illustrative series of event is probably the SEUs as observed in the 2 Gbit SSR. These upsets, between April 1996 and August 2001), was time plotted, as shown in Fig. 16. The initial average upset rate fluctuates around 1 SEU/minutes and changes towards 0.5 SEU/minutes over the 5 year period. The large peaks happened during major solar flares where the daily average event rate even exceeds 32 SEUs/minutes during the July 14, 2000 event. In addition to the solar events, the effect of solar activity is apparent in the decline in the upset rate as solar maximum is approached. This recording was coherent with other observations and predictions.

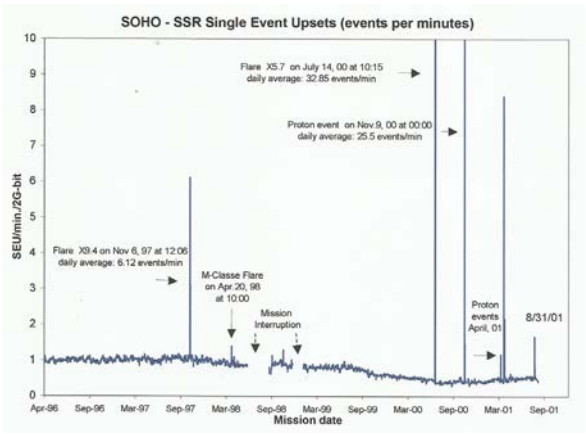

Fig. 16, SOHO SSR Upsets as recorded over 1562 days.

However, the 'self switch-off events' in the redundant and protected power units were really the main concern. Over the reported period, more than 20 power switch-off events occurred during normal

operations with bus, load, voltage, current and temperature nominal. The suspicion of these events to be SEE related was basically confirmed during a major ground test program using identical test conditions as used by SOHO [2]. Also SOHO flight spare devices were used at both heavy ion and proton facilities. The early suspicion that these events were caused by transient spikes produced by a small number of linear integrated circuits induced by cosmic rays or protons was substantiated through test results and predictions as presented in the paper [19]. This paper also stressed the importance of performing SEE tests with application configurations and operating conditions identical to those used in the mission, particular in the case of linear ICs. This is clearly shown in Fig. 17, with the different SET sensitivities of the Virgo (application) and the comparator mode of operation.

Finally the SOHO transient SEE experienced was used to create a safe margin standard validating future science mission using the same spacecraft platform.

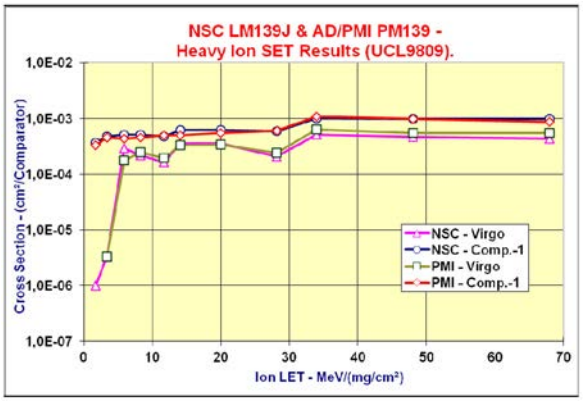

Fig. 17, NSC and PMI 139 Heavy ion SET results.

9. Conclusions

The main objective of this paper was to address some of the more interesting disciplines experienced over more than 30 years at the European Space Agency/ESTEC as a radiation SEE expert. However, most of the presented subjects have previously been proceeding published with a total page number probably close to 100 pages. So for each main subject please read these few pages as guidance and use the various references for detail explanations. The list of references is slightly longer than for a normal proceedings paper but hope this way to be able to guide the reader to further information's.

References

[1] A. Holmes-Siedle and L. Adams,"Handbook of Radiation Effects, " Oxford Science Publications, 1993.

[2] R. Harboe-Sørensen, F. X. Guerre, H. Constans, J. van Dooren, G. Berger and W. Hajdas, "Single Event Transient Characterisation of Analog IC's for ESA's Satellites" in *Proc. RADECS*, pp. 573-581,Sep. 1999.

[3] W. Hajdas, A. Zender, F. Burri, J. Bialkowski, L. Adams, B. Nickson and R. Harboe-Sørensen, "Radiation Effects Testing Facility in PSI Low Energy OPTIS Area," in *Proc. IEEE Rad. Effects Data Workshop Record*, July 1998, pp 152-155.

[4]G. Berger, G. Ryckewaert, R. Harboe-Sørensen and L. Adams, "The Heavy Ion Irradiation Facility at CYCLONE - A Dedicated SEE Beam Line", in *Proc. IEEE Rad. Effects Data Workshop Record*, July 1996, pp 78-83.

[5]R. Harboe Sørensen, F.-X. Guerre, J.-G. Loquet and C. Tizon "Heavy-Ion Single Event Effects Testing of Lead-On-Chip Assembled High-Density Memories", *IEEE Trans. Nucl. Sci., vol 50, pp2322-2327, Dec. 2003*.

[6]A. Virtanen, R. Harboe-Sørensen, A. Javanainen, H. Kettunen, H. Koivisto and I. Riihimäki, "Upgrades for the RADEF Facility", in *Proc. IEEE Rad. Effects Data Workshop Record*, July 2007, pp 38-41.

[7]A. Javanainen, T. Malkiewicz, J. Perkowski, W. H. Trzaska, G. Berger, W. Hajdas, R. Harboe-Sørensen, H. Kettunen, V.Lyapin, M. Mutterer, A. Pirojenko, I. Riihimäki, T. Sajavaara, G. Tyurin, H. Whitlow, A. Virtanen "Linear Energy Transfer of Heavy Ions in Silicon", *IEEE Trans. Nucl. Sci., vol 54, no. 4, pp1158-1162, August 2007*.

[8]A. Javanainen, M. Sillanpää, W. H. Trzaska, A. Virtanen, G. Berger, W. Hajdas, R. Harboe-Sørensen, H. Kettunen, T. Malkiewicz, M. Mutterer, J. Perkowski, A. Pirojenko, I. Riihimäki, T. Sajavaara, G. Tyurin and H. Whitlow, "Experimental Linear Energy Transfer of Heavy Ions in Silicon for RADEF Cocktail Species", *IEEE Trans. Nucl. Sci., vol 56, no. 4, pp2242-2246, August 2009*.

[9]A. Javanainen, W. H. Trzaska, R. Harboe-Sørensen, A. Virtanen, G. Berger, W. Hajdas, "Semi-empirical LET Description of Heavy Ions Used in the European Component Irradiation Facilities", *IEEE Trans. Nucl. Sci., vol 57, no. 4, pp1946-1949, August 2010*.

[9a] https://www.jyu.fi/fysiikka/en/research/accelerator/radef/location-of-the-radef

10]R. Harboe Sørensen, "Radiation Pre-Screening of Commercially Available Memories for Space Applications," in *Proc. 3rd RASEDA Workshop, Tsukuba, Japan*, pp. 137-147, Oct. 1998.

[11]R. Harboe Sørensen, F.-X. Guerre and G. Lewis "Heavy-Ion SEE Test Concept and Results for DDR-II Memories", *IEEE Trans. Nucl. Sci., vol 54, no. 6, pp2125-2130, Dec. 2007*.

[12]R. Harboe-Sørensen, C. Poivey, N. Fleurinck, K. Puimege, A. Zadeh, F.-X. Guerre, F. Lochon, M. Kaddour, L. Li, D. Walter, A. Keating, A. Jaksic and M. Poizat, "The Technology Demonstration Module On-Board PROBA-II", *IEEE Trans. Nucl. Sci.*, vol 58, no. 3, pp. 1001-1007, June 2011.
[13]R. Harboe-Sørensen, F.-X. Guerre and A. Roseng,"Design, Testing and Calibration of a Reference SEU Monitor System", in *Proc. RADECS*, pp. B3.1-B3.6, Sep. 2005.
[14]R. Harboe-Sørensen, C. Poivey, F.-X. Guerre, A. Roseng, F. Lochon, G. Berger, W. Hajdas, A. Virtanen, H. Kettunen and S. Duzellier, "From the Reference SEU Monitor to the Technology Demonstration Module On-board PROBA-II," *IEEE Trans. Nucl. Sci.*, vol 55, no. 6, pp. 3082-3087, Dec. 2008.
[15]R. Harboe-Sørensen, C. Poivey, A. Zadeh, A. Keating, N. Fleurinck, K. Puimege, F.-X. Guerre, F. Lochon, M. Kaddour, L. Li, and D. Walter, " PROBA-II Technology Demonstration Module In-Flight Data Analysis", *IEEE Trans. Nucl. Sci.*, vol xx, no. x, pp. xxxx-xxxx, June 2012.
[16]L. Adams, R. Harboe-Sørensen and E. J. Daly, "Proton Induced Upsets in the Low Altitude Polar Orbit," *IEEE Trans. Nucl. Sci.*, vol. 36, no. 6, pp. 2339-2343, Dec. 1989.
[17]R. Harboe-Sørensen, E. J. Daly, C. I. Underwood, J. Ward and L. Adams, "The Behaviour of Measured SEU at Low Altitude During Periods of High Solar Activity," *IEEE Trans. Nucl. Sci.*, vol. 37 no. 6, pp. 1938-1943, Dec. 1990.
[18]L. Adams, E. J. Daly, R. Harboe-Sørensen, B. Nickson, J. Haines, W. Schafer, M. Conrad, H. Griech, J. Merkel and T. Schwall, "A Verified Proton Induced Latch-up in Space," *IEEE Trans. Nucl. Sci.*, vol. 39, no. 6, pp. 1804-1808, Dec. 1992.
[19]R. Harboe-Sørensen, E. Daly, F. Teston, H. Schweitzer, R. Nartallo, P. Perol, F. Vandenbussche, H. Dzitko and J. Cretolle, "Observation and Analysis of Single Event Effects On-Board the SOHO Satellite," *IEEE Trans. Nucl. Sci.*, vol 49, no. 3, pp. 1345-1350, June 2002.

Session A

Space Environments and Missions

Geospace Exploration Mission ERG

Takeshi Takashima[*1], Yoshizumi Miyoshi[2], Takayuki Ono[3], and ERG project team
1 Japan Aerospace Exploration Agency (JAXA) / ISAS, Japan
2 Solar-Terrestrial Environment Laboratory, Nagoya University, Japan
3 Graduate School of Science, Tohoku University, Japan
*Email: ttakeshi@stp.isas.jaxa.jp
Keyword(s): Particle acceleration, Space weather, Radiation belts, Space mission

Abstract

The ERG (Energization and Radiation in Geospace) is a Japanese geospace exploration mission for the solar maximum and early declining phase of this solar cycle, especially focusing on the relativistic electron acceleration as well as the dynamics of the space storms. The project consists of the satellite program, ground-based network observations, and integrated studies/simulations. The ERG satellite is the second mission candidate of the small satellite program of ISAS/JAXA and will be launched into the inner magnetosphere in FY2015. Comprehensive instruments for plasma/particle, fields and waves are installed in the ERG satellite to understand the electron acceleration process via the cross-energy coupling. This paper reports the overview and the current status of the ERG project.

1. Introduction

High-energy particles (ions and electrons) are trapped in the Earth's magnetic field and formed the Van Allen radiation belts. MeV electrons in the radiation belts are the highest energy of particles in the geospace. The radiation belts are unique area where "direct observation of relativistic electron acceleration" is possible which is too difficult with distant planets or celestial bodies. Therefore, the direct observations inside the radiation belts will give an important clue to understand the particle acceleration process in the universe.

As acceleration mechanisms of relativistic electrons of the radiation belts, two different ideas have been proposed. One is the external source process via the adiabatic acceleration [1]. In this process, when electrons transport from the plasma sheet to the inner magnetosphere, the energy of electrons increases due to the conservation of their first adiabatic invariant. This process has been modeled as the stochastic radial diffusion process, and the radial diffusion is a fundamental transportation mode of energetic electrons. The MHD pulsations with a few minutes have been considered as the main driver for the radial transportation via the drift-resonance with electrons [2].

On the other hand, there exists other candidate, so-called the internal acceleration process. In this process, the first adiabatic invariant is violated due to the wave-particle interactions. It has been suggested that wave-particle interactions via cyclotron resonance work for the electron acceleration inside the radiation belts [3][4]. In this process, the free-energy for generating whistler mode waves is the temperature anisotropy of tens keV electrons, and subsequent non-linear evolution will produce chorus waves [5], which can acceleration MeV electrons. Therefore, the whistler mode waves work as a mediating agent that can convert the energy from low energy electron population to higher energy one, and the concept of the cross-energy coupling would be a key idea to understand the electron acceleration process [6].

In order to examine which process (external supply process or internal acceleration process) occurs more efficiently for large flux enhancements of the outer belt, the phase space density observation is essential. When relativistic electrons of the outer belt increase, it is expected that, with the radial diffusion process, the phase space density increases monotonically with the distance from the Earth. On the other hand, with the internal acceleration process via the wave-particle interactions, the phase space density must have peak inside the outer belt. In order to measure the phase space density, it is necessary to observe the electron distribution function in a wide range of energy near the magnetic equator.

Besides these science interesting, a study of relativistic electrons in the radiation belts is important for the space weather. Space infrastructures such as GPS and meteorological satellites are indispensable to our lives in modern society. These satellites operate in the radiation belts. Some activities such as the International Space Station also take place at the bottom of the inner radiation belt. The high-energy particles can cause operational anomalies with satellites and exert a dangerous impact on the mankind's long-term stay in space. In fact, the close relationship is suggested between the satellite anomaly and the large flux enhancement of relativistic electrons of the outer belt. For humankind to act safely and comfortably in the outer space, the study of the radiation belts in space weather research is especially important.

2. The ERG satellite

2.1 Overview of the ERG satellite

The comprehensive observations for plasma/particles, fields and waves near the magnetic equator are important for understanding the cross energy coupling for relativistic electron accelerations and dynamics of space storms. Figure 1 shows a image picture for the ERG satellite in the space. The ERG satellite is sun-aligned spin stabilized with 7.5rpm. The apogee altitude is 4 Re (L~5) and the perigee altitude is ~300 km. The planned inclination angle will be ~31deg.

The ERG satellite will be launched around the early declining phase of cycle 24 (~ FY2014-15). The nominal mission life is planned to be longer than 1 year.

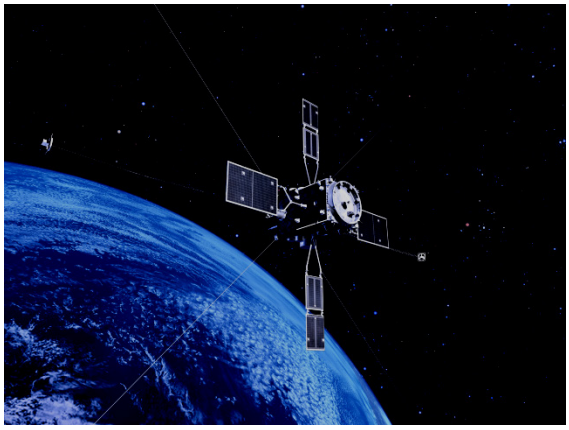

Fig. 1. Image of the ERG satellite in the space

2.1 Plasma and Particle experiments (PPE)

Plasma and Particle Experiment (PPE) consist of four electron sensors (LEP-e, MEP-e, HEP-e, and XEP-e) and two ion sensors (LEP-i, and MEP-i). PPE electron sensors can measure electrons from 10 eV to 20 MeV, while ion sensors can measure ions from 12 eV/q to 180 keV/q with mass discrimination. The energy ranges of each detector are designed to overlap each other, which can provide seamless energy spectrum.

About electron observations, both HEP-e and XEP-e instruments mainly observe relativistic electrons of the radiation belts, and these instruments are essential to derive the phase space density profile. On the other hand, LEP-e and MEP-e instruments observe hot electrons that are free energy source for plasma waves. Since anisotropies of the distribution function should be a free energy of plasma waves, observations of the distribution function is important to clarify how plasma waves generate inside the radiation belts. Measurements of particles at the energy range of tens keV is very difficult in the radiation belts. Newly developed technologies to remove background contamination can be applied in ERG/PPE, and detail observations of tens keV electrons will be possible.

About ion observations, LEP-i and MEP-i instruments observe several ion species in the inner magnetosphere. Although there are same contamination problems as electron observations, especially, at tens keV energies, the new technology is realize to observe ions up to 180 keV/q in the radiation belts. These ion observation data will be used for study of evolution of ring current ions, and ion observations with mass discrimination are essential to study the composition of ring current particles that come from both solar wind and the ionosphere.

2.2 Plasma Wave and Electric Field (PWE)

Plasma Wave and Electric Field (PWE) instrument observes electric fields at the frequency range from DC to 10 MHz as wells as the magnetic field at the frequency range from a few Hz to 20 kHz. The electric field is measured by two pairs of wire dipole antennas, and its length is about 30 m tip-to-tip. The high-frequency magnetic field is measured by the two orthogonal search coils.

There are various kinds of plasma waves in the inner magnetosphere. Whistler mode chorus waves and the ion Bernstein mode waves will be important for non-adiabatic acceleration to generate relativistic electrons. Electromagnetic ion cyclotron (EMIC) waves that are generated from ring current ions will work for rapid pitch angle scattering of relativistic electrons. Whistler mode hiss waves inside plasma-pause work for the pitch angle scattering of electrons. The PWE instrument can observe the frequency spectrum and wave-form of these plasma waves. The MHD pulsations with ~5 min periods are a driver for adiabatic acceleration by radial diffusion, which can be observed by the PWE instrument as well as the MGF instrument. Thermal plasma density that is important information for wave-particle interactions is determined from cutoff-frequency of the upper-hybrid resonance waves. The onboard measurement of the thermal plasma density will be developed for the ERG satellite.

2.3 Measurement of Geomagnetic Field (MGF)

Measurement of Geomagnetic Field (MGF) instrument observes the ambient magnetic field as well as the MHD pulsations. The fluxgate sensor with the boom is used for measurements.

Observations of ambient magnetic field are a key to know ambient plasma environment around the ERG satellite. The plasma distribution function and pitch angle distribution is obtained using the ambient magnetic field. The local cyclotron frequency is also determined from the MGF measurement.

The MGF instrument observes MHD pulsations and EMIC waves as well as the PWE instrument. Since the ring current evolution produces distortions of the ambient magnetic field, and its distortion affects the particle distribution and trajectories in the inner magnetosphere, the accurate measurements of magnetic field deviation from the intrinsic magnetic field is important to evaluate the ring current effect. The ERG/MGF instrument can measure such deviations of magnetic fields during space storms.

2.4 Software-Wave Particle Interaction Analyzer (S-WPIA)

In order to measure the wave-particle interactions, that is energy conversion process between plasma/particles and waves, the newly developed S-WPIA system will be installed in the ERG satellite. The vector cross-product of the particle velocity and the electric field velocity should be equal to the time derivative of the kinetic energy of particles; the positive $E \cdot v$ means the acceleration of particles by waves, while the negative $E \cdot v$ means the growth of waves. Therefore, the relative phase between the electric field and the velocity of particles determines the direction of the energy flow.

Using the particle data from MEP-e/HEP-e and the wave form data from the PPE, the S-WPIA system can calculate the relative phase between the waves and the particles for each particle. This will be the first observation to identify directly the wave-particle interaction process in space, and we can observe the cross-energy coupling process via wave-particle interaction process.

3. International Collaborations

The next solar maximum would be great chance for comprehensive study of geospace and the Van Allen belts, because some missions of foreign countries have been planned. In fact, RBSP (US), ORBITALS (Canada), RESONANCE (Russia) are planned for geospace exploration during the next solar maximum. Simultaneous observations at different radial distance from the Earth and different local times are possible by the international fleet of satellites, which are highly desirable for the ERG project.

4. Summary

The high-energy particle acceleration is a common scientific subject, not limited to the Earth's magnetosphere but applicable to particle acceleration in magnetospheres of other planets. The ERG satellite mission is particularly important for the future exploration of the Jovian magnetosphere. Science subjects in the Van Allen belts are readily common in the Jovian magnetosphere, where ultra relativistic electrons are generated. In fact, the non-adiabatic acceleration process via wave-particle interactions has been proposed based on the recent studies in the terrestrial radiation belts. Moreover, the science instruments developed for the ERG satellites, which are designed to work under the intense radiation environment, will also be an important heritage for instrumentation of the future Jupiter mission.

References

[1] Schulz, M., and Lanzerotti, L.: *Particle diffusion in the radiation belts*, Springer-Verlag, Berlin and Heiderberg, 1974.

[2] Elkington, S. R., M. K. Hudson, and A. A. Chan, Acceleration of relativistic electrons via drift‐resonant interaction with toroidal‐mode Pc‐5 ULF oscillations, Geophys. Res. Lett., **26**(1999), 3273-3276

[3] Summers, D., R. Thorne, and F. Xiao, Relativistic theory of wave‐particle resonant diffusion with application to electron acceleration in the magnetosphere, J. Geophys. Res., **103**(1998), 20487-20500.

[4] Miyoshi, Y., A. Morioka, H. Misawa, T. Obara, T. Nagai, and Y. Kasahara, Rebuilding process of the outer radiation belt during the 3 November 1993 magnetic storm: NOAA and Exos-D observations , , **108** (2003) , *1004, doi:10.1029/2001JA007542.*

[5] Katoh, Y. and Y. Omura (2007), Computer simulation of chorus wave generation in the Earth's inner magnetosphere, Geophys. Res., Lett., 34, doi:10.1029/2006GL028594.

[6] Ebihara, Y., and Y. Miyoshi, Dynamic inner magnetosphere: A tutorial and recent advances, in Dynamic Magnetosphere, IAGA Special Sopron Book Series, in press.

Asteroid Sample Return Mission Hayabusa2 - Next New Challenge

Makoto Yoshikawa*1, Hiroyuki Minamino[1], Noriyasu Inaba[1],Hitoshi Kuninaka[1],
and Hayabusa2 Project Team
[1]Japan Aerospace Exploration Agency (JAXA), Japan
*Email: yoshikawa.makoto@jaxa.jp
Keywords:Planetary Exploration, Asteroid, Hayabusa

Abstract

After the successful return of Hayabusa, we have started Hayabusa follow-on mission, Hayabusa2. It is an asteroid sample return mission again. The target asteroid is C-type, so we can study the organic matters and water that existed at the formation of the solar system. The spacecraft is similar to Hayabusa, but many parts are modified so that we will not have the troubles that we experienced in Hayabusa. The spacecraft has aimpactor, which will make an artificial crater on the surface of the asteroid. The planned launch year is 2014, arriving at the target asteroid 1999 JU3 in 2018, and coming back to the earth 2020.

1. Introduction

Hayabusa is the first asteroid sample return mission in the world. Hayabusa, which was launched on May 9, 2003, arrived at the target asteroid (25143) Itokawa on September 12, 2005 (Fig.1). We were surprised to see the strange and unexpected nature of Itokawa. After overcoming several serious problems, Hayabusa came back to the earth on June 13, 2010, and the capsule landed successfully on the desert of Australia. When Hayabusa returned to the earth, it became a large and bright fireball. It was quite dramatic and moving. Although Hayabusa had a lot of troubles and difficulties, it was successful to bring back the surface materials of Itokawa. The initial sample analysis has already been done, and we revealed a little about the birth of Itokawa.

After Hayabusa, we have started next asteroid sample return mission, Hayabusa2. Hayabusa2 is similar to Hayabusa, but the target asteroid is C-type, which is different from Itokawa, S-type. Many parts in the spacecraft will be modified so thatHayabusa2 will not have the same trouble occurred in Hayabusa. From the next section, we show the outline of Hayabusa2 mission. In the following part of this section, we summarize the importance of explorations of small solar system bodies.

There are several purposes for exploration of small solar system bodies. The small solar system bodies, such as asteroids and comets, are not outstanding except that comet shows long tail near the sun. However, the number of these small bodies is quite large, and at present about 600,000 asteroids have been found. These objects are supposed to have information at the time of the birth of the solar system. Therefore, the study about the formation and evolution of the solar system is the one of the major purposes of the exploration to the small solar system bodies.

Another important thing is spaceguard. Asteroids or comets may collide to the earth. If such collisions occur, we will have large disaster. So we must prevent such collision. In order to do this, at first we must discover the objects that will come close to the earth or that have possibilities to collide to the earth. If we find such objects, then we must try to do something to avoid the collision. We must know the characteristics of colliding objects to avoid their collision. These are the activities of the spaceguard, and asteroid exploration is quite important to know the nature of such colliding objects.

Small bodies will have such materials like metal or water. These materials are necessary when mankind goes into the interplanetary space. Of course, these materials cannot be used right now, because it costs a lot to get them form asteroids or comets to the earth. However, in the future, it may be possible that such materials are utilized. In addition to these, the asteroids that approach to the earth have another important aspect. Such asteroids can be the targets of manned mission. Human beings have already been to the moon, and it is said that the next target is Mars. However, Mars is too far form the earth to send manned spacecraft in near future. Asteroids approaching to the earth will be the good targets before manned mission to Mars. In Fig.2, the purposes of exploration to the small solar system bodies are summarized.

Fig.1: Hayabusa and Asteroid Itokawa

2. Hayabusa2 Mission

In Japan, we have several categories of space mission to the solar system bodies, such as lunar mission like "Kaguya (SELENE)", planetary missions like "Nozomi (PLANET-B)" and "Akatsuki (PLANET-C)", and missions to small solar system bodies like "Sakigake (MS-T5)", "Suisei (PLANET-A)", and "Hayabusa (MUSES-C)". Hayabusa2 is the next mission to the small solar system bodies.

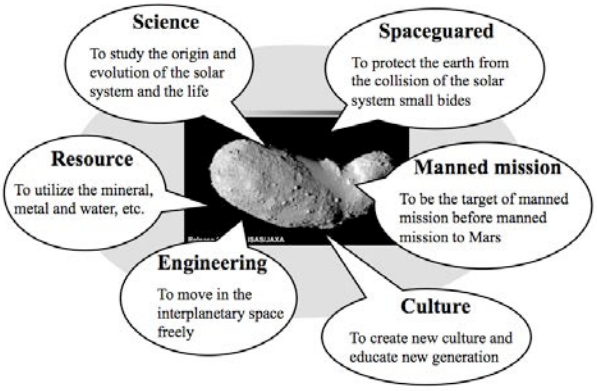

Fig.2: The purposes of exploration of the small solar system bodies

2.1 History

The Hayabusa2 mission was proposed in 2006 at first. In the year before this, 2005, Hayabusa tried to get the surface material from Asteroid Itokawa, but it could not do this as planned. Moreover Hayabusa had very serious problems, and we were not sure whether it could come back to the earth or not. Therefore, we proposed another mission to try again. Asteroid 1999 JU3 was selected as the target object for Hayabusa2, because it is C-type asteroid. Since Asteroid Itokawa is S-type, we thought that we would have much more new scientific results if we explore a different kind of asteroid.

In this first proposal, the spacecraft was almost same as that of Hayabusa, because we wanted to start it as soon as possible. Of course, we will modify the parts where trouble occurred in Hayabusa, but there were no major changes. The launch windows to go to 1999 JU3 were in 2010 and 2011. However, since we could not start Hayabusa2 mission immediately, we missed these launch opportunities. The next launch windows are in 2014. Therefore, we have changed our original plan and we are now planning to launch Hayabusa2 in 2014.

Since the launch was delayed, we changed our plan a little. The new plan of Hayabusa2 is basically same as that of the first proposal, so the spacecraft is similar to Hayabusa. However, we are planning to have new equipment. One of them is what we call "impactor." The impactor is a small box that contains explosive. After released from the spacecraft about a few hundred meters above the surface of the asteroid, the impactor will explode and a lump of copper will be accelerated at the speed of 2 km/s or so. The mass of the copper is about 2 kg, so wethink that a crater about a few meters in diameter will be created on the surface. Then we will try to get the materials inside the crater or those ejected from it. Then we may get the material which would be less changed in quality.

The status of Hayabusa2 project shifted to Phase-B in May 2011, and we have stated to develop the spacecraft of Hayabusa2 for the launch in 2014. The critical design review (CDR) was finished in March 2012, and the first interface test will be done at the beginning of the year of 2013.

2.2 Mission Scenario

The launch window that we are aiming at now is December 2014. We use H-IIA rocket to launch Hayabusa2. The launching site is in Tanegashimaisland in Japan. There are other launch windows in 2015, which are backup windows. After the launch, the spacecraft comes back to the earth in December 2015 to execute the earth swingby, and departs from the orbit near the orbit of the earth.

In the cruising phase, Hayabusa2 uses the ion engine, which is the modified one that was used for Hayabusa. Hayabusa2 will arrive at 1999 JU3 in June 2018. It will stay near the asteroid for about one and half years. This period is much longer than the case of Hayabusa. Hayabusa had only three month to explore Itokawa and this was too short to do the many missions. Therefore we have the period long enough for Hayabusa2.

At the asteroid, Hayabusa2 observes the asteroid in detail at first. Next it releases small rovers and a lander. Then Hayabusa2 performs touchdown to collect the surface material. The method of sample correction is almost same as that of Hayabusa. Finally, we use the impactor to make a small crater and touchdown again to the crater to collect the material revealed from the subsurface.

Hayabusa2 will leave the asteroid at the end of 2019, and come back to the earth at the end of 2020. The capsule will be released and it will land on the desert in Australia. The spacecraft will flyby near the earth and go somewhere. The capsule will be brought back to Japan and it will be opened in the curation facility in JAXA. We hope that we will find the sample of 1999 JU3 in it. If we find some samples then the initial analysis will be done by the science team of Hayabusa2 first. And later, the samples will be distributed to researchers in the world.

The whole scenario is summarized in Fig.3.

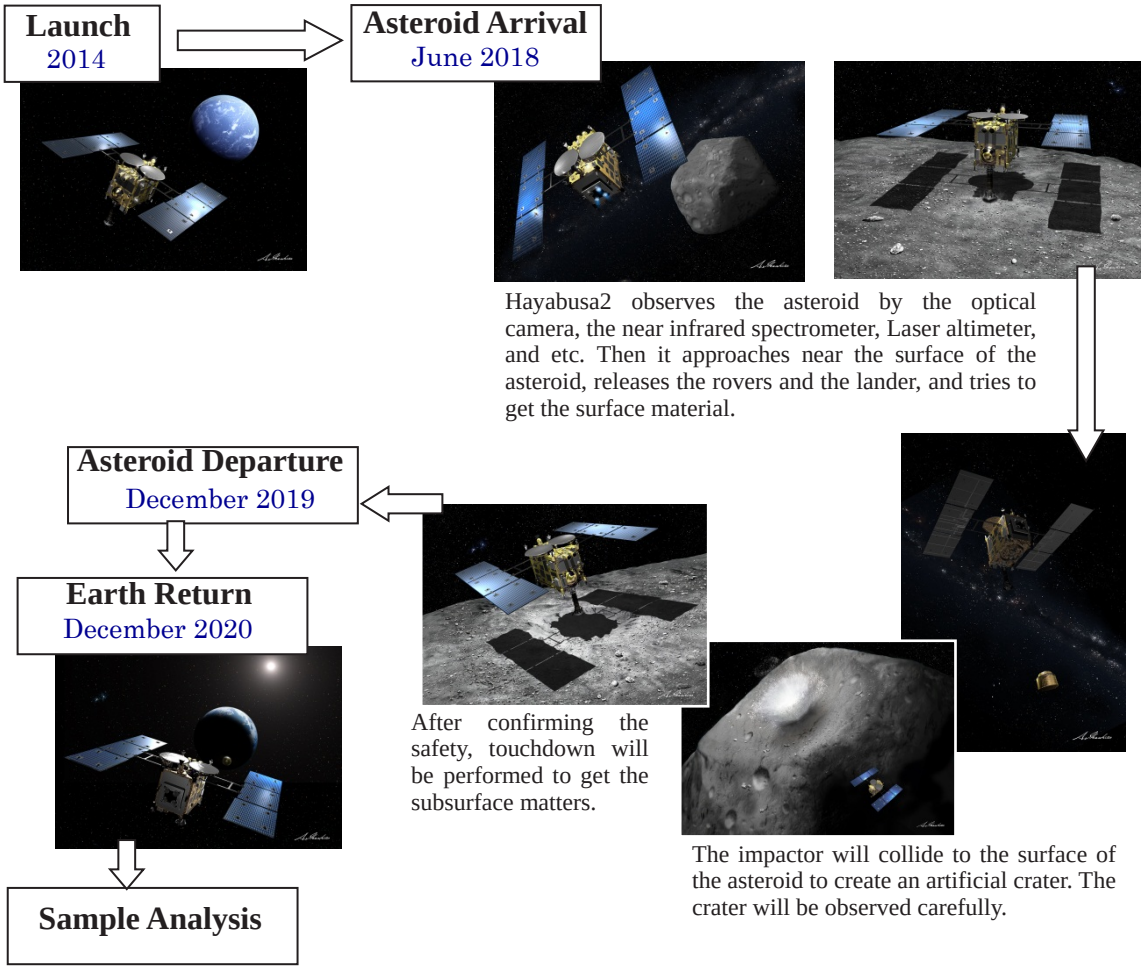

Fig. 3: The current scenario of Hayabusa2 mission

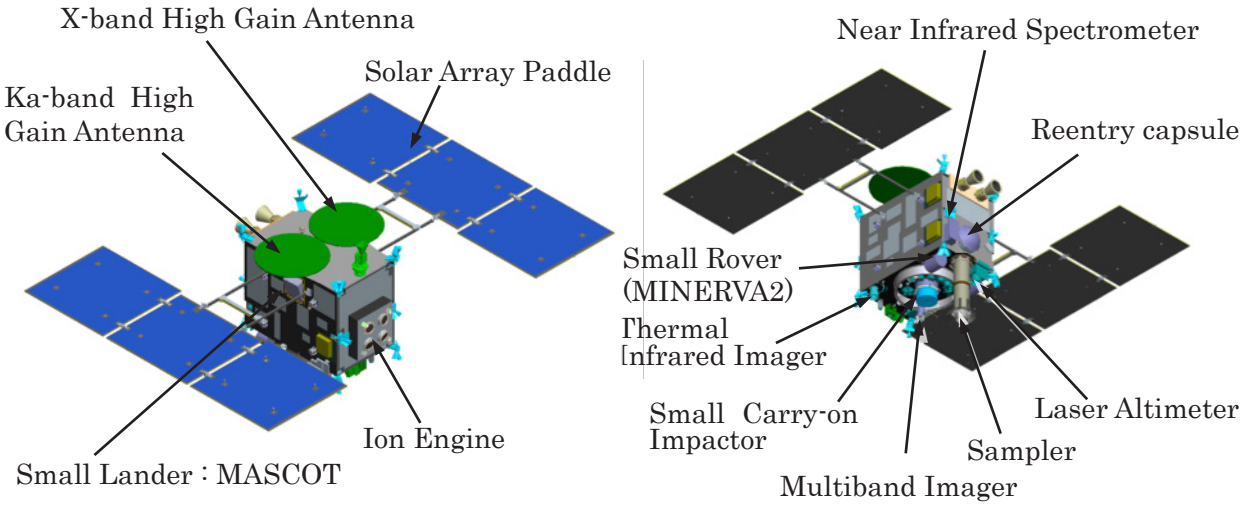

Fig. 4: Hayabusa2 spacecraft

2.3 Spacecraft and Payloads

As we already mentioned, the spacecraft of Hayabusa2 is basically similar to that of Hayabusa (Fig.4). However, we have the experience of Hayabusa, so we will modify many parts of Hayabusa2 so that the mission will be more reliable and robust. Especially we will modify the attitude control system, the ion engine, the chemical thruster system,and etc. One of the new things for Hayabusa2 is Ka-band communication. Since it is better to have high-rate downlink, we have Ka-band in addition to X-band. Ka-band communication will be used when the observed data of 1999 JU3 are sent to the earth.

As for the guidance and navigation in the proximity phase, we consider more precise method than Hayabusa using the experience of Hayabusa. For example, Hayabusa2 will have five target makers in order to navigate Hayabusa2 more accurately at the touchdown (Hayabusa has three target makers).

The mission payloads of Hayabusa2 are summarized in Table I. As for the science, we have four instruments; Multiband Imager (ONC-T), Near IR Spectrometer (NIRS3), Thermal IR Imager (TIR), and Laser Altimeter (LIDAR). ONC-T and LIDAR are almost same as those of Hayabusa, although the filter of ONC-T is changed slightly. NIRS3 is the same as NIRS of Hayabusa, but the wavelength is different. Since we want to study the absorption by water, NIRS3 must observe 3 μm wavelength. TIR is new for Hayabusa2, but we have already developed it for the Venus mission of Japan, "Akatsuki" (PLANET-C).

Other mission payloads are the sampler and the small rover (MINERVA2) , which were the payloads of Hayabusa. They will be a little changed from those of Hayabusa, but the basic functions are similar. The completely new payload is Small Carry-on Impactor (SCI), which is already mentioned in the previous subsection.Another new payload is a small lander called MASCOT, which is mentioned in the next sub-section.

2.4 International Collaborations

At present three international collaborations are under consideration. One is the collaboration with DLR (The German Aerospace Center). DLR provides a small lander called MSCOT (Mobile Asteroid Surface Scout). MASCOT will have four science payloads to investigate the surface properties of 1999 JU3. The second collaboration is with NASA (The National Aeronautics and Space Administration). The collaboration with NASA was done for Hayabusa, so similar collaboration is under consideration for Hayabusa2. The third collaboration is with the government of Australia for the capsule reentry.

Table I: Payloads of Hayabusa2

Payloads	Specifications
Multiband Imager (ONC-T)	Wavelength: 0.4 – 1.0 μm, FOV: 5.7 deg x 5.7 deg, Pixel Number: 1024 x 1024 px, filter (ul, b, v, w, x, p, Wide)
Near IR Spectrometer (NIRS3)	Wavelength: 1.8 – 3.2 μm, FOV: 0.1 deg x 0.1 deg
Thermal IR Imager (TIR)	Wavelength: 8 – 12 μm, FOV: 12 deg x 16 deg, Pixel Number: 320 x 240 px
Laser Altimeter (LIDAR)	Measurement Range: 30 m – 25 km
Sampler	Minor modifications from Hayabusa
Small Carry-on Impactor (SCI)	Small, deployed system to make an artificial crater on the surface
Separation Camera (DCAM)	Small deployable camera to observe the SCI operation
Small Rovers (MINERVA-2)	Almost same as MINERVA of Hayabusa
Small Lander (MASCOT)	Provided by DLR

3. Target of Hayabusa2

As it is already mentioned in the previous sections, the target object of Hayabusa2 is Asteroid (162173) 1999 JU3, which is C-type asteroid. The observation campaign for this asteroid was done in 2007 and 2008. We know the physical parameters of 1999 JU3 as shown in Table II ([1], [2]). The size is about 920m in diameter, so it is larger than Itokawa but still it is very small object. The shape estimated up to now is not so elongated like Itokawa (Fig. 5). The spin period is about 7.6 hours and this is rather shorter than Itokawa, the spin period of which is 12hours. However, for the purpose of the sample collecting, this spin rate is no problem. The albedo of 1999 JU3 is small, because it is C-type asteroid.

Fig.6 shows the orbit of 1999 JU3. The orbit is

Table II: Physical parameters of Asteroid 1999 JU3

Parameter	Value
Spin period	0.3178 day (~7.6h)
Spin axis	(λ,β) = (331, 20) Kawakami model = (73, 62) Müller model
Ratio of axis	1.3 : 1.1 : 1.0
Size	0.87±0.03 km
Albedo	0.070±0.0006
Magnitude	H=18.82±0.021,G=-0.110±0.007
Type	Cg

(λ,β) = (ecliptic longitude, ecliptic latitude)
These data were reported by [1] and [2].

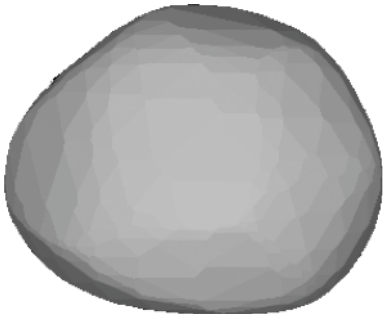

Fig.5: Estimated shape of 1999 JU3 based on Müller model.

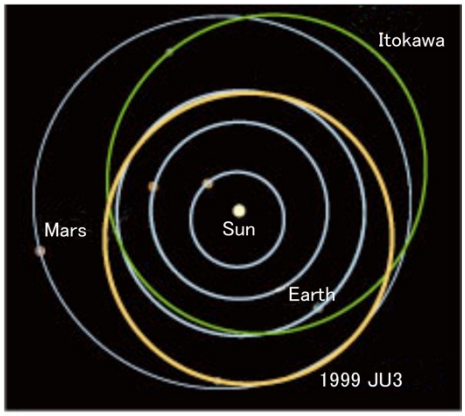

Fig.6: The orbit of 1999 JU3

similar to that of Itokawa, and it is orbiting from just inside the orbit of the earth to just outside the orbit of Mars. The inclination of the orbit is small like Itokawa. Such orbit is suitable for a small spacecraft like Hayabusa2 to reach and go back to the earth.

The observations of 1999 JU3 were done in 2011 and 2012, and we have already had some new results of observation. We think we can get more information about the physical properties of 1999 JU3. Especially the orientation of the spin axis is quite important to make the mission scenario around the asteroid, so we hope that we can get much precise values of the spin axis from the observations in 2011 and 2012.

4. Summary

In Japan, we do not have so many planetary missions, but most of our missions are very ambitious and also very advanced. Hayabusa is the most ambitious mission among them, and we have tried many new things that have not been tried yet in the world. Hayabusa gave us a lot of very precious experiences. Although there were many unexpected things and problems during the mission of Hayabusa, we could manage the mission up to the final stage. Based on such experiences, we are planning the next mission, Hayabusa2. Hayabusa2 will do the similar mission as Hayabusa, but its technology will be (and should be) much more mature than that of Hayabusa. This is the most important purpose of Hayabusa2 from the point of engineering.

Another important point is the science. Although the main purpose of Hayabusa mission is not science but technology, the results of the scientific study of Itokawa attracted considerable attention from a lot of researchers, because it was the first time that we investigate such a small object of the solar system. We can say that we saw the building block of planets. The first science results were reported in the special issue of the journal of Science in 2006 [3] and the first sample analysis results were also reported in the special issue of Science in 2011 [4]. As for Hayabusa2, science is quite important as well as technology. Therefore, we chose a C-type asteroid 1999 JU3 as the mission target of Hayabusa2. We expect that we can study organic matters and waters at the beginning of the solar system. Asteroid 1999 JU3 is also small object and it is one of the near earth objects. Therefore the study about small near earth objects will be much advanced by Hayabusa2, which will surely contribute to the spaceguard activity.

The small solar system bodies still have a lot of mysteries and potentials for the human in future. We are sure that Hayabusa2 will contribute a lot. After Hayabusa2, we want to plan the next mission, which may totally different from Hayabusa and Hayabusa2. so that we can study the origin and evolution of the solar system much further. Hayabusa was the starting point to the new exploration of the solar system, and Hayabusa2 is the next, and we hope post-Hayabusa2 will follow. We are on the way to the full understanding of our solar system.

References

[1]Kawakami, K., Abe, M., Hasegawa, S., Kasuga, T.,YuSeiJin:The journal of the Japanese Society for Planetary Science, Vol.19, No.1, pp.4-11 (2010), in Japanese.

[2] Müller, T. G., Durech, J., Hasegawa, S., Abe, M., Kawakami, K., Kasuga, T., Kinoshita, D., Kuroda, D., Urakawa, S., Okumura, S., Sarugaku, Y., Miyasaka, S., Takagi, Y., Weissman, P. R., Choi, Y.-J., Larson, S., Yanagisawa, K. and Nagayama, S., Thermo-physical properties of 162173 (1999 JU3), a potential flyby and rendezvous target for interplanetary missions, Astronomy & Astrophysics Manuscript no.15599, November 24 2010.

[3]Hayabusa at Asteroid Itokawa, Science, 312, pp.1327-1353 (2006).

[4]HAYABUSA Dust from Itokawa, Science, 333, pp.1113-1131 (2011).

Space Environments and Missions A – 3

Analysis of Radiation Damage in On-orbit Solar Array of Venus Explorer Akatsuki

Hiroyuki Toyota[*1], Takanobu Shimada[1], You Takahashi[1], Takeshi Imamura[1],
Yuko Hada[2], Hiroaki Isobe[3], Ayumi Asai[3], Takako T Ishii[2], and Daikou Shiota[4]
1 Institute of Space and Astronautical Science, JAXA, Japan,
2 Kwasan and Hida Observatories, Kyoto University, Japan ,
3 USSS, Kyoto University, Japan, 4 Advanced Science Institute, RIKEN, Japan
*Email: htoyota@isas.jaxa.jp
Keyword(s): Space weather, Solar flare, Solar cell, Radiation damage

Abstract

This paper describes an analysis of radiation damage in solar array of Venus explorer Akatsuki observed on orbit. The output voltage of the solar array have shown sudden drops, which are most reasonably associated with radiation damage, three times since its launch. The analysis of these radiation damages is difficult, because no direct observation data of the spectra and the amount of the high-energy particles is available. We calculated the radiation damage using the relative damage coefficient (RDC) method assuming a typical spectral shape of protons.

1. Introduction

JAXA has been operating a Venus explorer Akatsuki, which is on the orbit similar to that of Venus at the moment, since its launch in 2010. We have observed sudden drops in the solar array output voltage three times so far. We presumed that solar energetic protons caused the voltage drops as described later. In this paper, we report the telemetry data and analytical results of the radiation damage. On-orbit observation of radiation damage on solar arrays is limited, though the radiation damage is one of the most important issues of solar arrays. We believe the telemetry data of the Akatsuki is very valuable.

2. Mission Overview

The Akatsuki in flight configuration is depicted in Fig. 1. The spacecraft mass is 502 kg, including the fuel and the oxidizing agent of 189 kg and the observation cameras of 33 kg. It is equipped with two solar array paddles, which are mounted on the north and the south surfaces of the body and rotate to track the sun. Each panel is 1.43 m wide and 1.036 m long, with a boom about 0.9 m long. The front side of the panels are covered by triple junction solar cells with an efficiency of 28.3% from SHARP Corp., recognized as JAXA-QTS-2130/502. The solar cells are covered by 100 μm-thick CMG cover glasses with AR coats. The predicted generated power is more than 480 W at 1.0781 AU and more than 660 W on the Venus orbit. The rear side is covered by optical solar reflectors (OSRs) to lower albedo input from Venus. The designed temperature range of the solar array is –170ºC - +184ºC. The output voltage of the solar arrays are regulated not by a shunt regulator but by a series switching regulator, because the distance between the spacecraft and the sun varies from 0.7 AU to1.07 AU, resulting in large output voltage variation.

The main objective of the Akatsuki mission is to observe a mysterious atmospheric circulation on Venus

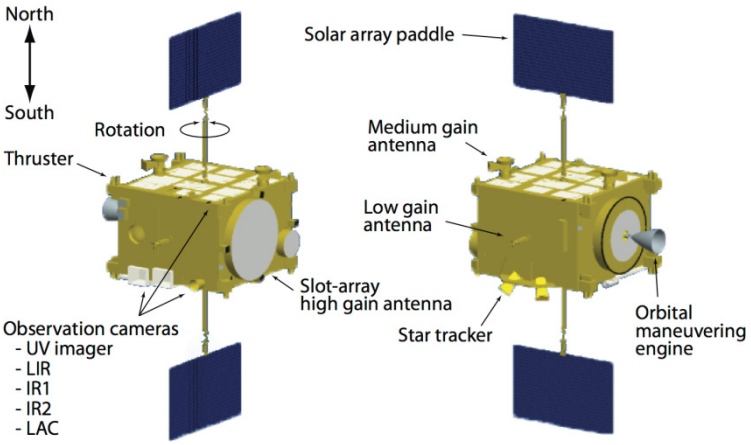

Fig. 1. Venus Explorer Akatsuki

using five cameras covering from ultraviolet to near infrared light.

3. On-orbit Performance of Solar Array

3.1 Operation history

The Akatsuki was launched on May 20, 2010 (UTC) by the H2A launch vehicle. The solar array-related telemetry of the Akatsuki is shown in Fig. 2. At first, the spacecraft went away from the sun to the distance of 1.07 AU, where the solar array temperature was +33ºC. After that, the solar array temperature increased as the spacecraft went nearer to the sun, and reached at +106ºC when it met Venus on December 6, 2010 (UTC). Regrettably the Akatsuki failed in the orbit insertion and is on a orbit around the sun with the perihelion distance of 0.61 AU and the aphelion distance of 0.7 AU. The solar array temperature is between +100ºC and +140ºC, which is below the expected temperature of +144ºC on the orbit around Venus. The output voltage of the solar arrays has been changing according to the temperature. The Akatsuki is expected to meet Venus in November, 2015 again. The mission life extended by 2 years and temperature raise near the perihelion are the important problems for the Akatsuki.

3.2 Radiation damage analysis

The output voltage of the solar arrays have shown sudden drops three times so far as indicated in Fig. 3. Fig. 4 shows the output voltage trend during the first voltage drop on June 5, 2011. It fell gradually by 1.63 V in about two hours.

We examined three possible causes: failure in the electronic circuits, change in the solar array temperature and/or the load, and radiation damage. The possibility of the failure in the electronic circuits was denied, because it is unlikely to cause gradual voltage drop. No change in the solar array temperature or the load that could cause the voltage drop was not observed. Radiation damage could cause the gradual voltage drop shown in Fig. 3, and we confirmed occurrence of two large solar flares that correspond to the voltage drop.

It is, however, difficult to analyze the solar flares and the voltage drop for two reasons: the output voltage of the solar arrays are regulated by a series switching regulator, and almost no observation data of solar energetic protons (SEP) generated by the flares are available. When output voltage of solar array is regulated by a series switching regulator, the operation point on the current and voltage (IV) curve comes to the constant voltage part, resulting in difficulty in estimating the entire IV curve or at least the short circuit current (I_{sc}), the open circuit voltage (V_{oc}) or the maximum power (P_{max}). Fig. 4 shows the positions of the Akatsuki, the sun and the earth, and the direction of the corona mass ejection (CME) which could cause the voltage drop. The Akatsuki was on the opposite side of the sun from the earth when the CME was released, therefore, the energy spectrum of the SEP was not observed by any satellites. Optical images captured by the STEREO satellite of NASA were the only

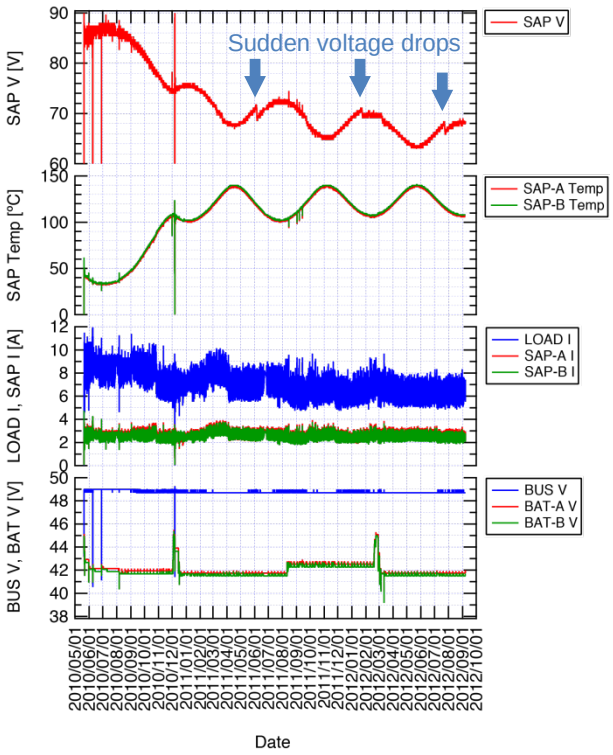

Fig. 2 Solar array-related telemetry data since launch.

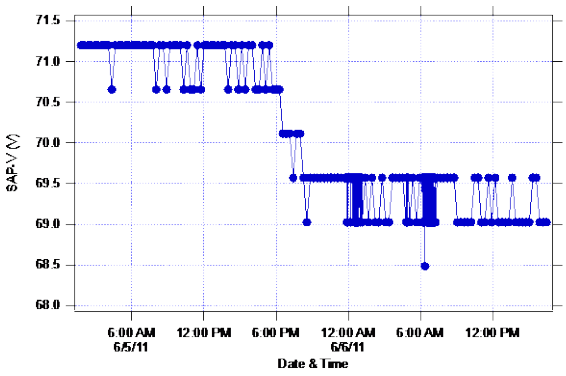

Fig. 3 Solar array output voltage trend showing sudden voltage drop on June 5, 2011.

observation data available. We took two approaches to estimate the SEP spectrum. Firstly we estimated the SEP spectrum from the CME speed, but the calculated degradation did not agree with the observation. Then we calculated a SEP spectrum which gives degradation which agrees with the observation. The following is the procedure and the results of the analysis. We used the relative damage coefficient (RDC) method to estimate the degradation of the solar cells in both approaches.

Fig. 5 shows ultraviolet (UV) images and white-light coronagraphs taken by the STEREO/Ahead satellite. Fig. 5 (a) and (b) shows the first flare (flare 1), which occurred at around 6:50 on June 4, 2011, and (c) and (d) shows the second flare (flare 2), which occurred at around 21:50 on the same day. From successive pictures captured by the STEREO/Ahead satellite, we estimated the speed of the CME 1 and the CME 2 to be 1200 km/s and 2200 km/s respectively at their occurrence. The CME 2 is supposed to catch up the CME 1 and they were merged before hitting the Akatsuki. Fig. 6 shows the relationship between the proton intensity and the CME speed when two CMEs occurs successively [1]. We assumed a typical SEP spectrum shown in Fig. 7 [2]. Actually we estimated the degradation of the solar cells based on several different shape of SEP spectra, but they did not make a significant difference, because the degradation is dominated by protons of 4-5 MeV as seen from the RDC shown in Fig. 8. From the relationship shown in Fig. 6, the Proton intensity is estimated to be 10^2-10^4 cm^{-2} s^{-1} sr^{-1}, because the speed of the CME 2 was 2200 km/s. We changed the SEP fluence so that the integral proton fluence over 10 MeV is 10^4 cm^{-2} s^{-1} sr^{-1} keeping the spectral shape shown in Fig. 7. Calculated IV curves before and after the voltage drop are shown in Fig. 10 as a green and a blue line respectively. The telemetry data are also shown as green and red crosses. The estimated degradation is too small to explain the observed voltage drop.

Next, we calculated a SEP spectrum which causes the same amount of degradation in the solar cells as the observation. Fig. 9 shows the result. The degraded IV curve is shown as a red line in Fig. 10. The SEP spectrum

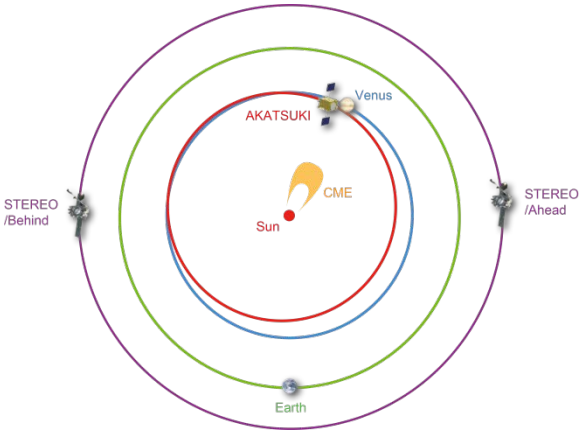

Fig. 4 Position of Akatsuki, Earth and Venus when solar array voltage dropped.

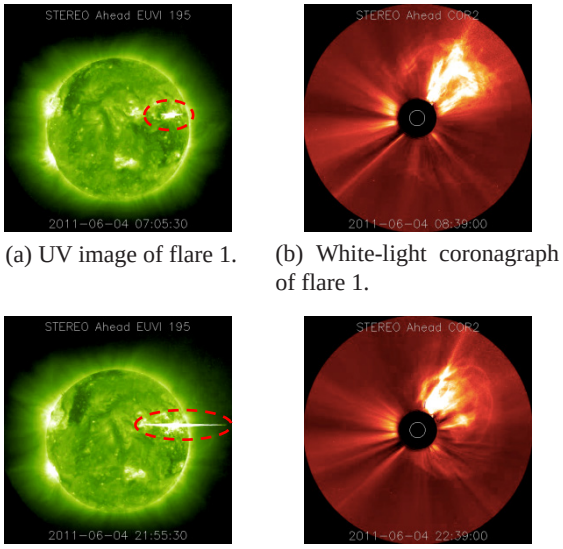

(a) UV image of flare 1.

(b) White-light coronagraph of flare 1.

(c) UV image of flare 2.

(d) White-light coronagraph of flare 2.

Fig. 5 Optical images of solar flares that could cause voltage drop captured by STEREO/Ahead satellite.

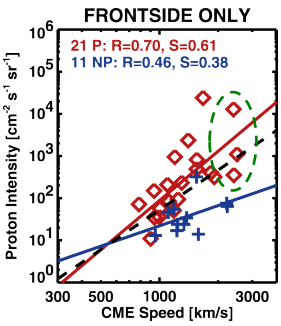

Fig. 6 Proton intensity over 10 MeV vs corona mass ejection (CME) speed [1].

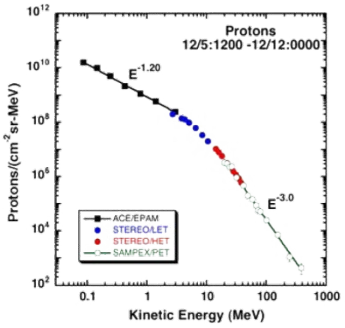

Fig. 7 Solar proton spectrum used for analysis [2].

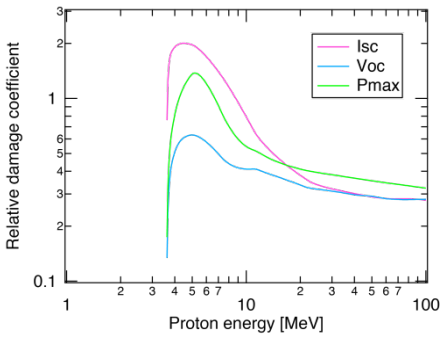

Fig. 8 Relative damage coefficients of solar cells for Akatsuki.

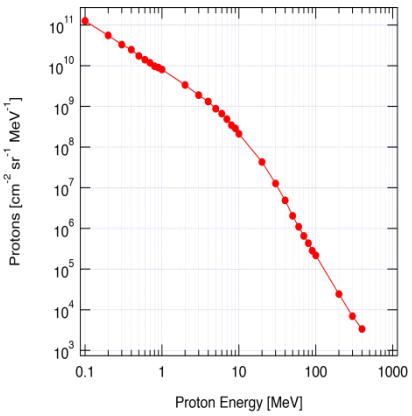

Fig. 9 Solar proton spectrum which gives radiation damage corresponding to observed voltage drop.

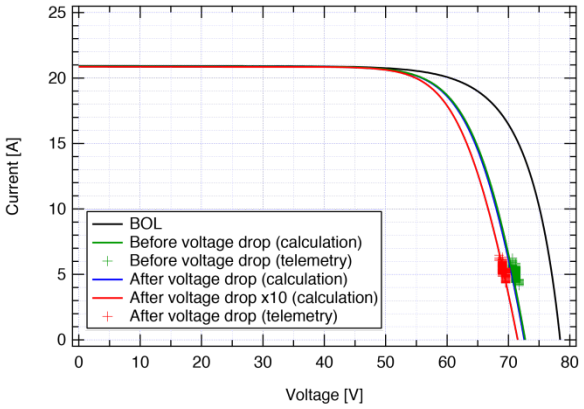

Fig. 10 IV curves calculated using RDC method and telemetry data before and after solar array output voltage drop.

shown in Fig. 9 is ten times as intense as that shown in Fig. 7 and at the same level as the most intense SEP on record. Though no proof of this SEP spectrum can be shown, it is at least within the realm of possibility.

4. Summary

This paper reported telemetry data of the solar arrays for our Venus explorer Akatsuki, which is on a orbit similar to that of Venus. Sudden voltage drops of the solar array were observed three times so far. Since estimating the entire IV curve is difficult due to the use of a series switching regulator and no observation data on the solar energetic protons are available, we calculated the spectrum of the protons which could cause the observed voltage drop using the relative damage coefficient method. The calculated spectrum was at the same level as the most intense one on record.

Acknowledgments

We would like to express our gratitude to Dr. Kazunori Shimazaki of JAXA for providing the RDC data of the solar cells.

References

[1] N. Gopalswamy *et al.*, Journal of Geophysical Research, Vol. 109, A12105 (2004).
[2] R.A. Mewaldt *et al.*, Proceedings of 30th International Cosmic Ray Conf., pp. 107-110 (2008).

Space Environments and Missions A – P1

Research of the radiation tolerance in space environment of general electronic devices

Takahiro MAEDA[*1], Yukitaka KAKIMI[1], Kenji AKASHI[1],
Takeshi OHSHIMA[2] and Shinobu ONODA[2,]
1 Advanced Engineering Services Co., Ltd. (AES), Japan
2 Japan Atomic Energy Agency (JAEA), Japan
*Email: t_maeda@aes.co.jp
Keyword(s): small satellite, general electric devices, single event effect

Abstract

In small satellite development, general electronic (COTS) devices are needed to use due to some severe restrictions of resource for installed components. For this reason, it is important to keep reliability for using COTS devices in small satellite development. Therefore, in order to ensure reliability for small satellite, our company has evaluated COTS devices mainly for tolerance of single event at Japan Atomic Energy Agency (JAEA) Takasaki Advanced Radiation Research Institute from fiscal year 2008.

1. Introduction

We are developing 50cm-class small satellite, “SOCRATES” (See Fig. 1), which will be launched in 2013. Spacecraft generally use high reliability devices, such as devices for space. However there are many severe restrictions of power, size and so on for components of small satellite, we have to use COTS devices which are favorable than devices for space. But radiation tolerance of COTS devices is not understood. For this reason, it is important to keep reliability by radiation tests for using COTS devices in small satellite development.

We have evaluated COTS devices mainly for single event tolerance at Japan Atomic Energy Agency (JAEA) Takasaki Advanced Radiation Research Institute from fiscal year 2008.

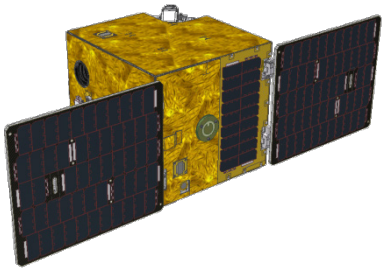

Fig. 1. Our satellite "SOCRATES"

In this paper, we report how to conduct the tests, the method of evaluation and their results.

2. Effects of radiation to electronic devices

In the space environment, various failures are caused to electronic devices by space radiation such as β, γ, proton and heavy-ion. Total ionization dose (TID) effect arose by β, γ and proton is a performance degradation of electronic device by space radiation. Since we plan a short term operation (One year) for our small satellite, we believe that risk of failure caused by TID effect is very small. However, single event effect (SEE) may occur in a short term operation, because it is caused by even one particle, and it can lead to a fatal error of satellite. Therefore, it is required to understand single event tolerance of electronic device to ensure reliability.

3. Test and evaluation method

The radiation test is conducted by using AVF cyclotron of JAEA Takasaki Advanced Radiation Research Institute. In this test, test circuit board is made for every specimen, and installed in a chamber on the beam line (See Fig. 2). During the test, specimen is operated and its consumption current, output voltage, etc. are monitored from outside of a chamber. We can evaluate linear energy transfer (LET) dependence of single event because we use 4 kinds of different LET rays, i.e. Nitrogen, Neon, Argon, and Krypton. Radiation test is conducted with over 10^6 fluencies for each kind of rays.

In evaluation of the tolerance, we presume threshold of LET and cross-sectional area for single event from test results, and then evaluate on-orbit single event probability with on-orbit integral flux of heavy-ion calculated by Cosmic Ray Effects on Micro-Electronics (CREME).

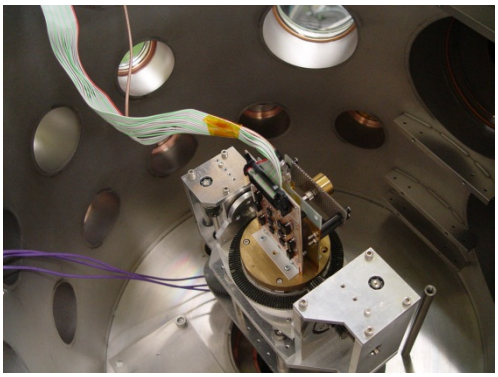

Fig. 2 Test circuit boad in the chamber

4. Test result and utilization

The test results of Field Effect Transistor (FET), Micro-Processing Unit (MPU) and multiplexer (MUX) which will be loaded in SOCRATES are shown in Table I. As shown in Table I, we figured out that FET, MPU and MUX have low probability of single event occurrence in assumption orbit during operating term and sufficient reliability for loading to SOCRATES.

Thus, we can use COTS devices in our small satellite development with satisfying resource restriction and ensuring reliability.

Finally, all specimens are COTS devices, which are not made for the space environment. The test results are probabilities of occurrence predicted when they are brought to orbit, and these do not mean the superiority or inferiority of parts.

Table I. Single Event Probability

No.	Specimen	Evaluation Item*1	Single Event Probability	Installed Component
1	FET	SEGR	< 0.16 [event/year]@max. rating	PCU (See Fig. 3)
			< 10^{-8} [event/year] @63% rating	
2	MPU	SEL	< 0.08 [event/year]	VSGA (See Fig. 4)
		SEU	< 0.007 [bit/year]	
3	MUX	SEL	< 10^{-10} [event/year]	OBC (See Fig. 5)

*1
SEGR: Single Event Gate-Rapture
SEL: Single Event Latch-up
SEU: Single Event Upset

Fig. 3 PCU (Power Control Unit)

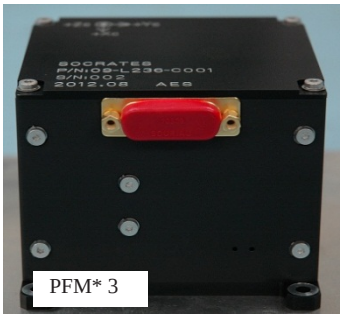

Fig. 4 VSGA (Vibrating Structure Gyroscope Assembly)

Fig. 5 OBC (On Board Computer)

* 2 BBM: Bread Board Model
* 3 PFM: Proto Flight Model

Session B

Space Solar Cells and Related Materials

The Impact of Ultraviolet Radiation in High Temperature Space Missions

Claus G. Zimmermann
EADS ASTRIUM
81663 Munich
Germany
Email: claus.zimmermann@astrium.eads.net
Keyword(s): UV radiation, solar cell, high temperature

Abstract

Concentrated ultraviolet (UV) radiation in combination with high temperature was found to constitute an aggressive environment for standard space photovoltaic assemblies. A high intensity, high temperature (HIHT) environment, typical for missions to the inner planets of the solar system like Mercury, characterized by temperatures of 500 K and 11 solar constant irradiance in the UV region below 400 nm, was simulated in vacuum. Independently of the triple junction cell technology used, module degradation up to 20 % in maximum power was observed during several hundred hours of test. Electroluminescence analysis identified discrete top cell shunts close to the cell edge, in particular around the front side contact pads. Cross-sectional transmission electron microscopy performed on several degraded cells revealed an etched contact pad metallization / cap layer interface and more importantly, several 100 nm large, oriented Cu_3P inclusions at the shunted locations. A chemical degradation mechanism is proposed. Short wavelength UV light interacting with polysiloxanes used as module encapsulant produces hydrogen and methyl radicals. With these building blocks an organic acid can be formed on external reaction surfaces like the Ag busbars that simultaneously serve as a source of oxygen. Cu traces present in the Ag segregate to the surface and are transported by this acid to the contact pad of the cell in the liquid phase. This UV induced degradation mechanism is also able to explain the distinctly non-equilibrium surface morphology found on Ag surfaces after HIHT exposure: Ag particles of different aspect ratios, 50–1000 nm in size, including a small fraction of nanorods, had formed on the surface.

1. Introduction

For the success of high intensity, high temperature (HIHT) missions to the inner region of the solar system it is important to understand how the solar array, one of the most exposed subsystems, behaves in this environment. To phrase the question more specifically: Is a stable operation of the photovoltaic assembly (PVA), consisting of the solar cell and its immediate surroundings, possible in a HIHT environment? As a model environment the HIHT conditions typical for the joint JAXA / ESA mission Bepi Colombo to Mercury were chosen. These are characterized by maximum temperatures of 230 °C, combined with 11 solar constants irradiation. Since the ultra-violet (UV) part of the spectrum below 400 nm is assumed to be the most damaging, the focus in this work was to reproduce the solar irradiance in this wavelength regime accurately, while neglecting the longer wavelength part of the spectrum.

2. High temperature UV testing

PVA representative samples were prepared. The carbon fiber structure was replaced by an Al plate, but all sun exposed parts of the PVA were reproduced accurately. The multijunction cell was assembled with a 100 µm thick cerium doped CMX coverglass. A transparent Pt addition cured silicone was used as a coverglass adhesive. Another addition-cured silicone served as laydown adhesive to bond the solar cell assembly to the Kapton surface. The 50 µm thick Kapton foil was in turn bonded with the same adhesive on the Al plate. The electrical interconnection was performed with Ag interconnectors welded to Ag busbars. For external connection, Kapton insulated, Ag plated Cu wires were attached. A photograph of this sample configuration is shown in Fig. 3.

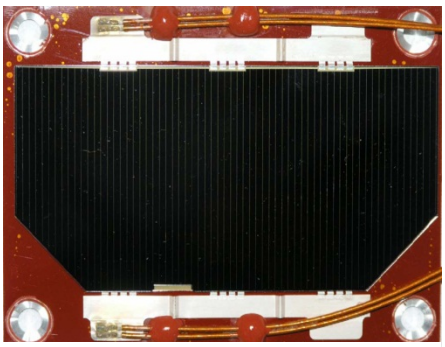

Fig. 3: PVA representative sample layout. The carbon fiber structure was replaced by an Al plate. A Kapton foil was bonded with silicone adhesive containing iron oxide particles to the Al plate, which explains the red color.

To cover a broad range of technologies, different current multijunction cell technologies were tested, labeled A - D. In addition, the outermost cell surface, the antireflection (AR) coating, which interfaces with the surrounding materials, was varied as well. The standard dual layer TiOx/AlOx AR coating as well as

pure AlOx and no AR coating were used. Furthermore the spatial distribution of the AR coating was varied. Shadow masking and photolithographic AR structuring can be used to ensure that the welding pads remain free of AR coating. The shadow mask technique leads to a larger AR free area.

Specialized vacuum chambers available at the European Space Research and Technology Center (ESTEC) of ESA were used to simulate the UV high temperature environment. An external array of up to 8 specialized arc discharge lamps produced the UV radiation that entered the chamber through a fused silica viewport. The integrated intensity between 200 and 400 nm was measured and adjusted at the desired number of solar constants. The samples were mounted on a base plate with heating and cooling capacity to reach the desired sample temperatures during test. A liquid nitrogen cooled cold shroud reduced the base pressure to the low 10^{-6} Torr range. 3 similar facilities were available at ESTEC and were used in a series of UV tests that accumulated several thousand actual hours of UV exposure. The results of a particular illustrative test are outlined here.

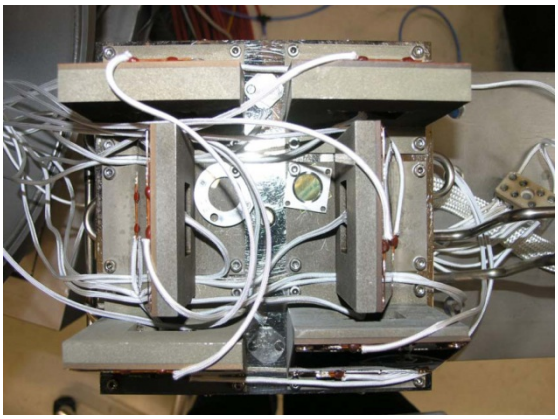

Fig. 4: Test setup for high temperature UV testing under inclined conditions.

Six 8 x 4 cm^2 sized multijunction solar cells did fit in the same test chamber as illustrated in Fig. 4. To reduce the effective solar irradiance and thus the array temperature, the PVA is often operated under high inclination angles in HIHT missions. This was reproduced in this particular test as well with the help of Al prisms that allowed to position the cell normal at angles α of 60°, 70° and 80° relative to the incident UV radiation. The details of the sample configuration tested are summarized in Table 1. The test was performed at 230 °C and 11 solar constants for two exposure durations of 600 h each. 3 samples were replaced after the first phase by 3 new samples.

Table 1: Maximum power degradation P_{max} in a two phase UV test of 600 h test duration each.

cell	description	α	P_{max} 600 h	P_{max} + 600 h
1	cell A, AlOx AR (s)	70°	-2.6 %	-3.5 %
2	cell A, TiOx/AlOx AR (s)	60°	-5.0 %	-7.1 %
3	cell A, w/o AR	80°	-1.8 %	-13.8 %
4	cell C, AlOx AR (s)	70°	-19.0 %	n/a
5	cell B, TiOx/AlOx AR (p)	70°	-9.0 %	n/a
6	cell A, AlOx AR (s)	80°	-8.1 %	n/a
7	cell A, AlOx AR (s)	80°	n/a	-2.2 %
8	cell A, AlOx AR (s)	70°	n/a	-11.7 %
9	cell A, AlOx AR (s)	70°	n/a	-11.9 %
s: shadowmask structuring p: photolithographic structuring				

The changes in maximum power output P_{max} of the cells before and after exposure are summarized in Table 1. The results of this UV test show all typical features of the HIHT degradation corroborated by several similar tests. There is always significant statistical spread in the data, i.e. there are always some cells like cell 1 that degraded by only 3 %, in line with pure darkening in the coverglass adhesive, while other cells degraded in the ≈ 10 % range. In some cases degradations up to 20 %, as for cell 4, were measured. This performance degradation was not related to the cell technology used. The behavior of cell 3, which was stable in the first phase, but started to degrade in the second phase was observed only in this instance.

In order to identify the root cause of this unexpected degradation, a set of specifically designed tests was carried out. They contained the triple junction solar cell and only a limited number of material combinations. Worst case test conditions of 230 °C and 11 solar constants under perpendicular incidence were chosen. The nominal test duration was 400 h. Each test included an identical set of six 8 x 4 cm^2 sized solar cells. Cells 1 and 2 were B type cells with a photolithographic TiOx/AlOx AR coating, cell 3 was an A cell with a shadow mask TiOx/AlOx coating, cells 4 and 5 A type cells with an AlOx shadow mask coating, and cell 6 represented an A cell completely without AR coating. Only in the first test, the bare cell test, cell 4 was replaced by a D type cell with shadow mask TiOx/AlOx AR coating and cell 5 was another A cell with TiOx/AlOx coating.

In the bare cell test (test 1), the cells were mounted with the help of 5 small magnets embedded in the Al sample plate. A fused silica window, completely UV transparent, was placed on the cell and supported the corresponding magnets applied on top of the cell. The frontside cell interconnector was welded directly onto an Ag foil that protruded from underneath the cell thus ensuring short circuit conditions during test. No other PVA material was present in the test. On cells 2, 3, 5 and 6 a CMX coverglass was placed underneath the fused silica window to expose the cell surface to the realistic, filtered UV radiation. The first additional PVA material investigated in test 2 was the coverglass adhesive. 100 µm thick CMX coverglasses were bonded onto the cell

with a transparent silicone adhesive. The remainder of the sample configuration was identical to the bare cell test. In the next test group, test 3, a silane primer was applied in addition on the cell rearside. The final three testgroups all contained the laydown silicone adhesive. They all resembled the sample layout illustrated in Fig. 1, including the Kapton foil, Ag busbars and Kapton insulated wiring. Three different combinations were tested. Test 4 used in addition coverglass adhesive, but no primer on the cell rearside, test 5 the silane primer, but no coverglass adhesive and test 6 used neither coverglass adhesive nor primer. In the last two configurations the cell was protected by a 100 µm CMX coverglass, that was attached with the help of the fused silica / magnet configuration.

Table 2: Relative P_{max} degradation of different cell / PVA material combinations during a 400 h, 11 solar constant UV irradiation at 230 °C

cell	Description	test 1: bare cell	test 2: only coverglass adhesive	test 3: coverglass adhesive + primer	test 4: coverglass + laydown adhesive	test 5: laydown adhesive + primer	test 6: only laydown adhesive
1	cell B, TiOx/AlOx AR (p)	0.9	-2,2	-3,4	-8,6	-5.1 / -9,2**	-4,9
2	cell B, TiOx/AlOx AR (p)	-0.9	-3,3	-5,3	-4,7	-5.2 / -9,4**	-9,6
3	cell A, TiOx/AlOx AR (s)	1.9	-12,1	-11,0	-4,7	--	--
4	cell A, AlOx AR (s)	0.9*	-4,3	-2,6	-2,8	-4.1 / -7,4**	-7,6
5	cell A, AlOx AR (s)	--	-4,5	-4,2	-2,6	-7.3 / -13,3**	-9,7
6	cell A, no AR	0.4	-4,2	-4,7	-2,5	-9.1 / -16,5**	-8,5

* cell replaced by cell D, TiOx/AlOx AR (s)
-- cell mechanically damaged during test
** extrapolated linearly from 240 h to 400 h
s: shadowmask structuring
p: photolithographic structuring

The change in performance is summarized in Table 2. Several important conclusions can be drawn from these tests. First and foremost, it can be concluded from test 1 that bare cells do not degrade, despite the fact that the test duration was shortened to 200 h in this case. Degradation, however, started to occur as soon as silicones were present, either in their function as laydown or as coverglass adhesive. The remaining PVA materials did not appear to make any difference. Likewise, the degradation showed no correlation to the cell type and AR configuration used. A pronounced difference, however, could be observed between the test groups in which the coverglass was bonded with silicone adhesive, i.e. test 2, 3 and 4, and the test groups 5 and 6 which featured comparably unprotected cell surfaces. The average degradation in the latter group is ≈ 8 %, twice as high than the average degradation observed in the first group. It has to be noted that the duration of test 5 was only 240 h, therefore the results were extrapolated linearly to 400 h.

This implies that the coverglass adhesive can both act as a source of the degradation as in tests 2 and 3, but at the same time also function as a barrier against it. This barrier seems to limit the degradation to 4 % in most cases, but in every test there was at least one cell where it apparently failed to work and the cell degraded as much as the unprotected cells in tests 5 and 6. It was verified experimentally that photovoltaic assemblies according to Fig. 3 did not degrade upon exposure to high temperature alone, without the presence of UV light. The degradation mechanism is thus linked to a photochemical reaction of the silicones initiated by UV light. Coverglass as well as laydown adhesive are both methyl-phenyl polysiloxanes, which have an absorption maximum at ≈ 260 nm [1]. Only this short wavelength light can initiate photochemical processes. For longer wavelength UV light they are highly transparent and no energy is absorbed. This explains the partly protective nature of the coverglass adhesive. The adhesive behind the coverglass is protected from UV light below 325 nm, since this part of the spectrum is absorbed in the glass itself. Only silicones which are exposed to the UV irradiation directly either at the cell edge or at reaction surfaces external to the cell can contribute to the degradation.

3. Discussion

3.1 Microanalysis

The IV curve of cell 4 according to Table 1 is shown in Fig. 5, which exhibits the typical features of a highly degraded cell. The IV curve changes its slope around 1.5 V, which is indicative of an ohmic shunt in one subcell. The fact that Voc is reduced as well indicates the presence of an additional diode like shunt component. Electroluminescence imaging is ideally suited to identify the location of shunts both spatially as well as in depth [2,3]. The middle cell electroluminescence image of cell 4, illustrated in Fig. 6, shows bright half moon shaped areas around the three frontside contact pads. The top cell electroluminescence image of cell 4 was exactly

inverse, with dark areas appearing at the contact pads. This is the signature of a shunt located in the top cell. The intensity of the half moon shaped areas increases towards the cell edge, as highlighted by the inset in Fig. 6. The shunts, which act as a current sink and affect the electroluminescence image in this characteristic fashion, thus have to be located very close to the cell edge.

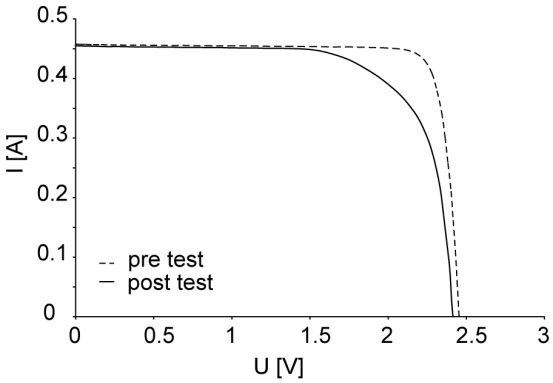

Fig. 5 : IV curve of cell 4 in Table 1 before and after test showing a large fill factor degradation

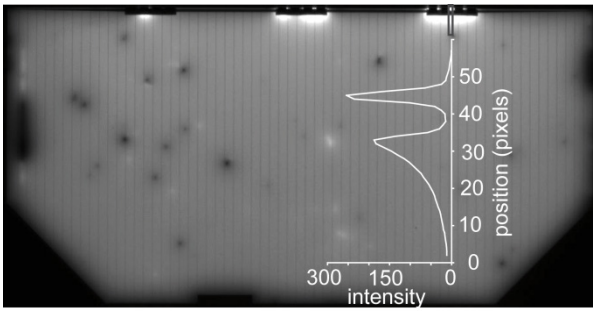

Fig. 6 : Middle cell electroluminescence image of cell 4 according to Table 1. The inset shows an intensity profile along the area indicated on the right contact pad.

To be able to analyze the shunts with standard analytical techniques, their exact position had to be determined with orders of magnitude better resolution than used in Fig. 6. For this investigation, a degraded cell (cell 6 from test 6 according to Table 2) without coverglass adhesive was chosen. The interconnector fingers at one contact pad were cut at the busbar and bent backwards. With a specialized electroluminescence setup [3], discrete shunts were located in the approximately 30 µm wide active cell region between the contact pad and the cell edge. Since the electroluminescence image had a µm resolution the position of the shunts could be identified with sufficient accuracy in a scanning electron microscopy (SEM) image acquired from the same area. A typical example is shown in Fig. 8. At discrete positions, always correlated to the location of the shunts in the electroluminescence image, a foreign substance is present at the edge of the contact pad. It appeared to be creeping from the contact pad onto the cell and had the morphological appearance of a dried liquid. Similar observations at the outermost cell edge, also highlighted in Fig. 8, further strengthen this observation. On untested samples similar areas were never observed.

At the most serve shunt of cell 6 from test 6, a cross sectional sample was prepared by focused ion beam (FIB) processing. The sample was further thinned to electron transparency and imaged in a transmission electron microscope (TEM), as shown in Fig. 7. The top cell region, extending about 2 µm underneath the contact pad is shown in Fig. 7a. The area highlighted in red is created as a result of the cap etch step during cell manufacturing and not test related. Three test related features, however, could be observed: i) The top cell surface is etched locally. The etching starts at the position where the foreign substance touches the top cell surface and proceeds underneath the contact pad. ii) Within the top cell surface, shown in higher magnification in Fig. 7b, Cu_3P inclusions are found as confirmed by the energy dispersive X-ray analysis plotted in Fig. 7c. These Cu_3P inclusions, next to the etching of the top cell, sufficiently explain the electrical degradation of the cell. They are

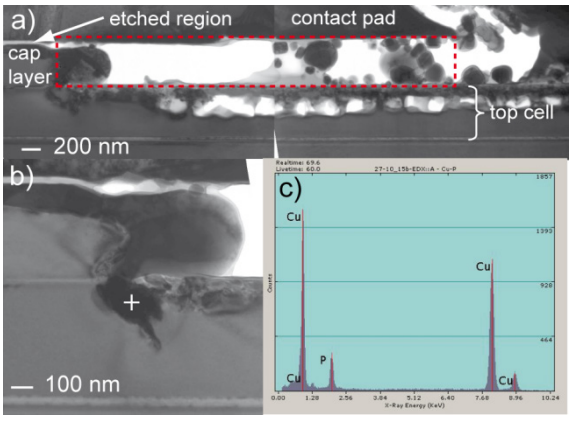

Fig. 7 : a) TEM cross-section through a shunted area of cell 6 from test 6. The area highlighted in red is caused by the cap etch process during cell manufacturing. A higher magnification image shown in b) reveals inclusions in the top cell which are identified by EDX measurements (c) as Cu_3P.

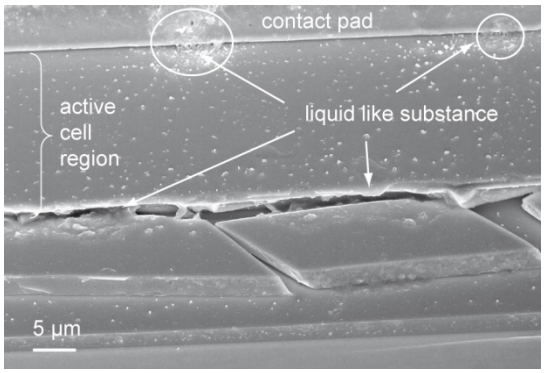

Fig. 8 : Scanning electron microscope (SEM) image of the outermost active cell region located underneath an interconnector finger. The shunted cell locations are highlighted by a circle.

both considerably larger than the top cell emitter thickness. iii) Another feature visible in Fig. 7a is the underetching that developed between the contact pad and the GaAs cap layer. By peeling off part of the contact pad a SEM analysis confirmed that this underetching occurs to a depth of approximately 5 µm, not only at positions were Cu_3P shunts had developed, but along the entire contact pad length.

3.1 Degradation mechanism

An explanation of the detailed failure mechanism is beyond the scope of this paper. Only a brief summary, albeit without the possibility to present all supporting facts [4], can be given here. The root cause test unambiguously proved that a photochemical reaction of silicones, initiated by short wavelength UV light, is essential for the degradation. The microanalysis revealed that cap as well as top cell material at the cell edge in front of the welding pad is etched away in the degraded cells. This is only possible in a liquid phase, with the cell interconnector serving as the transport pathway. This also explains why some cells encapsulated with coverglass and coverglass adhesive are affected as well. Even in this case a transport path along the interconnector can exist in some cells if the coverglass adhesive does not seal the interconnector completely. As cause of the ohmic shunts, Cu_3P inclusions in the top cell have been identified. Since Cu is an element that is not present in the bare cell at all, it has to be transported there as well, presumably by the same liquid-like transport mechanisms.

The only component in the PVA assembly that contains Cu is the Ag busbar and the Ag interconnectors. 0.1 % Cu is present there intentionally in the bulk to improve the mechanical properties of pure Ag by solid solution hardening. Close to the surface, however, Cu is enriched, since this is energetically favorable. The Ag busbar was analyzed by XPS in sputter depth profiling mode. 1-2 % Cu was detected in the first 5 nm. In addition, in a 30 nm layer underneath the surface, an average oxygen content of 10 % was found in the Ag. Finally on top of the Ag surface, a 6 nm thick layer of siloxane fragments was found. This is the result of the outgassing of short chain length silicone fragments in the HIHT test conditions. A CaF_2 witness plate contained a similar amount of silicone.

The Ag busbar is also fully exposed to the entire UV wavelength spectrum. Methyl phenyl polysiloxanes irradiate by short wavelength UV light provide hydrogen and methyl radicals [1]. Together with the oxygen contained in the Ag close to the surface, all building blocks for an organic acid are present. Based on the interaction probability, the formation of the simplest species like formic acid or acetic acid seems to be most likely. Such substances can be present as nm thick surface films even at temperatures of 200 °C and vacuum [5]. Alternatively, simple aromatic carboxylic acids such as benzoic acid, with a much higher boiling point, might form through the abstraction of a phenyl group. Due to the minimal amount of these substances found, they could not be identified directly by analytical techniques. They are, however, a likely explanation for the etching found on the degraded cell. Since Cu containing carboxylic acids are also easily formed, they appear to be also the transport vehicle for Cu to the top cell at the same time. The delivery of Cu to the cell in such an organic form is also well in line with the formation of oriented Cu-P inclusions. For any other delivery method it is very hard to explain the formation of such inclusions in an oriented fashion at the comparatively low test temperatures. A more detailed account of this proposed degradation mechanism can be found in Ref. [4].

The central nature of the busbar in this UV-high temperature cell degradation is further supported by the microstructure of the Ag surface after test. In Fig. 9a a SEM image of the Ag surface is shown. It presents a distinctly non-equilibrium surface morphology: Nanoparticles from 50 to 1000 nm in size have formed, together with a small fraction of nanorods. These features, although consisting of pure Ag, are only loosely attached to the surface and can be easily removed by an adhesive tape. As shown Fig. 9b, they are sitting on top of pits in the Ag

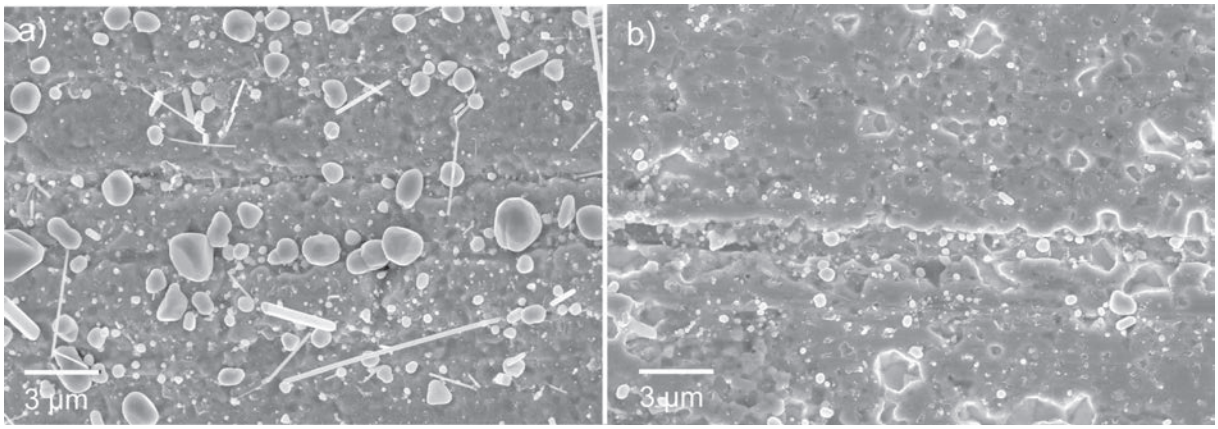

Fig. 5: a) SEM image of the Ag busbar surface morphology after UV testing. Up to micron-sized Ag particles are present on the surface. They can be easily removed by an adhesive tape. b) Pits in the Ag surface now become visible that were obscured by the particles originally. The pits appear to be aligned with Ag grains. Note that images a) and b) do not show an identical area.

surface, which are aligned with grain boundaries in the polycrystalline Ag. As reported in detail in [6], this morphology can be explained by the same photochemical reaction of the silicone layer on top of the busbar. The hydrogen radicals produced in this fashion diffuse very rapidly into the silver along grain boundaries. In pre-existing voids they form water molecules together with the oxygen already present in the Ag. The hydrostatic pressure created by this intrinsic water vapor drives the diffusion of Ag atoms to the surface. Modeling this process [6] results in slightly less than 400 h that are required for a 1 µm sized void with an internal pressure of 9 MPa during growth to form, in line with the experimental timescales.

4. Conclusion

Silicones, which are under standard geostationary environmental conditions a very inert substance, can exhibit a quite different behavior in a HIHT environment. Under short wavelength UV irradiation, reactive hydrogen and methyl radicals are released, which are the source of their aggressive nature. Current triple junction solar cells are nanostructure devices in one dimension, with a top cell emitter thickness below 100 nm. Therefore they are quite sensitive components that can be easily affected. Only a very small amount of Cu is required to create the observed Cu_3P shunts. By using a slightly modified cell design [4], a complete encapsulation of the cell is achieved and a stable operation in a HIHT environment is possible.

References

[1] S. Siegel, R. J. Champetier and A. R. Calloway, "Quantum efficiency of the 2357 Å photolysis of a mixed phenyl-methyl polysiloxane," J. Polymer Science **4**, 2107 (1966)
[2] C. G. Zimmermann, "Utilizing lateral current spreading in multijunction solar cells: an alternative approach to detecting mechanical defects," J. Appl. Phys, **100**, 023714 (2006)
[3] C. G. Zimmermann, "Performance mapping of multijunction solar cells based on electroluminescence," Electron Device Letters **30**, 825 (2009)
[4] C. G. Zimmermann, C. Nömayr, M. Kolb and A. Rucki, "A mechanism of solar cell degradation in high intensity, high temperature space missions" Prog. Photovolt: Res. Appl. 1195 (2011)
[5] H. G. Tompkins and D. L. Allara, ""The study of the gas - solid interaction of acetic acid with a cuprous oxide surface using reflection-absorption spectroscopy," Colloid and Interface Science **49**, 410 (1974)
[6] C G. Zimmermann, "Surface modification by subsurface pressure induced diffusion," Appl. Phys. Lett. 100 (2012) 04

Impacts of proton irradiation on optical and electrical properties of $Cu(In,Ga)Se_2$ thin films and solar cells

M. Sugiyama[*1], L. J. Sharon[1], H. Sakakura[1], Y. Hirose[1], I. Tsunoda[2], K. Takakura[2]
1 Tokyo University of Science, Japan
2 Kumamoto National College of Technology, Japan
*Email: mutsumi@rs.noda.tus.ac.jp
Keywords: CIGS solar cells, proton irradiation, degradation properties

Abstract

The optical and electrical properties of proton irradiated $Cu(In,Ga)Se_2$ (CIGS) solar cells and the thin films that compose the CIGS solar cell structure were investigated. The transmittance and resistivity of transparent conducting oxide window layers remained constant for a fluence of up to 3×10^{15} cm^{-2}. For CIGS thin films, the number of non-radiative recombination center increases under proton irradiation. In CIGS solar cells, decreasing J_{SC} reflected the degradation of the depletion layer of the CdS/CIGS interface. These results constitute the first step in clarifying the degradation mechanism of CIGS solar cells.

1. Introduction

Thin film solar cells composed of polycrystalline $Cu(In,Ga)Se_2$ (CIGS) show high conversion efficiency and excellent radiation tolerance, making them very promising for space applications. In fact, irradiation-damage studies of CIGS solar cells in space have revealed that their electrical properties show relatively less degradation due to proton[1-6], electron[1,4,7-9], or gamma-ray[10] irradiation compared with Si solar cells in case of space satellite application for several years. However, despite many reports on CIGS solar cells[1-3,6-10], the degradation and/or resistance mechanism of these solar cells under irradiation remains to be clarified, because there have been few reports on irradiated CIGS thin films[4,5].

The mechanism of solar cell degradation, as researchers have gradually come to realize, is a complex phenomenon. Apart from irradiation effects, CIGS solar cell performance is known to be influenced by conditions such as damp heat[11,12] or light soaking. For example, Weinert *et al*. reported that the degradation properties of open-circuit voltage (V_{OC}) and short-circuit current density (J_{SC}) are different, and Pern *et al*. reported that the ZnO:Al layer degrades under damp-heat conditions of 85°C temperature and 85% humidity when it is used in CIGS solar cells[12]. Therefore, understanding the degradation properties of each semiconductor composing CIGS solar cells is necessary before using the cells in commercial or space applications.

Our group has previously studied the irradiation effects on transparent conducting oxide (TCO), CIGS, and $CuInSe_2$ (CIS) thin films and CIGS solar cells subjected to alpha rays (irradiation energy: 6.2 MeV, fluence: 1.4×10^5 cm^{-2}), protons (30–70 MeV, 4.9×10^9 cm^{-2}), gamma rays (0.66 MeV, 4.7×10^{14} cm^{-2})[13], and electrons (2 MeV, 1.0×10^{13}–1.5×10^{18} cm^{-2})[14]. We found that particle irradiation tended to degrade primarily around the interfaces of the several layers that compose CIGS solar cells. These results suggest that the interfaces play an important role in defining the solar cell performance. From a scientific viewpoint, an investigation of the irradiation effects on CIGS thin films is needed to reveal the degradation mechanism of CIGS-based solar cells. On the other hand, from an industrial viewpoint, this investigation is needed to clarify the radiation tolerance of a variety of irradiation sources for practical applications. Therefore, in this study, the effects of proton irradiation on the properties of TCO and CIGS thin films are demonstrated by irradiating each thin film that composes a CIGS solar cell structure.

2. Experiment

Single-phase polycrystalline CIGS ($CuIn_{0.8}Ga_{0.2}Se_2$) films with thicknesses of approximately 2.0 μm were prepared by a conventional three-stage process on Mo-coated soda-lime glass (SLG). These films were used to fabricate CIGS solar cells with an undoped ZnO (~100 nm)/CdS (~50 nm) layer by RF sputtering and chemical bath deposition. Finally, several types of window layers (1.0 μm) were deposited by RF sputtering using different TCOs, namely, ITO, IZO, ZnO:Al, and ZnO:Ga. The solar cells exhibited an efficiency of about 7% measured under simulated air mass (AM) 1.5 illumination. TCO thin films were also deposited on bare SLG to enable the investigation of their optical and electrical properties.

CIGS solar cells and the CIGS thin films were irradiated in vacuum without intentional heating. Previous reports show that degradation tends to start at 1×10^{12} cm^{-2} [1,15]; hence, in this study, we applied proton fluence ranging from 1×10^{11} to 3×10^{15} cm^{-2}. TCO and CIGS thin films were irradiated with 200 keV protons. The proton energy was estimated to investigate proton irradiation effect on each part of the CIGS solar cells; the estimation was carried out using Stopping and Range of Ions in Matter (SRIM) simulations[16]. Figure 1 shows

the tracks of protons in CIGS solar cells at (a) 30, (b) 100, (c) 200, and (d) 380 keV, as simulated by SRIM. By adjusting the proton energy, selective regions in the solar cells could be irradiated: (a) only the surface of the window layer (30 keV), (b) from window layer to around *n*-layer (100 keV), (c) through the depletion layer (200 keV), and (d) through the bottom of the CIGS layer (380 keV).

Optical transmittance spectra were measured in the ultraviolet region by using a deuterium lamp and in the visible and near-infrared regions by using a halogen lamp. The transmittance values of the films were deduced by using irradiated bare SLG substrates as references. The resistivity ρ, Hall mobility μ, and carrier density n at room temperature (RT) were measured by the van der Pauw technique. For CIGS thin films and solar cells, photoluminescence (PL) was carried out at 77 K using the 532.0 nm line of a frequency-doubled quasi-cw Nd:YAG laser (60 mW) as an excitation source. Phase-sensitive detection was carried out from 950 to 1550 nm using a 50-cm focal length grating monochromator and liquid-N_2-cooled Ge photodetector. The performance of the solar cells was determined on the basis of the current density–voltage (J–V) curves measured at RT under AM 1.5 and 100 mW/cm^2 illumination.

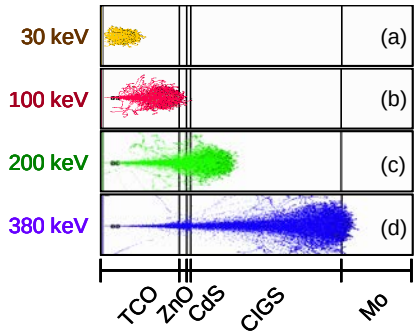

Fig. 1. The tracks of proton in CIGS solar cells with (a) 30, (b) 100, (c) 200, and (d) 380 keV, simulated by SRIM.

3. Results and Discussion

First, the proton irradiation effects on thin films composing the window layer and absorber in CIGS solar cells were investigated. Figure 2 shows the normalized (a) transmittance at 500 nm and (b) resistivity of several TCO thin films, namely, ITO, IZO, ZnO:Al and ZnO:Ga, as a function of irradiation fluence. It should be noted that the normalized values were defined by the values of the transmittance at 500 nm or resistivity after/before irradiation. These transmittance and resistivity values of TCO thin films did not change with respect to proton irradiation. Our group previously reported that the transmittance at 500 nm and resistivity of ITO and IZO did not change for less than 1×10^{18} cm^{-2} electrons and those of ZnO:Al and ZnO:Ga did not change for less than 1×10^{16} cm^{-2} electrons[14]. Moreover, K. S. Chan *et al.* reported that the structure of ZnO did not change at room temperature under 3×10^{16} cm^{-2}. These results indicate that ITO, IZO, ZnO:Al, and ZnO:Ga thin films have a good tolerance to particle irradiation[17], such as proton and electron irradiation at less than 3×10^{15} cm^{-2}.

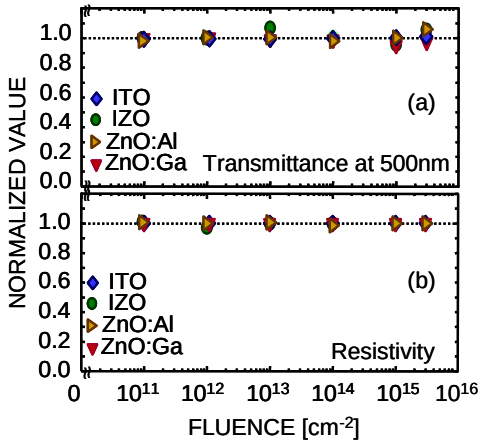

Fig. 2. The normalized (a) transmittance at 500 nm and (b) resistivity of ITO, IZO, ZnO:Al and ZnO:Ga as a function of irradiation fluence.

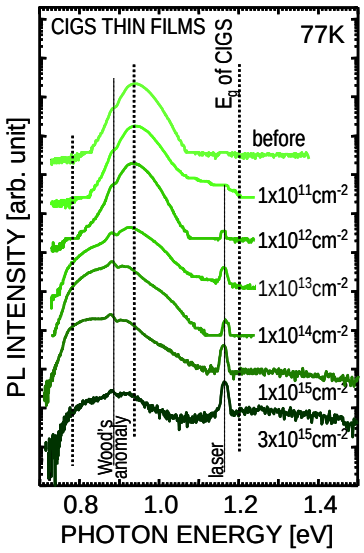

Fig. 3. PL spectra of CIGS thin films at 77 K as a function of irradiation fluence.

The PL spectra of CIGS thin films irradiated with 3×10^{15} cm^{-2} proton fluence are shown in Fig. 3 as a function of proton energy. With increasing irradiation fluence, the PL peak at 0.94 eV tends to disappear and a PL peak at 0.8 eV tends to appear. A previous report also showed that PL peak intensities due to deep level defects of CIGS were decreased under electron[14] and proton[6] irradiation. Note that XRD patterns and surface SEM images did not change (data not shown). Therefore, this result may indicate that the number of non-radiative recombination center increases under proton irradiation.

Next, the effects on proton irradiation on CIGS solar cells were investigated. The PL spectra of CIGS solar cells are shown in Fig. 4 as a function of proton irradiation energy at 3

× 10^{15} cm^{-2} fluence. The PL peak at 0.94 eV disappears under irradiation with 200 and 380 keV proton energy. This result taken together with the simulation results in Fig. 1 indicates that the region around the CdS/CIGS interface, which forms the depletion region of CIGS solar cells, degraded under 200 and 380 keV proton energy.

Finally, the effects of the degraded depletion layer on the electrical properties were investigated. Two normalized electrical performance parameters of the conventional CIGS solar cell, namely, V_{OC} and J_{SC}, were plotted as a function of irradiation fluence for each irradiation energy, as shown in Fig. 5. The proton irradiation energy indicates the degraded position, as mentioned earlier. In the case of 30 keV proton energy, which only degraded the surface of the window layer, V_{OC} and J_{SC} did not change when the fluence was around the order of 10^{15} cm^{-2}. Since the transmittance and resistivity of several TCO thin films did not change, this result indicates that the degradation of the window layer did not affect the solar cells properties. On the other hand, in case of 200 and 380 keV proton energy, which degraded through the depletion layer and through bottom of the CIGS layer, V_{OC} and J_{SC} tend to decrease with increasing irradiation fluence for fluence values greater than around the order of 10^{13} cm^{-2}. These results indicate that the degradation of the depletion layer of CIGS affects CIGS solar cell properties. In the case of 100 keV proton energy, intermediate results between only window layer degradation and through the CIGS layer degradation were obtained. These results taken together with those in Fig. 1 indicate that precisely controlling degraded position around the CdS/CIGS interface is difficult. A further in-depth investigation is needed to reveal the degradation mechanism of CIGS solar cells. Our study is the first step toward realizing practical applications of CIGS solar cells in space and clarifying their degradation mechanism.

4. Conclusion

The effects of proton irradiation on the optical and electrical properties of CIGS solar cells and the layers that compose the solar cell structure, namely, CIGS, ITO, IZO, ZnO:Al, and ZnO:Ga, were measured. The transmittance and resistivity of TCO thin films did not change after irradiation. PL peak intensity of CIGS thin films decreased with increasing proton fluence. The experimental *J–V* properties of CIGS solar cells indicated that the interface of the depletion layer might be weaker than that of the other layers in the bulk. This study partially clarifies the degradation mechanism of CIGS solar cells.

Acknowledgments

The authors thank Dr. S. Yamamoto, Dr. S. Sato, Dr. T. Ohshima, and M. Yoneoka for their contributions to the proton irradiation studies. In addition, the authors would like to thank C. Fujiwara, X. Liu, and Y. Kawasaki for their assistance in conducting CIGS solar cell fabrication. They would also like to thank Dr. K. Tang, Dr. B. Fan, and Prof. S. Kimura for their stimulating discussions. This work was supported in part by Inter-University Laboratory for the Joint Use of JAEA Facilities, Advanced Device Laboratories, Research Center for Green and Safety

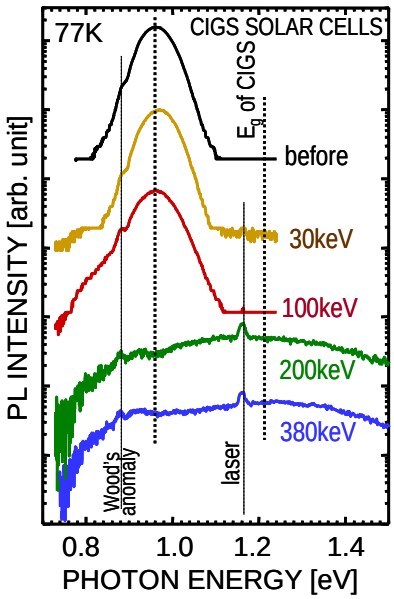

Fig. 4. PL spectra of CIGS solar cells at 77 K irradiated with 3 × 10^{15} cm^{-2} as a function of proton energy.

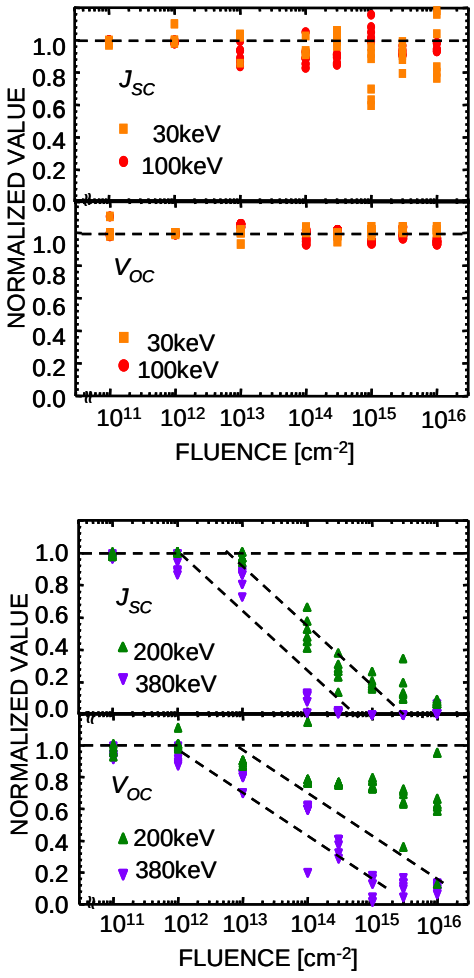

Fig. 5. The normalized (a) J_{SC} and (b) V_{OC} values of CIGS solar cells irradiated with 30 and 100 keV and (c) J_{SC} and (d) V_{OC} values of CIGS solar cells irradiated with 200 and 380 keV as a function of proton irradiation fluence.

Sciences, and Photovoltaic Science and Technology Research Division, under Research Institute for Science and Technology, Tokyo University of Science.

References

[1] A. Jasenek, U. Rau, "Defect generation in Cu(In,Ga)Se_2 heterojunction solar cells by high-energy electron and proton irradiation", J. Appl. Phys., vol. 90, pp. 650-658 (2001).
[2] S. Kawakita, M. Imaizumi, M. Yamaguchi, K. Kushiya, T. Ohoshima, H. Itoh, S. Matsuda, "Annealing Enhancement Effect by Light Illumination on Proton Irradiated Cu(In,Ga)Se_2 Thin-Film Solar Cells", Jpn. J. Appl. Phys., vol. 41, pp. L797-799 (2002).
[3] H. Lee, H. Okada, A. Wakahara, A. Yoshida, T. Ohshima, H. Itoh, S. Kawakita, M. Imaizumi, S. Matsuda, "Effect of proton irradiation on electrical properties of $CuInSe_2$ thin films", Sol. Energy Mater. Sol. Cells, vol. 75, pp.57-63 (2003).
[4] H. Lee, H. Okada, A. Wakahara, A. Yoshida, T. Ohshima, H. Itoh, "Photoelectromagnetic effects on electron and proton irradiated $CuInSe_2$ thin films", J. Appl. Phys., vol. 94, pp. 276-278,(2003).
[5] Y. Akaki, N. Ohryoji, K. Yoshino, S. Kawakita, M. Imaizumi, S. Niki, K. Sakurai, S. Ishizuka, T. Ohsihma, T. Ikari, "Proton irradiation damages in $CuInSe_2$ thin film solar cell materials by a piezoelectric photothermal spectroscopy", Solid-State Electron., vol. 48, pp.1815-1818 (2004).
[6] K. Yoshida, M. Tajima, S. Kawakita, K. Sakurai, S. Niki, K. Hirose, "Photoluminescence Analysis of Proton Irradiation Effects in Cu(In,Ga)Se_2 Solar Cells", Jpn. J. Appl. Phys., vol. 47, pp. 857-861 (2008).
[7] M. Yamaguchi, "Radiation resistance of compound semiconductor solar cells", J. Appl. Phys., vol. 78, pp. 1476-1480 (1995).
[8] A. Jasenek, U. Rau, K. Weinert, I. M. Kötschau, G. Hanna, G. Voorwinden, M. Powalla, H. W. Schock, J. H. Werner, "Radiation resistance of Cu(In,Ga)Se_2 solar cells under 1-MeV electron irradiation", Thin Solid Films, vol. 387, pp.228-230 (2001).
[9] K. Weinert, A. Jasenek, U. Rau, "Consequence of 3-MeV electron irradiation on the photovoltaic output parameters of Cu(In,Ga)Se_2 solar cells ", Thin Solid Films, vol. 431, pp. 453-456 (2003).
[10] V. V. Emtsev, Y. A. Nikolaev, D. S. Poloskin, V. Y. Rud', Y. V. Rud', E. I. Terukov, M. V. Yakushev, "Photosensitivity of Photocells Based on ZnO/CdS/Cu(In,Ga)Se_2 Heterostructures and Exposed to γ-ray Radiation", Semiconductors, vol. 39, pp. 1455-1458 (2005).
[11] R. Sundaramoorthy, F. J. Pern, C. DeHart, T. Gennertt, F. Y. Meng, M. Contreras, and T. Gessert, "Stability of TCO window layers for thin-film CIGS solar cells upon damp heat exposures: part II", Proc. of SPIE, vol 7412, p. 74120J (2009).
[12] F. J. Pern, S. H. Glick, X. Li, C. DeHart, T. Gennett, M. Contreras, and T. Gessert, "Stability of TCO window layers for thin-film CIGS solar cells upon damp heat exposures: part III", Proc. of SPIE, vol 7412, p. 74120K (2009).
[13] M. Sugiyama, T. Yasuniwa, H. Nakanishi, S. F. Chichibu, and S. Kimura, "Optical and solar cell properties of alpha-ray, proton, and gamma-ray irradiated Cu(In,Ga)Se_2 thin films and solar cells", Jpn. J. Appl. Phys. Vol. 49, pp. 042302-1-3 (2010).
[14] Y. Hirose, M. Warasawa, K. Takakura, S. Kimura, S. F. Chichibu, H. Ohyama, and M. Sugiyama, "Optical and electrical properties of electron-irradiated Cu(In,Ga)Se_2 solar cells", Thin solid Films, vol 519**,** pp. 7321-7323 (2011).
[15] J. R. Woodyard, and G. A. Landis, "Radiation resistance of thin-film solar cells for space photovoltaic power", Solar Cells vol. 31, pp. 297-329 (1991) .
[16] F. J. Ziegler, J. P. Biersack, M. D. Ziegler, "*The Stopping Range of Ions in Solids"* (Pergamon Press, New York, 1985).
[17] K. S. Chan, J. W. Leung, J. D. Ye, P. Parkinson, E. Monakhov, K. M. Johansen, L. Vines, C. Jagadish, and B. Svensson, "Defects in H Implanted ZnO: Implantation or H Related Effects", 2011 Materials Research Society (MRS) Fall Meeting, Boston, MA, USA, 2011, M12.12.

On-orbit Performance Analysis on Solar Array Paddle of X-ray Astronomy Satellite "Suzaku"

Takanobu Shimada*[1], Hiroyuki Toyota [1], Akio Kukita[1],
Kazuyuki HIrose[1], Yoshitomo Maeda[1], and Kazuhisa Mitsuda[1]
1 Institute of Space and Astronautical Science (ISAS), Japan Aerospace Exploration Agency (JAXA),
3-1-1 Yoshinodai, Chuo-ku, Sagamihara, Kanagawa 252-5210, Japan
*Email: shimada.takanobu@jaxa.jp
Keyword(s): Solar cell, HES, Solar flare, Radiation damage, X-ray astronomy satellite, Suzaku

Abstract

This paper presents the analysis results for the on-orbit performance of a solar array paddle of the X-ray astronomy satellite *Suzaku*. The current generated by the solar array was confirmed to be gradually but continuously decreasing since the middle of 2011. We estimated the degradation of the output to simulate the on-orbit environment according to the JPL prediction method. The analysis results indicated that greater on-orbit degradation of the solar cell occurred compared to the predicted performance degradation under the space environment when *Suzaku* was exposed to the orbit. We determined that the difference in the on-orbit data and analysis results could be attributed to an increase in cell temperature or radiation degradation due to solar flares.

1. Introduction

Suzaku, formerly known as ASTRO-EII, is an X-ray astronomy satellite developed by the Japan Aerospace Exploration Agency (JAXA) and has been successfully making observations since its launch in July 2005. However, the current generated by its solar array was confirmed to be gradually but continuously decreasing since the middle of 2011. Consequently, we estimated the degradation of the solar array output to simulate the on-orbit environment according to the JPL prediction method. The analysis results indicated that on-orbit degradation of the solar cell was greater than that of the predicted performance in a space environment. In this paper, we discuss the on-orbit performance of the solar array paddle for *Suzaku*.

2. Mission Overview and Solar Array Paddle

Suzaku is the fifth Japanese X-ray astronomy satellite and observes a wide variety of X-ray sources; it has a higher energy resolution and higher sensitivity than other previous satellites over a wide range from soft X-rays to gamma rays (0.4–600 keV) [1]. *Suzaku* is an international collaboration between the United States and Japan and was launched on July 10, 2005, by an M-V rocket.

Figure 1 shows a schematic diagram of *Suzaku*. The body consists of eight side panels with solar array paddles and five X-ray telescopes on an extensible optical bench; it has dimensions of approximately 6.5 m × 5.4 m × 1.9 m when deployed in orbit configuration. The total mass of the satellite is approximately 1700 kg; this includes the scientific observation instruments, which have a mass of 950 kg. After launch, the satellite cruised to an approximately circular orbit around Earth with an inclination of 31°, periapsis altitude of 570 km, and orbital period of approximately 96 min. *Suzaku* has continued to observe beyond the mission duration of 3 years.

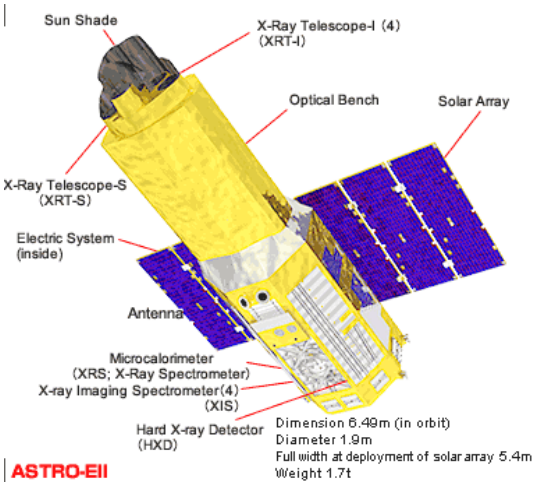

Fig. 1. Schematic drawing of *Suzaku*

Suzaku is equipped with two wings of solar array paddles (SAP) mounted next to each +Y directional side panel. The solar irradiance in the orbit ranges from 0.87 to 1 sun because the sun angle is up to +/-25° perpendicular to the sun normal due to the scientific observation. The estimated temperature of the solar panels reaches up to 73 °C.

We used high-efficiency silicon (HES) solar cells (Sharp Corp.) with an efficiency of 16.7% at the beginning of life (BOL); these cells qualify as NASDA-QTS-1013. The HES cells used for *Suzaku* are 100 μm thick, and the base material has a resistivity of 2 Ω cm. The solar array has 26 solar cell strings consisting of 132 cells in series and four strings consisting of 131 cells in series. The minimum power requirement at the end of life (EOL) (3 years) was 1530 W. The SAP operating point on the I–V curve was constantly controlled at 51.5 V of the interface voltage during sunshine periods because shunt dissipators were adopted as an unregulated 50 V bus power control method.

3. On-orbit Status

Figure 2 shows the telemetry of status transition for the *Suzaku* electrical power subsystem after launch. The current generated by the SAP (SAP I is indicated in Fig. 2) was calculated from the sum of the input current to power control unit (PCU in I) and the shunt current because the onboard SAP generated current was not directly monitored by telemetry.

Suzaku has been successfully operating since its launch in July 2005. However, SAP I was confirmed to be gradually but continuously decreasing, as shown in Fig. 2, since the middle of 2011. No sudden decline in SAP I due to string open failure was observed by the telemetry data during this time. Consequently, the satellite function of the under voltage controller (UVC) to protect the onboard battery was activated on January 24, 2011. This is the reason for the sharp decline in the battery voltage (BAT V) in Fig. 2; it caused a decrease in the output current of the power control unit (PCU out I) to lower the load power. To accommodate this deterioration in SAP-generated power, *Suzaku* has been limited to operating at a solar incidence angle range from 25° to 20°, and the battery charging voltage level has been raised.

The telemetry of SAP I and SAP temperature (SAP T) periodically shows a seasonal change—i.e., a slight increase in winter and a slight decrease in summer—due to the change in solar intensity caused by the Earth's orbit around the Sun. Shorter-term variations seen in these telemetries are assumed to be changes in the sun incidence angle to the solar array.

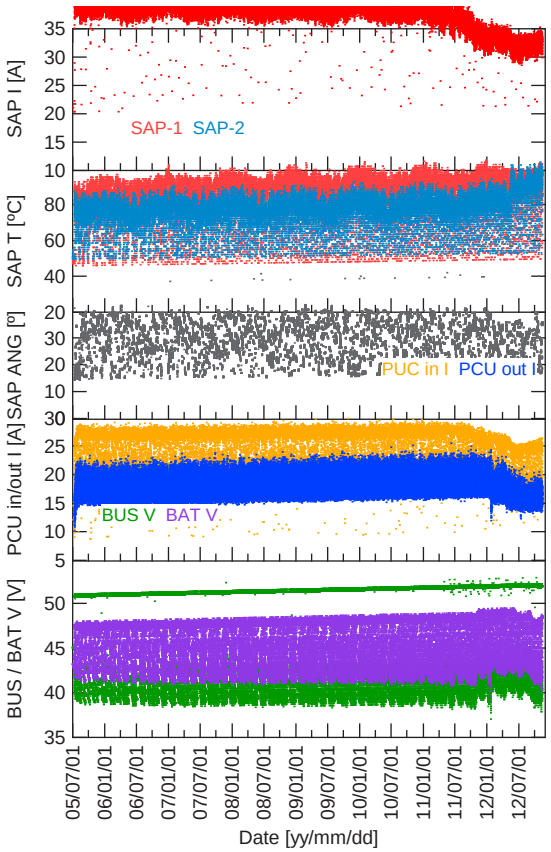

Fig. 2. Telemetry of on-board status for the *Suzaku* electrical power subsystem since the launch

The temperature of SAP-1 is around 10 °C higher than that of SAP-2 because the onboard temperature sensor is on the non-cell side of the inner panel, close to the satellite body, of SAP-1 while it is on the outer panel of SAP-2. Although the increase in temperature of SAP-2 has been observed since the middle of 2012, a definitive cause for this phenomenon has not been identified so far. The power generated by the SAP has been presumed to be reduced due to the increase in SAP temperature. However, the occasions when both occurred do not correspond. Therefore, we decided to verify the *Suzaku* solar array degradation using the analysis model described below, and we discuss the results in the following section.

4. Analysis Results and Discussion

4.1 Analysis Model

We estimated the degradation of the solar array output to simulate the on-orbit radiation environment according to the JPL prediction method in the *Solar Cell Radiation Handbook* using the relative damage coefficient (RDC) obtained in ground tests [2]. Figure 3 shows the calculated integral fluence spectra of trapped protons and electrons derived from the *Suzaku* orbit and the elapsed year after launch using AP-8 and AE-8 trapped particle models. To obtain the equivalent 1-MeV electron fluence to the environment, the RDC of the HES cell was applied. To consider the shielding effects, a 100-µm-thick coverglass on the cell side and infinite thickness on the non-cell side were assumed.

Table I. Analysis conditions to predict solar array output

Solar cell area	24 cm^2 (4 cm × 6 cm)
Coverglass thickness	100 µm
Array configuration	30 strings × 131 cells in series
Launch date	2005/07/10
Orbit	Semi-major axis: 6928.1 km Inclination: 31.0°
Radiation environment model	AP-8 (Solar activity: min) AE-8 (Solar activity: max)
Solar intensity	1307 W/m^2 (*summer solstice)
Sun incidence angle	25°
Cell temperature	73 °C
Conversion factor to 1 MeVe- from 10 MeVp+	3000 (Voc)/4350 (Isc)

Figure 4 indicates the remaining factor of the outputs of the HES solar cell as a function of 1-MeV electron fluence; this was used to predict the radiation degradation. Table I summarizes the analysis conditions used to calculate the *Suzaku* solar array output. Current–voltage (I–V) characteristics of the SAP were computed by means of a solar cell predictive equation proposed by Picciano [3] using the derived remaining factor and each temperature coefficient.

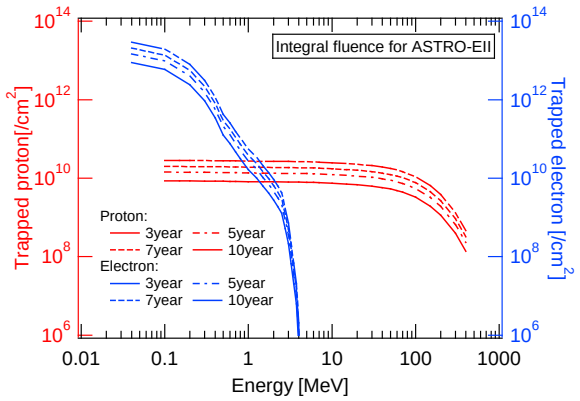

Fig. 3. Integral fluence spectra of trapped protons and electrons in the *Suzaku* orbital environment

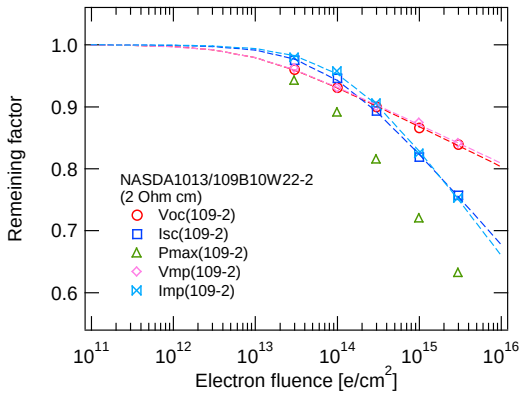

Fig. 4. Remaining factor of outputs of the HES solar cell as a function of 1-MeV electron fluence

4.2 On-orbit Performance Analysis

Table II summarizes the obtained equivalent fluences of a 1-MeV electron from each elapsed year and the predicted remaining factors of Voc, Vmp, Isc, and Imp of the HES cell. Figure 5 illustrates the calculated I–V characteristics based on these remaining factors and the conditions listed in Table I.

Table II Obtained equivalent fluence to 1-MeV protons and the remaining factors

1-MeV electron fluences [cm^{-2}] (Remaining factor)				
Elapsed year	3	5	7	10
Voc	1.82E+13 (0.969)	3.03E+13 (0.959)	4.24E+13 (0.951)	6.06E+13 (0.943)
Vmp	(0.969)	(0.959)	(0.952)	(0.944)
Imp	(0.989)	(0.983)	(0.977)	(0.968)
Isc	2.18E+13 (0.983)	3.63E+13 (0.973)	5.08E+13 (0.965)	7.26E+13 (0.954)

In Fig. 6, the calculated SAP generated current and power at an I/F voltage of 51.5 V are plotted together with the telemetry data. The results indicate that greater degradation of the solar cell proceeded 7 years after launch into orbit compared to the predicted performance degradation under the given space environment. Based on this difference, the deterioration in current generated by the solar array can be attributed to (a) the increase in SAP temperature according to the telemetry or (b) radiation degradation due to solar flares.

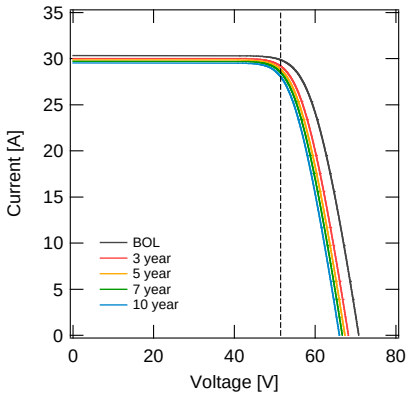

Fig. 5. Calculated I–V characteristics based on the *Suzaku* analysis conditions

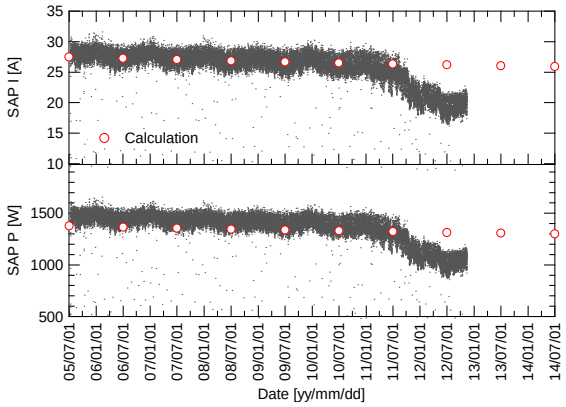

Fig. 6. Comparison of SAP generated current and power at 51.5 V between the on-orbit status and the calculated results

We predicted the variation in transition of the solar array output with cell temperature because the SAP-2 temperature telemetry indicated a sudden increase, although it occurred approximately 1 year after the SAP current began to decrease. Figure 7 illustrates the calculated I–V characteristics when the cell temperature changed to 73, 83, and 93 °C. In Fig. 8, the calculated SAP-generated current at 51.5 V is plotted together with the telemetry data.

The analysis results showed that the solar array operated at a lower current point in the constant voltage region of the I–V curve when the cell temperature was higher. As shown in Fig. 8, there was no temperature condition exactly consistent with the on-orbit transition. However, the deterioration in the current generated by the solar array can be explained by the assumption that a temperature rise of more than 20 °C occurred 6 years after launch. As a factor for the increase in SAP temperature, we are examining degradation in the cell adhesion to the substrate and in the thermo-optical properties of the CG and adhesive at that time.

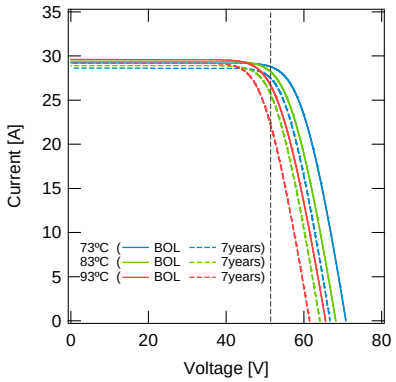

Fig. 7. Calculated I–V characteristics when the cell temperature was changed to 73, 83, and 93 °C

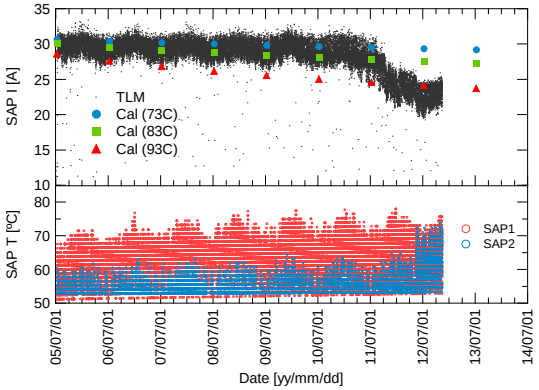

Fig. 8. Comparison of SAP-generated current between the on-orbit data and calculated temperature dependency

The slight decrease in SAP current after 2011 was predicted due to the relatively moderate radiation environment of the low Earth orbit (LEO) for the HES solar cell. However, for the radiation degradation to be a factor explaining the decrease in SAP current, a certain type of radiation exposure needs to have increased since July 2011 to accelerate the degradation of the cell. Therefore, we suspected the radiation degradation of the solar cell to be due to solar flares because solar activity is expected to reach its maximum from 2012 through 2013.

Figure 10 shows the number of occurrences of class-M and class-X solar flares and high-energy proton fluxes observed by the GOES-13 satellite in its geosynchronous orbit. Figure 10 shows that the proton fluxes increased with frequent occurrences of solar flares since 2011, which corresponded to when degradation of the *Suzaku* solar array performance was observed. In general, the Earth is protected from high-energy radiation coming from outer space by a magnetic shield, especially at low latitudes. On the other hand, radiation from the Sun is known to reach the ground at the South Atlantic Anomaly (SAA) because of magnetic anomalies. *Suzaku* cruises along the SAA. The calculation results are consistent with the on-orbit deterioration under the assumption that the solar cells were irradiated with an equivalent 1-MeV electron fluence of 3.0×10^{14} particles/cm^2 7 years after launch. At present, we are examining the equivalent fluence for its validity.

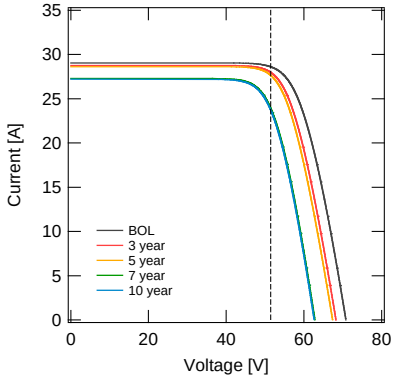

Fig. 9 Calculated I–V characteristics when the SAP was exposed to a solar flare 7 years after launch

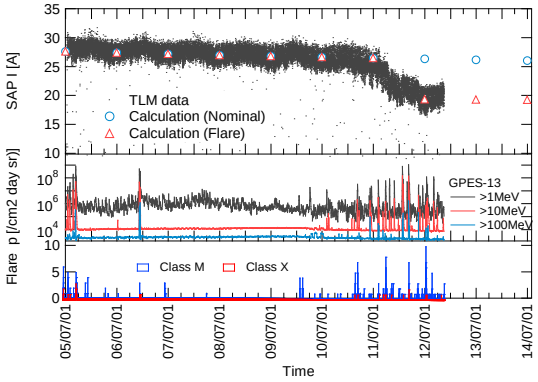

Figure 10 Comparison of SAP-generated current between on-orbit and calculated data upon exposure to a solar flare

5. Summary

Suzaku has been successfully making observations since its launch in July 2005. However, the current generated by the solar array was confirmed to be gradually but continuously decreasing since the middle of 2011. The SAP current deterioration could be attributed to the increase in SAP temperature as indicated by telemetry and radiation degradation due to solar flares. Based on analysis results, the deterioration can be explained under the assumption that the temperature rose up to around 93 °C 6 years after launch. On the other hand, the calculated results showed good consistency with the on-orbit deterioration under the assumption that the solar cells were irradiated with an equivalent 1-MeV electron fluence of 3.0×10^{14} particles/cm^2 7 years after launch. At present, we are examining the equivalent fluence for its validity.

References

[1] K. Mitsuda et al., “The X-ray observatory Suzaku,” Publications of the Astronomical Society of Japan, 59, S1-S7 (2007)
[2] B.E. Anspaugh, “Solar Cell Radiation Handbook,” JPL Publication, 82-69, Addendum 1 (1989).
[3] W. T. Picciano et al., “Determination of the Solar Cell Equation Parameters, Including Series Resistance, from Empirical Data,” Energy Conversion, Vol. 9, pp. 1-6 (1968).

Proton Irradiation Effects on Amorphous Silicon Triple-Junction Solar Cells

Shin-ichiro Sato[*1], Kevin Beernink[2], and Takeshi Ohshima[1]
1 Japan Atomic Energy Agency (JAEA), Japan
2 United Solar Ovonic LLC, USA
*Email: sato.shinichiro@jaea.go.jp
Keyword(s): Thin Film Si Solar Cell, Radiation Effects, Proton Irradiation

Abstract

Degradation behavior of a-Si/a-SiGe/a-SiGe triple-junction solar cells irradiated with various energy protons are investigated *in-situ*. It is clarified that the degradation due to proton irradiation is scaled by a unit of displacement damaged dose and thus the proton-induced degradation is mainly caused by the displacement damage effect. The performance recoveries immediately after irradiation are also investigated and it is clarified that all the parameters recover significantly at room temperature. In particular, the remarkable recovery is observed in the short-circuit current. This is thought to be due to recovery of the carrier lifetime, which is based on annealing of radiation defects.

1. Introduction

Amorphous silicon (a-Si) thin film solar cells are expected to be utilized as flexible space solar cells, since it is known that they have not only good radiation tolerance, but also the potential for reductions of both cost and stowage volume [1, 2]. Although radiation degradation of a-Si solar cells and their thermal recovery of post-irradiation have been investigated [3–5], systematic knowledge of the radiation degradation of a-Si solar cells has not been obtained compared to other types of solar cells, such as crystalline Si and III-V compounds.

Recently, we have reported that the temperature during irradiation strongly affects performance degradation of a-Si single-junction solar cells, and the cell performance significantly recovered immediately after irradiation even at room temperature (RT) [6]. These results indicate that thermal recovery always occurs simultaneously with radiation degradation. Thus, temperature during irradiation, irradiation rate, and the elapsed time between irradiation and measurement should be controlled in conducting radiation ground tests for a-Si solar cells.

In this paper, we report degradation behavior of a-Si/a-SiGe/a-SiGe triple-junction (TJ) solar cells irradiated with 10 keV to 10 MeV energy protons and discuss the degradation mechanism. In addition, we report the performance recovery at RT just after irradiation by using *in-situ* current-voltage (*I-V*) measurement system. High energy protons penetrate and deposit their energies uniformly in the cell, whereas low energy protons stop in the active layers (top, middle or bottom layer) of the cell and selectively degrade each layer. Thus, structural dependency on radiation tolerance can be clarified by analyzing proton energy dependency of the degradation behavior.

2. Experimental

Samples used in this study were a-Si/a-$Si_{0.8}Ge_{0.2}$/a-$Si_{0.6}Ge_{0.4}$ TJ solar cells, which were not light-soaked. The cells were fabricated at United Solar Ovonic LLC. The typical cell characteristics are listed in Table I. Proton irradiation from 10 keV to 10 MeV was performed at the Takasaki Ion Accelerators of advanced Radiation Application (TIARA), Japan Atomic Energy Agency (JAEA). *I-V* characteristics under AM-0, 1 sun conditions were measured *in-situ* in an irradiation chamber (*in-situ* measurement). Note that 20 keV H_2 ion beams were used for 10 keV proton irradiation. A control cell was prepared in order to check the light-induced degradation due to repetition of *I-V* measurement. The control cell was not irradiated and was simultaneously measured with an irradiated cell. No light induced degradation due to the *in-situ I-V* measurement was observed in the irradiation experiments.

Proton beam flux, temperature during irradiation, and elapsed time between irradiation and measurement were strictly controlled in order to compare the degradation behavior accurately. The proton beam flux and the irradiation temperature were 1.4×10^{10} $cm^{-2}\cdot s^{-1}$ and 298 K, respectively, and the *I-V* measurement was done 1 minute after irradiation was stopped. The proton irradiation was performed until the short-circuit current (Isc) decreased to around 45 %, and the recovery of the cell performance after irradiation was investigated for 60 minutes at 298 K in vacuum. The cells were kept under dark conditions

Table I. Initial electric performance of sample at AM-0, 1 sun conditions.

Isc (mA/cm^2)	8.84
Voc (V)	2.18
Pmax (mW/cm^2)	13.3
FF	0.689
Efficiency (%)	9.73
Active Area (cm^2)	1.00

except when the *I-V* measurement was performed.

3. Results

Degradation curves of Isc, open-circuit voltage (Voc), and maximum output (Pmax) of the cells irradiated with 10 keV, 20 keV, 40 keV, 65 keV, 80 keV, 100 keV, 200 keV, 2 MeV and 10 MeV protons are shown in Figs. 1 (a), (b), and (c), respectively. The degradation of Isc was larger as the proton energy was lower, except the results of 10 keV and 20 keV proton irradiations. Whereas the remaining factors of Isc intensively decreased in the high fluence regime, the Voc gradually decreased and kept the relatively higher value. Here, remaining factor is defined as the ratio of the values after irradiation to before irradiation. The remaining factor of Voc was around 80 % independent of incident proton energy when the Isc decreased to around 45 %. With respect to the proton energy dependence of degradation behavior, similar results were obtained in the degradation of Isc and Voc. As for Pmax, similar degradation curves were obtained in all cases. The degradation of Pmax is mainly attributed to the degradation of fill factor (FF) rather than that of Isc and Voc.

The cell performance recovery after 80 keV proton irradiation at the fluence of 2.0×10^{13} cm^{-2} is shown in Fig. 2. All the parameters (Isc, Voc, FF, and Pmax) significantly recovered immediately after the irradiation was stopped. In particular, the Isc values prominently recovered in all cases. This indicates that radiation defects in the active layers were annealed and the minority carrier lifetime recovered (RT annealing) [6].

Figure 3 shows the comparison of the Isc recovery after irradiation. In this figure, recovery amount is defined as the amount of increase one hour later after irradiation (all the values are normalized so that the values before irradiation are 100 %). It is shown in Fig. 3 that the recovery amount of Isc had a tendency to be large in low energy proton irradiation.

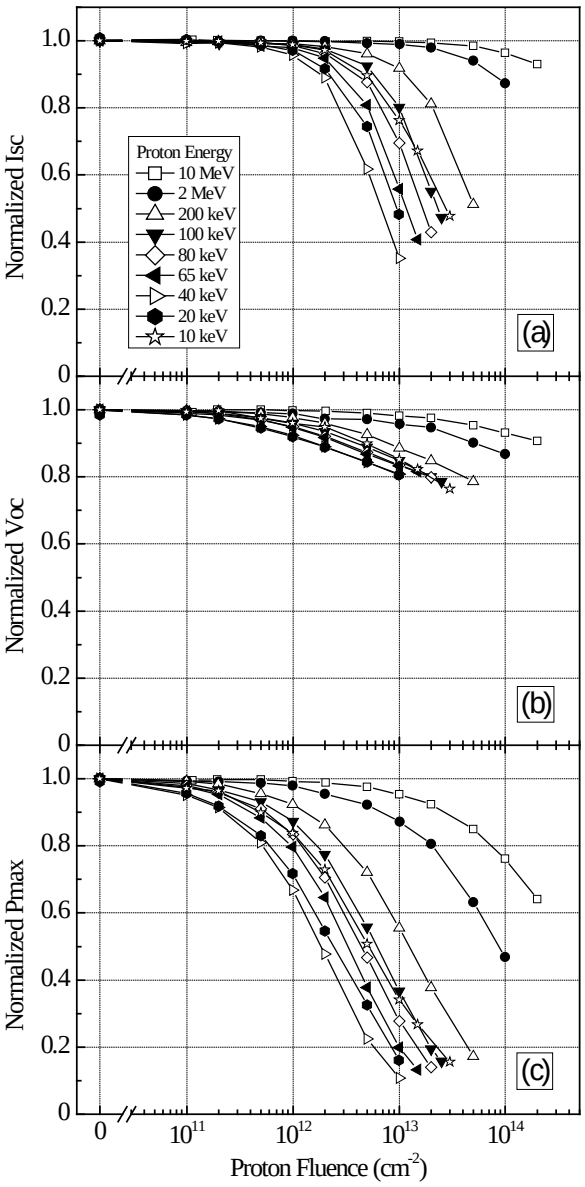

Fig. 1. Degradation curves of (a) Isc, (b) Voc, and (c) Pmax of the cells as a function of proton fluence. All the values are normalized by the values before irradiation.

4. Discussion

By analyzing the degradation curves of Isc and Voc shown in Figs. 1 (a) and (b), clarification is given as to which energy deposition process of incident protons is dominant in the degradation of the cell performance. The radiation degradation of a-Si solar cells is expected to be affected by both the electronic excitation effect and the displacement damage effect, although it is unclear which effect is the main cause of the electrical degradation. Srour *et al.* have investigated radiation degradation of a-Si solar cells using protons, electrons and X-rays, and have concluded that the electrical degradation correlated with 'ionizing dose' of radiations, which reflected the amount of excited electrons [4]. On the contrary, Shimazaki *et al*. have also reported proton irradiation effects on a-Si solar cells and have concluded that the electrical degradation did not correlate with the ionizing dose, but rather correlated with 'displacement damage dose (DDD)', which reflected the amount of displacement damage [5]. This discrepancy might be caused by an uncertainty of the degradation data they used. Since *in-situ* measurement techniques were not used in both studies, radiation degradation of the cells was expected to recover substantially and substantial error might be introduced in the data. On the other hand, fluctuation of the data based on the annealing effect was minimized in this study by not only using the *in-situ* measurement technique, but also by strictly controlling the irradiation conditions. Therefore, a definite conclusion could be obtained from the results of this study.

Figure 4 shows the degradation curves of Isc and Voc of the cells which are scaled using the ionizing dose

(J/kg) and the DDD (MeV/g). Although the data shown in Figs. 4 (a) and (b) are the same as Fig. 1 (a), the abscissa axes in Figs. 4 (a) and (b) are converted from a unit of fluence to ionizing dose and DDD, respectively. The same is true of Fig. 4 (c) and (d). The ionizing dose is defined as the product of the electronic energy depositions (eV/cm, or J/cm), the mass density (g/cm^3), and the proton fluence (cm^{-2}). The electronic energy deposition was derived from the TRIM code [7]. The DDD is defined as the product of the NIEL value (Non-Ionizing Energy Loss, MeV·cm^2/g) and the proton fluence. The NIEL value was derived from Ref. [8] by considering the mass density and the elemental composition of the cell. In order to consider the deposited energy distribution in the depth direction, both the electronic energy deposition and the NIEL value per unit depth were calculated using the TRIM code and their average values in the whole region of the cells were used.

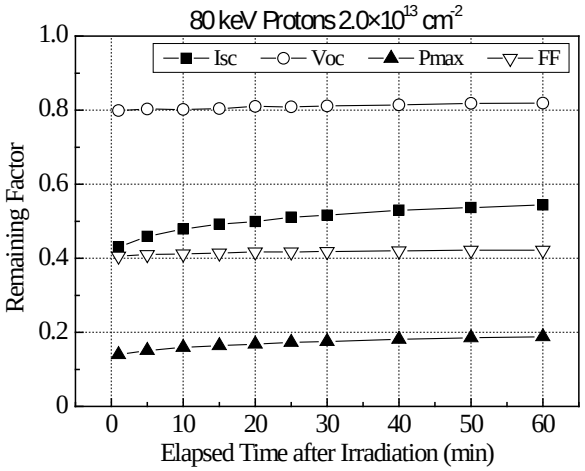

Fig. 2. Performance recoveries after 80 keV proton irradiation at the fluence of 2.0×10^{13} cm^{-2}. Isc: closed squares, Voc: open circles, Pmax: closed triangles, and FF: open inverted triangles. All the values were normalized by the values before irradiation.

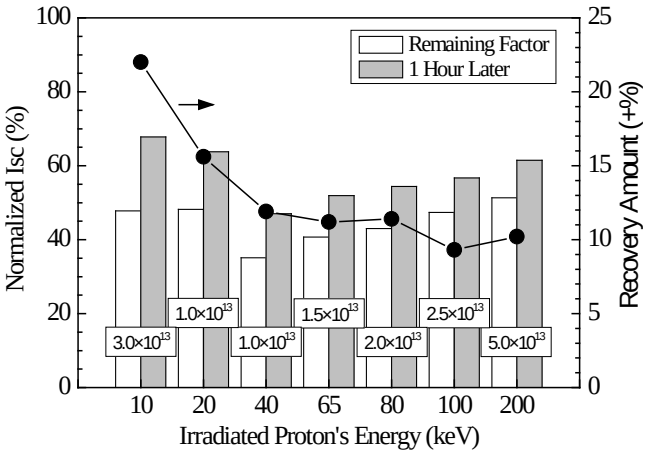

Fig. 3. Comparison of recovery of Isc after irradiation. The abscissa represents the irradiated proton's energy and the irradiation fluence (cm^{-2}) is shown in the boxes. White and shaded bars represent the normalized Isc values 1 minute and 1 hour later after irradiation, respectively. Recovery amount is defined as a difference of them.

The results clearly showed that a universal curve was drawn by the DDD scaling, while not being drawn by the ionizing dose scaling. This indicates that the degradation in Isc and Voc is mainly attributed to the displacement damage effect, and the degradation due to proton irradiation is different from the light-induced degradation [9]. However, the degradation curve of 10 keV proton irradiation slightly deviated from the universal curve (open star symbols in Fig. 4 (b)). In principle, the Voc of triple-junction solar cells is represented as the sum of the Voc's of the three sub-cells, and the Isc value is equal to the minimum Isc among them (current-limiting cell). Thus, it seems reasonable that the degradation in Voc is correlated with the average DDD value in the whole region of the cell, whereas the degradation in Isc should be correlated with the average DDD value in the current-limiting cell. Since the current matching between sub-cells was achieved in the cells before irradiation, the most degraded sub-cell was expected to become the current limiting cell. According to the calculation using TRIM and NIEL, the current-limiting cell was expected to be the top cell in the case of 10 keV proton irradiation, the middle cell in 20 keV proton irradiation, and the bottom cell in 40 keV to 80 keV proton irradiation. However, universality of the degradation curves scaled by the DDD was not improved when the DDD values in the 'expected' current-limiting cell were used. This is thought to be due to the differences of radiation tolerance and RT annealing rate between the sub-cells. As shown in Fig. 3, the more remarkable recovery of Isc at RT was observed in 10 keV and 20 keV proton irradiations. This strongly indicates that the recovery of the top cell is more remarkable than that of middle and bottom cells.

5. Summary

The degradation behavior of a-Si/a-SiGe/a-SiGe TJ solar cells irradiated with 10 keV to 10 MeV protons and the performance recoveries after irradiation were investigated using the *in-situ I-V* measurement system. The irradiation conditions were strictly controlled to clarify the annealing behavior at RT, and the following findings were obtained.

The degradation in Pmax is mainly due to the degradation in FF independent of irradiated proton's energy, and both the Isc and Voc degradations are relatively smaller. Significant recovery of all the parameters appears

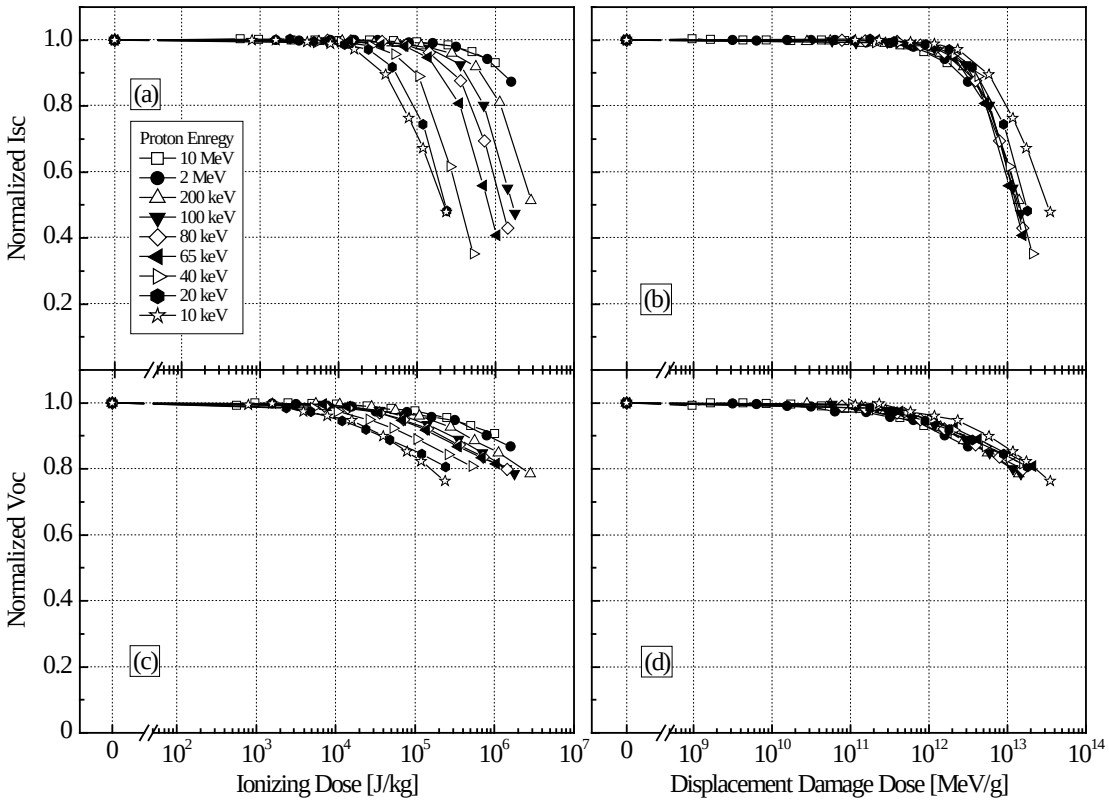

Fig. 4. Ionizing dose scaling and displacement damage dose (DDD) scaling for the degradation curves of Isc and Voc. The abscissa axes are converted from fluence (cm^{-2}) to ionizing dose (J/kg) in (a) and (c), DDD (MeV/g) in (b) and (d). The ordinate axes are the remaining factors of Isc in (a) and (b), Voc in (c) and (d).

immediately after proton irradiation and the Isc value remarkably recovers in particular. This is due to recovery of the carrier lifetime, which is based on RT annealing of radiation defects. The recovery of top (a-Si) cell at RT is more remarkable than the other sub-cells. The degradation due to proton irradiation is scaled by a unit of displacement damage dose. Therefore, the proton-induced degradation is mainly caused by the displacement damage effect, although the electronic excitation effect, which is the cause of light-induced degradation, may partly contribute.

Acknowledgments

Work at United Solar was funded by Air Force Research Laboratory, Space Vehicles Directorate under contract FA9453-06-C-0339.

References

[1] S. G. Bailey *et al*., "The Future of Space Photovoltaics," in *Proceedings of 34th PVSC*, Philadelphia, PA, pp. 001909-001913 (2009).
[2] A. Banerjee *et al*., "Advances in Cell Efficiency of a-Si:H and nc-Si:H-Based Multi Junction Solar Cells for Space and Near-Space Applications," in *Proceedings of 35th PVSC*, Philadelphia, PA, pp. 002651-002655 (2009).
[3] R. A. C. M. M. van Swaaij *et al*., "Comparison of Amorphous Silicon Solar Cell Performance Following Light and High-Energy Electron-Beam Induced Degradation," *J. Non-Cryst. Sol.*, vol. 354, pp. 2464-2467 (2008).
[4] J. R. Srour *et al*., "Radiation Effects and Annealing Studies on Amorphous Silicon Solar Cells," *IEEE Trans. Nucl. Sci.*, vol. 56, pp. 3300-3306 (2009).
[5] K. Shimazaki *et al*., "Analysis of Radiation Response and Recovery Characteristics of Amorphous Silicon Solar Cells," in *Proceedings of 4th WCPEC*, Hawaii, HI, pp. 1797-1800 (2006).
[6] S. Sato *et al*., "Electron and Proton Irradiation Effects on Substrate-Type Amorphous Silicon Solar Cells," in *Proceedings of 37th PVSC*, Seattle, WA (2011) *in Press*.
[7] Available: http://www.srim.org/
[8] I. Jun *et al*., "Proton Nonionizing Energy Loss (NIEL) for Device Application," *IEEE Trans. Nucl. Sci.*, vol. 50, pp. 1924-1928 (2003).
[9] D. L. Staebler *et al*., "Reversible Conductivity Changes in Discharge-Produced Amorphous Si," *Appl. Phys. Lett.*, vol. 31, pp. 292-294 (1977).

Estimation Method for Radiation Resistance of Multi-junction Solar Cells using I-V Characteristics of Subcells

Tetsuya Nakamura[1], Mitsuru Imaizumi[1], Mitsunobu Sugai[2], Shin-ichiro Sato[3], and Takeshi Ohshima[3]
1 Japan Aerospace Exploration Agency (JAXA),
2 Advanced Engineering services (AES),
3 Japan Atomic Energy Agency (JAEA),
*Email: nakamura.tetsuya@jaxa.jp
Keyword(s): Photovoltaic cells, Radiation effects, Space technology

Abstract

The radiation degradation characteristic of a multi-junction (MJ) solar cell is more complicated compared to a single-junction (1J) solar cell. To perform the quantitative radiation resistance evaluation of a MJ solar cell, it is necessary to estimate the parameter of subcells in the MJ solar cell, such as the reverse saturation current density (J_0), photo current (I_{photo}) and shunt resistance (R_{sh}). In this work, the technique used to estimate each parameter (J_0, I_{photo}, R_{sh}) of each of the subcells in the MJ solar cell is suggested by combining the electroluminescence (EL) method, which proposed by Fraunhofer group, and the LED bias light (LBL) method. Furthermore, the decline in the maximum power (P_{max}) of the MJ solar cell was predicted on the circuit simulator using this technique before and after 1 MeV electron irradiation.

1. Introduction

Multi-junction (MJ) solar cells of high conversion efficiency are attractive for space use. At present, an InGaP/GaAs/Ge triple-junction (3J) solar cell [1], which efficiently absorbs a broad spectrum of sunlight, is used in space. The inverted metamorphic (IMM) 3J solar cell [2], which is both lightweight and flexible in addition to having high conversion efficiency, attracts considerable attention as a next-generation space solar cell.

To utilize such solar cells in a space environment, we need to experimentally clarify the radiation resistance of their output performance, since this performance declines with exposure to radiation [3]. However, since the MJ solar cell comprises a number of subcells which are electrically connected in series, their degradation behavior is complicated and therefore difficult to understand.

Fig. 1 shows the equivalent circuit of a dual-junction (2J) solar cell, the output current of which is determined with Eq. (1) below.

$$I = I_{photo} - I_{sh} - I_{d1} - I_{d2} \qquad \text{(Eq. 1)}$$

where I_{photo}, I_{sh}, and I_d are the photo, shunt and diode currents, respectively. I_{d1} can be expressed by the diffusion model, and I_{d2} can be expressed by the recombination model. Since I_{sh} and I_d are determined by the shunt resistance (R_{sh}), I_{photo} and the reverse saturation current density (J_0) of all the subcells, it is difficult to estimate I_{sh} and I_d. To evaluate the output current correctly, it turns out that it is necessary to estimate J_0, I_{photo} and R_{sh}.

Recently, it was reported that a new method of estimating the J_0 and open-circuit voltage (V_{oc}) of subcell in a MJ solar cell by using electroluminescence (EL) [4-6] before and after irradiation [7]. In this work, the estimation of each parameter which constitutes an equivalent circuit is enabled by combining the EL method and the LED bias light (LBL) method. In addition, it was adapted before and after 1MeV electron irradiation, and we succeeded in predicting the degradation curve of the maximum power (P_{max}) of the 2J solar cell by obtaining the degradation characteristics of J_0, I_{photo} and R_{sh}.

2. Experimental procedure

We prepared bare type (no coverglass) InGaP/GaAs 2J solar cells which were 2 × 2 cm in size. The cells were irradiated with 1 MeV electrons in fluence up to 1×10^{16} e^-/cm^2 at the Japan Atomic Energy Agency (JAEA). Before and after the irradiation, the current-voltage (IV) characteristics were estimated using EL and LBL methods. The EL method is a technique used to estimate the dark IV (DIV) characteristic of a subcell from the EL emission spectrum [4-7]. Since the MJ solar cell comprises a number of subcells which are connected in series, each subcell DIV characteristic is inseparable in electrical property measurement. However, when the EL method is used, since the emission EL spectra of each subcell differ, the DIV characteristic of each subcell in the MJ solar cell is separable. Conversely, the LBL method is a technique used to estimate the R_{sh} and I_{photo} of each

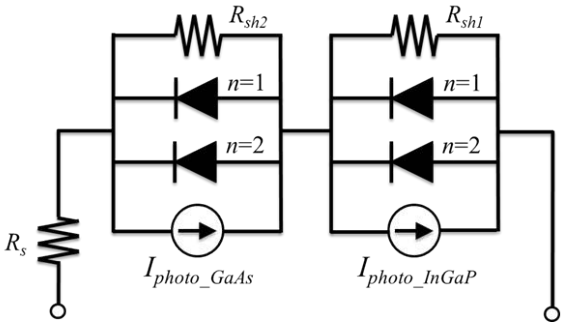

Fig.1: Equation circuit of 2J solar cell

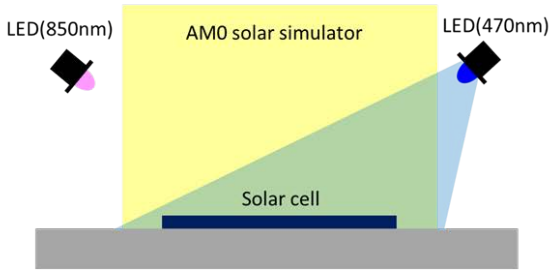

Fig.2: Experimental setup of LBL method

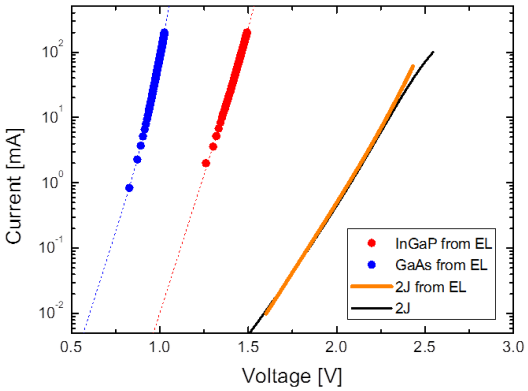

Fig.3: Dark IV characteristics of subcell and 2J solar cell using the EL method before 1MeV electron irradiation.

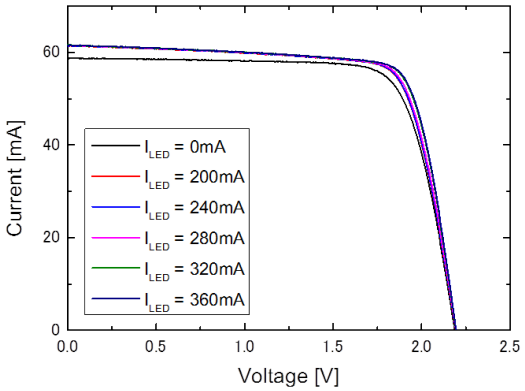

Fig.4: Light IV characteristics of 2J solar cell with 470nm-LED bias light after 1 MeV electron irradiation.

subcell in the MJ solar cell. By irradiating with the solar simulator light adjusted to AM0 and the bias light of LED as shown in Fig. 2, the characteristics of each subcell can be estimated.

3. Results and Discussion

Fig. 3 shows the characteristics of DIV of the 2J solar cell using the EL method before 1 MeV electron irradiation. In Fig. 3, dashed red and blue lines show the DIV characteristics of each subcell, which were fitted by the 2-diode model and obtained with $J_{01\_InGaP} = 6.2 \times 10^{-28}$ A/cm^2, $J_{02\_InGaP} = 9.3 \times 10^{-15}$ A/cm^2, $J_{01\_GaAs} = 1.7 \times 10^{-19}$ A/cm^2, $J_{02\_GaAs} = 2.7 \times 10^{-11}$ A/cm^2, respectively. The merger of the InGaP and GaAs subcell IV, as calculated from the EL method (dashed orange line), correlated well with the actual DIV measurement results (solid black line) of the 2J solar cell, except for series resistance (R_s) and R_{sh}.

Fig. 4 shows the IV curve after 1 MeV electron irradiation. The solid black line is IV curve under the AM0 solar simulator, while the others are under AM0 with a 470nm LED bias light. Since the current-limiting subcell is InGaP subcell under the AM0 solar simulator, R_{sh} of InGaP shows up as an inclination of the plateau region in the solid black line. Conversely, where the injection current into the 470nm LED is 200 mA or more, the short-circuit current (I_{sc}) and inclination of the plateau region are saturated. This inclination shows up R_{sh} of GaAs subcell. If the GaAs subcell is a current-limiting subcell under the AM0 solar simulator, it is irradiated with the 850nm LED, and the current-limit subcell changes to an InGaP subcell.

I_{photo} is calculated by the LBL method and the circuit simulator, SPICE. I_{photo} is also calculated from external quantum efficiency (EQE), but there is no evidence of correlation with the IV curve under AM0 solar simulator. In the case of a MJ solar cell, since there are two or more current generators, measured I_{sc} include I_{photo}, I_d and I_{sh}. Since J_0 and R_{sh} were already estimated, compatibility I_{photo} with the IV curve was calculated by estimating I_d and I_{sh}. The equivalent circuit of Fig. 1 was used in the circuit simulator. Fig. 5 shows I_{sc} of the 2J solar cell and I_{photo}, I_d and I_{sh} of each subcell as a function of 470nm-LED luminescence intensity after 1MeV electron irradiation. Where the luminescence intensity of the LED is zero, the current-limiting subcell was the InGaP subcell. The open black square shows the experimental result of I_{sc} of a 2J solar cell, while others are simulation results. I_{photo} of InGaP and GaAs was calculated by fitting I_{sc} of the experimental results. The red asterisk shows

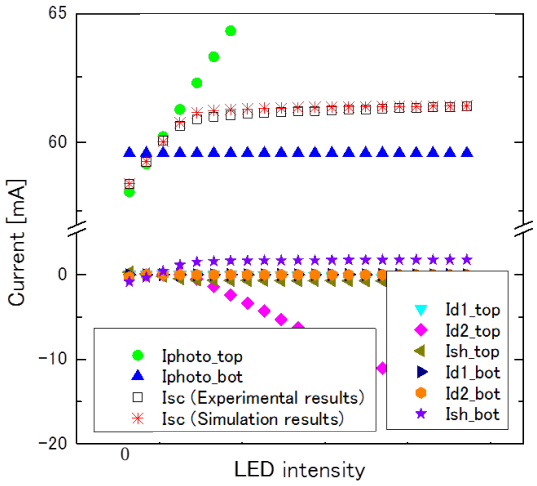

Fig.5: I_{sc} of 2J and the diode and shunt currents of the subcell as a function of 470nm-LED intensity. The open black square shows the experimental results and the other figures are simulation results.

I_{sc} of the circuit simulation results, which correlated well with the open black square. There are two types of change of I_{sc}. In the region where the luminescence intensity of LED is weak, I_{sc} increases to alignment according to the increase in I_{photo} of InGaP (type A). In the region where the luminescence intensity of LED is considerable, I_{sc} is almost unchanged as a function of LED intensity since the current-limiting subcell changes from InGaP to GaAs (type B). In Type A, I_{sc} and I_{photo} of InGaP are almost the same. Conversely, in type B, I_{sc} differs from 2 mA of I_{photo} of GaAs. This is considered to be one factor explaining why the change in R_{sh} in the GaAs subcell with radiation exceeds the InGaP subcell. The advantage of the LBL method is that we can obtain compatibility I_{photo} with an IV curve. The output value obtained by the AM0 solar simulator is compared with the output value of the solar cell, which substitutes each parameter estimated by the LBL and EL methods for the circuit simulator, both of which show good agreement, as shown in the table.

Figure 6 (a) shows the dependence of the remaining factors of I_{photo}, which are obtained by LBL method, on fluence for each subcell after the 1 MeV electron irradiation. The remaining factors of I_{photo} for the InGaP subcell were superior to those of the GaAs subcell. The dashed lines are fitting curves based on the use of Eq. (2) below.

$$I_{photo} = I_{photo\,0} - C_I \log\left(1 + \frac{\Phi}{\Phi_{xI}}\right) \qquad \text{(Eq. 2)}$$

where $I_{photo\,0}$ is initial values before irradiation, C and Φ_x are coefficients computed from the fitting.

The changes in J_{01} and J_{02} for each subcell due to 1 MeV electron irradiation are shown in Fig. 6 (b). Since EL intensity is quite small and cannot be observed in the high fluence region, the estimation result of J_0 is up to 3×10^{15} e^-/cm^2. J_{01} and J_{02} rose with linear increase in fluence. Results which matched and fitted in relative terms were expressed with dotted and solid lines and used to estimate the degradation of P_{max} here in this work.

Figure 6 (c) exhibits the dependence of the reciprocal of R_{sh} on fluence. For lower fluence cases, the R_{sh} of each subcell was sufficiently large hence its change could be ignored. However, a significant decrease of R_{sh} was confirmed in the case of high fluence. Also, with regard to the degradation/decrease of R_{sh}, the InGaP subcell outperformed the GaAs subcell in terms of radiation resistance, which means the radiation resistance of the fill-factor (FF) worsens, when a current-limiting subcell changes from InGaP to the GaAs subcell. Conversely, no degradation/increase of R_s depending upon fluence was distinctly observed or measured.

Based on the results exhibited in Figs. 6 (a) – (c), the degradation trend of P_{max} of the 2J cell was estimated, as indicated with the solid blue line in Fig. 6 (d). J_0, R_{sh} of the current-limiting subcell, and R_{sh} of the 2J cell that determine FF were evaluated using SPICE. The dashed black line shows the fitting result using Eq. (3), which excludes consideration of FF or the current-limiting subcell change for 1J.

$$P_{max} = P_{max_0} - C_P \log\left(1 + \frac{\Phi}{\Phi_{xP}}\right) \qquad \text{(Eq. 3)}$$

There is discrepancy between the dashed and solid lines in the high fluence region, which is attributable to change in the current-limiting subcell from the InGaP to the GaAs subcell at around $\Phi = 3 \times 10^{15}$ e^-/cm^2. Given these findings, this technique is thought to be effective in verifying degradation, especially in the high fluence

Table: Output parameter of the 2J solar cell using the measurement result under the AM0 solar simulator and the circuit simulation results.

	Isc [mA]	Voc [mV]	Pm [mW]	Ipm [mA]	Vpm [mV]
①Solar simulator	58.48	2187	98.06	54.52	1799
②circuit simulator	58.43	2183	98.01	54.88	1786
①/②	100.09%	100.18%	100.05%	99.34%	100.73%

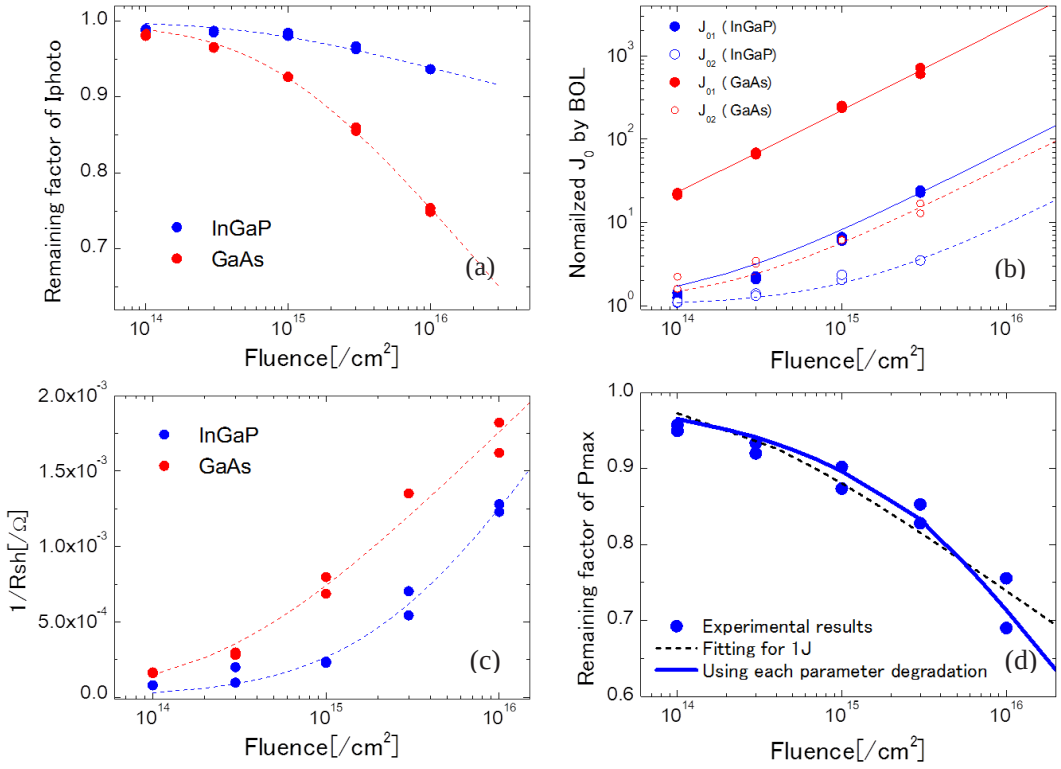

Fig. 5: Characteristics of the radiation resistance of I_{photo}, J_0, R_{sh} and P_{max} in the 2J solar cell after 1MeV electron irradiation. (a) Degradation curves of I_{photo} of the InGaP and GaAs subcells. (b) Degradation curves of J_{01} and J_{02} of the InGaP and GaAs subcells. (c) Degradation curves of $1/R_{sh}$ of the InGaP and GaAs subcells. (d) Degradation curves of P_{max} of the 2J cell. The dashed line was fitted without considering changes in FF and the current-limiting subcell for 1J. The solid line shows the degradation curve with consideration of changes in FF and the current-limiting subcell. The circle indicated experimental results of the remaining factor of P_{max}.

region, which changes a current-limiting subcell. These results promise to allow us to analyze the radiation degradation behavior of MJ cells more precisely, which will help establish a degradation model and consequently an accurate degradation prediction methodology for MJ cells.

4. Summary

The IV characteristics of subcells in InGaP/GaAs 2J solar cells were determined using EL and LBL methods before and after 1 MeV electron irradiation. I_{photo}, J_0 of InGaP and GaAs subcells as well as R_{sh} of each subcell were computed. By obtaining these degradation characteristics, the degradation trend of P_{max} of the 2J solar cell could thus be obtained with sufficient accuracy.

References

[1] M. Yamaguchi et al., "Novel materials for high-efficiency III–V multi-junction solar cells," Sol. Energy, vol. 82, pp.173-180 (2008).
[2] J. F. Geisz et al., "40.8% efficient inverted triple-junction solar cell with two independently metamorphic junctions," Appl. Phys. Lett., vol. 93, 123505 (2008).
[3] D. C. Marvin, "Assessment of Multijunction Solar Cell Performance in Radiation Environments," Aerospace Report, No. TOR-2000(1210)-1 (2000).
[4] U. Rau, "Reciprocity relation between photovoltaic quantum efficiency and electroluminescent emission of solar cells," Phys. Rev. B, vol. 76, 085303 (2007).
[5] T. Kirchartz et al., "Subcell I-V characteristic analysis of GaInP/GaInAs/Ge solar cells using electroluminescence measurements," Appl. Phys. Lett., vol. 92, 123502 (2008).
[6] S. Roensch et al., "Determination of the subcell photovoltage in multijunction solar cells via voltage-dependent capacitance analysis," Appl. Phys. Lett., vol. 98, 251113 (2011).
[7] R. Hoheisel, "Electroluminescence analysis of irradiated GaInP/GaInAs/Ge space solar cells," Sol. Energy Mater. Sol. Cells , in press.

Space Solar Cells and Related Materials B – P1

Effect of 250keV Electron Irradiation on Properties of CIGS Thin-Film Solar Cells

S. Kawakita[*1], M. Imaizumi[1], S, Ishizuka[2], H. Shibata[2], S. Niki[2], S. Okuda[3], and H. Kusawake[1]
1 Japan Aerospace Exploration Agency (JAXA), Japan
2 National Institute of Advanced Industrial Science and Technology (AIST), Japan
3 Osaka Prefecture University (OPU), Japan
*Email: kawakita.shirou@jaxa.jp
Keyword(s):Solar Cell, CIGS, Radiation

Abstract

Electrons with energy of 250keV introduce copper-related defects. The cells were irradiated with the electrons at below 150 K because the radiation defects could be recovered with a thermal annealing effect. The carrier density increased with increasing electron fluence. The electrons can generate Cu-related Frenkel-pairs. Copper vacancy could result in increased carrier density since the shallow acceptor level V_{Cu} is assumed to be the main defect in the CIGS absorbing layer. In contrast, a drop in the carrier density of CIGS solar cells irradiated with 1MeV electrons has been reported. In addition, activation energies of defects induced by 250 keV electrons with thermal annealing differ from those by 1MeV electrons. These results indicates that copper-related defects in CIGS induced by radiation do not degrade the CIGS solar cells.

1. Introduction

Cu (In, Ga) Se_2 (CIGS) solar cells have excellent radiation tolerance and their electrical properties are not degraded by high-energy electrons. Conversely, similarly to other types of solar cells, the cell performance does decline with exposure to high-energy proton irradiation. The radiation damage to cells due to proton irradiation gradually recovers when the irradiated cells are kept even at room temperature. In addition, the recovery rate is temperature-dependent[1)]. The radiation defect in CIGS solar cells, causing their performance to decrease, has been reported as an In antisite defect[2)]. However, it is unclear whether the other types of defects in CIGS, namely Cu, Ga, In and Se Frenkel-pairs, which are simultaneously generated by radiation, result in cell performance declining. Therefore, we have investigated these defects in CIGS solar cells induced by low energy electrons that can select the type of radiation defect in the solar cells.

2. Experimental Details

2.1CIGS Solar Cells

CIGS solar cells on glass substrate were fabricated using a co-evaporation method[3)]. The [Ga] / ([Ga + In]) composition ratio of the CIGS layers was about 0.4. The solar cells were of the bare type without anti-reflective coatings and cover glass. The electrical performance under AM 0 condition was described in Fig. 1.

2.2 Irradiation Experiments

The electron irradiation experiments were carried out using a Cockcroft Walton electron accelerator at Osaka Prefecture University (OPU). The cells were irradiated with electrons at an energy of 250 keV in a vacuum. The cells were cooled to less than 150K during experiments to prevent the thermal annealing effect using LN_2[4)]. Carrier profiling by capacitance-voltage (C-V) was carried out by using an HP 4284A impedance analyzer. Light current-voltage characteristics（LIV） were measured using an HP 4155C semiconductor analyzer and AM0 solar simulator with one Xe light source. These measurements were alternately performed during the irradiation experiments and executed at each designated fluence stage until the fluence reached the final value.

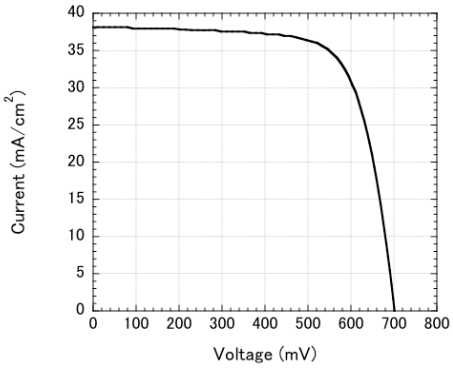

Fig. 1. Current-Voltage characteristic under AM0 condition of the CIGS solar cell.

3. Results & Discussions

Fig. 2 shows the relation between electron energy and the CIGS defect introduction rate. Our calculation indicated that the threshold energy of electrons to recoil Cu in CIGS is around

200keV, while that to recoil Ga atoms exceeds 350 keV, as illustrated in Fig. 2. Therefore, only the Cooper-related Frenkel-pair, namely, radiation defects can be generated in a CIGS cell that is irradiated with 200 – 300 keV electrons. According to these electron irradiation tests for CIGS solar cells, it is confirmed whether Cu related defects are radiation-related, which could degrade the electrical performance of the solar cells.

A 250keV electron irradiation test was carried out for a CIGS solar cell. The temperature during electron irradiation peaked at 150K. Figure 3 shows the carrier profile of the cell before and after electron irradiation, as calculated by the C-V measurement. The carrier density increased with increasing electron fluence. Conversely, it was reported that the density of the CIGS solar cell declined with increasing fluence of 1MeV electrons, which degraded the electrical performance[5]. This result implies that the defect introduced by 250 keV electrons is not radiation-related, which would impair the performance of the CIGS solar cells.

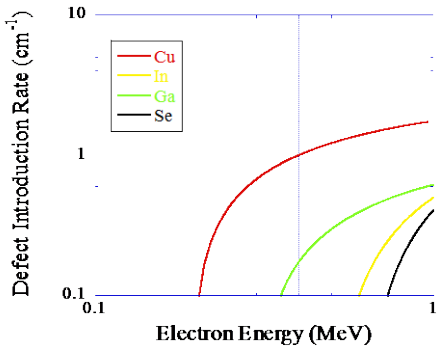

Fig. 2. Defect introduction rate of CIGS solar cells by electrons.

The defect induced by 250keV electrons is Cu-related, since the electrons can recoil only copper in CIGS. V_{Cu} defect is said to be the dominant accepter in P type of CIGS. Therefore, the increased carrier density would result in the V_{Cu} defect generated by the electrons.

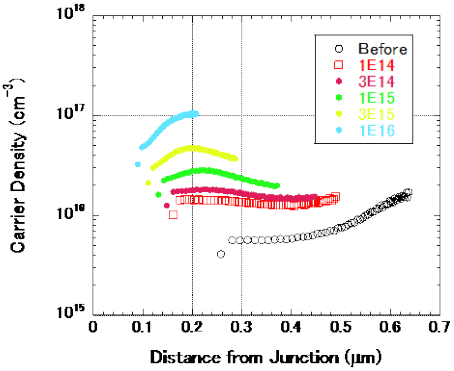

Fig. 3. Carrier profile of the CIGS solar cell irradiated with electrons.

Figure 4 indicates change in the LIV characteristics of the cell irradiated with electrons. Note that 1E14, 3E14, 1E15, 3E15, and 1E16 denote irradiations to fluences of 1×10^{14}, 3×10^{14}, 1×10^{15}, 3×10^{15}, and 1×10^{16} cm^{-2}, respectively.The feature of the LIV is the blocking behavior of the diode forward bias called "roll-over". The roll-over behavior is due to a second junction in the CIGS solar cells[6] and may be related to the Na-content in a CIGS absorber layer[7]. The Na in CIGS eases this effect, since the Na increases the accepter density. According to the result of the carrier profile of the CIGS solar cell irradiated with 250keV, the electrons increased the carrier density in the CIGS solar cell. Therefore, the increased carrier density reduced the roll-over of the cells, as in the Na effect for CIGS solar cells.

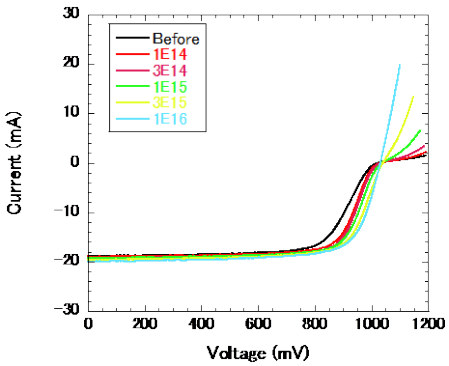

Fig. 4. Current-Voltage characteristics under AM0 condition before and after electron irradiation at 120K.

Annealing tests for the irradiated cell were performed to investigate the origin of the defect introduced by 250 keV electrons in CIGS. Figure 5 illustrates the change in the CIGS carrier profile following thermal annealing at 180 K. It is observed that the carrier density is reduced by thermal annealing. The reduction rate was estimated by the change of carrier density at 0V. It was established that the recovery rate of the carrier density has two types, namely fast and slow rates. The relationship between the reduction rate and temperature within the temperature range 140K to 200K is described in Figure 6. The activation energies of thermal annealing were calculated at 0.1 and 0.14eV, respectively. In constant terms, the activation energy, which was observed in the 1MeV electron irradiation test for CIGS solar cells, was reported at 1.0 eV[8]. This result is not consistent with our result. Thereby the Cu-related defect differs from the radiation defect that can impair the electrical performance of CIGS solar cells.

Furthermore the reduction in carrier density is attributable to the light soaked effect for CIGS solar cells[9]. The activation energy is reported to be 0.35eV. This effect is said to be attributable to metastable defects that are V_{Se}-V_{Cu} complex defects. However, the defect induced by 250keV electrons differs from the metastable defect since the activation energy does not correlate well to the energy introduced by the light soaked effect.

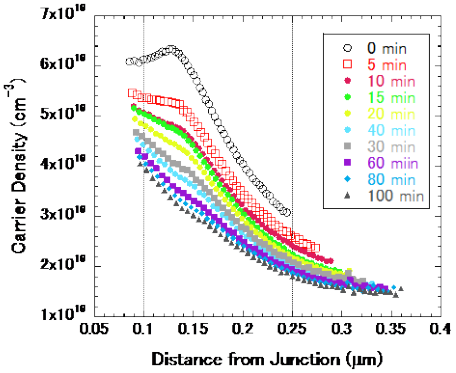

Fig. 5. Carrier profile of the CIGS solar cell conducted with a thermal annealing test at 180K.

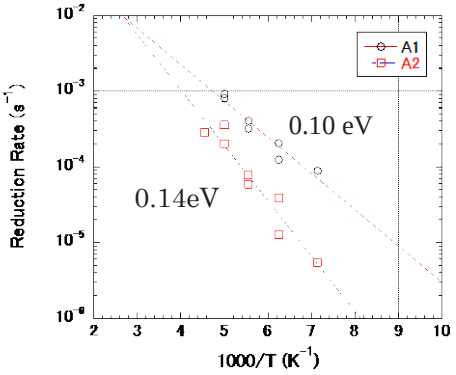

Fig. 6. Relationship between temperature and reduction rate of the CIGS solar cells.

4. Conclusions

The electrical performance of CIGS solar cells was not degraded by 250 keV electrons. In addition, the roll–over in the LIV feature was reduced by the electrons.It is revealed that the increase in carrier density produced by electrons caused this reduction in the effect. Although this phenomenon is similar to those that were founded in the Na and light soaked effects for CIGS solar cells, the activation energies of the defects with the thermal annealing differs from those by these effects. These results suggest that Cu-related defects introduced by electrons differ from defects that degrade the electrical performance of CIGS solar cells.

Acknowledgments

We would like to thank Mr. Takashi Oka of OPU and Mr. Mitsunobu Sugai of Advanced Engineering Services for their great help with the electron irradiation tests and electrical measurements.

References

[1] S. Kawakita, M. Imaizumi, M. Yamaguchi, K. Kushiya, T. Ohshima, H. Yoh, S. Matsuda, Jpn. J. Appl. Phys., **41**,(2002) L797.
[2] J. F. Guillemoles, L. Kronik, D. Cahen, U. Rau, A. Jasenek, H. W. Schock, J. Phys. Chem. B. **104** (2000) 4849.
[3] S. Ishizuka, K. Sakurai, A. Yamada, H. Shibata, K. Matsubara, M. Yonemura, S. Nakamura, H. Nakanishi, T. Kojima, S. Niki, Jpn. J. Appl. Phys. ,**44** (2005) L679.
[4] S. Kawakita et al., *Proceedings of the 29th Photovoltaic Specialists Conference*, (IEEE, New Orleans, 2002) p.978.
[5] A. Jaseneck, U. Rau, J. Apply. Phys., **90** (2001) 650.
[6] Y. J. Lee, J. L. Gray, Proceedings of the 12th European Photovoltaic Solar Energy Conference, Amsterdam, The Netherland, April 11-15, 1994, p.1561.
[7] R. Caballero, C. A. Kaufmann, T. Eisenbarth, A. Grimm, I. Lauermann, T. Unold, R. Klenk, H. W. Shock, App. Phys. Lett. **96** (2010) 902104.
[8] A. Jasenek, H. W. Schock, J. H. Werner, U. Rau, App. Phys. Lett. **79** (2001) 2922.
[9] M. Igalson, A. Urbaniak, A. Krysztopa, M. Edoff, Proceedings of the 25th European Photovoltaic Solar Energy Conference, Valencia, Spain, September 6-10, 2010, p.3436.

Session C

New Materials and Devices Designed by a New Concept

Large-area, flexible electronics for space applications

Tsuyoshi Sekitani*,Martin Kaltenbrunner, Takao Someya

The University of Tokyo, Electrical and Electronic Engineering and Information Systems, 7-3-1 Hongo, Bunkyo-ku, Tokyo 113-8656, Japan

Exploratory Research for Advanced Technology (ERATO),
Japan Science and Technology Agency (JST), 2-11-16, Yayoi, Bunkyo-ku, Tokyo 113-0032, Japan

*Email: sekitani@ee.t.u-tokyo.ac.jp

Keyword(s): Organic solar cells, Large-area electronics, Flexible electronics

Abstract

We report the thinnest, lightest, and most-flexible organic solar cell, with fabrication processes compatible with large-area processing (1). The efficiency of these ultrathin solar cells is equal to that of their glass-based counterparts. When transferred to a pre-stretched elastomeric support our ultrathin solar cells are shown to be ultracompliant.Our solar cells have an unprecedented power output per weight of 10 W/g, which is the highest specific weight and then, enabling new applications in ambient sensor nodes, remote sensing systems, weather balloons, unmanned aircraft,and space applications.

1. Introduction

Light-weight and mechanically resilient solar power sources are of increasing interest for modern applications such as electronic textiles, synthetic skin, and robotics (2,3). Organic photovoltaic (OPV) solar cells are highly promising in this sector. The thin-film devices comprise two electrodes, a light harvesting active layer and blocking or transport layers. The total thickness of a functional OPV cell is only a few hundred nanometers. Primary benefits of OPV cells are often listed as low cost, low weight, flexibility, and compatibility with reel-to-reel processing for high volume production (4,5). Efficiency and lifetime have reached commercially acceptable levels and flexible modules with roughly 1.5% power conversion efficiency and over 1 year lifetimes are already on the market (6). Mitsubishi Chemical Holdings have attained laboratory scale cell efficiencies exceeding 10% (7). Weight and flexibility are two of the primary benefits of OPV yet these mechanical properties are entirely dominated by the device substrate, which leaves much room for the advancement of OPV.

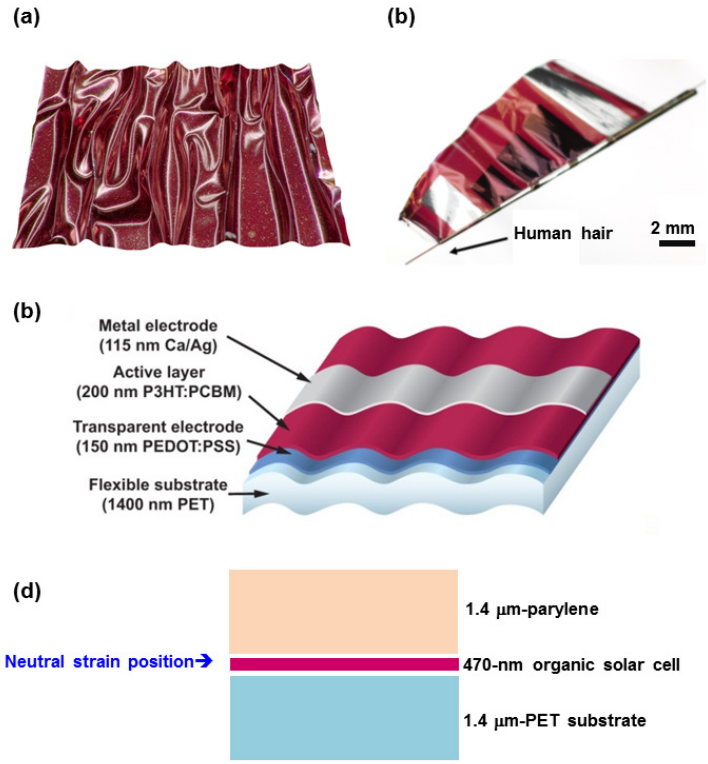

Fig. 1.(a) and (b) Pictures of a thin-film organic solar cells. (b) and (c) Schematic cross-sectional illustration.

In this work, we present ultra-thin, -light, -flexible and -compliant OPV devices constructed on only 1.4-μm-thick poly(ethylene 2,6-)naphthalate (PEN) substrates. We obtain 4.2% power conversion efficiency, an unprecedented specific weight value of 10 W/g and can reversibly attain strains of 70% on elastomeric

support.Other than the substrate, all of the materials used for our devices are well-established materials for OPV, including poly(3,4-ethylenedioxythiophene):poly(styrenesulfonate) (PEDOT:PSS), poly(3-hexylthiophene) (P3HT), (6,6)-phenyl-C61-butyric acid methyl ester (PCBM), and Ca/Ag evaporated metal electrodes. Using these materials, OPV devices on indium tin oxide (ITO) coated glass substrates have been certified with efficiency up to 4.3% (8). Using the ITO-free architecture on PEN we obtain comparable efficiency while demonstrating the extreme mechanical properties of organic solar cells.

Among the thinnest reported substrates for OPV devices are 125 μm PET and PEN (9-11). The resulting solar cells are highly flexible with radius of curvature of 5 mm. Stretchable devices have been fabricated on pre-stretched PDMS (thickness 200-500 μm), which can then be compressed to 27% of their original size reversibly (12). A liquid metal back contact was used to improve mechanical stability. In all of these cases the actual solar cell still constitutes less than 0.25% of the total device thickness. Inorganic GaAs solar microcells (thickness 6.6 μm with polymer coatings) with high areal coverage allowed for 20% strain and wrapping around cylinders with 1.5 mm radius (13). Reducing the substrate thickness further to the 1.4 μm thin PEN films used here significantly improves the specific weight of the system but it also drastically improves the mechanical resilience under flex or compression.

2. Device manufacturing, results, and discussions

Pictures and schematic illustration of an ultra-thin solar cell is shown in Fig. 1. The total device thickness without an encapsulation layer is only 1.9 μm, where about one-quarter of the thickness is the active solar cell. The P3HT:PCBM bulk heterojunction solar cell is fabricated on a PEDOT:PSS coated 1.4 μm thick PEN substrate foil. Top electrodes are 115 nm Ca/Ag. Fig. 1b illustrates the extreme bending flexibility of the solar cell, wrapped around a human hair with a radius of 35 μm, and current density (J)-voltage (V) characteristics can be seen in Fig. 2. Fig. 3 depicts a solar cell on a 100 μm thick pre-stretched 3M VHB 4905 elastomer. As the strain of the elastomer is reduced by 30% and then 50%, it is evident that the solar cell becomes wrinkled. This enables the solar cell to be stretched back to the pre-strain defined by the elastomer.

The ultra-thin flexible substrate is completely compatible with scalable processing and, therefore, is advantageous for high throughput fabrication. During fabrication, we avoid complex transfer printing processes.

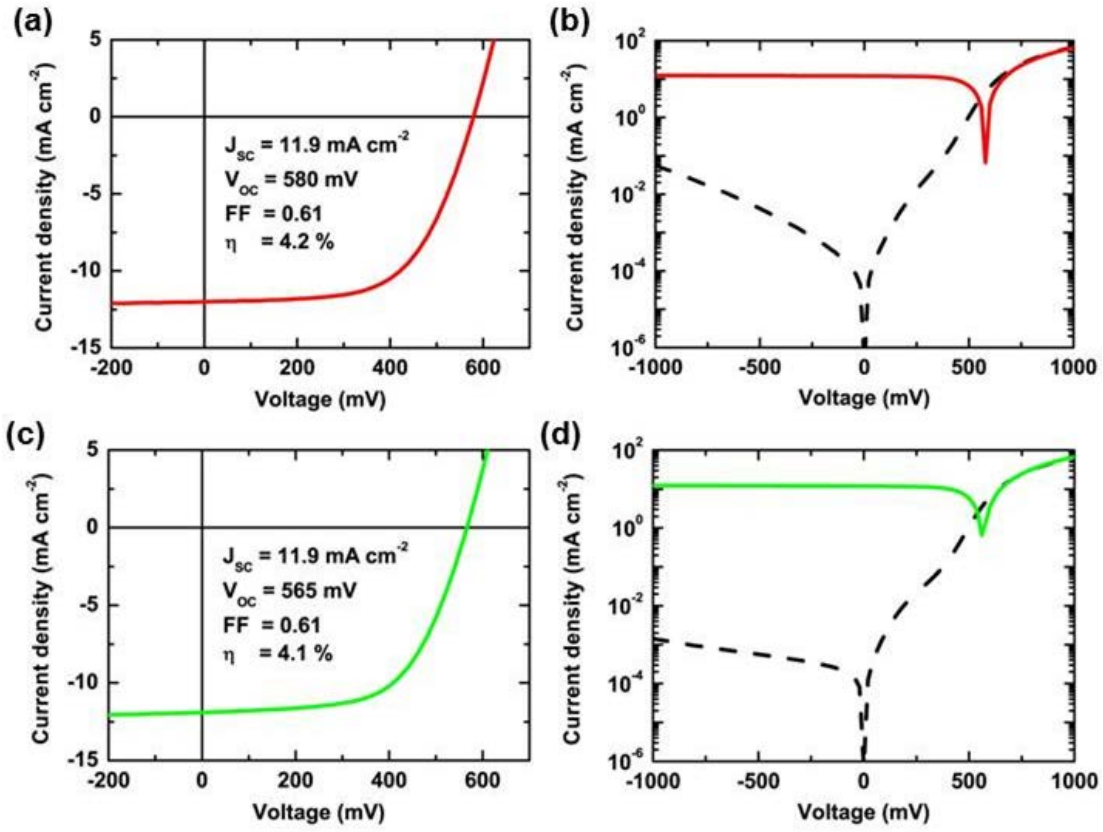

Fig. 2.Current density (J)-voltage (V)characteristics obtained from organic solar cells on 1.4-μm-thick PET substrate (a) and (b), and on glass (c) and (d). Dashed lines represent dark current density as a function of voltage.

For laboratory-scale device construction, the substrate is placed onto a supporting glass plate for processing ease. The PEN adheres to the PDMS coated glass via weak van der Waals bonding, which allows standard laboratory processes such as spin coating, thermal annealing, and vacuum evaporation. The primary functions of the glass support are to maintain planarity during processing and to ease the handling of the device, and the PEN can be easily removed by peeling it away. Exact processing details are found in the experimental details section.

Prior to removing the PEN from the supporting glass, the device J-V characteristics are measured under the solar simulator (approximately the A.M 1.5 Global spectrum with 100 mW/cm^2 intensity and spectral mismatch correction), and in the dark. After removal from the supporting glass, it is difficult to maintain planarity in the device, and therefore to know the incident area for calculation of current density (J) and power conversion efficiency (η). All measurements while the device is still attached to the glass support are scaled per unit area, using a conservative area estimate as the PEDOT:PSS transparent electrode is difficult to pattern exactly. The data reported in subsequent sections, for mechanical stretching and cycling, is not scaled to area and only total current and power are reported for comparison during mechanical manipulation. The J-V characteristics of an optimized device are shown if Fig. 2. This particular device performs with VOC = 580 mV, JSC = 11.9 mA/cm^2, F.F. = 61%, and η = 4.2% under 1 sun illumination. This is a representative sample from over 50 devices constructed with various parameters. Of primary concern here are the transparency and conductivity of the PEDOT:PSS transparent electrode. By varying the thickness of the layer, there is a trade-off between F.F. and JSC, as a thicker electrode will be more conductive but less transparent.

The device performance shown in Fig. 2a shows one of the best-performing devices. However, through mass construction of the devices with slight variations, we have obtained a wide range of F.F. (up to 71%) and JSC (up to 12 mA/cm^2) though not in the same device. The average η of the fabricated samples was 3.8%, and $\eta >$ 3.5% was easily reproducible. As seen in Fig. 2, the device shows reasonable dark diode rectification.
These results are very comparable to leading BHJ OPV devices using P3HT:PCBM on ITO-coated glass substrates (8). The scarcity and cost of indium, and the requirement of smooth substrates for thin films are considered to be significant hurdles for mass production of OPV devices (14,15). The surface roughness of the PEN substrate, and the high-conductivity PEDOT:PSS in place of ITO do not significantly reduce the device efficiency.

The primary goal in constructing such thin devices is to demonstrate continuous opto-electronic operation under extreme mechanical duress. In order to do so, we transfer the device from the glass support to a pre-stretched elastomer. (3M VHB 4905) The device on PEN sticks to the elastomer very well, and the glass support can be removed. Two rigid plastic spacers are placed on the elastomer, leaving a gap of 1 cm for the compression and stretching of the device. This assures that the strain will be nearly one dimensional and concentrated in the region of the active device, which occupies roughly half of the 1 cm gap. The rigid spacers are brought closer together in steps of 1 mm, corresponding to 10% compression. At each step the I-V characteristics are measured under the solar simulator, and the results are shown in Fig. 3. It is clear that the device remains a functional solar cell down to 80% compression. Upon re-stretching the device, it returns to its pre-compression operation state. The V_{OC}, I_{SC}, F.F., and output power are plotted as a function of compression in Fig. 3e-f, all normalized to their pre-compression value. As the incident area should track linearly 1 to 1 with the compression, we would expect the I_{SC} and power to scale exactly with the compression, following the black line in Fig. 3f. We can see that both values are consistently higher than the device area scaling.

The optimistic explanation for this would be an enhancement in light harvesting due to micro-texturing upon folding of the device. Light not absorbed on the first pass through the active layer would be reflected back into the device on the other side of the crease, allowing for improved overall absorption. Additionally, the compression does not decrease the device area uniformly. As the device area is defined by the metal back electrode, it is likely that the overall substrate compresses more on the edge. Thus, when the total compression is 50%, the device area is not reduced by exactly the same value. At compression greater than 60%, there is a sharp drop off in the I_{SC} and the power output. At such values, the elastomer no longer sticks to the rigid plastic delimiters, so the device begins to fold slightly behind and is shaded from the illumination.

Biaxial compression and stretch testing was also performed. The OPV devices on PEN substrates were attached to the same elastomer, now pre-stretched in two directions. In order to do so, the rigid plastic pieces that constricted the compression to one dimension were left off, which makes the actual compression of the device much less certain. We estimate 50% compression in one direction with an additional 20% compression in the other. The overall biaxial stretch behavior is similar to the uniaxial stretch described above.This approach for stretchable solar cells has several distinct advantages.The planar-only fabrication processes are fully reel-to-reel compatible.The complete solar cells show large, reversible quasi-linear stretching ratios over 70% when

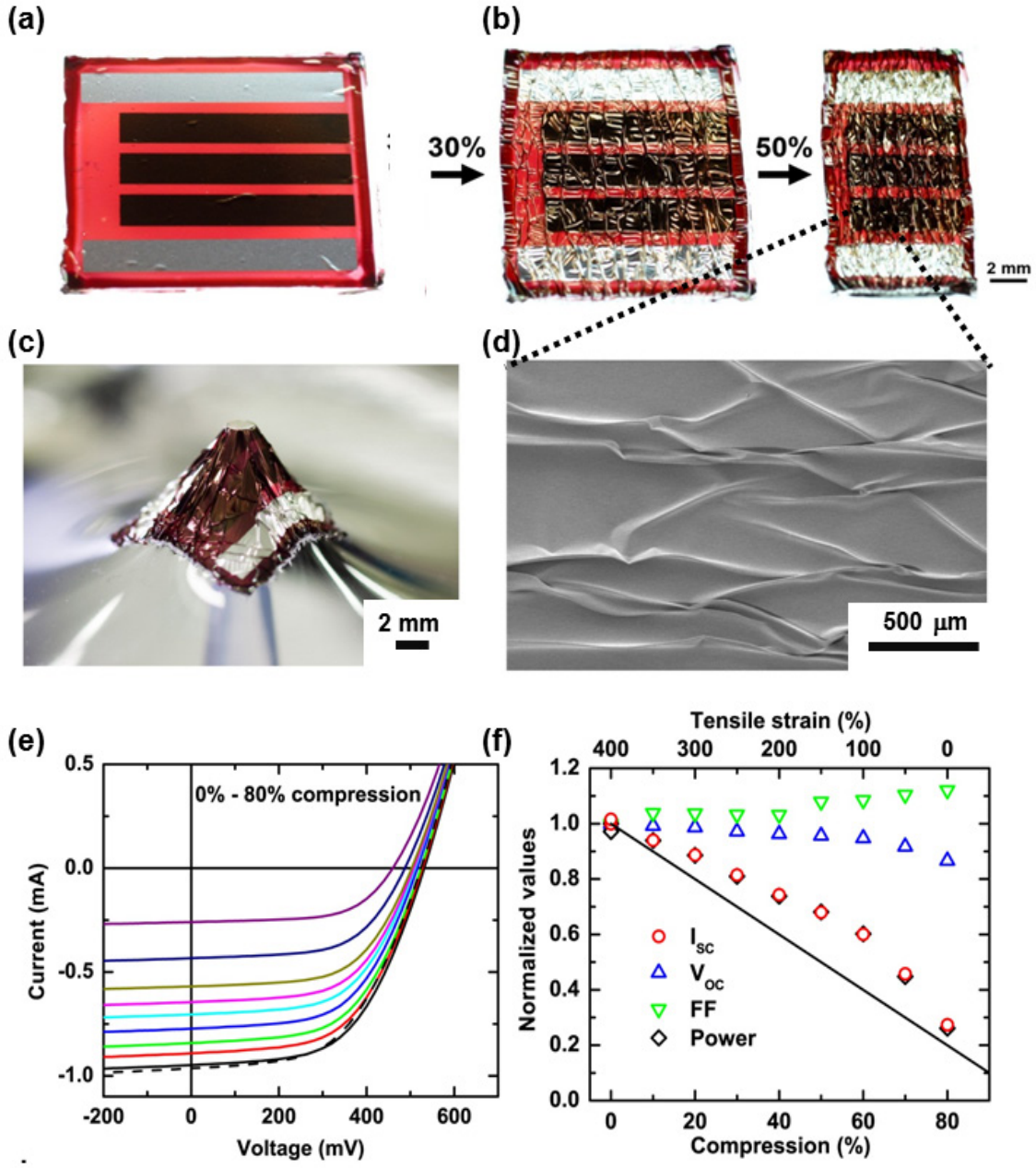

Fig. 3.1.4-µm-thick organic solar cell on rubber substrate with (a) 100%-pre-stretching (b) 50%- and 30%- compression., (c) An organic solar cellwith three-dimensional deformation. (d) Scanning electron microscope image of the surface of organic solar cell. (e) J-V characteristics with changing compressive strain from 0 to 80%. (f) I_{SC}, V_{OC}, FF, and Power as a function of compression.

transferred onto an elastomeric support.
Though compression and stretching of the device induces very little change in the device performance, there may be small changes that accumulate over many cycles. To investigate the durability of the devices under repeated stretching and compression, we cycled the device from 0% (original size) to 50% compression and back more than twenty times. At each cycle the I-V characteristics were measured under the solar simulator, both in the compressed and extended state. The cycling test showed gradual decrease in the I_{SC}, the F.F. and the output power, resulting in a 27% decrease in power after 24 cycles.

When considering solar power for certain applications, the power output per weight (specific weight) may be the most critical metric. This is particularly true for situations that require portable power; where payload is a premium such as aircraft, spacecraft, or personal pack-load. The specific weight of various solar technologies (panels and cells) for terrestrial and space applications is compared in Fig. 4. Commercially available space rated high efficiency Si and triple junction cells have 0.82 W/g and 0.39 W/g respectively (17).A recent report showed

CIGS cells constructed on thin (25 μm) polyimide films with 18.7% efficiency (17). These devices have extremely high specific weight of roughly 3 W/g.The OPV devices constructed on PEN presented here have a per-area mass of 4 g/m^2, and 4% efficiency, giving 10 W/g.

This extreme specific weight may be advantageous for certain applications. Total power and device lifetime are obviously primary factors for high-cost situations, like most space-based uses. But weather balloons, unmanned aircraft, or any other remote sensing systems may prioritize specific weight and have known project duration. The same is true for pack-weight for remote wilderness use, where there is often a need for light-weight power sources. Ultra-thin OPV may be ideal for such applications. Polymer based solar cells have been constructed on 1.4 μm thick PEN substrate material. The devices use standard OPV materials and obtain nearly identical efficiency to those constructed on ITO coated glass substrates with over 4% power conversion efficiency. Here, the high conductivity PEDOT:PSS electrode replaces the ITO which is considered a cost and volume limiting material (14). The polymer electrode is highly flexible compared to the ternary oxide (19). The device layers consist of roughly 450 nm total thickness, so the total device including substrate is less than 2 μm.

These ultra-thin, flexible solar cells show unprecedented mechanical resilience. By adhering the flexible device to a pre-stretched elastomer we have shown that the devices survive quasi-linear compression to below 70% of their original area. Furthermore, we have shown cyclic compression and stretching to 50%, over more than 20 full cycles with marginal loss in device performance and no visible defect formation beyond the external contact points.Though the electrically active components of this device are in principle no different than other standard OPV devices, the solar cell now constitutes roughly 25% of the total thickness and 45% of the total weight. OPV is emerging as a viable technology where temporary, high-volume, and low-weight power sources are required. The extreme flexibility and specific weight demonstrated here realize the unique potential for OPV as an ultra-thin-film power source.

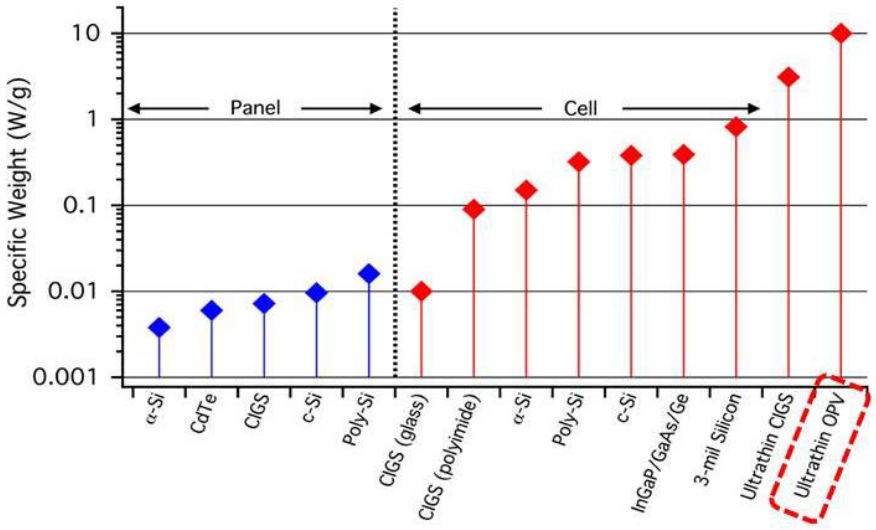

Fig. 4.Specific weight of various photovoltaic technologies for complete modules (left) and individual cells (right). Module data is taken from commercially available panels and should be representative: Kaneka 12V 55W PV Module, First Solar FS272, Sunforce 70W Pro Series, Bosch Solar Module c-Si M60, and Kyocera KD245Gx-LPB. Cell data was taken from published academic results. In many cases, the cell weight was not published and so was estimated from published layer thicknesses and known material densities, assuming 2% areal coverage for metal grids contacts (17,18,22-26).

Methods Summary

Rigid glass slides, coated with a ≈ 500 nm thick polydimethylsiloxane (PDMS) layer served as supporting substrates for the 1.4 μm thick PEN foils (obtained from Pütz GMBH + Co. Folien KG). Adhering the PEN film to the supports readily enabled all subsequent planar processing steps including spin-coating, thermal annealing and vacuum deposition. The devices could be peeled of the supporting stack without causing damage to the solar cells. We spun PEDOT:PSS (Clevios PH1000, with 5 vol% dimethylsulfoxide, and mixed with 0.5 vol% Zonyl FS-300 fluorosurfactant from Fluka to promote wetting on the hydrophobic PEN) at 1000 rpm for 60 s and then 2000 rpm for 60 s onto the PEN films. The samples were dried on a hotplate at 120 °C for 30 min, yielding 150 nm thick PEDOT:PSS layers with ~100 Ω/sq. A solution of 30 mg/ml P3HT (obtained from Plextronics and purified by repeated reprecipitaion) and 30mg/ml PCBM (from Solenne BV) in dichlorobenzene at 1500 rpm for 120 s. The P3HT:PCBM was partly wiped away with a toluene-soaked cotton swab, exposing some of the

PEDOT:PSS to allow for contacting. 200 nm thick P3HT:PCBM films were obtained. The samples were transferred to a nitrogen-filled glovebox and annealed on a hotplate at 150° C for 15 min. Finally, 15 nm Ca and 100 nm Ag were thermally evaporated at 1 Å/s and pressure of 10-6 mbar. Typical devices had an active area of 0.1 cm2. The devices were first characterized in the dark and under illumination of a solar simulator (A.M 1.5 Global spectrum with 100 mW/cm^2 intensity with spectral mismatch correction). I-V characteristics were recorded using a Keithley 236 source meter. Stretching experiments were performed with a purpose-built stage. All measurements were carried out in a nitrogen-filled glovebox. Layer thicknesses were measured with a Digital Instruments Dimension 3100 AFM.

Acknowledgments

The authors would like to thank Matthew S. White, Eric D. Głowacki, NiyaziSerdarSariciftci, Siegfried Bauer (Johannes Kepler University, Austria) for their contributions.

References

[1] Kaltenbrunner, M. at al., "Ultrathin and lightweight organic solar cells with high flexibility". Nature Communications, vol. 3, 770 (2012).
[2]Lipomi, D. J. &Bao, Z. "Stretchable, elastic materials and devices for solar energy conversion". Energy Environ. Sci. vol. 4, pp. 3314-3328 (2011).
[3] Baca, A. J. et al. "Compact monocrystalline silicon solar modules with high voltage outputs and mechanically flexible designs". Energy Environ. Sci. vol.3, pp.208-211 (2010).
[4] Brabec, C. J., Sariciftci, N. S. &Hummelen, J. C. "Plastic solar cells". Adv. Funct. Mater. 11, 15-26 (2001)
[5] Coakley, K. M. et al. Conjugated polymer photovoltaic cells. Chem. Mater. vol.16, pp.4533-4542 (2004)
[6] Hauch, J. A. et al. "Flexible organic P3HT:PCBM bulk-heterojunction modules with more than 1 year outdoor lifetime". Solar Energy Materials and Solar Cells vol.92, pp.727-731 (2008).
[7] Aramaki, S., et. al. Private communication (2011).
[8] Li, G. et al. "High-efficiency solution processable polymer photovoltaic cells by self-organization of polymer blends". Nat. Mater. vol.4, pp.864-868 (2005).
[9] Rowell, M. W. et al. "Organic solar cells with carbon nanotube network electrodes". Appl. Phys. Lett. vol.88, 233506 (2006).
[10] Galagan, Y. et al. "ITO-free flexible organic solar cells with printed current collecting grids". Solar Energy Materials and Solar Cells vol.95, pp.1339-1343 (2011).
[11] Yambem, S. D., Liao, K. S. & Curran, S. A. "Flexible Ag electrode for use in organic photovoltaics". Solar Energy Materials and Solar Cells vol.95, pp.3060-3064 (2011).
[12] Lipomi, D. J., et al."Stretchable organic solar cells. Adv. Mater. vol.23, pp.1771-1775 (2011).
[13] Lee, J. et al. "Stretchable GaAsphotovoltaics with designs taht enable high areal coverage". Adv. Mater. vol.23, pp.986-991 (2011).
[14] Fortunato, E., et al."Transparent conducting oxides for photovoltaics". MRS Bull. vol.32, pp.242-247 (2007).
[15] Tenent, R. C. et al. "Ultrasmooth, large-area, high-uniformity, conductive transparent single-walled-carbon-nanotube films for photovoltaics produced by ultrasonic spraying". Adv. Mater. vol.21, pp.3210-3216 (2009).
[16] Graz, I. M., et al."Extended cyclic uniaxial loading of stretchable gold thin-films on elastomeric substrates". Appl. Phys. Lett. vol.94, 071902 (2009).
[17] Fatemi, N. S., Pollard, H. E., Hou, H. Q. & Sharps, P. R. "Solar array trades between very high-efficiency multi-junction and Si space solar cells". Conference Record of the 28th IEEE Photovoltaic Specialists Conference, Anchorage, AK, USA (2000).
[18] Chirila, A. et al. "Highly efficient Cu(In,Ga)Se_2 solar cells grown on flexible polymer films". Nat. Mat. advance online pub. 18 Sept. (2011).
[19] Sierros, K. A., et al.,"Stress-corrosion cracking of indium tin oxide coated polyethylene terephthalate for flexible optoelectronic devices". Thin Solid Films vol.517, pp.2590-2595 (2009).
[20] Netter, T., "CIGS on plastic: efficiency goes high". http://www.interpv.net/magazine/mag_view.asp?idx=248&part_code=01 (2010).
[21] Soderstrom, T. Haug, F. J., Terrazzoni-Daudrix, V. &Ballif, C. "Optimization of amorphous silicon thin film solar cells for flexible photovoltaics". J. App. Phys. vol.103, 114509 (2008).
[22] Rath, J. K., et al."Fabrication of thin film silicon solar cells on plastic substrate by very high frequency PECVD". Solar Energy Materials and Solar Cells vol.94, pp.1534-1541 (2010).
[23] Zhao, J., Wang, A., Green, M. A. &Ferrazza, F. "19.8% efficient „honeycomb“ texturedmulticrystalline and 24.4% monocrystalline silicon solar cells". Appl. Phys. Lett. vol.73, pp.1991-1993 (1998).
[24] Zhao, J., Wang, A., Altermatt, P. & Green, M. A. "Twenty-four percent efficient silicon solar cells with double layer antireflection coatings and reduced resistance loss". Appl. Phys. Lett. vol.66, pp.3636-3638 (1995).

New Materials and Devices Designed by a New Concept C - 2

Annealing Effects on Charge Collection Efficiency of an Electron-Irradiated 4H-SiC Particle Detector

N. Iwamoto[*1], B. C. Johnson[1], T. Ohshima[1], N. Hoshino[2], M. Ito[2], and H. Tsuchida[2]
1 Japan Atomic Energy Agency (JAEA), Japan
2 Central Research Institute of Electric Power Industry (CRIEPI), Japan
*Email: iwamoto.naoya@jaea.go.jp
Keywords:Silicon Carbide, Particle Detector, Charge Collection Efficiency, Annealing Effect

Abstract

Thermal annealing effects on the charge collection efficiency (CCE) of an electron-irradiated4H silicon carbide Schottky barrier diode (SBD) particle detector have been studied.The CCE of the SBD detector is degraded by 1 MeV electrons with a fluence of 1×10^{15} cm^{-2}. The degraded CCE recovers with low temperature annealing up to 300 °C. However, CCE starts to decrease again by annealing at 350 °C. Conventional electrical characterization such as current and capacitance vs voltage measurements, deep level transient spectroscopy used to understand the CCE variation on annealing is discussed.

1. Introduction

Silicon carbide (SiC) is a promising material for high-energy charged particle detectors. Because of wide bandgap energies (3.2 eV for 4H-SiC, 3.0 eV for 6H-SiC) and small intrinsic carrier densities ($<10^{-6}$ cm^{-3} at room temperature), leakage currents of SiC diodes arevery small even above room temperature and under visible light. Therefore, SiC diode particle detectors can ideally be operated with a sufficient signal to noise ratio under such conditions where silicon diode particle detectors cannot [1]. Over the last decade, many researchers demonstrated that SiC detectors show excellent charge collection characteristics for high-energy particles[1-3]. The radiation resistance of SiC detectors for high-energy particles and gamma-rays has also been studied [4-6]. These data are very important to predict the detectors' lifetime. In addition, it is also important to study post-irradiation annealing effects on the detectors. Provided that a detector performance is recovered by annealing at a practical temperature, the detector's lifetime can be prolonged. However, only a few studies of post-irradiation annealing effects on SiC detectors have been carried out so far [7].

In this study we investigate thermal annealing effects on the charge collection efficiency (CCE) of an electron-irradiated SiC detector. We also attempt to explain the variation of CCE after electron irradiation and during annealing by comparing the data obtained by conventional electrical measurements.

2. Experiment

Schottky barrier diode (SBD) particle detectors were fabricated on an n-type 4H-SiC epitaxial wafer. The epilayer was grown on a low-resistivity n-type 4H-SiC substrate (Si-face, 8^{o}off) by a hot-wall chemical vapor deposition technique [8]. The thickness of the grown epilayer was 140 μm. Nickel (Ni) was deposited on the bottom side of the wafer and subsequently sintered at 1100°C for 3 minutes to form an Ohmic contact. For a Schottky contact on the top side, Ni with an area of 1 mm × 1 mm was deposited and no thermal treatments were carried out. The ideality factor and the Schottky barrier height of the SBD detector determined from the current-voltage (I-V) characteristics were 1.06 and 1.68 eV, respectively. The carrier density of the epilayer estimated from the capacitance-voltage (C-V) characteristics was 4×10^{13} cm^{-3}.We note that the C-V characteristics did not depend on the measurement frequencies between 1 MHz and 1 kHz.

In order to form defects in the SiC crystal, the SBD detector was irradiated with 1 MeV electrons to the fluence of 1×10^{15} cm^{-2}. The projected range of these electrons is approximately 1 mm, well beyond the active device region, with a relatively constant defect density generated throughout the sample. The SBD detector was mounted on a water-cooled plate to avoid an increase of the temperature during the irradiation. The electron-irradiated SBD detector was subsequently annealed between 100 °C and 400 °C for 30 minutes in an Ar atmosphere.

The CCE of the SBD detector was characterized at room temperature by using 5.5 MeV alpha particles and a standard pulse height analysis system which consists of an Ortec 142A charge sensitive preamplifier, an Ortec 571 spectroscopic amplifier with a shaping time of 0.5 μs, and a Canberra Multiport II multi-channel analyzer. I-V and C-V characteristics of the SBD detector were also measured at room temperature using an Agilent 4156B semiconductor analyzer and an Agilent E4980A LCR meter.

Deep level transient spectroscopy (DLTS) was also performed to characterize the defects in the SiC crystal. Since the SBD detector has a large series resistance making DLTS measurements difficult, a SBD made on a low-resistivity (highly-doped) epilayer was used. The highly-doped SBD was also irradiated with 1 MeV electrons to a fluence of 1×10^{15} cm^{-2}, and subsequently annealed at 300 and 400 °C for 30 minutes. For the

capacitance transient measurements, the highly-doped SBD was reverse-biased to8 V, and a carrier filling pulse of0 V for 50 ms was applied. The capacitance transients were measured at temperatures between 150K (-123 °C) and 350 K (77 °C) by using a Boonton 7200 capacitance meter, and were analyzed by the rate window method [9].

3. Results and Discussion

3.1 Charge Collection Efficiency, Capacitance, Leakage Current

Figure 1 shows the reverse bias voltage-dependent CCE of the SBD detector before and after the electron irradiation characterized by using 5.5 MeV alpha particles with the pulse height analysis system. We note that the fluence of alpha particles used for each bias voltage is as low as 7×10^4 cm^{-2}, and they did not affect the CCE and electrical measurements. Before the electron irradiation, pulse heights of the SBD detector increase with increasing reverse bias voltage and become constant at 15 V and higher. Since a good saturation of the pulse heights is observed above 15 V, we define the CCE of the SBD particle detector is 100% at these bias voltages. The depletion region width at 15 V is estimated to be 20 μm from the C-V characteristics, and is comparable to the projected range of a 5.5 MeV alpha particle in 4H-SiC.Therefore,all carriers induced by the alpha particle strike are efficiently collected by the drift effect within the depletion region. Degradation of the CCE is seen after the electron irradiation, and is more pronounced at lower bias voltages. Since the electric field formed in the depletion region is weaker and the carrier drift velocity is smaller at lower bias voltages, more carriers are captured by and/or recombine via defect levels formed by the 1 MeV electrons.

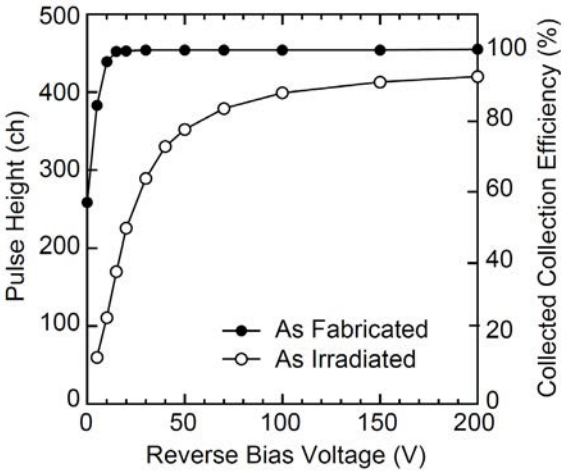

Fig.1 Reverse bias voltage dependence of CCE of a 4H-SiC SBD diode before and after the electron irradiation. The CCEs were characterized by using 5.5 MeV alpha particles at room temperature.

Figure 2 (a), (b) and (c) show CCEs, capacitances and leakage currents of the SBD detector, respectively, before and after the electron irradiation, and as a function of annealing temperature. As the CCEs decrease after the electron irradiation, capacitances of the SBD detector also decrease and become independent of the reverse bias voltage as shown in Fig. 2 (b). This implies that defects formed by the 1 MeV electrons compensate electrons supplied from donors, and decrease the effective carrier density in the epilayer. Since a wider depletion region is formed in an epilayer with a lower carrier density, the electric field and the carrier drift velocity in the depletion region decrease. This also reduces the CCE.

The degraded CCE recovers as the annealing temperature increases up to 300 °C as shown in Fig. 2 (a). At a reverse bias voltage of 50 V, the CCE, which had decreased to 78% by the electron irradiation, recovers to 93% after annealing at 300 °C. Namely, the 300 °C-annealing significantly suppresses the electron irradiation-induced degradation of CCE. On the other hand, the decreased capacitances of the SBD detector do not change up to 400 °C as shown in Fig. 2 (b). From these results it is speculated that various types of defects are formed by the 1 MeV electrons. Some defects act as traps and/or recombination centers for alpha particle-induced carriers and are removed by annealing up to 300 °C.Other defects reduce the

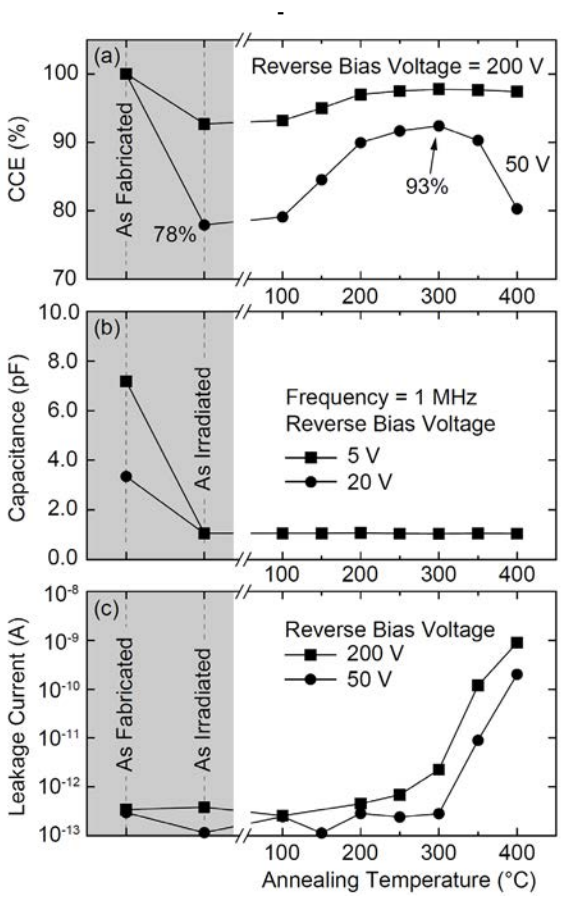

Fig. 2 (a) CCEs, (b) capacitances and (c) leakage currents of 4H-SiC SBD particle detector before and after the electron irradiation, and as a function of annealing temperature.

effective carrier density in the epilayer and persist up to 400 °C.

Recovered CCE starts to degrade again by annealing at 350 °C as shown in Fig. 2 (a). Re-degradation of CCE seems to be correlated with a drastic increase of the leakage current seen at same annealing temperatures (350-400 °C) as shown in Fig. 2 (c). The leakage current after annealing at 400 °C are three orders of magnitude larger than those after annealing at 300 °C. We have also measured temperature-dependent leakage currents of the SBD detectors at a reverse bias voltage of 50 V (not shown in the figure), and determined their activation energy (E_A) according to the Arrhenius equation,

$$I_{\mathrm{Leak}}(T) \propto \exp\left(-\frac{E_A}{kT}\right), \quad (1)$$

where $I_{\mathrm{Leak}}(T)$ is temperature-dependent leakage current, k is Boltzmann's constant and T is temperature. The E_A of the leakage current after annealing at 300 °C is estimated to be 1.16 eV around room temperature while the E_A after annealing at 400 °C is 0.70 eV. The change of the E_A indicates the change of electron-hole pair generation process in the depletion region. Namely, some defect levels which act as efficient electron-hole pair generation/recombination centers newly emerge in the bandgap of 4H-SiC after annealing at 350-400 °C. These defect levels may also act as efficient recombination centers for alpha particle-induced carriers.

3.2 Deep Level Transient Spectroscopy

Figure 3 shows the DLTS spectra of a highly-doped SBD before and after the electron irradiation, and after annealing at 300 and 400 °C. The spectra were obtained from the capacitance transients analyzed by the rate window method with an emission rate of 8.89 sec^{-1} [9]. We note that all peaks shown in Fig. 3 correlate to majority carrier (electron) traps. No peaks are found in the spectrum before the electron irradiation. On the other hand, three distinct peaks, labeled as EH_1, $Z_{1/2}$ and EH_3, emerge after the electron irradiation. These results are consistent with data often reported in the literature [10-12]. The energy levels of EH_1, $Z_{1/2}$ and EH_3 are known as E_C– 0.45, E_C– 0.68, E_C– 0.72 eV, respectively, where E_C is the bottom of the conduction band [12].Defect densities of these levels are reduced by annealing at 300 °C. EH_1 and EH_3 are completely removed by annealing at 400 °C while $Z_{1/2}$ still remains. Reductions of these defect densities may contribute to the recovery of CCE found in the annealing temperature range up to 300 °C. However, new defect levels, which correlate to the drastic increase of leakage current as shown in Fig. 2 (c), are not obvious in the DLTS spectrum after annealing at 400 °C. Such defect levels may be convoluted with other defect peaks oremerge at scan temperature outside of the range employed here. Danno *et al*. indeed reported that some defect levels emerge in the lower half of bandgap after post-electron irradiation annealing [13]. However, since the conditions of electron irradiation and annealing in their study are quite different from ours, it may be difficult to compare these results directly.

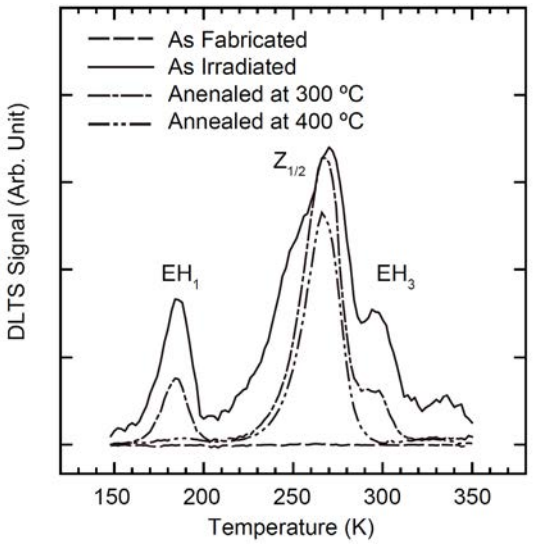

Fig.3DLTS spectra of a highly-doped 4H-SiC SBD obtained before and after the electron irradiation, and after annealing at 300 and 400 °C with a emission rate of 8.89 sec^{-1}. All peaks correlate to electron traps in n-type 4H-SiC epilayer.

4. Summary

Thermal annealing effects on CCE of an electron-irradiated4H-SiC SBD detector have been studied. It was found that the 300 °C-annealing significantly suppresses the electron irradiation-induced degradation of CCE. Since most materials such as metals and ceramics, which are conventionally used to assemble a commercial particle detector, withstand a temperature as high as 300 °C, it is possible to practically recover the SiC detectors' performance. It was also found that the annealing temperature should not exceed 300 °C, otherwise re-degradation of CCE occurs. Some hints to understand the CCE variation during annealing were found in the data of conventional electrical measurements. However, further systematic defect studies are needed for a comprehensive explanation.

References

[1] F. Nava et al., "Silicon carbide and its use as a radiation detector material," Meas. Sci. Technol., vol. 19, pp. 102001-102025 (2008).

[2] G. Verzellesi et al., "Investigation on the charge collection properties of a 4H-SiC Schottky diode detector," Nucl. Instr. Meth. A, vol. 476, pp. 717-721 (2002).
[3] S. Onoda et al., "Charge collection properties of 6H-SiC didoes by wide variety of charged particles up to several hundreds MeV," Mater. Sci. Forum, vols. 615-617, pp. 861-864 (2009).
[4] F. Nava et al., "Radiation tolerance of epitaxial silicon carbide detectors for electrons and γ-rays," Nucl. Instr. Meth. A, vol. 514, pp. 126-134 (2003).
[5] S. Onoda et al., "Decrease of charge collection due to displacement damage by gamma rays in a 6H-SiC diode," IEEE Trans. Nucl. Sci., vol. 54, pp. 1953-1960 (2007).
[6] N. Iwamoto et al., "Charge collection efficiency of 6H-SiC p^+n diodes degraded by low-energy electron irradiation," Mater. Sci. Forum, vols. 645-648, pp. 921-924 (2010).
[7] F. Moscatelli, "Silicon carbide for UV, alpha and X-ray detectors: Results and perspectives," Nucl. Instr. Meth. A, vol. 583, pp. 157-161 (2007).
[8] M. Ito et al., "Development of 4H-SiC epitaxial growth technique achieving high growth rate and large-area uniformity," Appl. Phys. Exp., vol. 1, pp. 15001-1-3 (2008).
[9] D. V. Lang et al., "Deep-level transient spectroscopy: A new method to characterize traps in semiconductors," J. Appl. Phys., vol. 45, pp. 3023-3032 (1974).
[10] C. Hemmingsson et al., "Deep level defects in electron-irradiated 4H SiC epitaxial layers," J. Appl. Phys., vol. 81, pp. 6155-6159 (1997).
[11] L. Storasta et al., "Deep levels created by low energy electron irradiation in 4H-SiC," J. Appl. Phys., vol. 96, pp. 4909-4915 (2004).
[12] S. Sasaki et al., "Major deep levels with the same microstructures observed in n-type 4H-SiC and 6H-SiC," J. Appl. Phys., vol. 109, pp. 13705-1-6 (2011).
[13] K. Danno et al., "Deep level transient spectroscopy on as-grown and electron-irradiated p-type 4H-SiC epilayers," J. Appl. Phys., vol. 101, pp. 103704-1-5 (2007).

Heavy-Ion-Induced Charge Enhancement in 4H-SiC Schottky Barrier Diodes

T. Makino[*1], M.Deki[2], N.Iwamoto[1], S. Onoda[1],N.Hoshino[3], H.Tsuchida[3],and T.Ohshima[1]
1 Japan Atomic Energy Agency (JAEA), Japan
2 The University of Tokushima, Japan
3CentralResearchInstituteof Electric Power Industry,Japan
*Email: makino.takahiro@jaea.go.jp
Keywords:Charge enhancement, Heavy-Ion, Silicon Carbide, Single Event Burnout

Abstract

Heavy ion induced anomalous charge collection was observed in 4H-SiC Schottky Barrier Diodes (SBDs). This result is a new process of Single Event Burnouts (SEBs) in the case of incident ions on SiC-SBDs. It is suggested that the range of the incident ions with respect to the thickness of the epi-layer, ion energy, and electric-field intensity of the SBD is key to understanding this observation and understanding the SEB mechanism.

1. Introduction

Silicon carbide (SiC) is regarded as a promising candidate for electronic devices requiring high radiation tolerance (rad-hard devices). Ohshima *et al*. [1] reported that SiC Metal-Oxide-Semiconductor (MOS) Field Effect Transistors (FETs) showed higher gamma-ray radiation resistance than Si MOSFETs. It was also reported that SiC Static Induction Transistors (SITs) [2] and Metal-Semiconductor FETs (MESFETs) [3]can be operated up to 10 MGy without significant degradation to their electrical characteristics. These results indicate that SiC has superior radiation tolerance from the point of view of Total Ionizing Dose effects (TIDs). For the development of rad-hard SiC devices, it is necessary to understand the response of their performance when dense charge is generated in them by an incident ion, resulting in Single Event Effects (SEEs). Permanent malfunctions are induced in power devices by SEEs, and the probability of SEEs increases with increasing electric field in the device. Since the electric field in SiC power devices must be higher than in Si power devices, it is very important to clarify SEEs in SiC devices. In a previous study on ion incidence effects, Nava *et al*. reported charge generated in SiC Schottky diodes by He ions and its response to damage creation for particle detector applications [4]. Charge generated in SiC pn diodes by heavy ions was also reported [5]. Previously, performance of the device was also affect by a high defect density. However, recently, several Schottky Barrier Diodes (SBDs) are commercially available by the improvement of crystalline quality.
For SEEs, Scheick*et al*. reported that a catastrophic failure appeared in SiC-SBDs caused by protons without any steady increase of leakage current, and a percolation theory was proposed to explain this effect [6]. The Single-Event Burnouts (SEBs) were also observed with high LET (>10 MeV•cm^2/mg) heavy ions in spite of the SiC-SBDs having no current sustaining mechanism such as in Bipolar Junction Transistors (BJTs) [7]. Kuboyama *et al*. showed that the SEB caused by anomalous charge collection by incident heavy ions with a high LET (>10 MeV•cm^2/mg) [8]. They proposed that the anomalous charge collection from SiC-SBD is caused by Trap Assisted Tunneling (TAT). At present, experimental data for understanding the exact mechanisms of SEEs in the SiC-SBDs are very scarce and SEB mechanisms of SiC-SBDs have not been fully understood.
The epitaxial layer (epi-layer) thickness of SiC-SBDs used in previous studies were thinner than the incident ion range [6, 8]. The thicker epi-layer is required for higher voltage devices. Therefore, in this study, we show the heavy ion induced charge collection from thicker epi-layer than previous studies. To reveal SEB mechanisms, we investigate the applied bias dependence of the charge collection on SiC-SBDs.

2. Experimental

The SiC-SBDs used in this study were fabricated on an n-type 4H-SiC epi-layer. The n-type epi-layer was grown on an n-type 4H-SiC substrate (Si-face, 8° off) using a Chemical Vapor Deposition (CVD) technique [9]. The thickness and doping concentration of the epi-layer are 30 μm and 2-3x10^{15} cm^{-3}, respectively. A Mo contact with a thickness of 50 nm was used as the anode of the SiC-SBD. The bonding pad on the Mo contact was made by Al (2 μm thick). The bonding pad area is 1 mm^2. Generally, the electric-field is concentrated around the edge of the bonding pad.To avoid degradation of the breakdown voltage by the electric-field concentration, commercial SiC-SBDs have a Junction Termination Extension (JTE) or a guard ring structure near the edge of the bonding pad. In this study, the SiC-SBD has a 3zone-JTE structure around the edge of the bonding pad to moderate the electric-field concentrate.

Fig. 1 shows a schematic view of the experimental setup used in this study. We measured the collected charge

induced by heavy ions in the SiC-SBD from its cathode in the same manner as Kuboyama *et al*. [8]. The SiC-SBD was mounted on a chip carrier with two strip-lines with short bonding wires from the anode to the strip-line kept under reverse bias conditions. The anode was grounded and the cathode biased from +400 V to +1000 V with 100 V to 200 V steps by a high-voltage supply via a charge-sensitive pre-amplifier. We used an ORTEC 142C for the charge-sensitive pre-amplifier. Collected charge signals from the pre-amplifier were shaped as voltage-pulses having pulse-heights proportional to the collected charges by an ORTEC 572 spectroscopic amplifier after attenuation by a 20 dB attenuator. The pulse-height distribution analyzed by PHA basically corresponds to the collected charge distribution. The absolute value of the collected charge was calibrated experimentally using ions from an accelerator incident on a Si-Solid State Detector (SSD) with the same measurement circuit used in this experiment. At the same time, the voltage-pulse waveform from the spectroscopic amplifier was stored by an oscilloscope to monitor pile-up waveforms and malfunction of the measurement circuit.

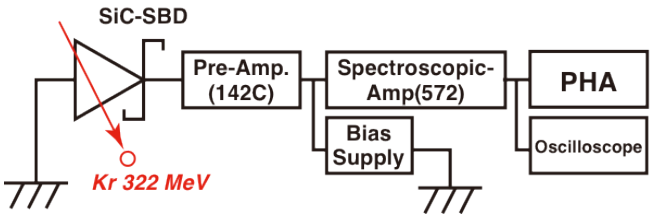

Fig. 1 The schematic view of experimental setup. The anode was grounded and the cathode biased by a high-voltage supply via a charge-sensitive pre-amplifier (ORTEC 142C). Collected charge signals from the pre-amplifier were shaped as voltage-pulses having pulse-heights proportional to collected charges by spectroscopic amplifier of an ORTEC 572. Pulse-heights were analyzed by the PHA. At the same time, voltage-pulses waveform from spectroscopic amplifier was stored by oscilloscope.

The heavy ion irradiation was performed using the AVF cyclotron at the Takasaki Ion Accelerators for Advanced Radiation Application (TIARA) in Japan Atomic Energy Agency (JAEA), Takasaki [10]. The SiC-SBDs were irradiated i4cuum chamber with a broad beam of 322 MeV Krypton (Kr) at an irradiation angle of 0 degrees. The beam flux (7 ions/device/s) was low enough to avoid pile-up of the ion induced charge collection signals.
The absolute value of the beam flux was measured using a Si-SSD with the measurement circuit used in this experiment. The projected ion range in the SiC was 26 µm evaluated by a SRIM calculation and is almost the same as the thickness of the SiC epi-layer.

3. Experimental Results

Fig. 2 shows the collected charge spectra from the SiC-SBD. The vertical axes are ion induced pulse generation cross-section. The horizontal axis shows the collected charge. Normally the collected charge spectrum might have a mono-peak similar to that found in the Si-SSD spectrum. In fact, an ion-induced mono-peak in SiC-SBD was observed in a previous study [8]. However, we observe two major peaks under bias conditions higher than 400 V as shown in Fig.2. The first peak exists at the smaller value of 6.2 pC in every bias condition. The upper limit of the first peak (6.2 pC) corresponds to the fully-stopped 300 MeV of Kr ion induced charge in 4H-SiC.
The second peak value increases with applied reverse bias up to 600 V for the SiC-SBD, and finally saturated.

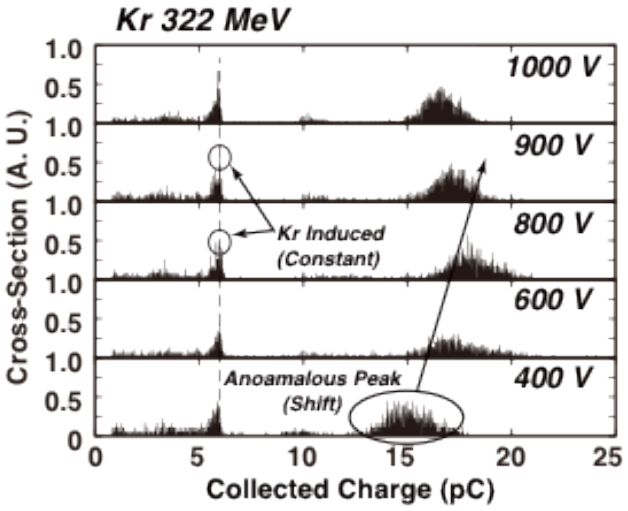

Fig. 2Collected charge spectra from the SiC-SBD.

The saturated second peak values are in the 15-18 pC range which is more than three times the charge induced by the Kr. A ratio between the total cross-section of the charge correction and ion fluence was almost one under all bias conditions. This result implies that an incident heavy ion induces a charge collection signal.

We verify that the second peak was induced by the heavy ion. Fig. 3 shows examples of charge collection pulse-waveforms shaped by the spectroscopic amplifier. A bias of 400 V was applied to the SiC-SBD during the measurement. These pulse-heights correspond to the value of collected charge from the SiC-SBD. The black line shows the highest charge collection of the 2nd peak. For comparison, charge collection pulse-waveform of the first peak is superimposed in Fig. 3 as a gray line. These waveforms show typical pulse-waveforms without a pile-up of charge collection signal from the charge amplifier. If the second peak consists of pile-up components, the black waveform had an artifact shoulder at tail. For other

waveforms, there were no artifact shoulders in this measurement. In addition, we could not find any malfunction of this measurement setup in pre- and post- energy spectrum measurements of Kr ions by using Si-SSD.

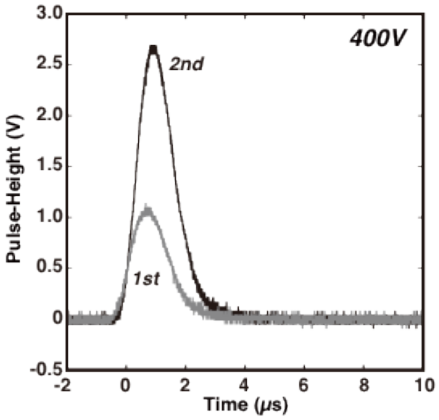

Fig. 3Charge collection pulse-waveforms shaped by the spectroscopic amplifier under the bias condition of 400 V. The black line shows the highest charge collection in the charge collection distribution under the bias condition of 400 V. Charge collection pulse-waveform of first peak in the charge collection distribution is superimposed.

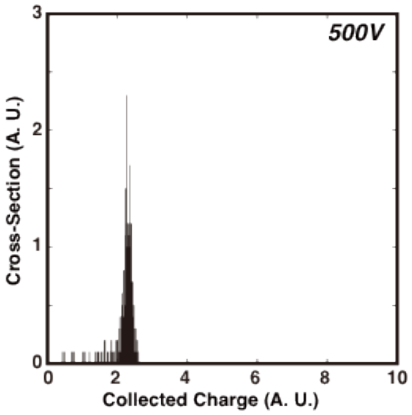

Fig. 4The collected charge spectrum from the post-irradiated the SiC-SBD induced by 5.4 MeV α particle from ^{241}Am under the bias condition of 500 V.

We measured the collected charge induced by heavy ions with lower energy. Fig. 4 shows the collected charge spectrum from the post-irradiated SBD induced by 5.4 MeV α particle from ^{241}Am under the bias condition of 500 V with the same measurement setup. The projected range of α particle in the SiC was evaluated to be 16 μm by SRIM calculation and is longer than the depletion width. There was no anomalous second peak in the α particle induced charge spectrum. We obtained typical 5.4 MeV α particle induced charge spectrum in SiC devices with low noise. This result also indicates that the measurement system works well.
From comparison between pre- and post- irradiation I-V characteristics of the SiC-SBD, we could not detect any permanent damage, i.e., a short of the Schottky contact. Therefore, we conclude that the second peaks are neither due to pile-up signals of ion induced charge collection nor steady leakage current signal. In other words, we can say that the anomalous charge collection signals were triggered by heavy ion incidence. We observed the anomalous collected charge peaks (2nd peaks) induced in SiC-SBDs by heavy ions in the case of the ion range nearly equal to epi-layer thickness.

4. Discussion

The experiment showed the anomalous charge collection peak. Moreover, the ion induced charge was enhanced in the SiC-SBD. The anomalous charge collection from SiC-SBDs was not observed in a previous reported study [8]. We can explain this discrepancy by a difference in the epi-layer thickness.
The epi-layer thickness of the SiC-SBD used in this study is 30 μm, while the epi-layer thickness of SDP06S60 is 3.7 μm. The depletion region of the SiC-SBD in this study is longer than SDP06S60. Thus the SDP06S60 could not collect the separate anomalous charge collection signal [8] even if the ion induced charge was enhanced in the epi-layer since the biased region was too short to a collect sufficient number of carrier. In other words, we could obtain the detail process of SEB by using the thick epi-layer. This result is a new process of the SEB in the case of incident ions in thick epi-layer of SiC-SBDs.
We would like to mention mechanisms of the charge enhancement in this section. In the case of Si power MOSFETs and BJTs, ion induced second peaks as an injection charge due to an activated parasitic bipolar transistor in the devices were reported [7, 11]. Constitutionally, however, parasitic bipolar effects dose not appear in SBDs.
Kuboyama *et al*. suggested that the anomalous charge collection in SiC-SBDs caused by Trap Assisted Tunneling (TAT) [8]. The TAT occurs under a high electric-field condition induced by ion incident. In addition, as shown in the previous simulation in [8], the high electric-field intensity produced by ion reached to a high enough electric-field intensity to induce impact ionization in epi-layer. These previous results suggest that the high electric-field induced by an incident ion in the SiC-SBD may be a possible reason for the charge enhancement since the higher electric-field induced the impact ionization and/or the TAT. Although future studies will have to reveal the effective mechanisms for the charge enhancement, ion induced electric-field may trigger charge enhancement and anomalous charge collection. In the case of α particles, we could not obtained

the second peak. Thus, we can conclude that key of this anomalous charge collection mechanism is related to the range of incident ions with respect to the thickness of the epi-layer, ion energy, and electric-field concentration.

5. Conclusion

We measured the bias dependence of the collected charge distribution induced by heavy ions in SiC-SBD fabricated in thick epi-layer. Anomalous collected charge peaks (2nd peaks) induced by the heavy ions were observed for the first time. The new process of the SEB was observed in the case of incident ions on thick epi-layer of SiC-SBDs. Previous results suggest that the high electric-field induced by incident ion on the SiC-SBD may be a possible reason for the charge enhancement. The higher electric-field may enhance the ion induced charge due to impact ionization and/or the TAT. Future studies will have to reveal the effective parameter for the anomalous charge collection on the SiC-SBD, since an increase of the collected charge may trigger SEB in any devices whatever the charge collection mechanism.

References

[1]T. Ohshima, H. Itoh, and M. Yoshikawa, “Effect of gamma-ray irradiation on the characteristics of 6H silicon carbide metal-oxide-semiconductor field effect transistor with hydrogen-annealed gate oxide,”*J. Appl. Phys.*, vol. 90, no. 6, pp. 3038-3041 (2001).

[2]Y. Tanaka, S. Onoda, A. Takatsuka, T. Ohshima, and T. Yatsuo, “Radiation hardness evaluation on SiC-BGSIT,” *Mater. Sci. Forum*, vol. 645-648, pp. 941-944(2010).

[3]S. Onoda, N. Iwamoto, S. Ono, S. Katakami, M. Arai, K. Kawano, and T. Ohshima, “Transient response of charge collection by single ion strike in 4H-SiC MESFETs,”*IEEE Trans. Nucl. Sci.*, vol. 56, no. 6, pp. 3218-3222 (2009).

[4]F.Nava, E. Vittone, P. Vanni, G. Verzellesi, P.G. Fuochi, C. Lanzieri, and M. Glaser, “Radiation tolerance of epitaxial silicon carbide detectors for electrons, protons, and gamma-rays,”*Nucl. Instr. and Meth. A*, 505 pp.645-655(2003).

[5]T. Ohshima, N. Iwamoto, S. Onoda, T. Kamiya, and K. Kawano, “Comparative study of transient current induced in SiC p^+n and n^+p diodes by heavy ion micro beams,”*Nucl. Instr. and Meth. B*, 267, pp. 2189-2192 (2009).

[6]L. Scheick, L. Selva, and H. Becker, “Displacement damage-induced catastrophic second breakdown in silicon carbide Schottky power diode,”*IEEE Trans. Nucl. Sci.*, vol. 51, no. 6, pp. 3193-3200 (2004).

[7]S. Kuboyama, N. Ikeda, T. Hirao, and S. Matsuda, “Improved model for single-event burnout mechanism,” *IEEE Trans. Nucl. Sci.*, vol. 51, no. 6, pp. 3336-3341 (2004).

[8]S. Kuboyama, C. Kamezawa, N. Ikeda, T. Hirao, and H. Ohyama, “Anomalous charge collection in silicon carbide Schottky Barrier Diodes and resulting permanent damage and single-event burnout,”*IEEE Trans. Nucl. Sci.*, vol. 53, no. 6, pp. 3343-3348 (2006).

[9]M. Ito, L. Storasta, and H. Tsuchida, “Development of 4H-SiC epitaxial grown technique achieving high growth rate and large-area uniformity,”*Appl. Phys.Express.*, 1, pp. 015001-1-3 (2008).

[10]Home page of JAEA Takasaki, http://www.taka.jaea.go.jp/tiara/index_e.htm

[11]S. Kuboyama, S. Matsuda, T. Kanno, and T. Ishii, “Mechanism for single-event burnout of power MOSFETs and its characterization technique,”*IEEE Trans. Nucl.Sci.*, vol.NS-39, pp. 1698-1703 (1992).

Microbeam Irradiation Effects on Transmission Diamond Detector

Wataru Kada[*1], Takahiro Satoh[1], Naoya Iwamoto[1], Shinobu Onoda[1], Veljko Grilj[2], Natko Skukan[2], Takahiro Makino[1], Masashi Koka[1], Milko Jakšić[2], Takeshi Ohshima[1], and Tomihiro Kamiya[1]
1 Japan Atomic Energy Agency (JAEA), Japan
2 Rudjer Boskovic Institute, Croatia
*Email: kada.wataru@jaea.go.jp
Keyword(s): Particle Detector, Radiation Hardness, Polarization, Microbeam, Single Ion Hit

Abstract

Response of thin film CVD diamond to the ionized particle irradiation was investigated for the utilization as a transmission detector in the end-station of the microbeam line connecting to the AVF cyclotron at JAEA/Takasaki. A spectroscopy-grade 50 μm-thick film Single Crystalline CVD diamond was characterized using Ion Beam Induced Charge (IBIC) and Transient Ion Beam Induced Current (TIBIC) systems. Significant decrease in IBIC signals was observed temporally during a microbeam irradiation period. Peak degradation was easily recovered in a short time by release of biases thus it seems to be caused by the polarization effect due to charge-capture by defects in the surface layer of diamond.

1. Introduction

Diamond is a kind of wide band-gap semiconductor as a promising candidate of radiation sensors with advantage in Signal to Noise (S/N) ratios [1,2]. The diamond detector is expected to have high charge collection efficiency, good thermal stabilities, and excellent radiation hardness [3,4]. Various researches had been already reported on the development of the radiation detectors of diamond [5, 6]. It was quite stable and several of them reached energy resolution better than 1% and transient time response of several nanoseconds.

On the other hand, focused high-energy heavy ion irradiation technique requires durable and sensitive transmission detector, at the same time, for single-ion-hits, such as 260 MeV Ne, 520 MeV Ar, or 220 MeV C from the AVF Cyclotron facility at Takasaki Advanced Radiation Research Institute (TARRI), Japan Atomic Energy Agency (JAEA) [7,8]. This is a new single-ion-hit detector for practical applications such as biological cell irradiation [9,10], fabrication of new materials enhancing polymer [11,12] or test of semiconductor devices [13,14].

Techniques of single MeV ion detection using CVD diamond film or other bulk scintillator were achieved through the measurement of secondary electrons and ion beam-induced photons [15,16]. These techniques are quite effective to detect the incident position of the ionized particle but they still have issues to be improved in their resolutions in energy and timings. Recent progresses in Chemical Vapor Deposition (CVD) process of diamond have enabled thin Single Crystal (SC) CVD diamond films with thickness under 50 μm and with quite low impurities [17]. With these progresses, a transmission high-energy particle detector made of a thin SC-CVD diamond film came to in a futuristic design of beam extraction window for the high-energy heavy ion microbeam line of AVF cyclotron at JAEA/Takasaki. The diamond is durable to mechanical stress and vibrations even in the thin film-form with thickness under 10 μm. Theoretically, thin diamond films under 10μm could still be operated as transmission radiation sensors. Great effort had been paid for the development of thin film diamond detector to use it in spectroscopic purpose [18]. However, there are still very few studies on the irradiation effects and radiation hardness on the intense ion microbeam irradiations.

In this research, transmission particle detectors using thin-film diamond were newly evaluated for the individual detection of single-hit of MeV ions. At first, this paper describes the preparation of SC-CVD diamond film detectors with thickness around 50 μm and the first trial of irradiation experiment of focused MeV ionized particles. To obtain the energy-response of the detectors, microbeam irradiation experiment was executed on Ion Beam Induced Charge (IBIC) and Transient Ion Beam Induced Current (TIBIC) systems at the heavy ion microbeam system on the tandem accelerator of JAEA [19]. It was experimentally examined the response to the MeV ions through energy spectrum and pulse signals.

2. Materials and Methods

2.1 Preparation of the diamond transmission detector

The high-purity spectroscopic-grade SC-CVD diamond films were provided and prepared as a body of transmission detector for heavy ions by Diamond detector ltd. A wafer with size of 4.6 × 4.6 mm^2 of one SC-CVD diamond film was grown in thickness of 50 μm. Metalized layers of Ti/Pt/Au were evaporated with thickness of approximately 50 nm on both side of the detector bodies of SC-CVD diamond films as an ohmic-contact electrodes. Leakage current was measured to be under 10^{-11}A at biases up to ± 70 V.

2.2 Irradiation Experiments

The SC-CVD diamond film detectors were first evaluated with alpha particles from ^{241}Am standard radiation source. One side of the detector faced to the source was connected to the Ortec 710 high voltage bias power supply and Charge Sensitive Amplifier (CSA) via SMA through, while the another side of the detector was terminated to the ground. The output of CSA was transmitted to the Ortec 572 shaping linear amplifier and Pulse Height Analyzer (PHA). Bias voltage was applied to the diamond films with maximum voltage of ±70 V.

Figure 1 shows the energy spectrum of 5.5 MeV alpha particles from ^{241}Am. The relations between the applied bias voltages and charge collection efficiency and counting-rate efficiency were also obtained with the same condition. Alpha particles were irradiated to the detector with an average density of 10 [particles/mm^2/s]. Irradiation was continuously performed for the evaluation of the durability in the energy-resolution of the detector. 2% in Full Width Half Maximum (FWHM) was sustained as the total fluence was reached to the 10^9 [ions/cm^2].

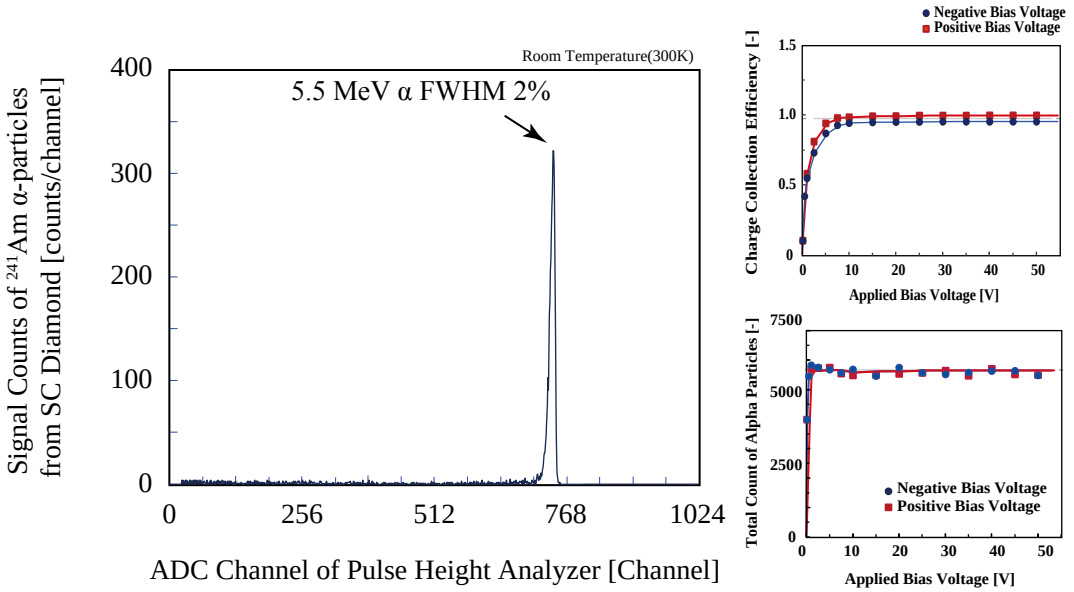

Fig. 1. (left) The energy spectrum of 5.5 MeV alpha particle obtained by the SC-CVD diamond detector. (right)The dependencies of Charge collection efficiency and counting rate efficiency to the applied bias voltages

Then the microbeam irradiation experiments were performed on the microbeam lines of single-ended and tandem accelerators at Takasaki Ion-accelerators for Advanced Radiation Application (TIARA), JAEA. Microbeam of 3 MeV H^+ and 15 MeV O^{4+} were irradiated into the SC-CVD diamond detector with beam current of approximately 100 cps by scanning microbeam probe with maximum area of 800 μm × 800 μm.

First, 3 MeV H^+ microbeam irradiation was performed to evaluate uniformity in the CCE by visualizing Ion Beam Induced Charge (IBIC) images. Same NIM electrical circuit chain for high voltage bias power supply (Ortec 710) and CSA was used for the IBIC signal process. Obtained signal was processed on the MCA system originally developed for Particle Induced X-ray Emission (PIXE) analysis [20]. Beam current was first monitored by faraday cup and count-rate was then decreased by installing the object slit to approximately 100 cps using the output signal from SC-CVD diamond detector.

Following experiment was demonstrated with heavy ion microbeam of 15 MeV O^{4+} at microbeam line of a tandem accelerator. The system equips IBIC analysis system and the Transient Ion Beam Induced Current (TIBIC) collection system [21]. Signal was processed the same NIM electrical circuit chain to obtain IBIC signal responses. Count-rate of the beam was previously controlled by pulse counting from Si Surface Barrier Diode (SBD) detector placed in front of the SC-CVD detector on a linear drive. The transient current was also monitored by a 3 GHz or 15 GHz Digital Storage Oscilloscope (DSO) Tektronix TDS694C via high voltage bias-tee. The transient current signals were stored on real-time by the NI Labview based digital signal processing system in the condition of single ion hit.

3. Results and discussion

3.1 Observation of the uniformity in CCE

Focused proton microbeam of 3 MeV was irradiated into SC-CVD diamond detector with spatial beam spot size of 1 μm with beam current of approximately 100 cps. A photograph of the detector was shown in Fig.2. 4×10^4 [particles/mm^2/s] was the typical density of the proton microbeam irradiation. Approximately 1.8% in Full

Width Half Maximum (FWHM) was obtained in the energy spectra. Several Positions (A)-(E) in the detector were irradiated by the microbeam with scanning area of 100 μm × 100 μm. IBIC images correspond to the area of (A) to (E) were also shown in the figure. Almost homogeneous distributions in charge collection were obtained in the IBIC image induced by 3 MeV proton microbeam. The CCE has decreased on the edge of the wafer in a scale of approximately 5 micrometers from the terminal of the electrode as shown in IBIC image of (D) and (E). The result suggest that this SC-CVD diamond film has uniform response to the ionized particle in its relatively-large detection plane of 4.6 mm × 4.6 mm that is well correspond to the area of beam extraction window on the AVF cyclotron.

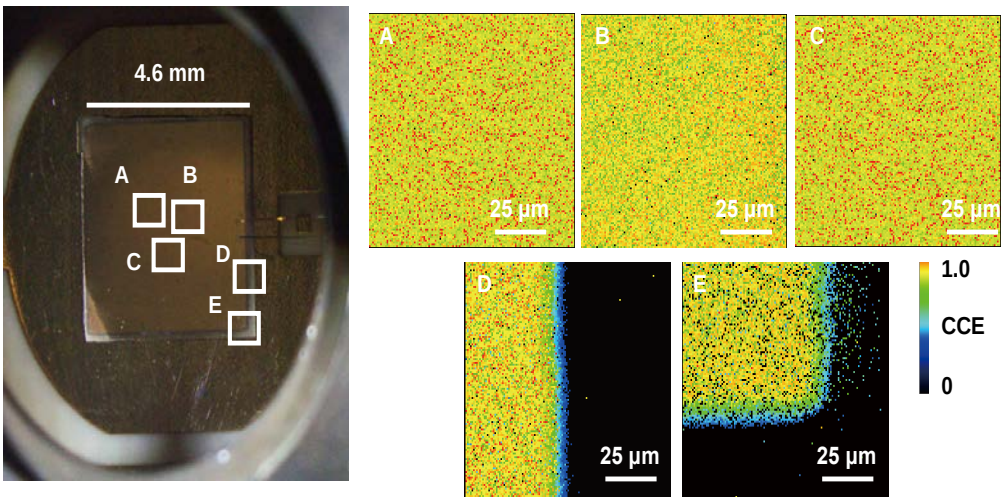

Fig. 2. (left) A photograph of the SC-CVD diamond detector and (right) IBIC images obtained by 3 MeV H+ microbeam in specific area (A) through (E) indicated in the photograph

3.2 Observation of the durability

The detector was then irradiated with 15 MeV O^{4+} microbeam. The count rate of this heavy ion microbeam was also reached to approximately 4×10^4 [particles/mm^2/s] with a scanning area of 50 × 50 μm^2 and approximately 5% in Full Width Half Maximum (FWHM) was obtained in the energy spectra. The experiment was first performed to reach the total fluence to 10^9 ions/cm^2. As shown in Fig.3, significant decrease of pulse height of IBIC signals was observed between 10^8 ions/cm^2 to 10^9 ions/cm^2, however, this peak degradation easily recovered in a short time by release of bias voltages. This temporal degradation effect was enhanced in areas damaged by previous ion irradiation. It was quite important that we did not obtained such a high temporal decrease with the microbeam of 3 MeV H^+ or higher-energy microbeam irradiation of 260 MeV Ne^{7+}. Therefore, the temporal peak degradation is expected to be caused by the polarization effect due to charge captured by defects in the near surface region of the single crystal diamond.

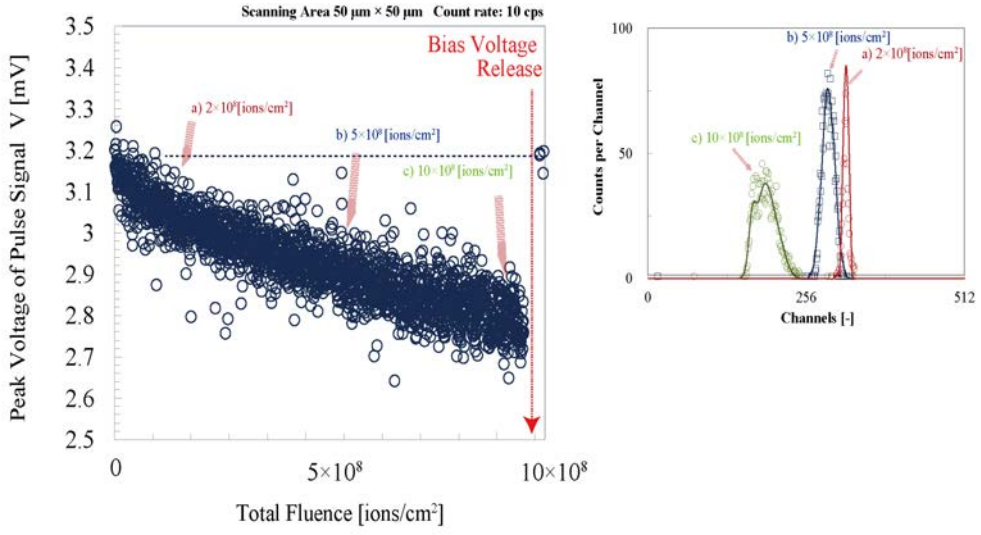

Fig. 3. (left) The decrease in pulse height spectra of IBIC signals with increase of the total fluences (right) IBIC spectra obtained at three different fluences.

4. Conclusion

The transmission particle detectors based on the CVD diamond film substrate were prepared and irradiated with microbeam for the evaluation to the futuristic usage of MeV ion microbeam irradiation. SC-CVD diamond detector with thickness of 50 μm was characterized by using the 241-Am standard alpha source and ion microbeam irradiations. Uniformity of the response of the detector was obtained by the irradiation of 3 MeV proton microbeam and IBIC analysis. Compared with the result of alpha-particles from radiation source, SC-CVD diamond showed totally different response to the irradiation with the 15 MeV O^{4+} microbeam. This temporal decrease of the CCE is quite unique phenomena of the microbeam irradiation where the intense charge generation occurs in high density. Additional experiments are being proceeded to characterize these temporal decreases by changing energy and ion species of the microbeam. It is also need to be take account the analysis and measurement of the defects distribution on the surface of the SC-CVD diamond that is expected to play a key role for the generation of temporal CCE distortion by so named polarization effect.

Acknowledgments

This work has been supported by Strategic Japanese-Croatian Cooperative Program "Development of high-energy ion microbeam technology for novel applications of diamond" on Materials Science of Japan Science and Technology Agency and the Ministry of Science, Education and Sports of the Republic of Croatia.

References

[1] E. Souw et al., “Response of CVD diamond detectors to alpha radiation,” Nucl. Instr. and Meth. A vol. 400, pp. 69–86 (1997).
[2] W. Adam et al., “The development of diamond tracking detectors for the LHC,” Nucl. Instr. and Meth. A., vol. 514, pp. 79–86(2003).
[3] D. R. Kania et al., “Diamond radiation detectors,” Diamond Relat. Mater.,vol. 2, pp. 1012–1019, 1993.
[4] J. Isberg et al., “High carrier mobility in single-crystal plasma-deposited diamond.,” Science, vol. 2977, pp. 1670–2 (2002).
[5] R.S.Sussmann, “CVD Diamond for Electronic Devices and Sensors,” John Wiley & Sons Ltd Press, 2009.
[6] C. Tuvè et al., “Single crystal diamond detectors grown by chemical vapor deposition,” Nucl. Instr. and Meth. A, vol. 570, pp. 299–302 (2007).
[7] T. Kamiya et al., “Microbeam complex at TIARA: Technologies to meet a wide range of applications,” Nucl. Instr. and Meth. B, vol. 269, pp. 2184–2188 (2011).
[8] M. Oikawa et al., “Focusing high-energy heavy ion microbeam system at the JAEA AVF cyclotron,” Nucl. Instr. and Meth. B, vol. 260, pp. 85–90 (2007).
[9] T. Funayama and N. Hamada, “Heavy-Ion Microbeams — Development and Applications in Biological Studies,” IEEE Nucl. Plasma Sci. Soc., vol. 36, pp. 1432–1440 (2008).
[10] Y. Kobayashi et al., “Irradiation of single mammalian cells with a precise number of energetic heavy ions – Applications of microbeams for studying cellular radiation response,” Nucl. Instr. and Meth. B, vol. 210, pp. 308–311 (2003).
[11] S. Tsukuda et al., “Fabrication of Nanowires Using High-Energy Ion Beams,” J. Phys. Chem. B, vol. 108, pp. 3407–3409 (2004).
[12] S. Seki et al., “Cross-linked silicon based polymer nano-wire formation by high energy charged particles,” Surf. Coat. Technol., vol. 201, pp. 8486–8489 (2007).
[13] T. Hirao et al., “Transient current mapping obtained from silicon photodiodes using focused ion microbeams with several hundreds of MeV,” Nucl. Instr. and Meth. B, vol. 267, no. 12–13, pp. 2216–2218 (2009).
[14] S. Onoda et al., “Transient currents generated by heavy ions with hundreds of MeV,” IEEE Nucl. Sci., vol. 53, pp. 3731–3737 (2006).
[15] T. Kamiya et al., “Secondary electron emission from boron-doped diamond under ion impact: Applications in single-ion detection,” Appl. Phys. Lett., vol. 71, pp. 1875 (1997).
[16] F. D. Mcdaniel et al., “Ionoluminescence decay measured with single ions,” Nucl. Instr. and Meth. B, vol. 190, pp. 1–10 (2002).
[17] S. Gkoumas et al., “Low temperature time of flight mobility measurements on synthetic single crystal diamond,” Diamond Relat. Mater., vol. 18, pp. 1338–1342 (2009).
[18] J. H. Kaneko et al., “Radiation detector made of a diamond single crystal grown by a chemical vapor deposition method,” Nucl. Instr. and Meth. A, vol. 505, pp. 187–190 (2003).
[19] T. Hirao et al., “Studies on single-event phenomena using the heavy-ion microbeam at JAERI,” Nucl. Instr. Meth. B, vol. 210, pp. 227–231 (2003).
[20] T. Sakai et al., “JAERI Takasaki in-air micro-PIXE system for various applications,” Nucl. Instr. Meth. B, vol. 190, pp. 271–275 (2002).
[21] J.S. Laird et al., “Development of a new data collection system and chamber for microbeam and laser investigations of single event phenomena,” Nucl. Instr. Meth. B, vol. 181, pp. 87–94 (2001).

3-D Simulation of Angled Strike Heavy-Ion Induced Charge Collection in SiGe HBTs

Jin-Xin Zhang *[1, 3], Hong-Xia Guo [1, 2], Lin Wen [1, 3], Qi Guo [1], Wu Lu[1], Jiang-Wei Cui [1], Xin Wang [1, 3], Wei Deng [1, 3], Qi-Wen Zhen [1, 3], Yao Xiao[2] and Xue Fan[4]
1 Xinjiang Key Laboratory of Electronic Information Materials and Devices, Xinjiang Technical Institute of Physics & Chemistry CAS, China
2 Northwest Institution of Nuclear Technology, China
3 Graduate University of Chinese Academy of Sciences, China
4 State Key Laboratory of Electronic Thin Films and Integrated Device, University of Electronic Science and Technology of China, China
*Email: zhangjinxin87@yahoo.com.cn
Keyword(s): SiGe HBT, Angled strike, SEE, Charge collection, 3-D numerical simulation

Abstract

This paper presents 3-D simulation of angled strike heavy ion induced charge collection in Silicon-Germanium Heterojunction Bipolar Transistors (SiGe HBTs). We select several different striking angles at various typical ion strike positions. The charge collection mechanism for each terminal is identified based on analysis of the device structure and simulation results. Angled strike ions induced charge collection present complex situation. With the change of striking angle, the longer the length of the ions track in sensitive volume, the more charge is collected. STI will prevent a part of diffused charge that charge collection reduces.

1. Introduction

In recent years, SiGe HBTs have become a strong contender in space applications because of outstanding low-temperature performance. For space applications, SiGe HBTs have demonstrated excellent hardness to both total ionizing dose radiation and displacement damage without radiation hardening. However, results of testing and simulations have shown that single-event effects are restrictions of space applications in SiGe HBTs [1]-[3].

Heavy ions in space strike electronic components in any possible angles. This work simulates the charge collection for angled strikes in SiGe HBTs [4]-[6]. We verify the sensitive volume of the SEE, and explore the mechanism of charge collection for angled strike through the analysis of device structure and simulation results.

2. Device structure

The SiGe HBT used for simulation is similar to the traditional NPN vertical bipolar transistor as shown in Fig.2. The difference is that the base region is constituted by gradient SiGe in SiGe HBT. Active region is formed using shallow trench isolation (STI) in the base around. This SiGe HBT has a heavily doped extrinsic base to decrease base resistance and collector-base capacitance [7]-[9]. Other structures include a lightly doped p-type substrate and a polysilicon emitter. An n^+ buried layer is provided for the lead-out collector contact, and the outermost ring as heavy boron-doped substrate contact.

3. single-event effects device 3D simulation

3.1 structure simulation

The structure model of 3-D SiGe HBT is structured based on device formation and process information. For accurate SEE simulation, it is important to built appropriate grid for device structure. In this work, the more mesh in the base and near the ion tracks, and less mesh in other regions. Fig. 2 shows the 3-D view of device and mesh. Fig. 3 shows the 2-D cross section which cut the simulated 3-D structure in central of z coordinate axis.

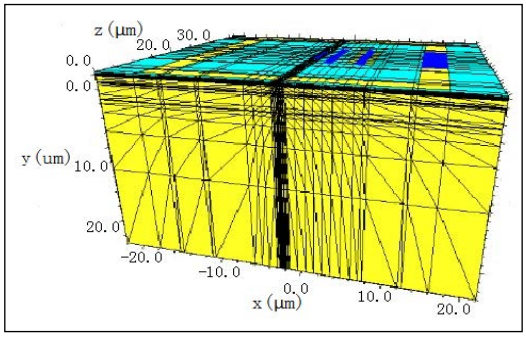

Fig. 1, 3-D view of device

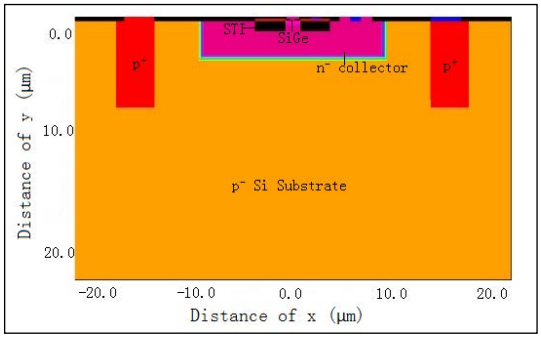

Fig. 2, 2-D view of the intrinsic portion of the device

3.2 Single-event effects simulation

The physical models for simulation include Phillips unified mobility, SRH recombination, Auger recombination, velocity saturation, and band gap narrowing (BGN). In the simulation, the substrate is biased at -5V, and all other terminals are biased at 0V. This is the worst bias situation in SiGe HBTs that would form a reverse biased pn junction in collector/substrate(C/S) junction. In order to investigate the worst case that ions traverse the entire device, we simulate charge deposition throughout the entire simulated structure. Thus, we chose a 0.2 $pC/\mu m$ charge deposition, which is equivalent to an LET=20$MeV/cm^2/mg$.

4. Result and Discussion

4.1 Charge Collection Mechanism and Sensitive Volume

Strike ions induce a large number of electron-hole pairs along the ion track so that potential equipotential lines along the ion track distort to the substrate to form a funnel potential. A part of charge is collected by drift in the funnel field. Subsequently, collector and substrate collect a part of charge because of diffusion effect. Holes are collected through substrate and base. Electrons are collected through collector and emitter. Fig. 4(a)-(c) show the charge collection by base, collector and substrate as a function of the x-coordinate of striking location. The z-coordinate is fixed at the centre of device. The area within the shallow trench isolation is affirmed the sensitive volume for base. Collector and substrate charge collection are sensitive in and nearby the C/S junction. Charge collection of emitter is negligible.

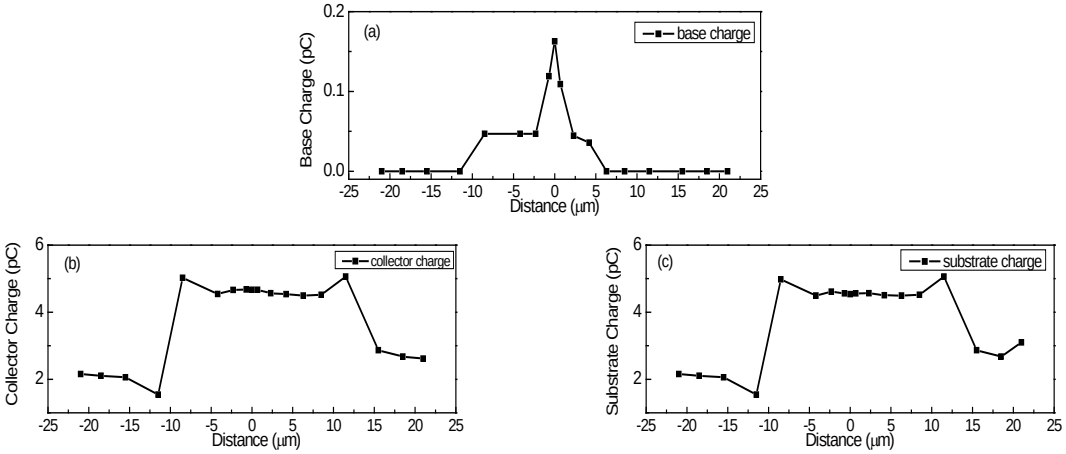

Fig. 4, Charge collected by base (a), collector (b) and substrate(c) as a function of the x-coordinate of strike location

4.2 Angled Strike Track Selection

In ground modeling experiment, angled strike is usually more complicated to achieve. However, it is relatively simple that computer simulate angle strike. Hence the computer simulation is an effective method to research angle strike. According to the different areas, different materials, different junction, as well as different length in specific structure of ions track, we chose eight kinds strike paths, as shown in Fig. 5.

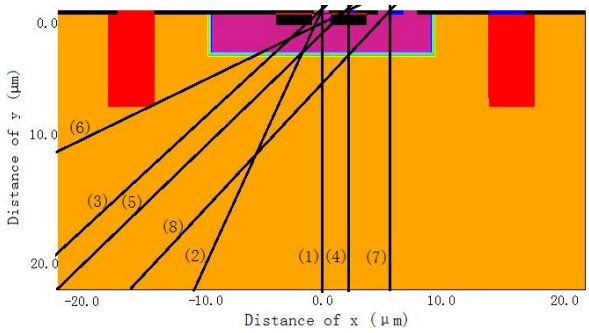

Fig. 5, Angled strike paths in simulation

4.3 Ion Angled Strike Dependence

Each terminal of the charge collection is closely related to the position and angle of strike ions. Angle dependency of charge collection can be obtained through the analysis of transient current, charge collection and device structure. Table I shows the charge collection of angled strike. Fig.6-Fig. 9 show transient terminal current as function of time of several typical position and angle.

Table I, The simulated charge collection of angled strike

Charge collection (C) / Position and angle	Base	Collector	Emitter	Substrate
(1) x=0μm-0°	-1.62851E-13	4.66546E-12	3.45768E-14	-4.53719E-12
(2) x=0μm-30°	-1.78975E-13	5.12988E-12	3.32266E-14	-4.98413E-12
(3) x=0μm-45°	-1.74344E-13	5.69374E-12	2.73509E-14	-5.54675E-12
(4) x=1.2μm-0°	-1.72978E-14	4.59674E-12	1.11523E-17	-4.57945E-12
(5) x=1.2μm-45°	-1.67557E-13	6.05033E-12	7.57121E-16	-5.88354E-12
(6) x=1.2μm-60°	-2.65368E-13	4.81177E-12	6.33744E-15	-4.55274E-12
(7) x=7μm-0°	1.65496E-17	4.47693E-12	3.39524E-19	-4.47695E-12
(8) x=7μm-45°	-2.1268E-16	6.12464E-12	-3.58287E-18	-6.12442E-12

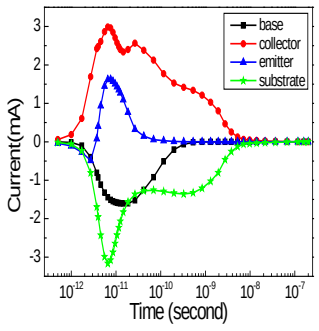

Fig.6, Transient terminal current for ions strike from x=0μm at 30°

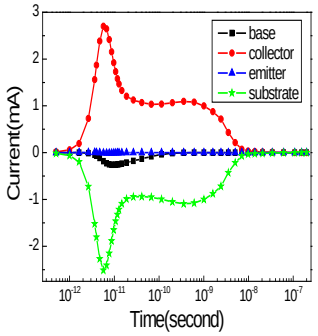

Fig.7, Transient terminal current for ions strike from x=1.2μm at 0°

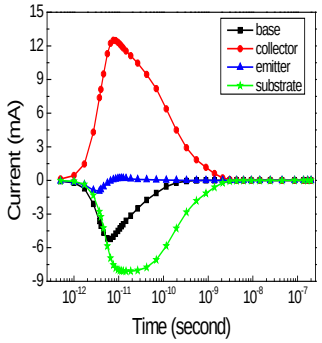

Fig.8, Transient terminal current for ions strike from x=1.2μm at 45°

The transient current of striking ions from x=0μm at 0° and 45° are very similar to the incidence at x=30° as shown in Fig. 6. Ions pass through the active region of the device, each transient terminal current generates a pulse crest because of drift effect. Then, collector and substrate current slowly change to 0 due to diffusion. Compared the first three rows of data in table I found that base charge collection for 0° is least. Ions track length of angled strike is longer than the length of normal strike in base. Thus, angled strike collects more charge. Base charge collection for 45° is less than 30° because STI prevent a part of collected charge by diffusion. This further verified that the region of STI surrounding is the sensitive volume for base charge collection. The ions track length become longer in collector and substrate due to increase of strike angle, so collector and substrate collect more charge, as shown in table 1.

Fig. 7-Fig.8 compare the transient current when ions strike device at x=1.2μm for 0°, and 45°. The graph of 60° is similar to the graph of 45°. For 45° and 60°, base current has a pulse, while it has not for 0°. In addition, the data of x=1.2μm in the table 1 shows that the base charge collection

for 60° is more than 45° than 0°. The reason is that ions pass through the inside of STI where sensitive area of base at 45° and 60°, and the ions track length is longer for 60° than 45° in base. Collector and substrate charge collection for 45° than 60° than 0°. The ions track of 45° is located in STI so that a part of charge cannot diffuse to the collector and substrate contact.

Transient current of strike ions from x=7μm at 0° and 45° is similar to the Fig.7. Base current is almost zero because ions do not pass through the base region. The collector and substrate charge collection for 45° is greatly more than 0°. As previously mentioned, the ions track length through device is greatly longer for 45° than 0°.

5. Conclusion

We have presented a simulation of angled strike ions induced charge collection in SiGe HBTs, and get the conclusions as follow. Whether the location of ions enter device, as long as ions track pass through the sensitive volume, it will cause vast charge collection. With the change of striking angle, the longer the length of the ions track in sensitive volume, the more charge is collected. STI prevents a part of diffused charge.

Acknowledgments

Thanks for the Institute of Microelectronics, Tsinghua University.

References

[1] John D.Cressler, SiGe HBT Technology: A New Contender for Si-Based RF and Microwave Circuit Applications, IEEE Transactions on Microwave Theory and Techniques, vol.46, pp. 572-589 (1998).
[2] John D.Cressler et al., On the potential of SiGe HBTs for extreme environment electronics, Proceedings of the IEEE, vol.93, pp. 1559-1582 (2005)
[4] Tianbing Chen et al., Proton Radiation Effects in Vertical SiGe HBTs Fabricated on CMOS-Compatible SOI, IEEE Trans. Nucl. Sci., vol.52, pp. 2353-2357(2005).
[5] Hua Yang. 3D Device Simulation of SEU-induced Charge Collection in 200GHz SiGe HBTs, Alabama: Auburn University, (2005).
[6] Muthubalan Varadharajaperumal. 3D Simulation of SEU in SiGe HBTS and Radiation Hardening by Design, Alabama: Auburn University, (2010).
[7] Guofu Niu et al., Simulation of a New Back Junction Approach for Reducing Charge Collection in 200 GHz SiGe HBTs, IEEE Trans. Nucl. Sci., vol. 52, pp.2153-2167 (2005).
[8] Muthubalan Varadharajaperumal et al., 3-D Simulation of Heavy-Ion Induced Charge Collection in SiGe HBTs, IEEE Trans. Nucl. Sci., vol. 5, 2191-2198 (2003).
[9] Muthubalan Varadharajaperumal et al., 3-D Simulation of SEU Hardening of SiGe HBTs Using Shared Dummy Collector, IEEE Trans. Nucl. Sci., vol. 54, 2330-2337 (2007).

LET Dependence of Gate Oxide Breakdown of SiC-MOS Capacitors due to Single Heavy Ion Irradiation

Manato Deki[*1,2], Takahiro Makino[2], Takuro Tomita[1], Shuichi Hashimoto[1],
Kazutoshi Kojima[3], and Takeshi Ohshima[2]
1 The University of Tokushima, Japan
2 Japan Atomic Energy Agency (JAEA), Japan
3 National Institute of Advanced Industrial Science and Technology (AIST), Japan
*Email: deki.manato@jaea.go.jp
Keyword(s): Metal-oxide-semiconductor capacitor, Single event gate rupture

Abstract

The currents through the gate oxide of the 4H-Silicon Carbide (SiC) Metal Oxide Semiconductor (MOS) capacitors at the accumulate condition were measured during heavy ion irradiation. Linear Energy Transfer (LET) dependence of the critical electric field (E_{cr}) at which the dielectric breakdown occurs in 4H-SiC MOS capacitors was studied. It was revealed that E_{cr} decreases with increasing LET. E_{cr} for SiC became higher than that for Si. This suggests that SiC MOS devices are promising candidates for high SEGR resistant devices.

1. Introduction

Galactic cosmic rays such as high energy heavy ions incidence in Metal Insulator Semiconductor (MIS) devices cause the catastrophic failure in the gate dielectric by amount of induced carrier. This phenomenon is well known as Single Event Gate Rupture (SEGR). In previous studies of SEGR in Silicon (Si) Metal Oxide Semiconductor (MOS) devices [1-7], it was reported that the probability of SEGR increased with increasing the electric field applied to devices. In addition, even on the ground, the issue of SEGR due to neutrons created by cosmic rays arises in Si MOS power devices operated under very high electric field.

Silicon Carbide (SiC) is applicable to the high power devices with high radiation hardness. Ohshima et al. [8] clarified the Total Ionizing Dose (TID) effect of SiC MOS Field Effect Transistors (FETs), and they showed SiC MOSFETs have higher radiation resistance than Si MOSFETs. However, SEGR in SiC MOS devices has not yet been understood. Since SiC power devices are expected to be operated under higher electric field than Si power devices, it is very important to study about SEGR in SiC devices.

In this study, by measuring the leakage current through the gate oxide of 4H-SiC MOS capacitors during heavy ion irradiation, we investigate the Linear Energy Transfer (LET) dependence of the critical electric field (E_{cr}) at which SEGR occurs in SiC MOS capacitors.

2. Experimental

The MOS capacitors samples (gate electrode either 180 or 280 μm in diameter) used in this study were fabricated on n-type epitaxial layer (4.9 μm thick). Epitaxial layer was grown on an n-type 4H-SiC substrate (8° off, Si-face). The donor concentration of the epitaxial layer was 3.7×10^{15} cm^{-3}. The MOS capacitors were fabricated by the following processes. Firstly, the field oxide at a thickness of 180 nm was formed on the sample surface by a pyrogenic oxidation process (H_2:O_2 = 1:1) at 1100 °C for 180 minutes. Next, the field oxide with a diameter of either 180 or 280 μm was removed by a conventional photolithography technique and a wet etching technique using buffered hydrofluoric acid (HF:NH_4F = 1:5). Next, the gate oxide was grown on the sample by pyrogenic oxidation at 1100 °C for 60 minutes. After the oxidation, the samples were cooled from 1100 to 900 °C for 1 hour under an argon (Ar) atmosphere. Then, re-oxidation under the pyrogenic condition was carried out at 900 °C for 15 minutes. The thickness of the gate oxide was estimated to be from 65 to 80 nm from Capacitance - Voltage (C-V) measurements. Aluminum (Al) electrodes with a thickness of 200 nm were formed on the gate oxide using Al evaporation followed by a conventional lift-off technique. Finally, Al bonding pads and interconnections (between the bonding pad and the gate electrode) were formed using Al evaporation followed by a conventional lift-off technique [9]. The leakage currents through the gate oxide of the samples were below 1.0 pA at an accumulate condition of 3 MV/cm. The flat band voltage shifts (ΔV_{FB}) of samples were estimated to be from 2.86 to 5.17 V from C-V characteristics.

The samples were irradiated with Nickel (Ni) at 9 and 18 MeV, Krypton (Kr) at 322 MeV, and Xenon (Xe) at 454 MeV. The LETs, ion species, energies, range in SiC and flux used in this study are described in Table 1. We used a 3MV tandem accelerator for Ni ion irradiation and an AVF cyclotron accelerator for Kr and Xe ion irradiation. Fluxes of ions were controlled to be low enough to avoid degradation of device characteristics due to the TID effect.

The leakage current of sample irradiated with ion at low electric field (E < 2MV/cm) did not change compared with pre-irradiation. This suggests that the TID effect did not affect to measurement. The leakage current through the gate oxide of the MOS capacitors was monitored under direct current (DC) biases. The gate oxide was applied DC biases from 20 to 100 V toward the accumulation condition. DC bias step rate was 0.2 V per 6 seconds. The compliance current set as 1 mA which the destruction of gate oxide occurs.

Table 1. List of ions and their characteristics.

LET [MeV • cm^2/mg]	Ion species	Energy [MeV]	Range [μm]	Flux [/cm^2 • sec]
0	No Ion	--	--	--
14.6	Ni	9	3.63	3.46×10^4
23.8	Ni	18	5.04	3.87×10^4
42.2	Kr	322	27.2	4.43×10^3
73.2	Xe	454	35.7	2.98×10^3

3. Results and Discussion

Figure 1 shows the leakage currents through the gate oxide of the 4H-SiC MOS capacitors as a function of the electric field applied to the gate oxides with and without ion irradiation. The effect of ΔV_{FB}, which was evaluated from C-V measurements, was considered in the estimation of the electric field shown in Fig. 1. The leakage currents for all samples sharply increase to compliance current (1 mA) after gradually increase of leakage current. In this study, the value of the electric field at leakage current of 1 mA is defined as E_{cr}. The E_{cr} of samples irradiated with ions are smaller than that of non-irradiated one (E_{cr0}), and decrease with increasing LETs.

Figures 2 (a) and (b) show optical microscope images of the gate electrodes of SiC MOS capacitors irradiated with Ni ions at 18 MeV and Xe ions at 454 MeV, respectively. As shown in Figs. 2 (a) and (b), the partial destruction of the Al electrodes are observed. Since the sharp increase in the leakage current through the gate oxide was observed (as shown in Fig. 1), the partial broken of the Al electrodes of SiC MOS capacitors is thought to be created by following steps. When an n-type MOS capacitor is irradiated with high LET heavy ions, the large amounts of electron-hole pairs are generated in SiC. Since the n-type SiC MOS capacitor is biased toward the accumulate condition, electrons generated near the interface between gate oxide and SiC drift to the interface. On the other hand, holes generated near the interface move away from the interface due to drift. Then the electric field applied to gate oxide increases by electrons collected at the interface. If the electric field in gate oxide exceeds the critical electric field, the breakdown of gate oxide occurs. As a result, a large current flow at the breakdown point(s), and the Al electrode is broken due to a large current. Thus, the spots observed in Figs. 2 (a) and (b) mean the generation points of SEGR. It is also mentioned that when the partial broken of the Al electrode occurred at the edge of the electrode connected to a bonding pad, a sudden drop in the leakage current was observed (not shown here). In such a case, although the sharp increase in the leakage current is not observed, we also defined the electric field at the sudden drop in the leakage current as E_{cr}.

Figure 3 shows the LET dependence of E_{cr} irradiated with ions. The values of E_{cr} reported for Si MOS capacitors are also plotted in the figure for comparison [2, 3]. The E_{cr0} for SiC was lower than that of Si reported by Sexton *et al.* However, as shown in Fig. 3, they also reported that the value of E_{cr0} depended on the thickness of SiO_2 and the thinner oxide showed the higher E_{cr0} [2]. Pre-irradiation breakdown in the gate oxide depends on the quality of the oxide, and the oxide thickness is fundamentally a function of the quality of the gate oxide. As mentioned above, the thickness of the gate oxide in this study ranged from 65 to 80 nm. Therefore, the smaller value of E_{cr0} for SiC is due to thicker oxide. As shown in Fig. 3, the values of E_{cr} for both SiC and Si decrease with increasing LET. Since ions with higher LET can generate larger amounts of electron-hole pairs in a sample, larger increase of the potential applied to the gate oxide can be induced by the incidence of ions with higher LET. This fact suggests that SEGR easily occurs at lower electric field by ions with higher LET. It is found that the gradient of the E_{cr} – LET curve for SiC is smaller than those for Si. This result can be explained in terms that electron – hole pair creation energy ($E_{e\text{-}h}$) is different between SiC and Si. The value of $E_{e\text{-}h}$ for SiC (7.8 eV) is larger than that for Si (3.6 eV). The result obtained in this study might relate to the difference of E_{cr}. In other words, the number of electron-hole pair generated in SiC is smaller than that in Si when the same ion (the same LET) penetrates. As shown in Fig.3, our study was also compared with Si vertical power MOSFETs (at the drain source voltage is zero) which were reported by Wheatley *et al.* [3]. Wheatley's E_{cr} was consistently lower than our results. This results suggested that the MOSFETs were needed several post-gate process for device fabrication which may give more defects in the gate oxide. Thus, this comparison is not necessarily justified. These results suggest that SiC MOS devices have a potential as the application for SEGR resistant devices.

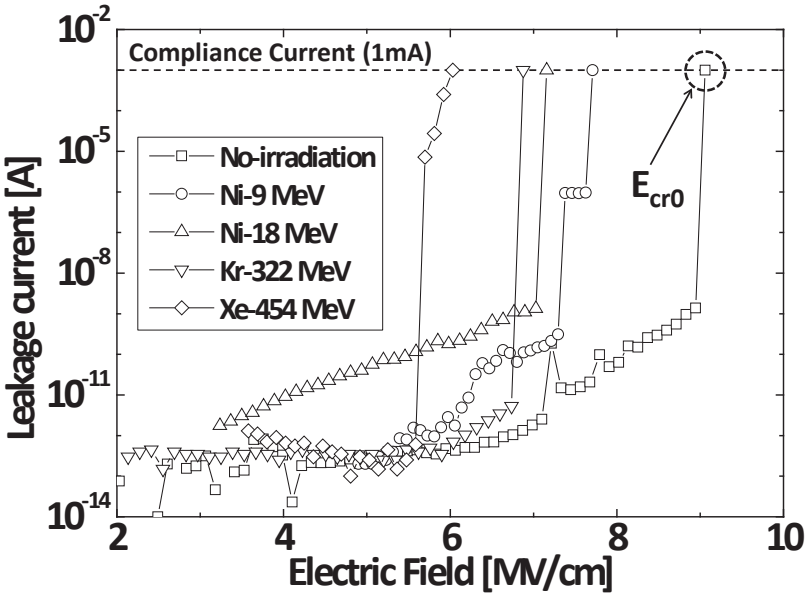

Fig. 1: Leakage currents of SiC MOS capacitors with and without heavy ion irradiation.

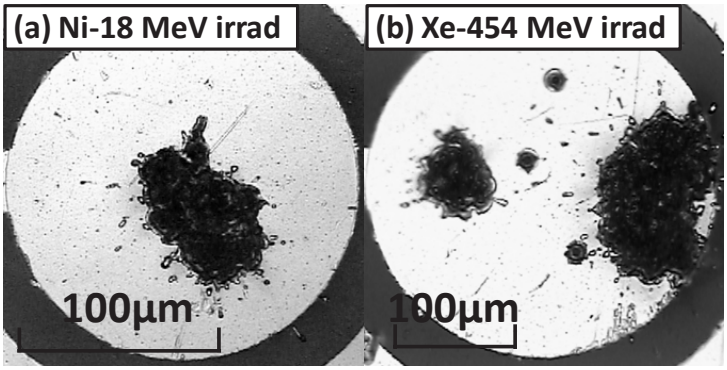

Fig. 2: Optical microscope images of electrode in MOS capacitor irradiated with Ni-18 MeV and Xe-454 MeV.

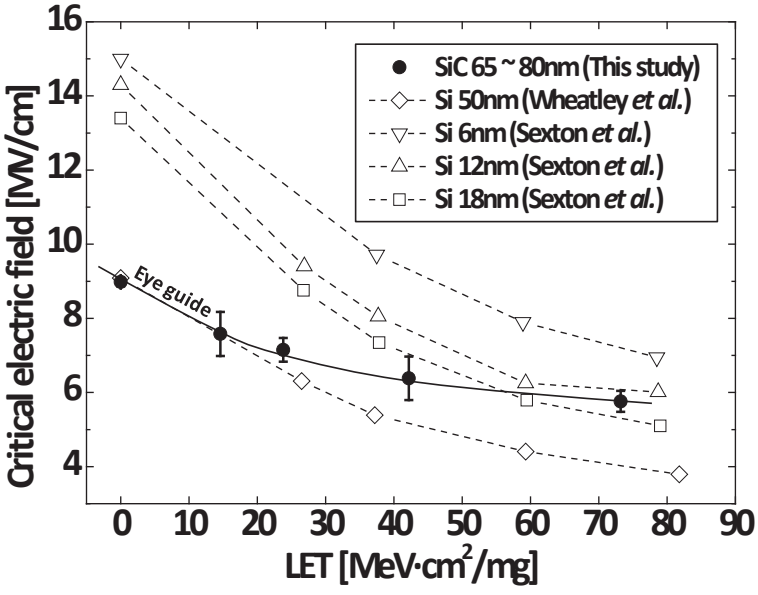

Fig. 3: LET dependence of SEGR electric field in SiC and Si MOS capacitors.

Summary

MOS capacitors were fabricated on an n-type epitaxial layer grown on an n-type 4H-SiC substrate. The currents observed through the gate oxide of the MOS capacitors biased toward the accumulate condition were measured during heavy ion irradiation. LET dependence of E_{cr} in 4H-SiC MOS capacitors under ion irradiation was studied. The E_{cr} for SiC MOS capacitors decreases with increasing LET. The gradient of the E_{cr} – LET curve for SiC is smaller than those for Si. This suggests that SiC MOS devices have a potential as the application for SEGR resistant devices.

References

[1] T. F. Wrobel, “On Heavy Ion Induced Hard-Errors in Dielectric Structures,” IEEE Trans. Nucl. Sci. NS-34, pp. 1262-1268 (1987).

[2] F. W. Sexton et al., “Single Event Gate Rupture in Thin Gate Oxides,” IEEE Trans. Nucl. Sci. 44, pp. 2345-2352 (1997).

[3] C. F. Wheatley et al., “Single-Even Gate Rupture in Vertical Power MOSFETs; An Original Experimental Expression,” IEEE Trans. Nucl. Sci. 41, pp. 2152-2159 (1994).

[4] G. K. Lum et al., “New Experimental Findings for Single-Event Gate Rupture in MOS Capacitors and Linear Devices,” IEEE Trans. Nucl. Sci. 51, pp. 3263-3269 (2004).

[5] N. Boruta et al., “A New Physics-Based Model for Understanding Single-Event Gate Rupture in Linear Devices,” IEEE Trans. Nucl. Sci. 48, pp. 1917-1924 (2001).

[6] M. J. Beck et al., “Atomic Displacement Effects in Single-Event Gate Rupture,” IEEE Trans.Nucl. Sci. 55, pp. 3025-3031 (2008).

[7] J. L. Titus et al., “Impact of Oxide Thickness on SEGR Failure in Vertical Power MOSFETs; Development of a Semi-Emprical Expression,” IEEE Trans.Nucl. Sci. 42, pp. 1928-1934 (1995).

[8] T. Ohshima et al., “Effect of gamma-ray irradiation on the characteristics of 6H silicon carbide metal-oxide-semiconductor field effect transistor with hydrogen-annealed gate oxide,” J. Appl. Phys. 90, p.3038 (2001).

[9] C. Carpenter et al., “Gate Electrode Formation Process Optimization in a GaAs FET Device,” 2004 CS Mantech Technical Digest, pp. 155-158 (2004)

Radiation damage of $Si_{1-y}C_y$ Source/Drain n-MOSFETs with different carbon concentrations

T. Nakashima[*1, 2], Y. Asai[3], M. Hori[3], M. Yoneoka[3], I. Tsunoda[3], T. Takakura[3], M.B. Gonzalez[4], E. Simoen[5],C. Claeys[5, 6],and K. Yoshino[1]
1 University of Miyazaki, 1-1, GakuenKibanadai-nishi, Miyazaki, Japan
2 Chuo Denshi Kogyo Co. Ltd., 3400 Kohoyama, Matsubase, Uki, Kumamoto, Japan
3 Kumamoto National College of Technology, 2659-2 Suya, Koshi, Kumamoto, Japan
4 Institut de Microelectronica de Barcelona (CNM -CSIC) Campus UAB, 08193 Bellaterra, Spain
5imec, Kapeldreef 75, B-3001 Leuven, Belgium
6E.E. Dept., KU Leuven, KasteelparkArenberg 10, B-3001 Leuven, Belgium
*Email: nakashima_t@cdk.co.jp
Keyword(s):strained device, electron radiation damage, degradation, electrical parameter

Abstract

The 2-MeV electron radiation damage of $Si_{1-y}C_y$ S/D n-type MOSFETs with different C concentrations is studied. Before irradiation, an enhancement of the electron mobility with C concentration of the S/D stressors is clearly observed. On the other hand, both the threshold voltage shift and the maximum electron mobility degradation are independent on the C concentration for all electron fluences. These results indicate that the strain induced electron mobility enhancement due to C concentration is retained after irradiation in the studied devices.

1. Introduction

The scaling of CMOS technologies leads to an intrinsic hardening against certain radiation effects, so that the development of ULSI components and circuits for harsh environments is becoming more popular [1].This has been driven by multiple factors, including the implementation of microelectronics components and circuits in nuclear plants, high-energy particle accelerators and artificial satellites. On the other hand, in the frame of high mobility substrates, new channel materials and promising methods to create strained channels are being explored [2-4].The potential of local compressive strain, based on the embedded or recessed silicon–germanium (SiGe) source/drain (S/D) method in p-type metal oxide semiconductor field effect transistors (p-MOSFETs) has been demonstrated at the 22 nm node and beyond [5]. For n-type MOSFET (n-MOSFETs), tensile strain is required for electron mobility and drive current enhancement. The embedded SiC S/D regions can be formed by using epitaxial silicon–carbon(SiC) $Si_{1-y}C_y$($0.01 \leqq y \leqq 0.02$) stressors [6, 7].However, it is not clear whether the strain will be maintained in a radiation-harsh environment due, for example, to a possible is placement damage in the stressors. In the present paper, we have investigated the degradation of the device performance of $Si_{1-y}C_y$ S/D n-MOSFETs irradiated by 2-MeV electrons. This leads to a better understanding of the reliability of $Si_{1-y}C_y$ S/D n-MOSFETs in a radiation harsh environment.

2. Experimental details

2.1 Sample preparation

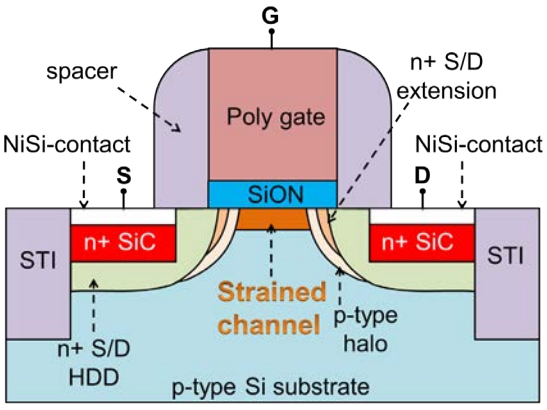

Fig. 1. Schematic cross-sectional view of the $Si_{1-y}C_y$ S/D n-MOSFETs

Figure 1 shows a schematic cross-sectional view of the $Si_{1-y}C_y$ (y = 0, 0.01, 0.015) S/D n-MOSFETs

fabricated on 200 mm p-type silicon wafers at imec. Active diode regions are defined by shallow trench isolation (STI), followed by boron (B) p-well implantations. Extension and halo implantations were also performed. Subsequently, a highly-doped drain (HDD) implantation of 4keV phosphorus (P) ions at a dose of 5 x 10^{15} cm^{-2} was carried out. The trenches of the S/D regions were dry-etched to a depth of 90 nm and were refilled by *in-situ* highly P doped SiC epitaxial layers with C concentrations y = 0.01and 0.015, using an Epsilon®chemical vapor deposition (CVD) tool manufactured by ASM. Unstressed reference Si transistors were also processed in order to allow comparison. Dopant activation was achieved by a 950°C spike anneal. The studied transistors were fabricated with a 1.5 nm SiON/poly-Si gate stack, 10µm gate width and 0.25µmgate length.

2.2 Experimental conditions

These devices were irradiated by 2-MeV electrons for a fluence of 1 x 10^{16}and1 x 10^{17} e/cm^2 at room temperature without applied bias. The electrons were irradiated using the electron accelerator at Takasaki Japan Atomic Energy Agency (JAEA). The fluence rate was fixed at 4.68 x 10^{13} $e/cm^2 \cdot s$. The degradation of the device performance of $Si_{1-y}C_y$ S/D n-MOSFETs has been evaluated by the input (I_{DS}-V_{GS}) characteristic with a drain voltage (V_{DS}) at 0.5V and gate voltages (V_{GS}) ranging from -0.5 to 1.2 V. The threshold voltage (V_{TH}) was extracted from linear extrapolation of the input characteristics. In addition, the electron mobility (μ_n) was calculated according to equation (1), where L, W and C_{OX} represent the gate length, the gate width, and the capacitance of the gate oxide, respectively.

$$\mu_n = \frac{\partial I_{DS}}{\partial V_{GS}} \cdot \frac{L}{W \cdot C_{OX}} \cdot \frac{1}{V_{DS}} \qquad \text{(Eq. 1)}$$

3. Results and discussion

3.1Carbondoping effect

First, the effect of the tensile strain in the Si-channel of $Si_{1-y}C_y$ S/D n-MOSFETs induced by different C concentrations was evaluated. Figure 2 (a) and (b) show the input characteristics, the maximum electron mobility and the threshold voltage of $Si_{1-y}C_y$ S/D n-MOSFET, as a function of C concentration (y = 0, 0.01 and 0.015), respectively. Before irradiation, the drain current and the maximum electron mobility increase with increasing the C concentration. In addition, the threshold voltages exhibit a limited tensile strain induced V_{TH} change with C concentration in line with literature observations [8]. These results suggest that the change of the drain current with C concentration can be mainly attributed to the increase of electron mobility due to the tensile strain in the Si-channel.

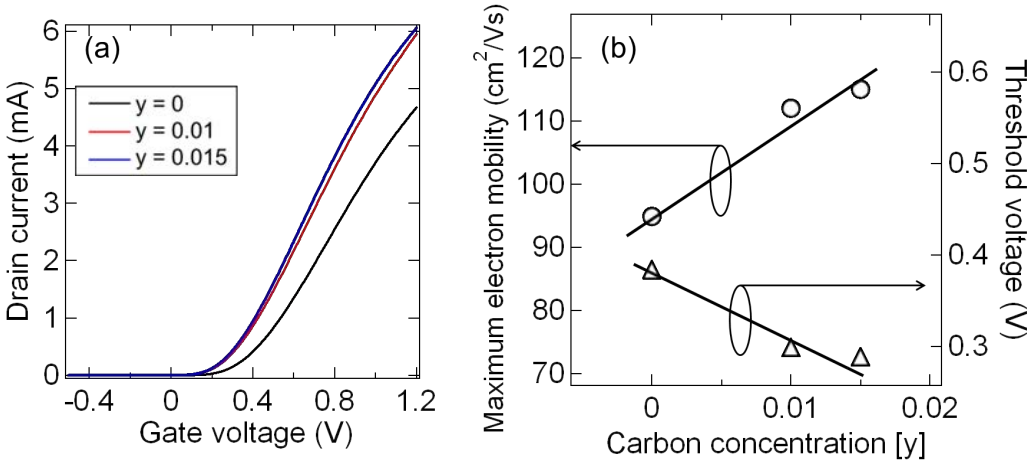

Fig. 2. Input characteristics (a), maximum electron mobility and threshold voltage (b) of $Si_{1-y}C_y$ S/D n-MOSFETs before electron irradiation.

3.2Electron irradiation effect

Next, the effect of electron irradiation on the electrical performance of $Si_{1-y}C_y$ S/D n-MOSFETs was evaluated. Figure 3 shows the input characteristics of 2-MeV electron irradiated $Si_{1-y}C_y$ S/D n-MOSFETs corresponding to different C concentrations. After 2-MeV electron irradiation, the gradient of the drain current significantly decreases with increasing electron fluence for all the C concentrations. The decrease of the drain current due to electron irradiation has two important causes. In the following, we will discuss separately the two causes.

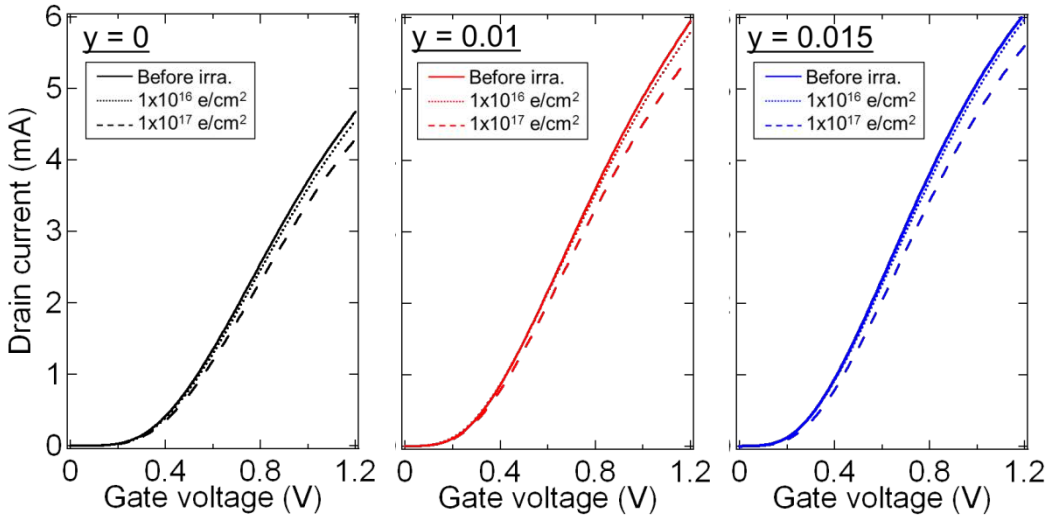

Fig. 3. Input characteristics of 2-MeV electron irradiated $Si_{1-y}C_y$ S/D n-MOSFETs.

One cause is a negative shift of the threshold voltage due to the generation of positive charge trapping in the gate dielectrics by electron irradiation. The threshold voltage corresponding with different electron fluences is summarized in Fig. 4 as a function of the C concentration. It is shown that the threshold voltage variations with electron fluence did not change markedly between the studied C concentrations. This result indicates that the generation of positive charge trapping in the gate dielectrics due to electron irradiation does not depend on the C concentration in the case of the studied electron fluence range.

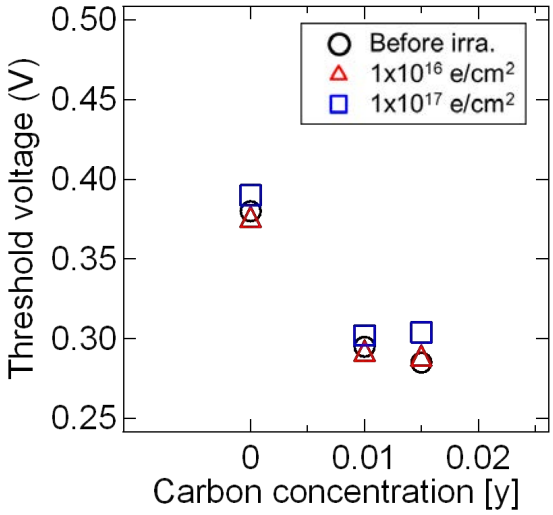

Fig. 4. Threshold voltage of 2-MeV electron irradiated $Si_{1-y}C_y$ S/D n-MOSFETs.

The second cause is electron irradiation induced displacement damage in the Si channel and at the interface between the SiON and the Si channel [9].Figure 5 shows the maximum electron mobility of 2-MeV electron irradiated$Si_{1-y}C_y$ S/D n-MOSFETs as a function of C concentration. It is observed that the maximum electron mobility decreases with increasing electron fluence. This result suggests that the series resistance in the Si channel region increased due to lattice defects created by 2-MeV electron irradiation. On the other hand, no clear relationship between the reduction of the maximum electron mobility and the C concentration can be noted in Fig. 5. This result indicates that the strain induced electron mobility enhancement due to the C concentration has been retained after electron irradiation in the studied C concentration and electron fluence range.

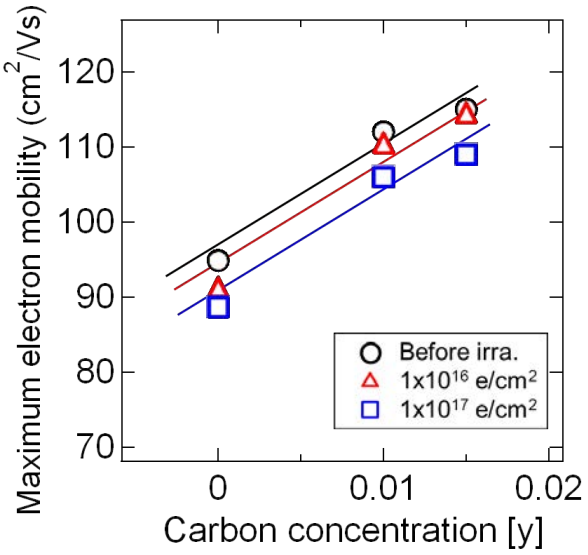

Fig. 5. Maximum electron mobility of 2-MeV electron irradiated $Si_{1-y}C_y$ S/D n-MOSFETs.

4. Conclusion

We have investigated the effect of 2-MeV electron irradiation on the input characteristics of $Si_{1-y}C_y$ S/D n-MOSFETs with different C concentrations and for different electron fluences. It has been shown that after electron irradiation, the drain current decreases with increasing electron fluence for all C concentrations. This can be attributed to two different factors which take place after electron irradiation. The first factor is a negative shift of the threshold voltage due to the generation of positive charge trapping in the gate dielectric. The second factor is the reduction of the maximum electron mobility because of lattice defects created in the Si channel. Both the threshold voltage shifts and the maximum electron mobility degradation are independent on the C concentration for all electron fluences. These results indicate that the tensile strain in the Si channel is maintained after electron irradiation in the studied devices.

Acknowledgments

Part of this work was supported by Inter-University Laboratory for the Joint Use of JAERI Facilities.

References

[1]C. Claeys and E. Simoen "Radiation Effects in Advanced Semiconductor Materials and Devices,"Springer Verlag, New York (2002).
[2]K. Kodera, et al., "Nanoscale stress field evaluation with shallow trench isolation structure assessed by cathodoluminescencespectroscopy, Raman spectroscopy, and finite element method analyses,"Jpn. J. Appl. Phys., vol. 47, pp. 2506-2510 (2008).
[3]K. Rim, et al., "Enhanced hole nobilities in surface-channel strained-Si p-MOSFETs,"IEEE. IEDM Tech. Dig., pp.517-519 (1995).
[4]C. K. Maiti, et al., "Hole mobility enhancement in strained-Si p-MOSFETs under high vertical field,"Solid-State Electronics., vol. 41, pp. 1863-1869 (1997).
[5]G. Eneman, et al,"Scalability of the $Si_{1-x}Ge_x$ source/drain technology for the 45-nmtechnology node and beyond," IEEE Trans Electron Dev.,vol. 53, pp. 1647-1655(2006).
[6]K-W.Ang, et al., "Thin bodysilicon-on-insulator n-MOSFET with silicon-carbon source/drain regions forperformance enhancement,"IEDM Tech. Dig., pp. 503-506 (2005).
[7]C-J.Chui, et al.,"n-MOSFET with silicon-carbon source/drain for enhancement of carriertransport," IEEE Trans Electron Dev.,vol. 54, pp. 249-256 (2007).
[8]C. Claeys, et al.,"Impact strain engineering on gate stack quality and reliability,"Solid-State Electronics., vol. 52, pp. 1115-1126 (2008).
[9]L. Almeida, et al.,"Analysis of UTBOX-1T DRAM memory cell at high temperatures,"ECS Trans., vol. 39(1), pp. 53-60 (2011).

Session D

Facilities and Test Methods

Facilities and Radiation Test Methods

Ari Virtanen[*1]
1 University of Jyväskylä, Finland
*Email: ari.j.virtanen@jyu.fi
Keyword(s): single-event effects (SEE), total ionizing dose (TID), LET, cyclotron, Co-60, RadHard

Abstract

This talk gives an overview of methods to test component failures caused by space radiation. First, a short introduction to the reasons such tests are necessary, and recent developments in test methodologies are given. Then, radiation environment and error effects, most specifically total dose and single-event-effects, are introduced. A more detailed description is given of the physics of different radiation interactions in semiconductors and the requirements they set for test methods. Facilities used worldwide to study radiation effects in electronics are listed, from which two commonly used test facilities are introduced in more detail.

1. Introduction

In the last decades, electronics has evolved very quickly. Since 1970, the number of components per chip has roughly doubled every two years (known as “Moore’s Law” [1]). The introduction of CMOS technology has raised radiation effects in components as an important issue in satellite projects and space missions. At the end of the cold war, the market for radiation hard (RadHard) components crashed and during the 90’s their fabrication practically stopped. The use of “commercial-off-the-shelf” (COTS) components has become more common but requires increased evaluation activities at radiation test sites. Hence, the radiation hardness assurance (RHA) questions and the test methods involved have been a growing issue among the radiation community.

The COTS components are small in physical size, their power consumption is low, the memory capacities are large and processors fast, and they typically represent the latest design. Moreover, their reliability is tested in everyday use and applications. All these properties are useful for satellite electronics, but one concern remains; their radiation tolerance. In order to determine the radiation durability of components, the space project engineers have turned to nuclear and material physicists, who have broad experience in the interactions of gamma ray and particle radiation. Their experience in using research instruments such as radiation sources and particle accelerators is essential to perform radiation studies of electronics. They also have knowledge of basic research and information available concerning the behavior of energetic gamma rays and ions and their effects in materials. Programs were begun to simulate the space environment at research sites and components were tested to levels exceeding mission requirements. For example, many accelerator laboratories have developed special beam lines and constructed dedicated test areas for component evaluations. In general, particle environments of space projects were predicted with respect to particle mass and energy distributions and with the expected fluxes and fluences. In order to validate this information in tests, concepts such as the stopping power, linear energy transfer, ion penetration range etc. have to be understood. The details of the component structure also define the method of irradiation. For example, higher ion energies result in much deeper ion penetration ranges which enables reverse side irradiation of thinned Integrated Circuits (ICs). This has generated new challenges for the ion source physicists to develop more energetic beams. In order to validate the test also the spectroscopic properties of the beam, like the ion identification, beam purity and energy must be defined in each individual test run. The beam homogeneity, flux and fluence must be calibrated and monitored with high precision during the irradiation [2].

2. Space radiation environments

In figure 1, the origins of space radiation and the relevant particle radiation components are given. The most important source of particles, the Sun, emits (besides photons, neutrons and electrons) 70% protons, 28% helium, 1.5% carbon, nitrogen and oxygen ions, and 0.5% heavier elements. Because the Sun cannot create heavier nuclei than oxygen, their existence proves that it is not a first generation star but was formed in a region of more massive stars.

Galactic cosmic rays (GCR) coming from outside of the solar system can have energies up to 10^{20} eV and are the debris from the novae and supernovae in the Milky Way or other galaxies.

Trapped particles in the two Van Allen belts consist of electrons and protons. According to their particle abundances the inner belt is known as the proton belt and the outer one the electron belt.

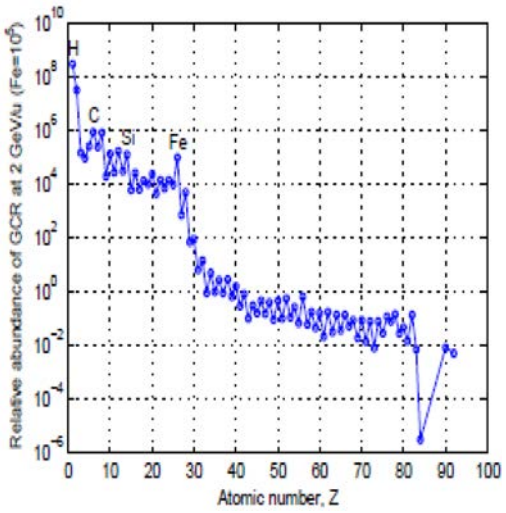

Fig. 7. Relative flux of particles in space as a function of atomic number [4,5].

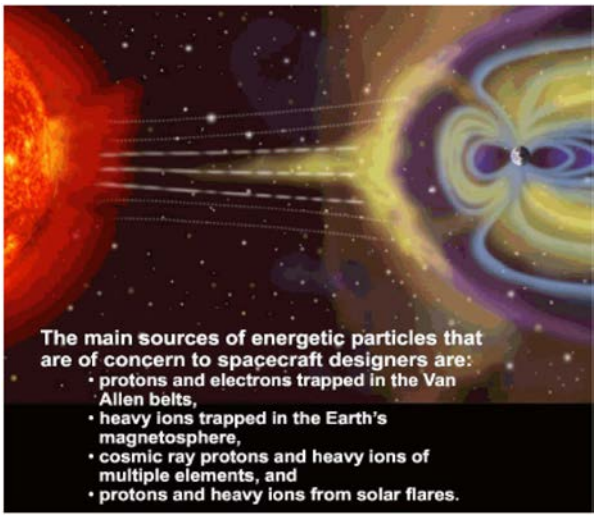

Fig. 6. Space radiation components (NASA MSFC).

Stars with masses of more than eight times that of the Sun are able to create heavy particles such as iron. Iron is the heaviest element, whose abundance in space is significant enough to cause single event effects (SEU) in spacecraft components. In figure 2 the relative abundances of elements in GCR are given.

3. Radiation interactions vs. test methodology

Radiation interacts with the component material primarily by creating electron-hole (e-h) pairs (through ionization) or atomic dislocations. The e-h pairs are the source of total ionizing dose (TID) and single-event effects (SEE). SEEs can be either temporary (soft) or permanent (hard) errors. Atomic dislocations cause displacement damage dose (DDD) effects in the target material.

3.1. Total ionizing dose

The cumulative absorbed ionizing dose in a given material is referred to as the total ionizing dose (TID). It gives a measure of the energy deposited in a medium by ionizing radiation per unit mass; in SI units 1 J/kg = 1 Gy. A more commonly used unit in the radiation community is the rad; 1 Gy = 100 rad,

Electromagnetic radiation primarily induces total ionizing dose effects in electronics. Typically in radiation testing, x-rays and gamma rays have been considered, at energies from a few keV up to several MeV, respectively. There are three primary photon-matter interactions involved: the Photoelectric effect (PE), Compton scattering (CS) and Pair production (PP). Their energy dependence in different materials is illustrated in figure 3. The solid lines correspond to the equal cross sections of neighboring effects. The horizontal dashed line indicates their mutual probability change in silicon (Z=14).

In PE, the photon interacts with a bound electron in an atomic inner orbit. This photoelectron receives the whole photon energy and is ejected from the atom. In CS, the photon interacts with a weakly bound outer orbit electron by transferring part of its energy. This Compton electron then leaves the atom. In PP, the interaction between the photon and the atom yields an electron-positron pair. The threshold energy for PP is 1022 keV, which corresponds to $2m_ec^2$.

These secondary electrons, from all of the above mentioned mechanisms, create e-h pairs in the semiconductor material and after recombination processes the leftover low mobility holes become trapped in the dielectric of the component. This accumulated extra charge can finally cause the total dose effect. Clearly, TID can also arise if the component is exposed to energetic electrons directly.

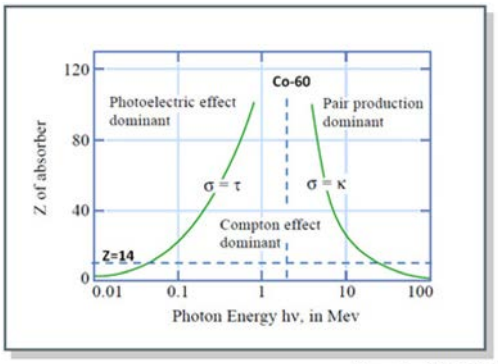

Fig. 8. Cross sections of the three photon interactions in different materials as a function of photon energy. After [6].

A typical test method for TID is to use a radioactive cobalt-60 source. Cobalt-60 has two gamma energies of 1.17 and 1.33 MeV. From figure 3 one can see that for these gamma rays in silicon CS is the dominating interaction mechanism (see the dashed vertical line at the mean energy of 1.25 MeV). The use of cobalt-60 sources is a cost-effective test method and the dosimetry is relatively simple. In addition, the dose rate can be controlled by adjusting the distance between the source and the device under test, DUT. For lower energy photons x-ray tubes can also be used.

Another test method in TID testing is to use electron accelerators [7]. These accelerators are expensive and their use is quite costly, especially if high doses at low dose rates are needed. The dosimetry is also more complicated than with radioactive sources. Due to the low penetration of electrons this is not favored as a test method (except for studies of solar cells). On the other hand, the radiation from accelerator-based sources can be controlled, which makes the operation of the source flexible and more secure.

3.2. Single event effects

When an energetic heavy ion traverses a medium at a velocity greater than the Bohr velocity, it loses electrons and becomes positively charged. This is described in figure 4.

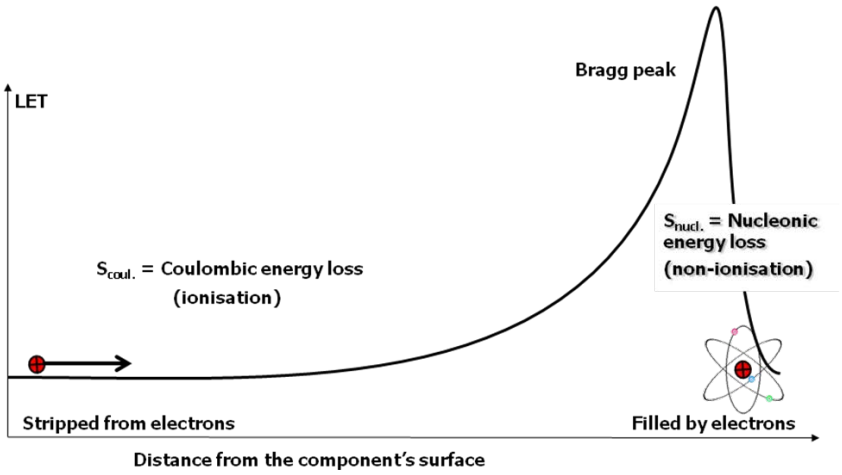

Fig. 4. Bragg curve behavior of the ionizing particle.

While traveling in silicon the ion loses energy via Coulomb interactions with the target electrons and an ionization column is formed. This electronic energy loss is typically considered to correspond to the Linear Energy Transfer, LET. It reaches a maximum at the Bragg peak, where the ion fills its orbitals with electrons captured from the surrounding target atoms. Once becoming a neutral atom it can approach closer to the target nuclei and rapidly slows down via nucleonic interactions. A term, which obeys Bragg curve behavior, is stopping power S (or stopping force). Stopping power is the sum of coulombic and nucleonic terms, i.e. $S = S_{coul} + S_{nucl} = LET + NIEL$ (see figure 4). NIEL is an acronym for non-ionising energy loss and is the cause for DDDs in crystalline materials, such as silicon. The terms LET and NIEL are commonly used terms within the space community. LET can be given in units of energy per unit length [MeV/μm], but most often the unit [MeV/(mg/cm^2)] is used.

In the SEE test method the error cross section of the component is determined as a function of LET. The principle is shown in figure 5. By increasing the LET and monitoring the SEE cross section the threshold and saturation levels of error creation can be obtained. In order to compare the radiation responses for different components, the cross section has to be normalized to the total fluence of particles per cm^2. The LET values are varied by changing ions with different masses (actually their atomic number, Z). The variety of LETs should cover the threshold and saturation regions as evenly as possible.

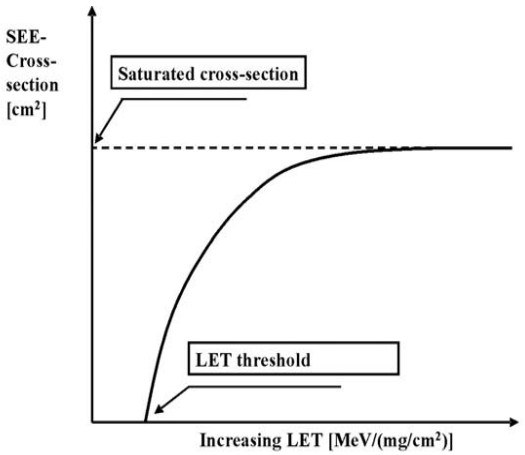

Fig. 5. Principle of SEE response characterization.

In the laboratory, artificial particle radiation sources, such as Ra-226 (100% α-emitter) and Cf-252 (3% spontaneous fission with heavy fragments having an average LET of 43 MeV/(mg/cm^2) and $T_{1/2}$=2.65 years) are convenient for radiation hardness assurance purposes because of their low price and ease of use. Their disadvantages are the restricted ion energies and species along with limited intensities. Due to these limitations, the use of radioisotope sources for SEE tests is prohibited in the official radiation hardness assurance (RHA) tests by the specifications [8, 9]. These sources are typically used only for trial runs of the setup for the RHA testing. Also, lasers are used for the same purpose, but the specifications for RHA testing against SEEs require particle accelerators or nuclear reactors.

4. Facilities

A compilation of worldwide test facilities, used for RHA testing, is listed in the table of Appendix A. The data are taken from [10]. In the following sections one TID and one SEE test facility are shortly introduced. The TID facility, the ESTEC Co-60 facility, is located in The Netherlands and is operated by European Space Research and Technology Centre (ESTEC) of ESA. The SEE facility, RADEF (Radiation Effects Facility), is operated by the University of Jyväskylä and is located in Jyväskylä, Finland. They are both ESA-accredited facilities and belong to the group of four European Component Irradiation Facilities (ECIF) of ESA.

4.1. ESTEC Co-60 facility

In figure 6 the ESA/ESTEC Co-60 irradiation station is illustrated as an example of a TID facility. The station is loaded with a 2000 Ci (June 2007) Co-60 gamma-ray source. It consists of a large control room and a radiation cell with 14 cable feed-throughs enabling monitoring and control of the experiments under test. Automated total dose and dose rate setting, monitoring and logging are available via software running on a PC. This system may also be used for automated monitoring of experiments under test. While irradiating dose rates between 0.5-136.8 rads/min. are easily changed by the use of a rail system installed in the radiation cell. The chamber housing the Co-60 source is shown in figure 7. Part of the rail system can also be seen in the figure.

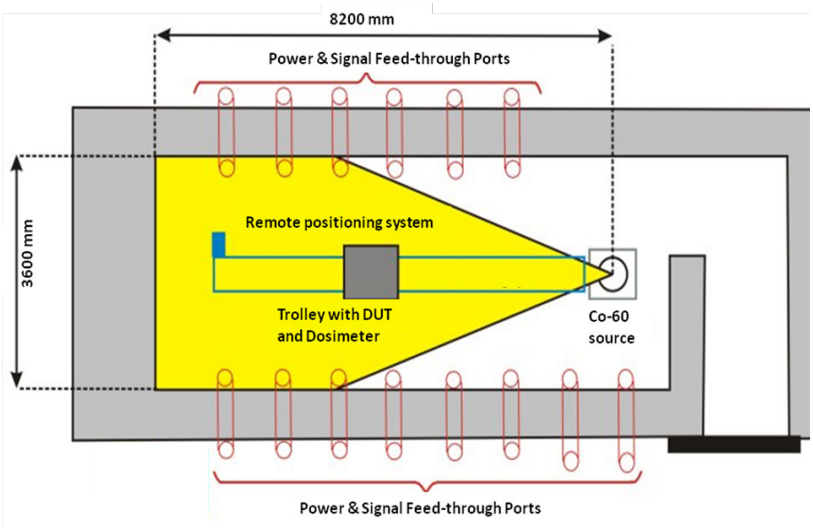

Fig. 6. A sketch illustrating ESTEC Co-60 facility. The distance from the source can be adjusted with a trolley, which includes a fixture for the DUT and the dosimetery system [11].

Fig. 7. ESTEC Co-60 gamma source inside the shielding chamber (photo courtesy by Bob Nickson).

4.2. RADEF facility

RADEF consists of two separated beam lines, one for heavy ions and another for protons. An overview of the facility is illustrated in figure 8, where both of the beam lines are marked. The proton beam is taken in air through a 200 µm thick tungsten window. The proton dosimetry consists of an ionization chamber at the beam exit, and particle detectors behind the target stage. The ionization chamber enables accurate and real-time monitoring of the beam intensity and the particle detectors are used for the initial beam calibration.

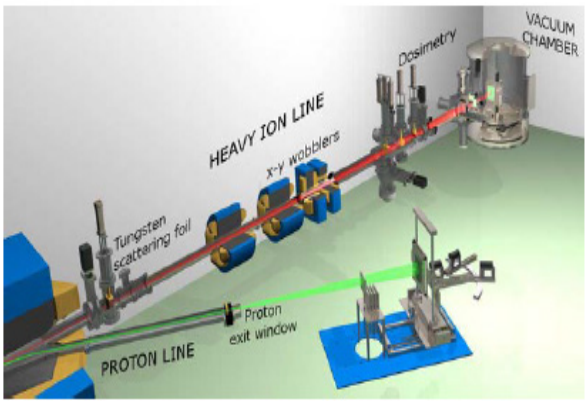

Fig. 8. An overview of RADEF facility [5].

In the heavy-ion line the beam homogeneity is obtained by using: (1) a 1 µm thick scattering foil made of tungsten, upstream in the beam line, and (2) x–y wobblers. With this equipment beam homogeneity of better than the required ±10% can be achieved over an area of 4 x 4 cm^2, or even larger if needed. Typically an area of 2 x 2 cm^2 is used. The heavy-ion dosimetry is made using four photomultiplier tubes (PMT) equipped with scintillator crystals. The PMT detector assemblies are used in the online monitoring of the beam by adjusting the scintillators on the edge of the beam during the experiment. The detectors provide also energy spectra, thus the beam purity can be assured [2, 5].

4.3. Development of ion cocktails for SEE tests

A high-energy, heavy-ion particle accelerator is a very expensive research tool. In addition, high running costs make its use costly, especially because the price of the test is charged according to the duration of the beam time. In order to keep the project costs low the tests should be performed in as short time as possible. A typical SEE-test campaign includes several different ions and all the calibration procedures have to be repeated for each individual beam. Therefore, fast changing of ion species is crucial in SEE tests. To solve this problem, a mixture of ions known as an ion cocktail, is used.

The operation of an electron-cyclotron-resonance (ECR) type ion source is based on microwave power, which ionises atoms by stripping electrons from their orbits. Several different ion species can be simultaneously fed into the ECR and they can be extracted together. Ions belonging to the same cocktail have almost identical mass-to-charge (m/q) ratios. These cocktail ions accelerate along the same path and in order to separate them the cyclotron is utilised as a mass analyser (note, that m/q ≠ A/q). This is done by shifting the cyclotron RF frequency and/or the trim coils in the extraction. These procedures make the fast beam change possible, but require a combination of both ECR type ion source and cyclotron type accelerator.

Two examples of a set of ion cocktails are depicted in figure 9, where the LET curves for different ions as a function of their penetration depths are given. In the low energy 3.6 MeV/amu cocktail the Bragg peak is located between 10 and 50 µm, except for xenon ions. Xenon impinges on the component at the energy corresponding to the maximum LET and its Bragg curve turns downward immediately after the penetration starts.

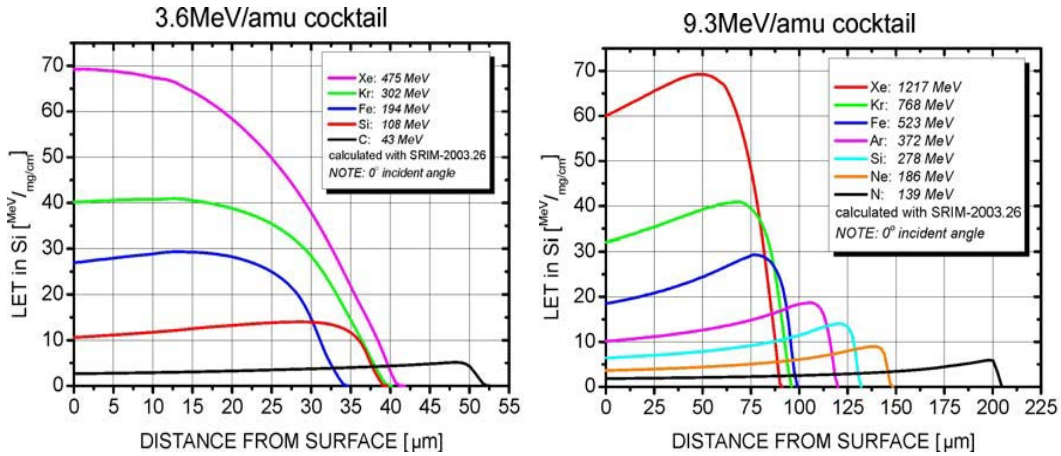

Fig. 9. LET curves of low and high energy cocktail ion species. Data calculated with SRIM-2003.26 code.

It is obvious, that in order to reach the sensitive volume with heavy ions from the RADEF ion cocktail, the component package has to be removed. If the sensitive area is close to the die surface, the low energy cocktail of figure 9 can be used. Unfortunately, today many components and practically all modern memories are assembled with the bond pads in the centre and the lead frame on top of the die. Therefore, the direct, front side irradiation is not possible, but irradiation from the back side is needed. In this case the component must be prepared before the test by thinning it from the back side. Typically thinning is done so that there is about 50µm of silicon left on top of the sensitive volume. The method is reliable, but testing requires a high penetration cocktail. An example of this is the cocktail as shown in right-hand side of figure 9. There the Bragg peaks of all ions are located at or after distances of 50 µm.

As has been shown, active development work is needed to improve the capabilities to perform SEE tests in a more reliable and cost effective way. This becomes more and more important along with the technological evolution, with its approach towards the nano-scale and the increased use of electronics “everywhere”. This will inevitably lead to higher demand for radiation hardness assurance, both by testing with radiation and by design and manufacturing.

Appendix A

A list of facilities, where radioactive photon sources, particle accelerators or reactors are used. Facilities are in alphabetical order and grouped according to their location and the type of radiation(s).

Europe	Country	Radiation
AWE	UK	n°
CAN	Spain	HI, p+, Co
CSL	Belgium	p+, n°, e-, Co, Cs, L
DELFT	Netherlands	n°
EADS	France	L
ENEA	Italy	n°, Co
ESA-ESTEC	Netherlands	Co
ESS BILBAO	Spain	p+, n°
FRAUNHOFER	Germany	p+, n°, e-, Co
GANIL	France	HI
GSI	Germany	HI
HZB	Germany	p+, n°, Co
IPN	France	HI, p+, e-
ISOTRON	UK	p+, n°, e-, Co
JYFL-RADEF	Finland	HI, p+
KVI	Netherlands	p+
LNS-INFN	Italy	HI, p+
MBDA	UK	L
NPL	UK	n°, e-, Co, Cs, Am
NUCLETUDES	France	Co, X
ONERA	France	HI, p+, e-, Co
PSI	Switzerland	p+
PTB	Germany	HI, p+, n°, e-, Co, Cs, X
RAL	UK	n°, L
SIRAD-INFN	Italy	HI, p+, Co, X
SVEDBERG	Sweden	p+, n°
TRAD	France	e-, Co
UCL	Belgium	HI, p+, n°, Co, L
USC	Spain	Co

North America	Country	Radiation
AEROFLEX	USA	n°, e-, Co, Cs
BNL	USA	HI
BREL	USA	HI
CNL	USA	p+, n°
DMEA	USA	Co, Cs
GSFC REF	USA	HI, p+, e-, Co
IUCF	USA	p+, n°, e-
LANL	USA	n°
LBNL	USA	HI, p+, n°
NASA-JPL	USA	e-, Co, L
NCC	USA	e-, Co
NSCL	USA	HI
SNL	USA	HI
TAMU	USA	HI
TRIUMF	Canada	p+, n°

Other	Country	Radiation
DUBNA	Russia	HI
ISDE	Russia	p+, Co, Cs
INFLPR	Romania	X, L
JAEA	Japan	HI, p+, e-, Co
NRNU	Russia	e-, Co, Cs, X, L
SINP MSU	Russia	HI, e-
NRC	Russia	n°, e-, X
RCNP	Japan	p+, L

Key to the table		
HI = heavy ions	Co = ^{60}Co	L = laser
p+ = protons	Cs = ^{137}Cs	
n° = neutrons	Am = ^{241}Am	
e- = electrons	X = x-rays	

Acknowledgments

This work was supported by the Academy of Finland under the Finnish Centre of Excellence in Nuclear and Accelerator Based Physics Research Programme 2012-2017 (Project No.251353) and European Space Agency (ESA/ESTEC contract No. 18197/04/NL/CP)

References

[1] G. Moore,“Cramming more components onto integrated circuits,” Electronics, vol. 38(8), pp. 114-116 (1965)
[2] A. Virtanen, “The use of particle accelerators for space projects,” J. Phys.: Conf. Ser., vol. 41, pp. 101–114 (2006)
[4] G. R. Piercy et al., “Experimental evidence for the increase of heavy ion ranges by channeling in crystalline structure,” Phys. Rev. Lett., vol. 10, no. 9, pp. 399– (1963)
[5] A. Javanainen, “Particle radiation in microelectronics”, PhD Thesis (2012)
[6] F. B. McLean and T. R. Oldham, “Basic mechanisms of radiation effects in electronic materials and devices”, US Army Lab Command, HDL-TR-2129, Harry Diamond Laboratories, MD, USA
[7] European Space Agency, “Total Dose Steady-State Irradiation Test Method”, 1. ed., ESA/SCC Basic Specification No. 22900 (2010)
[8] Electronic Industries Association, “Test Procedures for the Measurement of Single-Event Effects in Semiconductor Devices from Heavy Ion Irradiation”, EIA/JEDEC Standard No. 57 (1996)
[9] European Space Agency, “Single-Event Effects Test Method and Guidelines”, 1. ed., ESA/SCC Basic Specification No. 25100 (1995)
[10] S. Martin-Barbero et al., “Compendium of international irradiation test facilities”, proceedings of Thematic day in RADECS, Sevilla, Spain (2011)
[11] https://escies.org/webdocument/showArticle?id=251&groupid=6

Development of Ion Photon Emission Microscopy at JAEA

Shinobu Onoda[*1], Hiroshi. Abe[1], Takashi Yamamoto[1], Takeshi Ohshima[1],
Junichi Isoya[2], Tokuyuki Teraji[3], and Kenji Watanabe[3]
1 Japan Atomic Energy Agency (JAEA), Japan
2 University of Tsukuba, Japan
3 National Institute for Materials Science (NIMS), Japan
*Email: onoda.shinobu@jaea.go.jp
Keywords: Ion Photon Emission Microscopy, Microbeam, Diamond, NV center

Abstract

We are developing the Ion Photon Emission Microscopy (IPEM). Since the spatial resolution is determined by the spot size and the intensity of Ion Beam Induced Luminescence (IBIL), the scintillator is one of the most important parts of IPEM. We propose that the diamond containing Nitrogen Vacancy (NV) centers can be used as a scintillator. For both diamond and YAG:Ce proposed by Branson et al., the minimum spot size is a few micrometers. IBIL intensity from diamond is four times higher than that from YAG:Ce. Therefore, we propose that the diamond containing NV centers is a rival candidate of YAG:Ce for IPEM.

1. Introduction

When a high energy heavy ion passes through microelectronics, an unexpected transient current is generated and leads to microelectronic malfunctions so called Single Event Effects (SEEs). To study the origin of the transient current in specific device regions, a focused microbeam combined with a single ion hitting technique has a key advantage.Therefore, we have developed two systems to acquire two-dimensional maps of transient currents by using focused microbeams connected with the 3 MV tandem and the Azimuthally Varying Field (AVF) cyclotron accelerators at Japan Atomic Energy Agency (JAEA), Takasaki [1-3]. These are called Transient Ion Beam Induced Current (TIBIC) systems. Avariety of heavy ions can be focused such as Carbon (C), Nitrogen (N), Oxygen (O), Nickel (Ni), Gold (Au), etc. with the energies ranging from 3 to 18 MeV. In addition, Neon (Ne) 260 MeV and Argon (Ar)520 MeV can be focused. The similar system called Time Resolved Ion Beam Induced Current (TRIBIC) has been developed at Sandia National Laboratories (SNL) [4]. The powerful advantage of TIBIC mapping is the ability to determine the position dependence of the event induced by an ion. While the microbeam has many advantages for SEE testing, the transport and optimization of the microbeam requires much time and effort, especially for high energy heavy ions. Therefore the mapping system with less effort is required.

A different way to perform mapping has been proposed by SNL [5-7]. It is called the Ion Photon Emission Microscopy (IPEM). To observe map using IPEM, it is not necessary to focusheavy ions at all. Instead of microbeam to control the position of the ion strike, the position where ion strikes the sample is recorded together with the ion induced event at semiconductors. The event can be electrically detected by oscilloscope. To realize the position detection by single ion strike, a scintillator is placed on the semiconductor, and Ion Beam Induced Luminescence (IBIL) on the scintillator is detected by Position Sensitive Detector (PSD).Since the spatial resolution is determined by the spot size and the intensity of IBIL, the scintillator is one of the most important parts of IPEM system. Recently Branson et al. have studied the optical properties of various scintillators [7]. They suggested that $Y_3Al_5O_{12}$:Ce (YAG:Ce) is so far the best option for application in IPEM system, because of its high emission rate, short decay time, and high radiation hardness. Additionally, the emission spectrum is particularly important. In the case of high energy ion irradiation in air, the gas molecules are ionized, the subsequent luminescence of air disturbsefficient IBIL detection because it acts as noise. Therefore, the emission wavelength of the scintillator should be different from that of air (<450 nm) [7].

We have been developing IPEM at JAEA. One major difference between our system and IPEM developed by SNL is scintillator, which is one of the most important parts of IPEM system. At the beginning of IPEM setup, we have used Zinc Sulfide (ZnS) as a scintillator. However, the spot size of ZnS is one order of magnitudebigger than that of YAG:Ce [8]. Recently, we have proposed that the diamond containing a high concentration of Nitrogen Vacancy (NV) centers can be used as a scintillator for IPEM application. In this paper we focus on IBIL of diamonds containing NV centers.

2. Experimental

2.1 Setup

Fig. 1 shows a photograph of the measurement system connected with AVF Cyclotron at JAEA Takasaki. This system contains the following; (1) a beam extraction window (Kapton film, 7 μm in thick) is mounted at the end of beam line. On the film, a mirror with hole is placed. The angle of hole is 45 degrees with a diameter of 1

mm, and the mirror is mounted at an angle of 45 degrees to the objective lens.; (2) a scintillator and a semiconductor (diode) mounted on a micro XYZ stage.; (3) electronics for charge measurements including an amplifier, a bias-tee, a bias supply and an oscilloscope. At the moment, fast transient currents cannot be measured.; and (4) a photon detection equipment including the microscope (Olympus, BX51M), the GaAsP Image Intensifier (I.I.) (Hamamatsu, C8600), and the cooled Charge Coupled Device (CCD) camera (Hamamatsu, C4880-50-26A). The objective lens is the most important parts of optics. Working Distance (W.D.) and Numerical Aperture (N.A.) need to be long and large as much as possible. We used two objective lenses. One is the standard plan-achromatic lens for brightfield and darkfield microscopy(Olympus, Model: MPLN5x BD, W.D.: 12mm, N.A.: 0.10) as shown in Fig. 1. Another is the plan-achromatic lens with long W.D. (Olympus, Model: SLMPLN20x, W.D.: 25 mm, N.A.: 0.25).

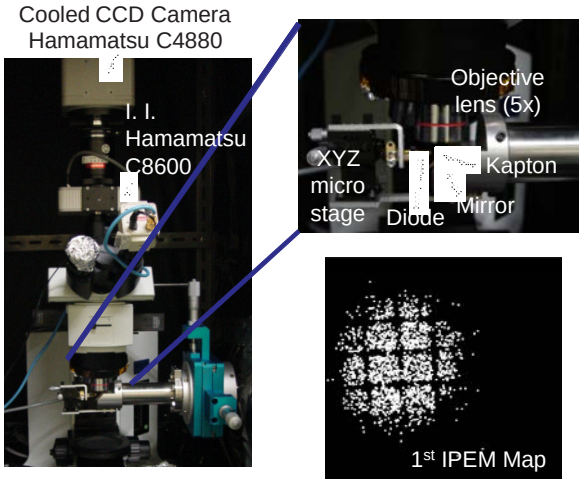

Fig. 1 Photograph of measurement system (left and top right). The first IPEM map of Cupper mesh on diode is represented (bottom right).

The high energy ion beams accelerated by the AVF cyclotron are extracted from vacuum to air via Kapton film. The extracted ion penetrates the scintillator on a semiconductor. The photons from the scintillator are detected by the cooled CCD camera. The position where the ion hit the scintillator can be calculated from the center of mass of ion induced luminescence. At the same time the ion induced transient current pulse generated at a semiconductor is recorded by the oscilloscope. Combining the position where ion hit and the transient current, two dimensional mapcan be observed as shown in Fig. 1.

2.2 Scintillators

Three different varieties of diamonds without NV centers are studied;one is aIb single crystal diamond particles (about 1 mm in diameter) purchased from Element Six (E6). The type Ib diamond contains dense nitrogen as an impurity(labeled as #1); second is an electronic grade IIa single crystal diamond plate (4x4x0.5mm) purchased from E6 (labeled as #2); third is a polycrystalline diamond synthesized at National Institute for Materials Science (NIMS) (labeled as #3). These samples do not contain NV centers.

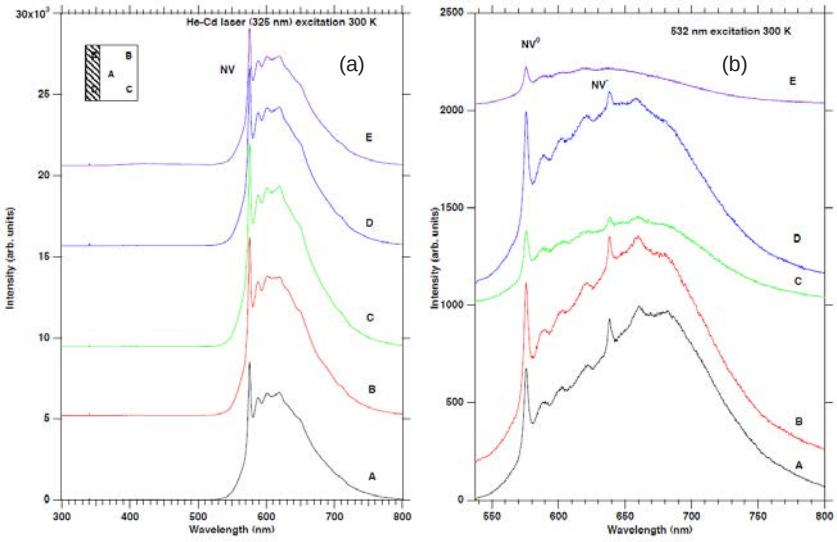

Fig. 2Photo-Luminescence (PL) spectra excited by 325 nm laser (a) and 532 nm laser (b) at room temperature.

On the other hand, a non-commercial High Presser High Temperature (HPHT) IIa single crystal diamond containing NV centers is studied(labeled as #4). NV centers are created by high energy electron irradiation and subsequent annealing. The distribution of NV centers is uniform and theaverage concentration of NV centers is evaluated to be 0.14 ppm ($2.5x10^{16}$ cm^{-3}). The distributionuniformity of NV centers is confirmed by Photo Luminescence (PL) spectra at various locations of the diamond. PL spectra excited by 325 nm (see Fig. 2(a)) and 532 nm (see Fig. 2(b)) are measured at NIMS. Inset of Fig. 2(a) shows the schematic top view of sample #4. The capital alphabets in the inset figure show the locations where PL spectra are measured. As shown, NV centers with negatively charged (NV^-) and non-charged (NV^0) are detected from whole area of sample #4. In the case of 532 nm excitation, Zero Phonon Lines (ZPLs) of NV^0 and NV^- are found at the wavelengths of 575 and 637 nm. The broad spectrum (550-800 nm) corresponds to vibronic side bands of each charge state. Although not shown here, Quantum Efficiency (QE) of I.I. decreases at the emission maximum of NV centers in the diamond. However, the portion of the emitted photons from NV centers in the diamond can be detected, since there is partial overlap.

In addition to sample #4, we prepare another diamond containing NV centers. We perform the electron

irradiation to type Ib diamond particles (sample #1), and subsequent annealing at 800 degree Celsius for 5 hoursto create NV centers (labeled as #5). Figure 3 (a, b) shows the diamondsbefore (sample #1) and after irradiation (sample #5) under illumination of Ultra Violet (UV) light with the wavelength of 254 nm. The yellow color corresponds to nitrogen impurity (see Fig.3 (a)), and the red color corresponds to NV centers (see Fig.3 (b)). This fact suggests that we successfully convert nitrogen impurity to NV centers by creating vacancies.

Fig. 3.Photograph of sample #1 (a) and #5 (b) under UV light with the wavelength of 254 nm.

3. Results and discussion

Figure 4 (a, b) shows the CCD images when 150 MeV Ar ions penetrate YAG:Ce and diamond containing NV centers (sample #4). The dashed circles highlight the ion induced spots. As shown, IBIL is observed from YAG:Ce and the diamond containing NV centers. However no spot is observed from diamonds without NV centers (samples #1, #2, #3). This fact suggests that NV centersarethe main contributor forIBIL. One possibility of the luminescence mechanism from a diamond containing NV centers is following. According to the ion track distribution theories, the radius of ion track created by the single ion with the several hundreds of MeV exceeds 1 μm. Since a lot of NV centers distribute in the ion track, these are excited. When the excited NV centers change to the ground state,IBIL is emitted. To confirm this, it is necessary to measure IBIL spectrum. Therefore it needs further consideration.

Figure4 (c) shows the typical spot distributions observed from YAG:Ce(closed symbols with red color)and sample #6 (open symbols with black color). The dashed line shows the noise level. The averaged Signal to Noise (S/N) ratios of each scintillator are 3.4 and 4.6, respectively. The Full Width at Half Maximums (FWHMs) of spot are evaluated to be 2.9 and 3.8 μm, respectively. After normalization by the maximum values, the shape of spot distribution of YAG:Ce agrees well with that of the diamond containing NV centers (sample #6). In contrast with our data, it was reported that the spatial resolution of about 5 μm has been achieved by using YAG:Ce [7]. In the case of n-type Gallium Nitride (n-GaN), the spatial resolution of about 2.5 μm has been demonstrated [6]. We suggest that a diamond containing NV centers is a rival candidate of YAG:Ce and n-GaNfrom the point of view of spatial resolution.

We perform the high energy heavy ion irradiation to sample #5. While no spot is observed from sample #1, spots are found in sample #5. This fact supports that NV centeris the main contributor of IBIL. Figure 5 shows typical spotsobserved from sample #5 when 56 MeV-N, 75 MeV-Ne, 150 MeV-Ar, 322 MeV-Kr and 454 MeV-Kr. The dashed circle highlights the ion induced spot. In this study, we successfully demonstrate that the

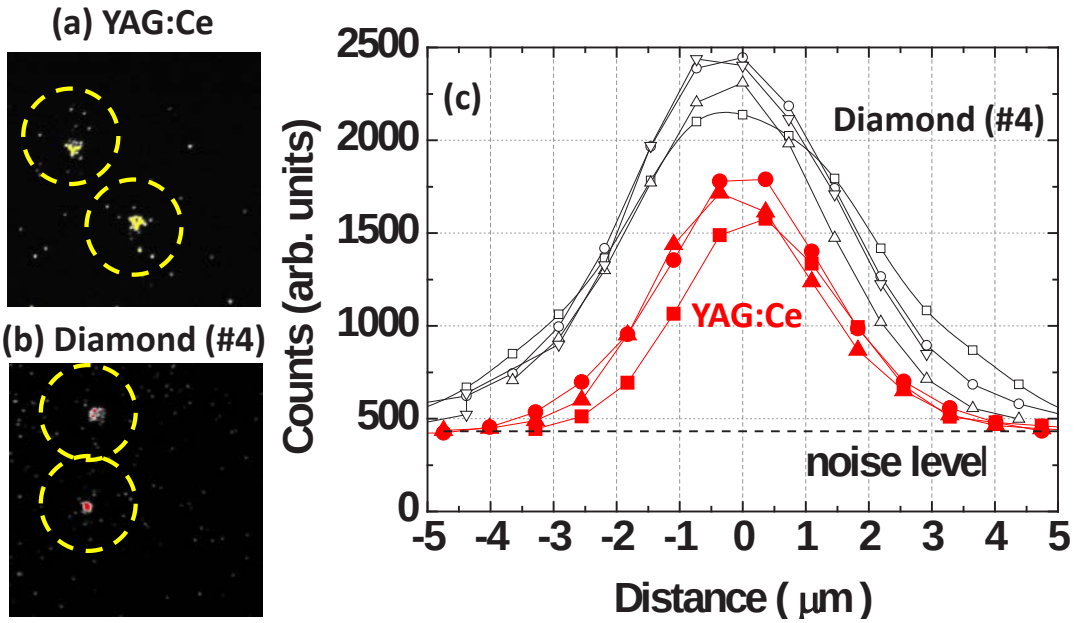

Fig. 4.CCD images when 150 MeV Ar ions strike YAG:Ce (a) and the diamond containing NV centers (sample #4) (b). Two spots are found for both cases. The cross sectional spectrum of luminescence observed fromYAG:Ce and diamond (sample #4) (c).

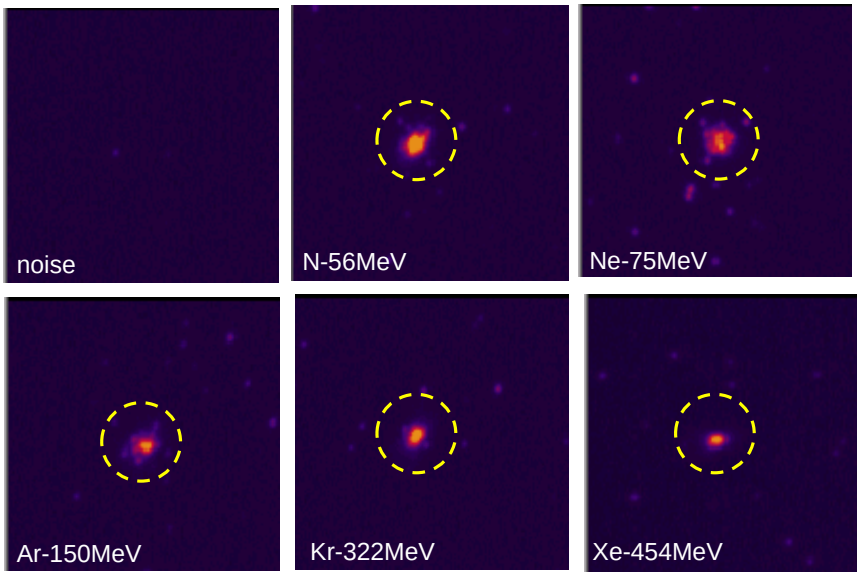

Fig. 5.CCD images when various ions with various energies penetrate the diamond containing NV centers (sample #5).

diamond containing NV centers can be used to detect a wide variety of ion species and energies. It is debatable whether the spot size and intensity of IBIL depends on the ion species and energies.

4. Summary

To achieve high spatial resolution mapping of Single Event Effects (SEEs) by using Ion Photon Emission Microscopy (IPEM) system, the exploration of optimum ion luminescent materials is required. It has been reported that YAG:Ce demonstrates the most promising properties [7]. As a result of ion irradiation, the IBIL is observed from the diamond containing NV centers as well as YAG:Ce. No IBIL is observed from diamonds without NV centers. These facts suggest that NV center mainly contributes to IBIL. We found that the spot size of the diamond containing NV centers is comparable with the YAG:Ce after normalization. S/N ratio of the diamond containing NV centers is better than that of YAG:Ce. To detect a single ion with high sensitivity, it is better to use the diamond containing NV centers instead of YAG:Ce. Finally, we demonstrate that the diamond containing NV centers can be used to detect the single ion with a wide variety of ion species and energies. According to these results, we therefore conclude that a diamond containing NV centers is a rival candidate of a YAG:Ce for IPEM applications.

Acknowledgments

YAG:Ce was provided by Mr. A. Yokoyama of the Department of Advanced Radiation Technology, JAEA. This work was partly supported by the Strategic Japanese-German Joint Research Program in 2009 from the Japan Science and Technology Agency.

References

[1] I. Nashiyama, et al., "Single-event current transients induced by high energy ion microbeams," IEEE Trans. Nucl. Sci.,vol. 40, pp. 1935-1940 (1993).
[2] J. S. Laird, et al., "Development of a new data collection system and chamber for microbeam and laser investigations of single event phenomena,"Nucl.Instr. and Meth.B, 181,pp. 87-94 (2001).
[3] T. Hirao, et al., "Transient current mapping obtained from silicon photodiodes using focused ion microbeams with several hundreds of MeV,"Nucl. Instr. and Meth.B,267, pp. 2216-2218 (2009).
[4] H. Schone, et al., "Time-resolved ion beam induced charge collection (TRIBICC) in micro-electronics,"IEEE Trans. Nucl. Sci., vol. 45, pp. 2544-2549 (1998).
[5] B. L. Doyle, et al., "Nuclear emission microscopies,"Nucl.Instr. and Meth.B, 181, pp. 199-210 (2001).
[6] J. V. Branson, et al., "The ion photon emission microscope on SNL's nuclear microprobe and in LBNL's cyclotron facility,"Nucl.Instr.And Meth.B, 267, pp. 2085-2089, (2009).
[7] J. V. Branson, et al., "Ion beam characterization of advanced luminescent materials for application in radiation effects microscopy,"Nucl. Instr. and Meth.B, 269, pp. 2326-2329(2011).
[8] S. Onoda, et al., "Diamonds Utilized in the Development of Single IonDetector with High Spatial Resolution,"Trans. Mat. Res. Soc. Jap., pp. (2012).

Large-Area Uniform Ion Beam Formed by the Nonlinear Beam Optics at the JAEA TIARA Cyclotron

Yosuke Yuri*, Takahiro Yuyama, Tomohisa Ishizaka, Ikuo Ishibori and Susumu Okumura
Takasaki Advanced Radiation Research Institute, Japan Atomic Energy Agency,
1233 Watanuki-machi, Takasaki, Gunma 370-1292 Japan
*Email: yuri.yosuke@jaea.go.jp
Keywords: Ion beam, Uniform irradiation, Multipole magnet, Beam transport system, AVF Cyclotron

Abstract

A uniform ion-beam formation/irradiation system has been developed at the accelerator complex TIARA in Japan Atomic Energy Agency (JAEA). In this system, a large-area beam with a uniform intensity distribution can be formed on the target by the nonlinear beam optics including octupole magnets. Therefore, the whole of a large-area sample can be irradiated uniformly at a constant fluence rate unlike a conventional scanning method and, thus, this uniform beam is suitable for short-time, low-fluence and/or low-fluence-rate irradiations. Recently, a versatile target chamber has been installed in order to conduct various beam studies and users' experiments efficiently. The ion-irradiation response of Gafchromic radiochromic films has been investigated for the evaluation of the transverse intensity distribution of the uniform beams. For several species of heavy ions, beam characteristics are explored toward realization of a heavy-ion uniform beam. We have, so far, obtained the uniform intensity distribution of 9 cm square with an rms uniformity of 5% for a 10-MeV proton beam. Such a large-area uniform beam has been used for the radiation degradation test of space solar cells.

1. Introduction

Large-area uniform irradiation is an indispensable accelerator technique for bringing about a homogeneous irradiation effect in various quantum-beam-applied researches such as radiation effect studies on space-use electronic devices. A new uniform-beam formation system has been developed at the JAEA TIARA azimuthally-varying-field (AVF) cyclotron for materials and biological sciences. The principle of the system is based on the nonlinear focusing method (NFM): The tail of the Gaussian transverse intensity distribution is folded into the inside by the nonlinear focusing force of multipole magnets so that the intensity distribution can be made uniform [1, 2]. Therefore, the particle fluence rate can be made constant anywhere on a large-area sample. This characteristic of the method is suitable for uniform irradiation in a short time, at a low fluence and/or at a low fluence rate. It is, thus, anticipated that NFM can compensate shortcomings of conventional irradiation methods (a beam scanning method and a beam scattering method) and is helpful in advanced applications [3].

In these proceedings, the recent progress is summarized related to the uniform beam formation. In Sec. 2, a brief overview is given on the system of the uniform beam formation and irradiation including a versatile target chamber installed recently. The transverse intensity distribution of the uniform beam is evaluated using Gafchromic radiochromic films. The ion-irradiation response of the films is investigated in Sec. 3. Commissioning toward the formation of heavy-ion uniform beams is explored in Sec. 4. Finally, the present status is summarized in Sec. 5.

2. Overview of the uniform-beam formation system

The schematic view of the JAEA AVF cyclotron [4] and its beam lines is shown in Fig. 1. One of the high-energy beam transport lines has been improved dedicatedly for uniform beam formation and irradiation. The beam line has been equipped with two couples of sextupole and octupole magnets and a target chamber. The total length of the beam line is 42 m from the exit of the cyclotron to the target.

2.1 Procedure of the uniform beam formation

The uniform beam is formed and provided for irradiation by following the procedure below: The initial intensity distribution of the beam should be Gaussian (or parabolic) as a prerequisite for uniform beam formation. However, the profile of the ion beam extracted from the cyclotron is not Gaussian but usually asymmetric, which is a severe obstacle to forming a uniform beam. The ion beam is, therefore, multiply-scattered through a thin foil so that a Gaussian-like distribution can be obtained. The installation location of the foil and the beam optics is optimized for efficient multiple Coulomb scattering [3, 5]. Then, the Gaussian-like beam is focused by the multipole magnets installed near the target. Octupole magnets are mainly employed to form a uniform distribution. Sextupole magnets can be also utilized since they have different effects on the distribution transformation [2, 3, 6]. A dedicated beam optics has been realized for the prevention of betatron coupling due to multipole magnets [3]. During beam tuning, the on-target intensity distribution of the beam is monitored using a

fluorescent screen such as DRZ-high (Mitsubishi Chemical) and AF995R (Desmarquest) [7].

For irradiation with the uniform beam, the particle fluence can be adjusted using a beam attenuator [8] and/or an electrostatic beam chopper [9]. The attenuator, composed of metallic foils with pores, can reduce the spatial intensity of the beam widely. The chopper can change the time-average intensity by adjusting the duty of the beam injected into the cyclotron. The irradiation time of the beam can be controlled also by the chopper.

2.2 Target chamber

A target chamber was installed at the end of the beam line in 2011 for efficient beam studies and users' experiments. The chamber consists of two parts as shown in Fig. 2: One is a main target chamber on the beam axis, equipped with several flanges designed for different types of beam measurement and sample irradiation. For example, a viewport, which can be seen in Fig. 2, is available for a solar simulator required in a degradation test of space-use solar cells. The other is a small side chamber that can keep 22 sheet samples (up to 21 cm square in size), which enables us to replace the samples readily without affecting a vacuum pressure in the main chamber. A sample on the target position can be exchanged within two minutes by a motor-driven changer. A vacuum pressure of the order of 10^{-4} Pa, which is required for beam transport, can be attained in about one hour if samples are sufficiently pre-degassed.

To meet the need in some experiments, the uniform beam irradiation can be performed also in air by changing the chamber setup. The beam of more than about 10 MeV/u can be extracted into the air through a 30-μm-thick titanium foil window.

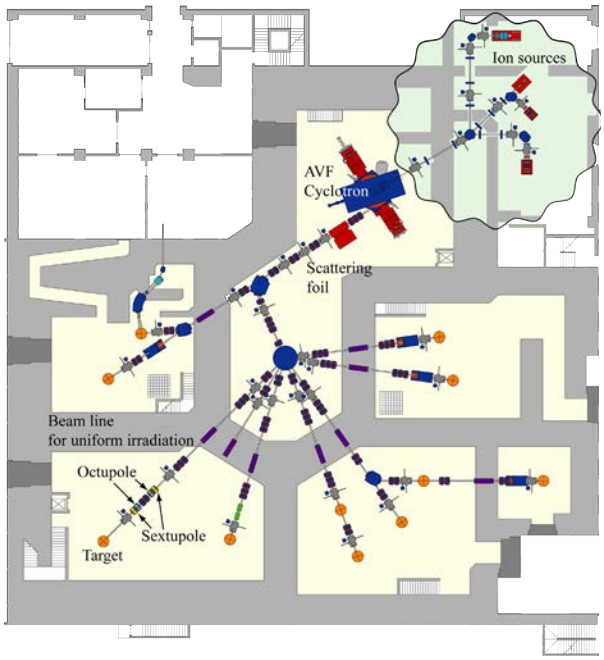

Fig. 1: Schematic layout of the JAEA AVF cyclotron (K number of 110 MeV) facility. There are four ion sources in the basement, which can produce proton and various heavy ions up to osmium. The beam attenuator and the electrostatic chopper are installed in the low-energy injection line. The scattering foil can be inserted at the first straight section after the cyclotron. A uniform beam is formed at the LB beam line equipped with multipole magnets.

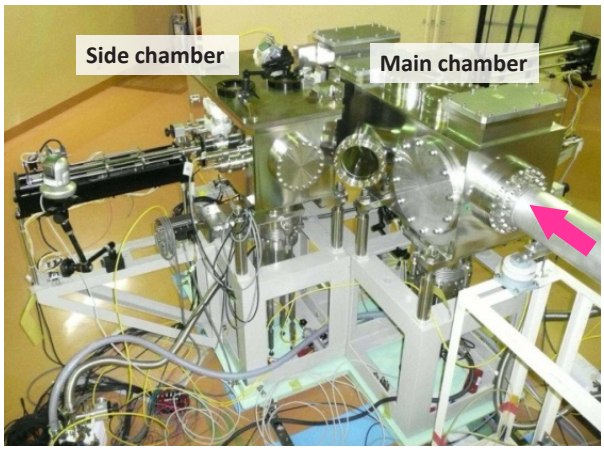

Fig. 2: Versatile target chamber for experiments using large-area uniform beams. The beam comes from the direction of the pink arrow in the picture. The whole of the chamber is settled on a linear motion guide for the quick arrangement of the target setup.

3. Intensity distribution measurement using Gafchromic films

Gafchromic radiochromic films (Ashland Inc.), whose color turns blue due to radiation exposure, are used for the measurement of the two-dimensional (2D) intensity distribution of the beam on the target. Various characteristics of the film, such as high spatial resolution, large area, relatively low-dose range, and easy handling, are appropriate as a handy measurement technique of a large-area beam. The coloring response of ion-irradiated films has been investigated as a change in the optical density using general-purpose scanners for precise analysis [10]. 10-MeV ^{1}H and 520-MeV ^{40}Ar ion beams have been used for the investigation.

3.1 Film calibration

Two types of Gafchromic films have been chosen for the present study: One is HD-810, whose active layer (6.5 μm thick) is behind a 0.75-μm-thick surface layer and coated on a 97-μm-thick polyester substrate. The other is EBT2, whose active layer (30 μm thick) is put between 80-μm and 175-μm polyester layers. According to the manufacturer, the available photon dose ranges of the films are 10~400 Gy and 0.01~10 Gy, respectively.

The following procedure was taken for film calibration: First of all, the films were irradiated uniformly with

the ion beam. The beam current was measured by a Faraday cup near the target. The irradiation time was controlled by the electrostatic chopper between 10^{-3} and 10^{1} s, depending on the fluence, intensity of the beam, and the film type. Then, irradiated films were read by general-purpose scanners to digitize them into TIFF images with 16-bit RGB color intensity values. Two different kinds of flat-bed scanners were employed: Canon LiDE50 (reflection type) and Epson ES-10000G (reflection/transmission type). The irradiated films were scanned in more than one day after irradiation to prevent the color variation right after irradiation. Finally, the optical density d_X was determined for each X of RGB color values by the equation: $d_X = \log_{10}\left(2^{16} - 1/X\right)$.

Figure 3 shows the fluence response of HD-810 films irradiated with the 10-MeV H beam and scanned by LiDE50. The optical densities of all three color intensities increase linearly with the particle fluence in the low fluence range and then are saturated in the high one. The optical density obtained from the red color component is the largest in the linear-response range. On the other hand, the blue component is the least sensitive. This reflects the characteristic that the absorption of the irradiated film is the highest in the wavelength between 650 and 700 nm. Thus, the fluence of the 10-MeV H beam can be measured from 1×10^{9} to 2×10^{11} cm^{-2} with a moderate S/N ratio by choosing an appropriate color component of HD-810. When the films were scanned by ES-10000G with a transmission mode, the optical densities were slightly smaller than that in Fig. 3 although a similar linear response of the optical density was observed in almost the same fluence range.

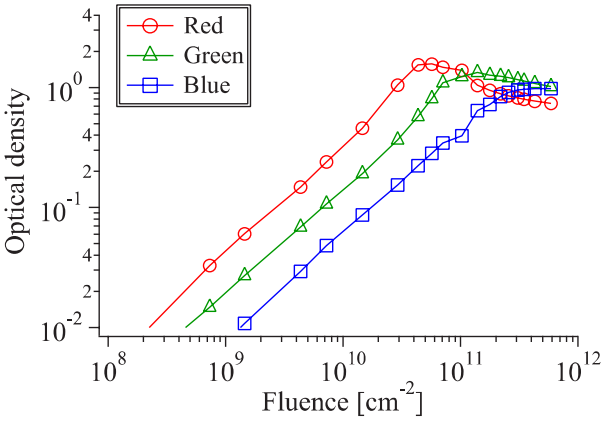

Fig. 3: Optical density of Gafchromic film HD-810 as a function of the 10-MeV H beam fluence. LiDE50 was used for film scanning. The background value (i.e., the optical density of a non-irradiated film) of about 0.04 has been subtracted from each optical density.

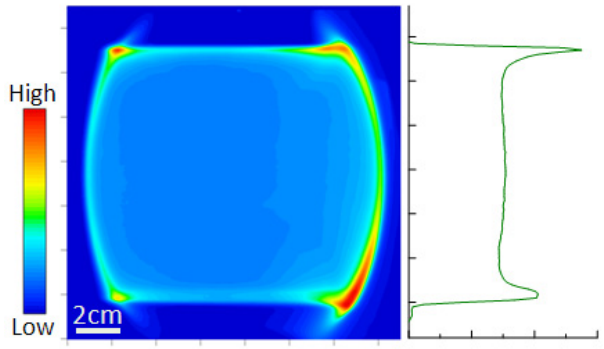

Fig. 4: Relative transverse intensity distribution of an octupole-focused uniform beam measured with a Gafchromic film. The HD-810 film was irradiated with 10-MeV H beam of a few nA for 90 s. The left and right panels show the 2D distribution and the vertical distribution along the beam central axis, respectively.

The fluence response of EBT2 to proton irradiation behaves very differently from Fig. 3. The optical density from the blue color is always high and less sensitive to beam irradiation due to the yellow fundamental color of the film. Only the optical density from the green component is approximately proportional to the fluence in the low fluence range. As expected, the available fluence (from 1×10^{8} to 3×10^{9} cm^{-2}) of EBT2 was lower as compared to HD-810, but the practical range was not as wide as the specification.

Similarly, we have found that, for 520-MeV Ar, the linear-response ranges of HD-810 and EBT2 are $1 \times 10^{7} \sim 2 \times 10^{9}$ cm^{-2} and $1 \times 10^{6} \sim 2 \times 10^{7}$ cm^{-2}, respectively.

3.2 Uniform-beam measurement

The measurement technique above is applied to the evaluation of a large-area uniform beam formed by the nonlinear beam optics. Note that the fluence evaluated from the optical density does not always guarantee the absolute value since it is not easy to control film's external conditions strictly, such as the fluence rate, elapsed time from irradiation to film reading, and environmental temperature and humidity, as well as lot-to-lot variation of the film. However, we have confirmed, by repeated experiments, that the response curve is reproducible within a tolerable level and that there always exists the linear regime of the fluence response as long as the optical density is below unity, as shown in Fig. 3. Employing this feature of the Gafchromic-film response, the relative transverse intensity distribution of the beam can be measured readily without considering various external conditions.

The relative transverse intensity distribution of the large-area uniform beam measured is shown in Fig. 4. The rms uniformity of the distribution is evaluated as 5% in the central region of 9 cm × 9 cm [11]. The uniformity is better in the inner area of the uniform region. Note that the circumferential peak, which is produced due to over-focusing of the Gaussian-like tail and unnecessary for uniform irradiation, can be flattened by removing the

tail of the Gaussian beam at a specific location upstream of the octupole magnet and, thus, the nearly uniform profile can be formed [3].

4. Commissioning of heavy-ion beams

An experimental beam study with a few kinds of heavy ions has been conducted toward realization of a heavy-ion uniform beam. Generating a Gaussian-like beam by multiple Coulomb scattering is the first necessary step also for heavy-ion beams. Therefore, the kinetic-energy loss and the charge-state transformation due to multiple scattering of the heavy-ion beams were investigated in detail since they are pronounced as compared to proton beams and directly related to the beam quality.

Several different kinds of thin foils (Al, Ti Cu and Ta with 1~3 μm thicknesses) were tested for a 520 MeV $^{40}Ar^{14+}$ beam. For each foil, the loss ratio of the kinetic energy was estimated at 1~2% (5~10 MeV), which is much larger than that of the proton beam but is not significant. The charge state of the beam was also changed. It was confirmed, by analyzing with a dipole magnet, that the charge state of a large part of the Ar ions changed to 17. The equilibrium charge state and the charge distribution observed agreed with theoretical prediction [12, 13]. For a 450 MeV $^{129}Xe^{23+}$ beam, by a 3-μm-thick Al foil, the kinetic energy was reduced down to about 400 MeV and the charge state was widely distributed between 30 and 40. Only one charge state of the beam can be transported down to the target through bending magnets. We have confirmed that the heavy-ion beam intensity of the order of 10^8 s^{-1} is still available for irradiation and that a Gaussian-like beam distribution can be obtained on the target, although large reductions of kinetic energy and intensity are unavoidable in multiple scattering of low-energy heavy-ion beams.

5. Summary

We have developed the formation/irradiation system of proton and heavy-ion large-area uniform beams by means of NFM at TIARA as a new tool in the quantum-beam-based technology. The procedure of the uniform beam formation has been almost established. The 2D intensity distribution of the uniform beam can be evaluated handily using Gafchromic films. A uniform beam of 9 cm square with 5% uniformity has been achieved for a 10-MeV proton beam. The proton uniform beam has been already used for the radiation degradation test of space solar cells in collaboration with JAXA [14, 15]. For heavy-ion beams, R&D studies related to the production of functional polymer membranes have been started recently.

References

[1] P. F. Meads, Jr., IEEE Trans. Nucl. Sci. **30** (1983) 2838.
[2] Y. Yuri, N. Miyawaki, T. Kamiya, W. Yokota, K. Arakawa, and M. Fukuda, Phys. Rev. ST Accel. Beams **10** (2007) 104001.
[3] Y. Yuri, T. Ishizaka, T. Yuyama, I. Ishibori, S. Okumura, and K. Yoshida, Nucl. Instrum. Methods Phys. Res. A **642** (2011) 10.
[4] K. Arakawa, Y. Nakamura, W. Yokota, M. Fukuda, T. Nara, T. Agematsu, S. Okumura, I. Ishibori, T. Karasawa, R. Tanaka, A. Shimizu, T. Tachikawa, Y. Hayashi, K. Ishii, and T. Satoh, in Proceedings of the 13th International Conference on Cyclotrons and their Applications, Vancouver, Canada, 1992, p. 119.
[5] Y. Yuri, J. Phys. Soc. Jpn. **79** (2010) 125002.
[6] Y. Yuri, T. Yuyama, T. Ishizaka, I. Ishibori, and S. Okumura, J. Phys. Soc. Jpn. **81** (2012) 064501.
[7] T. Yuyama, Y. Yuri, T. Ishizaka, I. Ishibori, and S. Okumura, in Proceedings of the 1st International Beam Instrumentation Conference, Tsukuba, Japan (2012), in press.
[8] T. Ishizaka, S. Okumura, I. Ishibori, T. Yuyama, and Y. Yuri, JAEA Takasaki Annual Report 2007, JAEA-Review 2008-055, 2008, p. 184.
[9] W. Yokota, M. Fukuda, S. Okumura, K. Arakawa, Y. Nakamura, T. Nara, T. Agematsu, and I. Ishibori, Rev. Sci. Instrum. **68** (1997) 1714.
[10] Y. Yuri, T. Ishizaka, T. Yuyama, I. Ishibori, and S. Okumura, in Proceedings of the 1st International Beam Instrumentation Conference, Tsukuba, Japan (2012), in press.
[11] Y. Yuri, T. Yuyama, T. Ishizaka, I. Ishibori, and S. Okumura, in Proceedings of the 3rd International Particle Accelerator Conference, New Orleans, USA (2012) 1062.
[12] Y. Baudinet-Robinet, Nucl. Instrum. Methods. **190** (1981) 197.
[13] G. Schiwietz and P.L. Grande, Nucl. Instrum. Methods Phys. Res. B **175-177** (2001) 125.
[14] M. Saito, M. Imaizumi, T. Ohshima, and Y. Takeda, in Proceedings of the 35th IEEE Photovoltaic Specialist Conference, Honolulu, USA (2010) 2606.
[15] M. Imaizumi, Y. Yuri, P. R. Bolton, S. Sato, and T. Ohshima, in Proceedings of the 38th IEEE Photovoltaic Specialist Conference, Austin, USA (2012) 2831.

PL/EL IMAGE ANALYSIS OF RADIATION DETERIORATION IN TRIPLE-JUNCTION SOLAR CELLS

Yuki Kobayashi*[1], Mitsuru Imaizumi[1], Shirou Kawakita[1] and Masato Takahashi[1]
1 Japan Aerospace Exploration Agency (JAXA), Japan
*Email: kobayashi.yuki@jaxa.jp

Keyword(s): Triple-junction solar cell, photoluminescence, electroluminescence, radiation degradation

Abstract

We are developing a compact and lightweight automated inspection system of solar panel that can acquire photoluminescence (PL) and electroluminescence (EL) images of InGaP/GaAs/Ge triple-junction solar cells simultaneously (PL and EL images acquisition system; PEAS). We would like to contribute to reduce the burden for visual checking inspections of solar cells on solar panel and improve inspection accuracy by applying PL/EL observation to solar panels. For that purpose we consider that building knowledge-based PL/EL images is necessary. Currently, we are studying the interrelation between environmental test effects and PL/EL images. In this paper, we evaluate correlation between radiation degradation of triple-junction solar cells and change in PL/EL images.

1. Introduction

To enable anyone to check the mechanical defects and electro-current constriction spots of solar cells or solar panels easily and quickly through observation of Photoluminescence (PL) and electroluminescence (EL) images, we are developing an automated inspection system for solar panels, which simultaneously takes PL and EL images of triple-junction solar cells on a panel.

PL and EL observations are highly sensitive methods for examining impurities, a variety of imperfections such as crystal defects and mechanical cracks within materials, and are extremely effective methods for assessing solar cell imperfections. Two-dimensional PL and EL image observation allows us direct visual evaluation with the naked eye. Although the EL method requires an external power source to supply current, it has the advantage of being able to quickly detect solar cell output power failures, which is shunting, since such a shunting spot is detected as a bright point caused by currents concentrating there. On the other hand, the PL method is advantageous in that evaluations can be conducted in a completely noncontact manner; therefore, it can be applied when we cannot apply electric bias or current to a subject solar cell.

The imperfections in PL and EL images on solar cells can be grouped into two cases substantially: One is native defects originated from epitaxial growth such as crystal defects in the layers, and the other is mechanical defects caused by extrinsic factors such as mechanical stress during coverglass/interconnector/cell (CIC) assembly, lay-down processes, or environmental tests. PL and EL images exhibit a variety of contrast patterns in a solar cell regardless of whether the origin of the pattern influences solar cell output. Thus, it is necessary for us to determine whether the observed imperfections on PL/EL images of solar cells or solar paddles will eventually cause electrical power loss. The imaging of PL and EL can show, in a simple and visual manner, the patterns reflecting various properties of solar cells, regardless of whether or not the source of the observed luminescence pattern has influence on the output power of solar cells. Therefore, it is necessary for us to figure out what the image observed is to be ascribed to and whether or not that is the image to be called into account in evaluating the panels of the solar cells. For that reason, we think it is needed to construct a knowledge base about the luminescence patterns of PL and EL. Currently we are conducting, in preparation for the construction of the knowledge base, the examination on the changes in the luminescence patterns before and after the environmental load test.

In the following proceedings we explain the automated evaluation device for PL and EL and report on the radiation impact of the solar cell panels, which have a characteristic leak path.

2. PL and EL Image Acquisition System (PEAS)

We are currently developing an automated inspection system using PL and EL images for solar panels composed of InGaP/GaAs/Ge triple-junction cells. Fig. 1 depicts a schematic of an acquiring unit of the PL and EL images acquisition system (PEAS). The PEAS can simultaneously acquire PL and/or EL image in a scan. The image acquiring unit of PEAS consists of two charge-coupled device (CCD) cameras equipped with band-pass filters suitable for observing luminescence from InGaP and GaAs subcells in a triple-junction solar cell, and a pair of light-emitting diode (LED) units as excitation light sources for the PL; a unit consists of two types of LEDs, namely, one for excitation of InGaP subcells, the other for GaAs subcells. Two LED units are mounted with certain angle against the solar panel to achieve the uniformity of light intensity. The LEDs were selected for

excitation as they have peak wavelengths (λ_D) and half width suited for the EQE of each subcell. Band-pass filters are also selected in the same way as they have transparent wavelength bands suited for each LED and PL from each subcell.

A simplified schematic of the system is shown in Fig. 2. The system consists of an image acquiring XY-stage including an acquiring unit on the Z-stage, an XYZ-stage control unit, and a mobile personal computer (PC). A solar panel is set on the fixture flame. The PC allows us to control the XYZ-stage and the two CCD cameras to obtain the EL and PL image on the solar panel. Communications to those devices are made by original software written in the LabVIEW program (National Instruments, Inc.). The system can obtain three images of a triple-junction cell in a scan. The four images are EL images of InGaP top and GaAs middle subcells, and PL images of either subcell.

Shown in Fig.3 is a picture of a X- and Y-axis extendable PEAS (XY-PEAS). XY-PEAS is suitable for a diagnosis of larger solar panels. XY-PEAS consist of the main-PEAS, extendable Y-axis unit and X-axis rail unit. Each unit can be separated. And the each units can be detached easily for transport and reconstructed easily. The maximum scan length along the Y-axis is extended to 1.8 m. The minimum footprint is around 1.2 m × 1 m, including the rail unit. The rail unit can be extended every 1.2 m. This makes it possible to expand the observation area to accommodate any size of solar panel. The control unit of XY-PEAS was improved from three axes (X-, Y- and Z-axis) to five axes (with the addition of the extended X- and Y-axis). XY-PEAS can be driven automatically along the five axes via the PC.

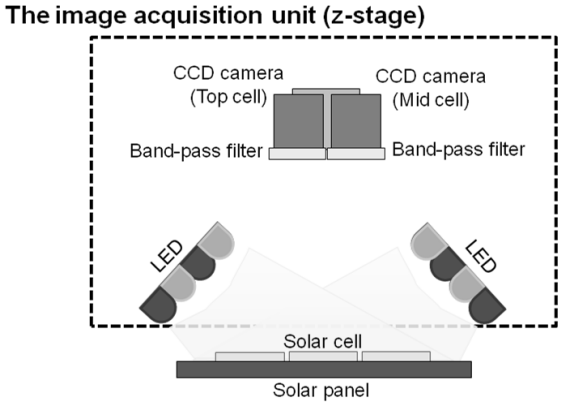

Figure 1. Schematic of the acquiring unit of the PL and EL image acquiring unit

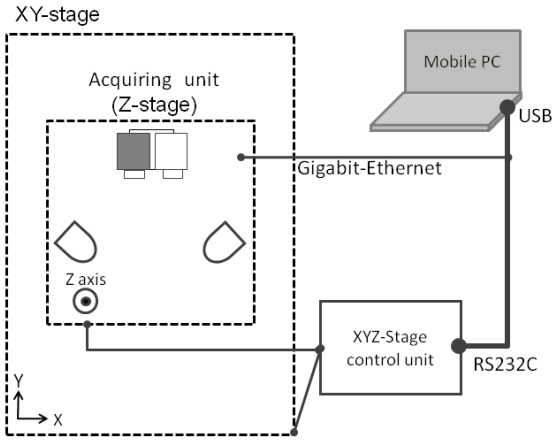

Figure 2. Simplified schematic of the PL and EL image acquiring system (main-PEAS)

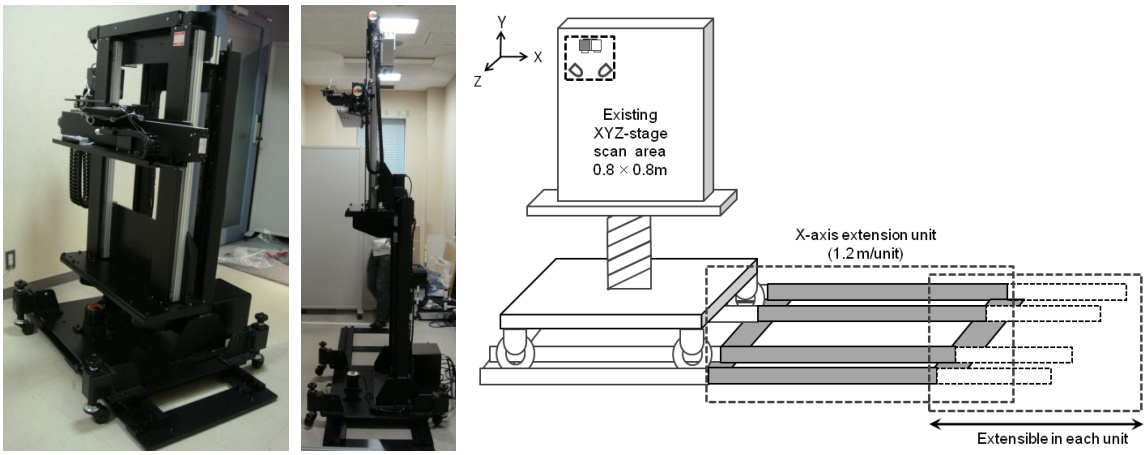

Figure 3. Schematic of X- and Y-axis extendable PEAS (XY-PEAS)

3. Various PL and EL Evaluations for Knowledge-base constraution

3.1 Experiment

We have used the InGaP/GaAs/Ge triple-junction solar cells with cover glass 4 × 8cm as samples. PL / EL images were evaluated. The 1MeV electron beam irradiation test was carried out regarding 3J cells (#1) that do not have a special light emission pattern both on the top and mid layer and 3J cells (# 2) that have dark spots on the top layer. The dose ammount was 1×10^{13} and 1×10^{15} e^-/cm^2. PL / EL imaging evaluation was conducted before the electron beam irradiation and after the irradiation at each dose. In addition, we have evaluated the light IV characteristics and spectral sensitivity characteristics before the irradiation and after the irradiation at 1×10^{15} e^-/cm^2.

3.2 Result& discussion

Table 1 shows PL/EL image of before and after electron beam irradiation(1 MeV electron,$1x10^{13}e^-/cm^2$) of sample #1 and #2. Table1 indicates that the cell of #2 has a typical dark spot in the top layer and the image of PL/EL in the middle layer shows a tiny dark spot and two small bright ones make a large dark spot. (Recognized as a singular and specific spot.) While the cell of #1 that does not posses a large dark spot decreases the overall emission intensity, not a substantial change of relative distribution has been found. On the other hand, #2 cell that has a typical dark spot in the top layer does not show a big relative change of emission distribution but in the middle layer a substantial change of emission intensity and a relative change of emission distribution with the singular and specific spot have been noticed.

Table 1 Acquired PL and EL images of top and middle subcells of before and after the irradiation.

	#1		#2	
	BOL	1MeV, 1×10^{13} e/cm²	BOL	1MeV, 1×10^{13} e/cm²
PL image of InGaP		Exposure time: 1.3*BOL		Exposure time: BOL
EL image of InGaP (I=1/2Isc)		Exposure time:1.2*BOL		Exposure time:1.3*BOL
PL image of GaAs		Exposure time:5.2*BOL		Exposure time:5*BOL
EL image of GaAs (I=1/2Isc)		Exposure time:8.6*BOL		Exposure time:3*BOL

Fig. 4 shows The light IV characteristics of #1 and #2 before and after the irradiation of 1MeV electron beams (1 x10^{15} e^-/cm^2). Comparison of the beginning of life (BOL) characteristics in Fig. 4 indicates that while both the short circuit current (I_{sc}) and open circuit voltage (V_{oc}) decreased, the presence of dark spots in the cells did not lead to any significant performance deterioration.

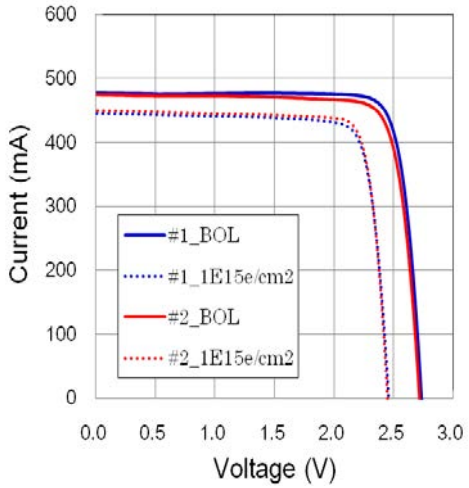

Fig.4 The light IV characteristics of #1 and #2 cells before and after the irradiation. The fluence is 1×10^{15} e^-/cm^2.

Table 2 Performance parameters of #1 and #2 cells before and after the irradiation.

	Case	Isc(mA)	Remaining factor of Isc	Voc(V)	Remaining factor of Voc	FF(%)
#1	BOL	478	-	2.74	-	84.01
	EOL 1MeV,1 x10^{15} e/cm^2	446	0.934	2.46	0.898	82.47
#2	BOL	468	-	2.72	-	82.26
	1MeV, 1 x10^{15} e/cm^2	449	0.959	2.45	0.904	83.72

4. SUMMARY

When 1 MeV electron beams with irradiation energy of 1 x10^{13} and 1 x10^{13} e^-/cm^2 were irradiated on 3J cells (CIC), the electron beam irradiation caused changes in PL/EL emission intensity in the mid cell of a 3J cell having dark spots with a particular characteristic. Examinations of electrical properties and spectral responses suggested no significant performance deterioration regardless of whether the cells had dark spots due to the irradiation of 1 MeV electron beam.

Since results in this research is based on a small number of observations, we plan to repeat the experiments in future. Further, we plan to conduct investigations on the effects of defects other than dark spots.

Acknowledgments

We would like to thank to Dr. Kazunori Shimazaki of JAXA, Mr. Jiro Harada and Mr. Yoichi Hagiwara of Advanced Engineering Services Co., Ltd,

Session E

Single Event Effects

Single-Event Effects in Microelectronics Induced by Through-Wafer Sub-Bandgap Two-Photon Absorption

Dale McMorrow[1], Stephen Buchner[1], and Jonathan Pellish[2]
Email: dale.mcmorrow@nrl.navy.mil
[1]Naval Research Laboratory, Code 6816, Washington, DC 20375
[2]NASA Goddard Space Flight Center, Greenbelt MD 20771

Keywords: space radiation, laser SEE, single-event upset, single-event effects, two-photon absorption, heavy ions

Abstract

Carrier generation based on nonlinear absorption in semiconductors has become an important tool for the investigation of single-event effects in modern microelectronic devices. Recent advances and the present status of two-photon absorption induced single-event effects interrogations are described.

1. Introduction

Electronic systems operating in space are exposed to radiation in the form of energetic charged particles, such as protons and heavy ions. When a single charged particle passes through the semiconductors and insulators that make up an integrated circuit (IC), it liberates electrons from the constituent atoms. These carriers can disturb the normal operation of the IC, causing a variety of different and potentially harmful effects that are referred to as single-event effects (SEEs). SEEs are of great concern because they may lead to a loss of information, functional interruptions, physical failures or, in the worst case, to a total loss of control of the spacecraft. In space, heavy ions responsible for SEEs originate from solar flares and cosmic rays, or from proton-induced reactions in low earth orbit. In addition, ions resulting from the interaction of atmospheric neutrons with the silicon and boron atoms in electronic circuits themselves have become a threat for modern advanced technologies, even at ground level.

Over the past two decades, picosecond pulsed lasers operating in the visible and near-infrared regions of the spectrum have become essential tools for evaluating the SEE susceptibility of microelectronic devices by injecting carriers at well-defined locations, permitting detailed studies of single-event effects that are not possible with other ionization sources. Such approaches, however, are based on Beer's Law absorption, and are severely limited by the multiple metallization layers that are characteristic of modern semiconductor technologies.

To alleviate this problem, and permit carrier injection through the wafer from the back-side of the device, a new method of carrier generation based on two-photon absorption (TPA) has been developed and demonstrated [1-3]. This method is based on nonlinear absorption at sub-bandgap optical wavelengths using high peak-power femtosecond laser pulses. For two-photon absorption processes to dominate carrier production, the laser wavelength is chosen to be less than the bandgap of the semiconductor material. Under this condition no carriers are generated at low light intensities. At sufficiently high irradiances the material can absorb two (or more) photons simultaneously, to generate a single electron-hole pair. Because carrier generation in the two-photon process is proportional to the square of the laser pulse intensity, significant carrier generation occurs only in the high-intensity focal region of the focused laser pulse. This enables charge injection at any depth in the structure, permits three-dimensional mapping of the SEE sensitivity of a device, and backside illumination of circuits fabricated on silicon wafers. The two-photon method represents a novel approach to SEE evaluation that provides insights that are not accessible with other techniques, and places a renewed emphasis on obtaining a detailed understanding of semiconductor nonlinear-optical properties that can exert a significant influence on the propagation and absorption of ultrashort laser pulses. Over the past few years the through-wafer TPA SEE approach has become the method of choice for evaluating single-event effects in state-of-the-art micro- and nano-electronic circuits.

This paper presents experimental results illustrating the utility of the through-wafer TPA approach for basic mechanisms studies. We focus here on the charge-collection transients induced in a silicon-germanium heterojunction bipolar transistor (SiGe HBT).

2. Results and Discussion

2.1 Experimental

The single-event upset and single-event transient experiments at wavelengths below the silicon bandgap were performed using an amplified titanium sapphire laser system (Clark-MXR CPA 1000) that pumps a tunable optical parametric amplifier and produces nominally 120 fs optical pulses at 1.26 μm with about 100 μJ of energy per pulse. The strong IR beam is attenuated by a waveplate-polarizer combination to precisely control the pulse energy incident on the device under test (DUT). The pulse energy is monitored with a calibrated large area InGaAs photodiode. The DUT is mounted on a motorized x-y-z translation platform with 0.1 μm resolution, and the optical pulses are focused through the wafer onto the front surface of the DUT with a 100 microscope objective, resulting a near-Gaussian beam profile with a diameter of 1.4 μm at focus [1]. Because the carrier deposition varies as I^2, this corresponds to a carrier density distribution with a 1.0 μm diameter (full-width-at-half-maximum). All experiments are performed at room temperature (295 K). The DUT is imaged through the wafer using near-infrared (NIR) imaging optics in conjunction with an InGaAs focal plane array.

2.2 Results

When two-photon absorption is the primary means of carrier generation, the optical loss and penetration depth can be deterministically manipulated: because carrier generation is proportional to the square of the laser pulse irradiance, the generated carriers are highly concentrated in the high-irradiance region near the focus of the beam, as is illustrated in Fig. 1 [1],[4-5]. For a material that is transparent to the incident radiation, the high irradiance region can be directed to any depth in the material by translation of the device under test (DUT) with respect to the focusing element. This characteristic permits three-dimensional mapping of single-event effects, and backside, through-wafer irradiation of devices. The ability to interrogate SEE phenomena through the wafer using backside irradiation was a primary motivating factor for development of the TPA SEE technique. Backside irradiation eliminates interference from the metallization layers, and circumvents many of the issues associated with testing flip-chip mounted parts. A photograph of a flip-chip mounted device illustrating the back-side wafer access and a schematic diagram illustrating the through-wafer, backside TPA approach is shown in Fig. 1.

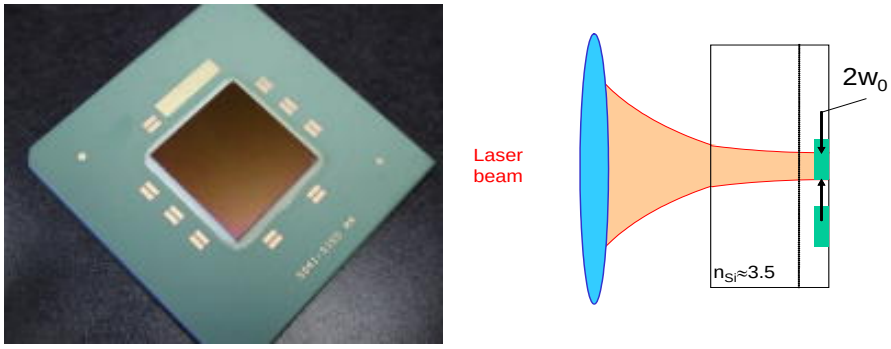

Figure 1. Photograph of a flip-chip packaged silicon device and schematic diagram illustrating the through-wafer two-photon absorption approach.

A wide variety of device types have been evaluated using the through-wafer TPA approach. This summary describes transient charge-collection measurements performed on silicon-germanium heterojunction bipolar transistors (SiGe HBTs). Considerable effort and resources have been expended to investigate the viability of SiGe HBTs for space applications because they provide full integration with commercial silicon CMOS, they enable system-on-a-chip (SoC) applications, they have speed and switching characteristics similar to III-V technologies, and they offer high levels of inherent total ionizing dose tolerance. However, despite these encouraging characteristics, circuits designed with SiGe HBTs can suffer from unacceptably high levels of single-event upsets (SEUs), manifested in high-speed serial data applications as burst errors that present an extreme SEU hazard for applications operating at Gbit/s data rates where the bit period is greater than 1 ns. Direct measurements of the ionization-induced current transients are necessary to calibrate TCAD tools for model development and evaluation of the basic mechanisms of carrier transport and collection in HBT structures, leading to a better understanding of circuit- and system-level SEE effects.

The experimental results presented here were obtained from a SiGe HBT test structure from the IBM 5AM BiCMOS process technology, which has a single emitter stripe with dimensions of 0.5 μm by 2.5 μm. The deep trench isolation surrounding the active device has outer dimensions of 6.2 μm by 6.4 μm and inner dimensions of 4.1 μm by 4.3 μm. The depth of the deep trench isolation is between 7 and 8 μm. The n+/p−

subcollector-substrate junction resides in the area enclosed by the deep trench isolation. Figure 2 shows a cross section of an IBM SiGe HBT device, illustrating the device structure as is largely defined by the deep-trench isolation. Figure 3 shows representative base and collector transients measured for two different bias conditions. The data of fig. 3 illustrate the general characteristics of the ionization-induced transients for this technology. Single-transistor data of this type are used to calibrate and validate TCAD models, which then can be used for predictive purposes in complex circuits and systems.

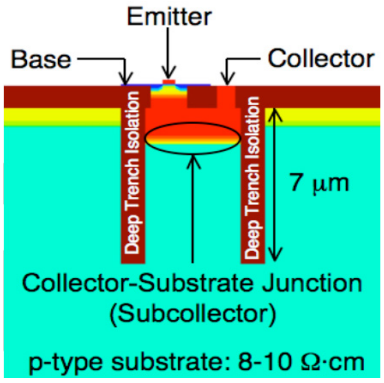

Figure 2. TCAD cross section of an IBM 5AM SiGe HBT. The three process features relevant to transient production and charge collection are the deep trench isolation, the subcollector-substrate junction, and the lightly doped p-type substrate.

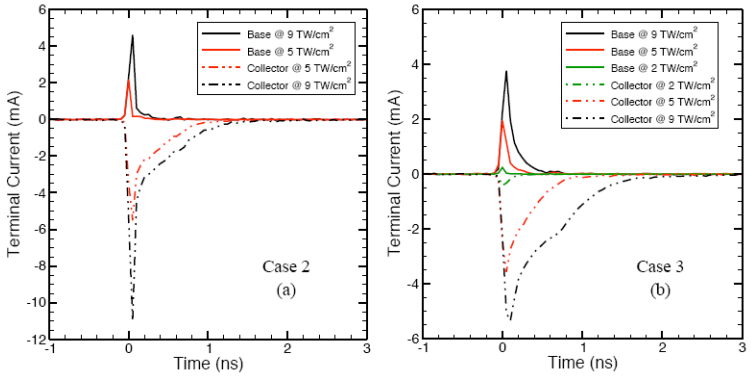

Figure 3. Base and collector current transients for (a) Case 2 (V_C = 3 V) and (b) Case 3 (V_{Sub} = -3 V). In all cases the beam focal point was at the device surface and focused to a diameter of 1.6 μm. Note the different y-axes on each of the charts. In each case, the base transients are largely unaffected. The Case 2 collector transients are up to 2x larger than their Case 3 counterparts.

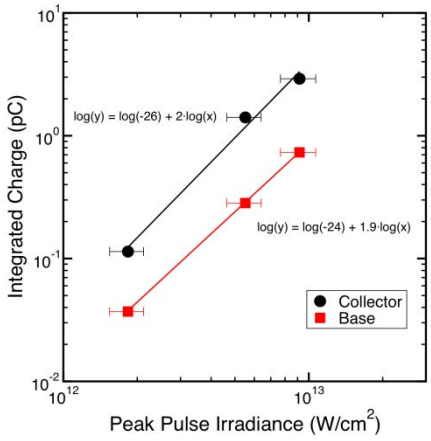

Figure. 4. Plot of integrated charge vs. the peak pulse irradiance measured for a bias of -4 V on the substrate with all other terminals grounded. These data serve to verify the quadratic character of the observable, and the two-photon absorption origin of the carrier generation.

Figure 4 shows a plot of integrated charge vs. the peak pulse irradiance measured for a bias of -4 V on the substrate, with all other terminals grounded, verifying the quadratic character of the observable, and the TPA origin of the carrier generation. Figure 5 shows a series of two-dimensional maps of the TPA-induced current transient amplitude for through-wafer irradiation. The data of fig. 5 illustrate that the primary charge-collection region is localized within the confines of the deep trench isolation. The measurements shown in figs. 3-5 are for charge localization near the surface of the device. Measurements also have been performed as a function of the depth (z) below the surface, illustrating the significant effects of long-range diffusion and potential collapse in these devices.

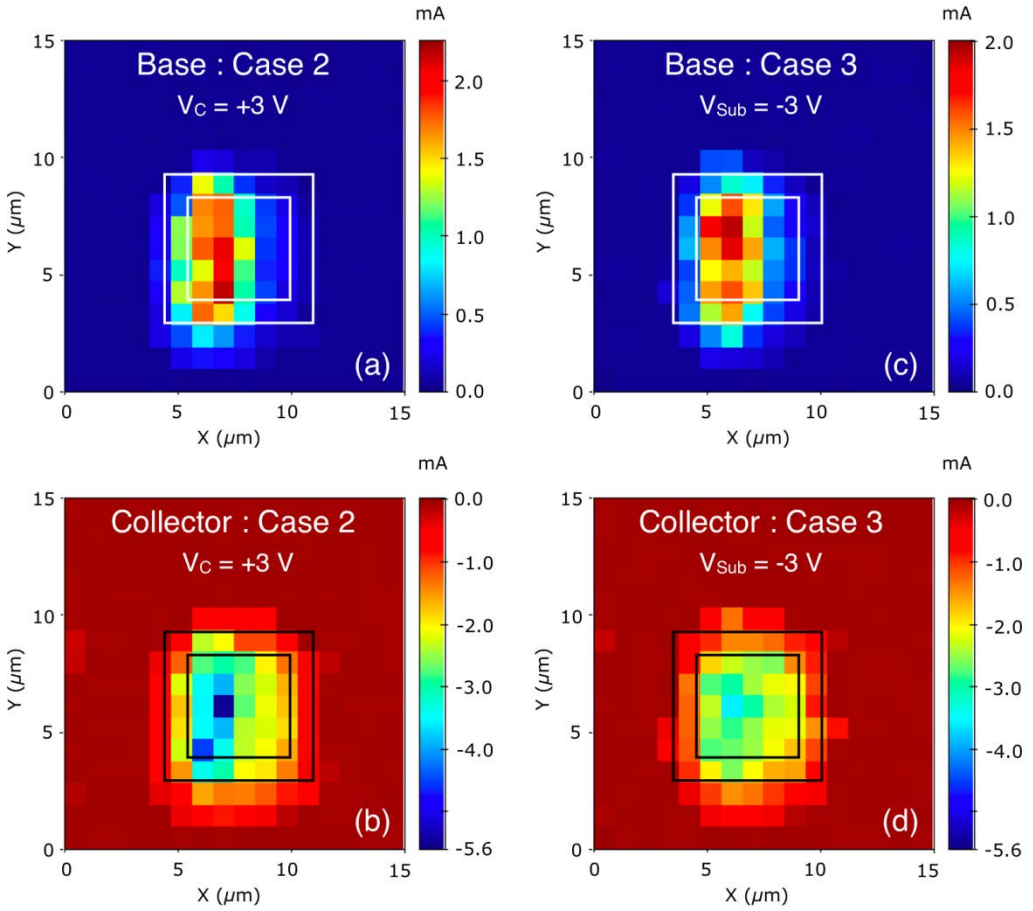

Figure 3. X-Y charge-collection maps show the maximum current-transient magnitude for carrier generation by TPA for an IBM 5AM SiGe HBT for bias conditions indicated. The laser was focused at the device surface to a diameter of approximately 1.6 μm; with the position incremented in 1 μm steps for all cases. The geometry of the deep trench isolation is overlaid on all four images for reference.

3. Conclusions

This report describes the fundamental aspects of the through-wafer TPA SEE approach for single-event effects studies, with application to measurement of the charge-collection transients for a SiGe HBT device. The results illustrate the utility of the TPA SEE approach for basic mechanisms investigations. Additional details of the SiGe study can be found in [6].

References

†The authors acknowledge support of the Defense Threat Reduction Agency (DTRA).

[1] D. McMorrow, W. T. Lotshaw, J. S. Melinger, S. Buchner, and R. L. Pease, "Sub-bandgap laser-induced single event effects: Carrier generation via two-photon absorption," *IEEE Trans. Nucl. Sci.*, vol. 49, no. 6, 3002–3008 (2002).

[2] D. McMorrow, W. T. Lotshaw, J. S. Melinger, S. Buchner, Y. Boulghassoul, L. W. Massengill, and R. Pease, "Three dimensional mapping of single-event effects using two-photon absorption," *IEEE Trans. Nucl. Sci.*, vol. 50, no. 6, 2199–2207 (2003).

[3] D. McMorrow, S. Buchner, W. T. Lotshaw, J. S. Melinger, M. Maher, and M. W. Savage, "Demonstration of through-wafer, two-photon-induced single-event effects," *IEEE Trans. Nucl. Sci.*, vol. 501, no. 6, 3553–3557, (2004).
[4] M. Goppert-Mayer, "Ueber elementarakte mit zwei quantenspruengen," *Ann. Phys.*, vol. 9, 273–294 (1931).
[5] E. W. Van Stryland and M. Sheik-Bahae, "Z-scan" in *Characterization Techniques and Tabulations for Organic Nonlinear Optical Materials* (Marcel Dekker, 1998), Chap. 8
[6] J.A. Pellish, R.A. Reed, D. McMorrow, J.S. Melinger, P. Jenkins, A.K. Sutton, R.M. Diestelhorst, S.D. Phillips, J.D. Cressler, V. Pouget, N.D. Pate, J.A. Kozub, M.H. Mendenhall, R.A. Weller, R.D. Schrimpf, P.W, Marshall, A.D. Tipton, A.D. and G. Niu, "Laser-Induced Current Transients in Silicon-Germanium HBTs", IEEE Trans. Nuc. Sci., 55, 2936-2942, (2008).

Dual-PLL based on Temporal Redundancy for Radiation-Hardening

SinNyoung KIM*1, Akira TSUCHIYA[1], and Hidetoshi ONODERA[1, 2]
1 Graduate School of Informatics, Kyoto University, Japan
2 JST, CREST
*Email: snkim@vlsi.kuee.kyoto-u.ac.jp
Keyword(s): Phase-locked loop (PLL), RHBD, DMR, Temporal redundancy

Abstract

This paper proposes a dual-PLL based on temporal redundancy for radiation-hardening. A common practice technique for radiation-hardening is the triple modular redundancy (TMR). However, it is inefficient to apply for PLLs because PLLs include huge size of capacitance and static current consumers, means analog circuits. Thus, we propose a dual-PLL and a detective circuit that detects a perturbed PLL by radiation-strike. Although our proposal is based on DMR, it allows both detecting and correcting the clock-perturbation. The detective circuit based on temporal redundancy switches a clock-path from one perturbed PLL to the other PLL. In radiation-simulation, 88.4% of cycle-to-cycle jitter is suppressed.

1. Introduction

Phase-locked loops (PLLs) in digital circuits are source of the clock signal. Perturbation on PLLs is a crucial because change or lack of clock signal leads whole system malfunction. Single-event (SE) is considered as one of the causes of PLL malfunctioning. Thus, importance of radiation-hardened PLL is increasing.

Fig. 1 shows block diagram and microphotograph of unhardened PLL. The unhardened PLL consists of both digital sub-circuits such as the divider and phase frequency detector (PFD) and analog sub-circuits such as the charge-pump (CP), loop filter (LF) and voltage controlled oscillator (VCO). The CP and VCO are static current consumers and the capacitors in LF consume large silicon area as shown in the microphotograph. Therefore, the triple modular redundancy (TMR) is inefficient for PLLs because PLLs includes the huge size of capacitance and static current consumers, means analog circuits.

To mitigate penalties of the TMR in power and silicon area consumption, some studies applied TMR for the VCO and digital sub-circuits [1], [2]. Even though this strategy improves radiation-hardening in PLLs, other analog sub-circuits that cannot apply the TMR are out of protection. For the unprotected analog sub-circuits, circuit-design has to be changed in order to harden radiation-strike. One example is that the current-mode CP is replaced by the voltage-mode CP [3]. Nevertheless, changing circuit-design leads to degradation in performance of PLLs such as the jitter. Consequently, designers must optimize trade-off between these penalties and radiation-hardening.

This paper proposes a dual-PLL based on temporal redundancy for radiation-hardening. The proposed radiation-hardened PLL (RHPLL) utilizes dual modular redundancy (DMR) with a detective circuit. Although the proposed RHPLL is DMR, the detective circuit enables not only detecting but also correcting clock-perturbation. The detective circuit based on temporal redundancy switches a clock-path, which goes to digital circuits, from one perturbed PLL to the other PLL. Since the RHPLL is based on the DMR technique, the power and silicon area is smaller than TMR. Furthermore, all sub-circuits are in protection without degradation of performance. For the simulation of radiation-strike, the proposed RHPLL designed by TSMC 0.18um achieves 88.4% of cycle-to-cycle jitter improvement, which is from 1588ps to 184ps, in 2.5ns normal clock period.

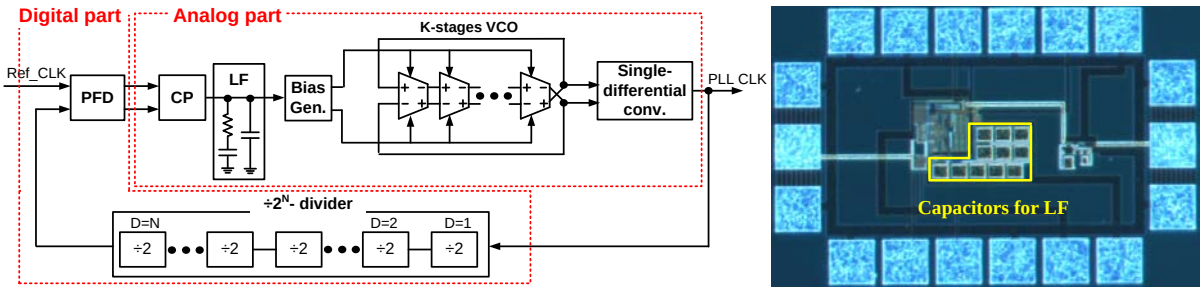

Fig. 9. Block diagram and microphotograph of an unhardened PLL.

2. Proposed Radiation-Hardened PLL

2.1 Basic concept: dual-PLL and detective circuit

The proposed RHPLL consists of dual-PLL and one detective circuit. If one of two PLLs has clock-perturbation by radiation-strike, the detective circuit detects the PLL that has clock-perturbation. Then, it switches the clock-path from the detected PLL to the other PLL. The clock that goes to digital systems is called 'final clock' in this work. Fig. 2 shows the basic concept of the dual-PLL and detective circuit.

Unlike TMR, use of DMR has an issue that distinguishes between perturbed clock and non-perturbed clock. In case of TMR, it is easy to distinguish non-perturbed clock because identical two of three clocks is definitely the non-perturbed clock. In contrast, DMR can only recognize that clock-perturbation occurs but cannot distinguish which PLL has clock-perturbation. To overcome this issue in DMR, we utilize temporal redundancy for the detective circuit.

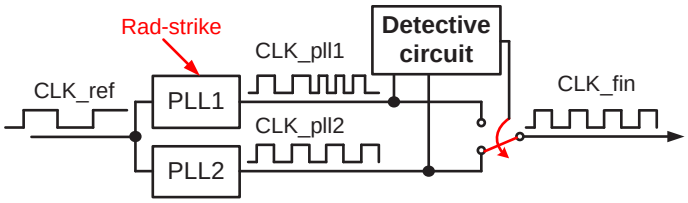

Fig. 10. Basic concept of the dual-PLL and detective circuit.

2.2 Detective circuit based on temporal redundancy

The key idea to distinguish perturbed and non-perturbed clocks is comparison of clocks between before and after radiation-strike at each PLL output. The constant periods of PLL clocks are changed after radiation-strike as shown in Fig. 3 (a). Hence, if the clock before radiation-strike (past clock) and the clock after radiation-strike (present clock) are different in a PLL, it means the PLL has clock-perturbation. On the other hand, if the past and present clocks are identical, the PLL is in normal operation. To generate the past clocks, delay-lines that generate one-period delayed clocks are used in this work. The past and present clocks are compared by an XOR-gate in order to check whether they are identical or not as shown in Fig. 3 (b). Due to this detective circuit based on temporal redundancy, the proposed RHPLL enables to both detect and correct clock-perturbation unlike the conventional DMR technique.

Fig. 4 shows waveforms when radiation-strike occurs on one side of PLL. While the past clock emits clock-perturbation after one period of radiation-strike, the present clock emits the clock-perturbation as soon as radiation-strike occurs. The difference between the past and present clocks produces a perturbation-detecting signal at the output of XOR-gate. Based on the perturbation-detecting signal, the detective circuit selects one the final clock.

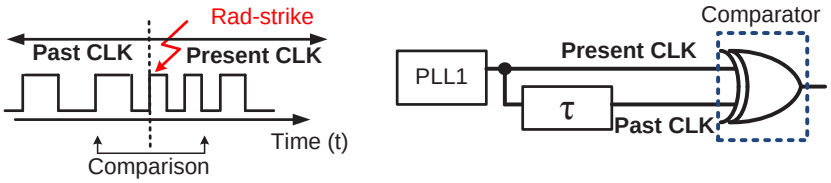

(a) (b)

Fig. 11. (a) The key idea to distinguish perturbed and non-perturbed clocks (b) detective circuit based on temporal redundancy

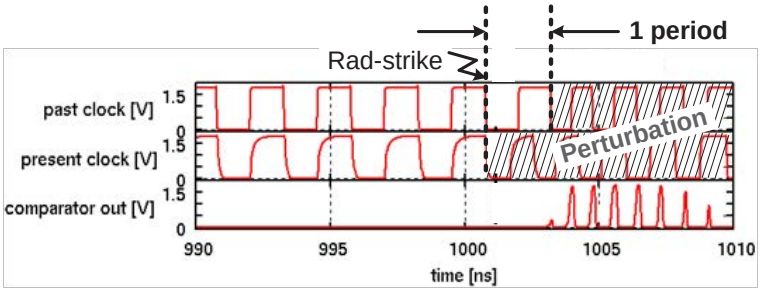

Fig. 12. Production of perturbation-detecting signal at the output of XOR-gate

2.3 Implementation

The delay-line for the detective circuit should be carefully implemented to ensure exact 'one period' clock delay because deviation of phase leads to a perturbation-detecting signal even without radiation-strike. To implement perfect one period delay, unit-cells for the delay-lines are identical with those used for VCOs. The unit-cells need two bias voltages for NMOS tail current sources (Vbn) and PMOS active-load (Vbp) as shown in Fig. 5 (a). There are two requirements for these bias voltages in the detective circuit design. Firstly, in non-perturbation, the bias voltages for the delay-line must be identical with those for VCOs in order to ensure 'one period' clock delay. Secondly, in perturbation, the delay-lines must have different bias voltages from perturbed bias voltages of VCOs. If the bias voltages for delay-lines are identical with the perturbed bias voltages of VCOs, the detective circuit cannot detect perturbation as shown in Fig. 5 (b).

As the solution of the requirements, the bias voltages for the delay-lines are generated by taking average of two VCO bias voltages with a pair of resistors as shown in Fig. 6. In non-perturbation, the bias voltages for the delay-lines (Vbn_d, Vbp_d) are identical with those of VCOs because the two VCO bias voltages are identical. However, if one VCO bias voltage is changed by radiation-strike, Vbn_d and Vbp_d have averaged value between the changed and normal VCO bias voltages. Thus, this solution satisfies those two requirements.

Fig. 7 shows the full structure of the proposed RHPLL. Each perturbation-detecting signal goes out from the XOR-gates and then is driven as inputs of SR-latch. The SR-latch generates control signal for switching of MUX. If PLL1 has clock-perturbation, the final clock becomes PLL2's clock through switching of the SR-latch. During non-perturbation in both PLLs, the SR-latch keep previous control signal.

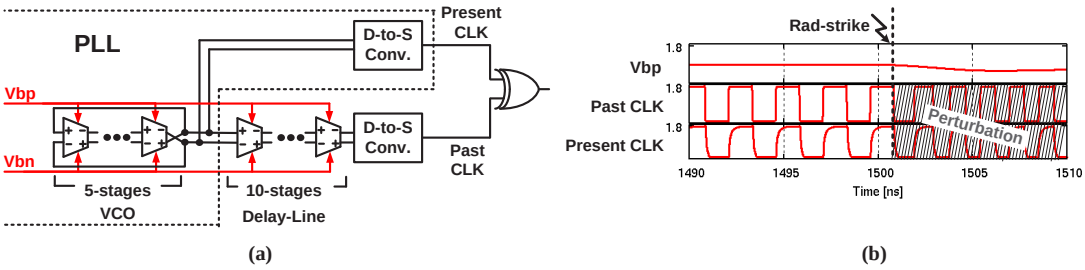

Fig. 13. Bias voltages issue in implementation of the delay-lines.

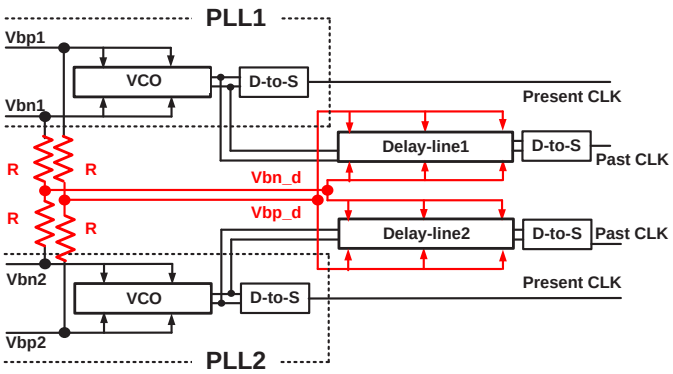

Fig. 14. Solution of the bias voltage issue using a pair of resistors.

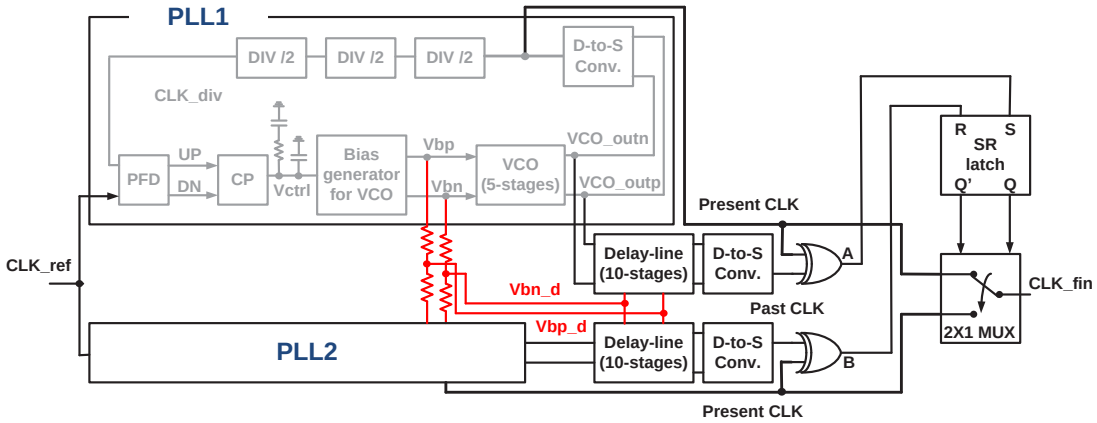

Fig. 15. Full structure of the proposed RHPLL.

3. Simulation Results

Fig. 8 shows the PLL output clock of an unhardened PLL and the final output of the proposed RHPLL after radiation-strike and their eye-diagrams. For the simulation of radiation-strike, the proposed RHPLL designed in TSMC 0.18um achieves 88.4% of cycle-to-cycle jitter improvement, which is from 1588ps to 184ps, in 2.5ns normal clock period. Compared to conventional technique' recovery time [2], this RHPLL reduce the time to recover clock periods from 35 clock cycles to 3 clock cycles. Although the recovery time depends on energy of radiation or circuit condition, the time for detection in our case is consistently 3 clock cycles.

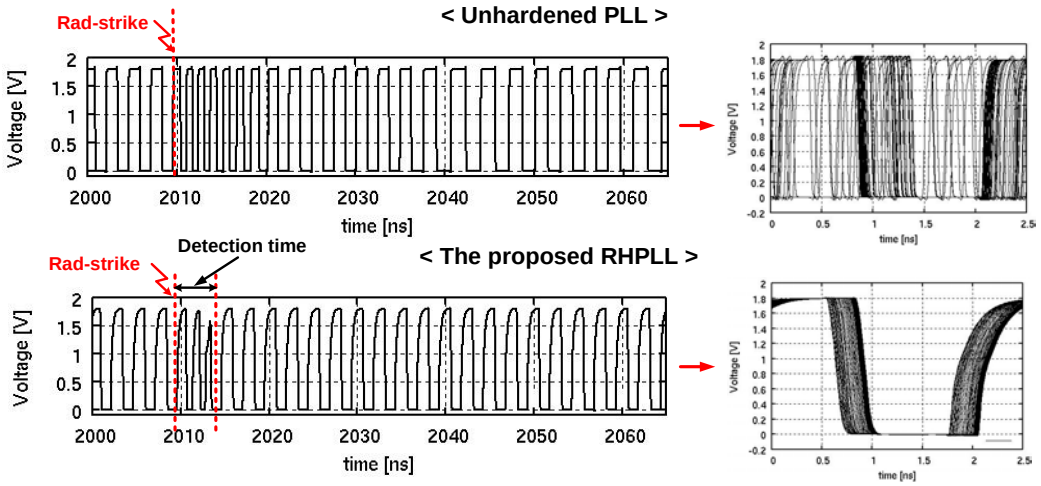

Fig. 16. Comparison of PLL output clocks and eye-diagrams between an unhardened PLL and the proposed RHPLL after radiation-strike.

4. Conclusion

A dual-PLL based on temporal redundancy for radiation-hardening is proposed in this paper. To achieve not only detection but also correction of perturbation in DMR technique, the detective circuit based on temporal redundancy is designed. This proposal has three advantages. First, it consumes less power and silicon area than the TMR technique due to use of the DMR technique. Second, all sub-circuits are protected by the DMR technique. Third, the penalties in performance are mitigated because there is no design modification of sub-circuits. As a simulation result of 400MHz PLL output clock, 1588ps of cycle-to-cycle jitter in unhardened PLL is reduced to 184ps in the proposed RHPLL.

References

[1] T.D. Loveless, et al., "A Probabilistic Analysis Technique Applied to a Radiation-Hardened-by-Design Voltage-Controlled Oscillator for Mixed-Signal Phase-Locked Loops," IEEE Trans. Nucl. Sci., vol. 55, No. 6, pp. 3447-3455(2008).
[2] D. Matsuura, et al., "Radiation-Hardened Phase-Locked Loop Fabricated in 200nm SOI-CMOS," in proc. IEEE European Conf. on Radiation and Its Effects on Components and Systems (RADECS), pp.150-155(2011).
[3] T.D. Loveless, et al., "A Hardened-by-Design Technique for RF Digital Phase-Locked Loops," IEEE Trans. Nucl. Sci., vol. 53, No. 6, pp. 3432-3438(2006).

Relationship between soft error rate in SOI-SRAM and amount of generated charge by high energy ion probes

Masatoshi Hazama*[1], Satoshi Abo[1], Naoyuki Masuda[1], Fujio Wakaya[1], Shinobu Onoda[2], Takahiro Makino[2], Toshio Hirao[2], Takeshi Ohshima[2], Toshiaki Iwamatsu[3], Hidekazu Oda[3], Mikio Takai[1]

1 Center for Quantum Science and Technology under Extreme Conditions, Osaka University, Japan

2 Japan Atomic Energy Agency (JAEA), Japan

3 Renesas Electronics Corporation, Japan

*Email: hazama@nano.cqst.osaka-u.ac.jp

Keywords: silicon-on-insulator (SOI), soft error, floating body effect, body-tie structure, nuclear microprobe

Abstract

Soft error rates (SERs) in partially depleted (PD) silicon-on-insulator (SOI) static random access memories (SRAMs) with a technology node of 90 nm have been investigated by hydrogen, helium, lithium, beryllium, carbon and oxygen ions, accelerated up to a few tens of MeV using a tandem accelerator. The SERs increased with increasing the amount of the generated charge in the SOI body by a floating body effect, even if the amount of the generated charge was less than the critical charge. The SERs with the generated charge in the SOI body more than the critical charge were almost constant.

1. Introduction

In recent years, a size of a semiconductor device is shrinked for low power consumption and high speed operation. Therefore the amount of charge, inducing soft errors, i.e. critical charge, for an advanced device decreases compared with that for a previous device. In 1970s, active radioisotopes of the package material used for a semiconductor device induced the soft errors [1]. However, in the present time, the cosmic ray is the main factor for the soft error, since the purity of the package material is improved. As the primary cosmic ray from the sun impinges the atmosphere, secondary cosmic rays which include muon, pion, neutron and proton are generated. The main factor for the soft error is a neutron, since a high energy neutron strikes a semiconductor device without energy loss at its flight path. When the neutron strikes a semiconductor device, the neutron induces a nuclear reaction with the device material, resulting in high energy particles and electron-hole pair generations along its track and soft error occurrences. A silicon-on-insulator (SOI) device realizes a low power consumption and high speed operation. In addition, the SOI device can suppress the soft error, since the amount of the generated charge in the SOI body with a separated active area by a buried oxide (BOX) layer from the substrate is less than that in the conventional bulk device. However, even if the amount of the generated charge in the active region is less than the critical charge, the soft errors occur by a floating body effect which appears in the partially depleted (PD) SOI device in the electrically floated active region from the substrate. When a high energy particle irradiates the active silicon region of an n-type SOI-metal-oxide-semiconductor field-effect transistor (MOSFET) with an off state, the generated electrons are moved to the source and drain electrodes. The generated holes are moved to the neutral region which exists at the bottom part in the active silicon region. The accumulated holes in the neutral region make the body potential higher than the normal potential, i.e. floating body effect. The increased body potential by the floating body effect enhances the source-drain current in the n-SOI-MOSFET, resulting in the turning on the transistor with an off state to an on state, even if the amount of

the generated charge in the active region by a high energy particle is less than critical charge.

One of the ways to suppress the floating body effect is the use of a body-tie structure. On the body-tie structure, a body electrode is fabricated at the side of the neutral region in the SOI-MOSFET by a partial trench isolation (PTI). The accumulated holes in the neutral region can be retrieved through the body-electrode. However the body-tie structure can't perfectly suppress the floating body effect, since the mobility of an electron is much faster than that of a hole [2].

In this study, hydrogen, helium, lithium, beryllium, carbon and oxygen ions, accelerated up to a few tens of MeV by a tandem accelerator, were irradiated to the body-tie PD SOI-static random access memories (SRAMs) to generate the various amounts of the charge in the SOI body in order to clarify the relationship between the soft error rate and the amount of the generated charge. The generated charge in the SOI body is calculated by "The Stopping and Range of Ions in Matter (SRIM)" simulator [3].

2. Experimental

In this study, the soft error rates (SERs) in the 8 Mbits body-tie PD SOI-SRAM with a technology node 90 nm was investigated by various ion probes. The operating voltages for the SRAM cell and the peripheral circuit in the experimental device were 1.2 V and 2.5 V, respectively. The thicknesses of the SOI and BOX layers were 75 nm and 145 nm, respectively. The gate capacitor was 1.5 fF, resulting in the critical charge of 1.8 fC. The experimental SRAM had 6-MOSFETs (2 p- and 4 n-MOSFETs).

The SERs were calculated as a probability that the soft error occurred by only one ion irradiation to the SRAM chip. The number of irradiated particles to the SOI-SRAM was counted by a solid state detector (SSD) before and after ion irradiation. Avoiding multi ion hits to the single SRAM cell, the irradiation time was determined in order that the number of irradiated particles was less than the number of the SRAM cells.

The SER was calculated by comparing the memorized values before and after ion irradiation. To clarify the relationship between the amount of the generated charge and the SERs, it was necessary to generate the various amounts of charge in the SOI body. Therefore, hydrogen, helium, lithium, beryllium, carbon and oxygen ions, accelerated from 0.525 to 18 MeV by the tandem accelerator, were irradiated to the SOI-SRAM.

3. Results and Discussion

Fig. 1 shows the amount of the generated charge in the SOI body as a function of incident energy of hydrogen, helium, lithium, beryllium, carbon and oxygen ions calculated by SRIM simulator. The horizontal dotted line shows the critical charge (1.8 fC). The various amounts of charge (0 ~ 5.5 fC) can be generated in the SOI body using various ions

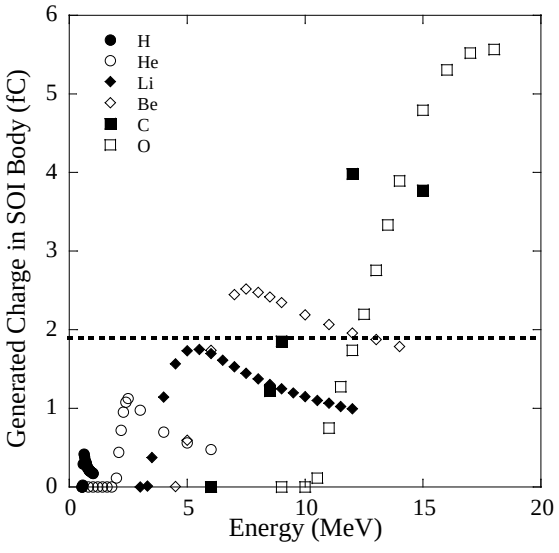

Fig. 1 The amount of the generated charge in the SOI body as a function of incident energy of H, He, Li, Be, C, and O ions calculated by SRIM simulator. The horizontal dotted line shows the critical charge of 1.8 fC.

accelerated to various energies. The generated charges were started to increase with energies of 0.55, 1.8, 3.3, 4.5, 6.0 and 10 MeV for hydrogen, helium, lithium, beryllium, carbon and oxygen ions, respectively. When the ion energies were less than these energies, the ions stop at the top passivation and wiring layers above the SOI-MOSFET, resulting in no charge generation in the SOI body.

Fig. 2 shows the soft error maps in the SOI-SRAM by Li ion irradiation with energies ranging from 3.0 to 11.9 MeV. The points show the SRAM cells where the soft errors occurred. No soft error occurred by 3.0 MeV Li ion irradiation, since the Li ions did not reach the SOI body. The uniform points show that the particles irradiated the SOI-SRAM uniformly above 3.0 MeV Li ion irradiation. Table. 1 shows the parameters include the energies, the number of particles and the number of soft errors by Li ion irradiation. It is necessary to clarify the probability to induce soft errors by single ion irradiation, since the number of the irradiated particles was not constant.

Fig. 3 shows SERs by hydrogen, helium, lithium, beryllium, carbon and oxygen ion probes for the PD SOI-SRAM with a technology node of 90 nm as a function of incident energy. The SERs started to increase with energies of 0.525, 2.0, 3.5, 4.5, 8.5 and 10.5 MeV for hydrogen, helium, lithium, beryllium, carbon and oxygen ions, respectively. The energies for charge generation (Fig. 1) and the SERs (Fig. 3) were almost the same for each incident ion, though the difference of the thickness of the top passivation and the wiring layers between the devices in the simulator and in the experiment exists.

Fig.4 shows the relationship between the SERs and the amount of the generated charge in the SOI body. The vertical dotted line shows the critical charge of 1.8 fC. The soft errors occurred by the floating body effect, even if the amount of the generated charge in the SOI body was less than the critical charge of 1.8 fC. When the amount of the generated charge in the SOI body was less than the critical charge, the SERs increased with

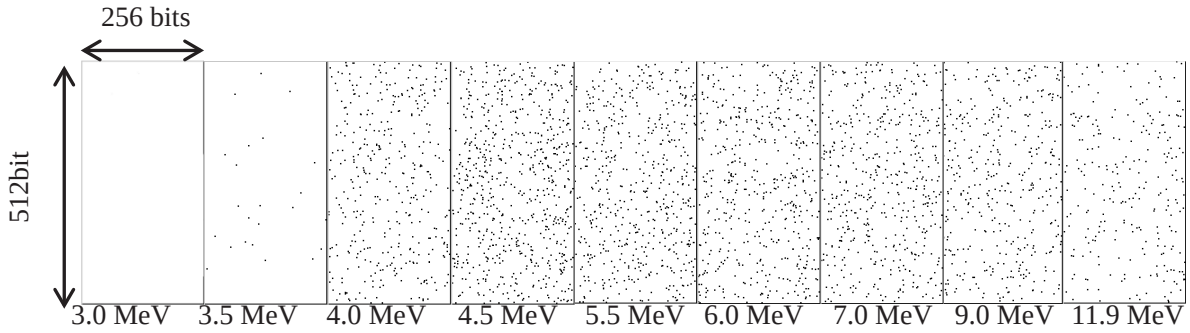

Fig. 2 Soft error maps in the SOI-SRAM by Li ions irradiation with energies ranging from 3.0 to 11.9 MeV.

Table. 1 The energies, the number of particles and the number of errors by Li ion irradiation to the SOI-SRAM.

Energy(MeV)	3.0	3.5	4.0	4.5	5.5	6.0	7.0	9.0	11.9
Particles	113816	57409	10885	12917	13804	15318	14772	14709	24428
Errors	0	23	378	652	537	491	488	407	254

increasing the amount of the generated charge in the SOI body. When the amount of the generated charge in the SOI body was more than the critical charge, the SER was almost constant. The SERs for hydrogen and helium ions were 2 orders of magnitude lower than those for lithium, beryllium, carbon and oxygen ions, when the amount of the generated charge was less than the critical charge. The reason of that would be the difference of the nuclear stopping power for each ion.

4. Conclusion

The SERs in a SOI-SRAM with a technology node of 90 nm were investigated by hydrogen, helium, lithium, beryllium, carbon and oxygen ions, accelerated up to a few tens of MeV by a tandem accelerator. When the amount of the generated charge in the SOI body was more than the critical charge, the SERs were almost constant. When the amount of the generated charge in the SOI body was less than the critical charge, the SERs increased with increasing the amount of the generated charge in the SOI body. Even if the amount of the generated charge is less than the critical charge, the floating body effect induces soft errors by enhancing the source-drain current and increasing the body potential.

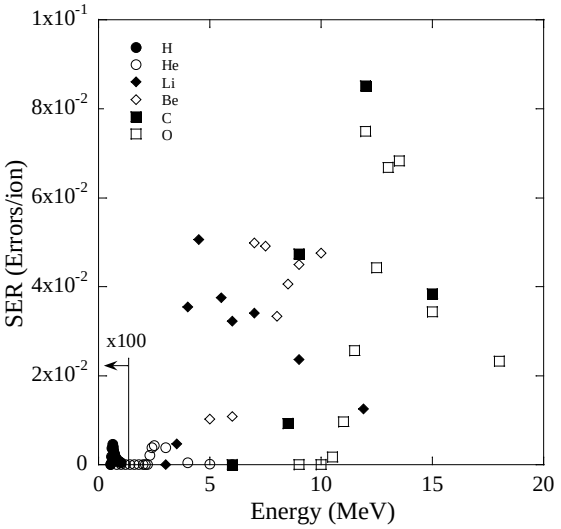

Fig. 3 SERs by H, He, Li, Be, C and O ion probes for 90 nm node PD SOI-SRAM as a function of incident energy.

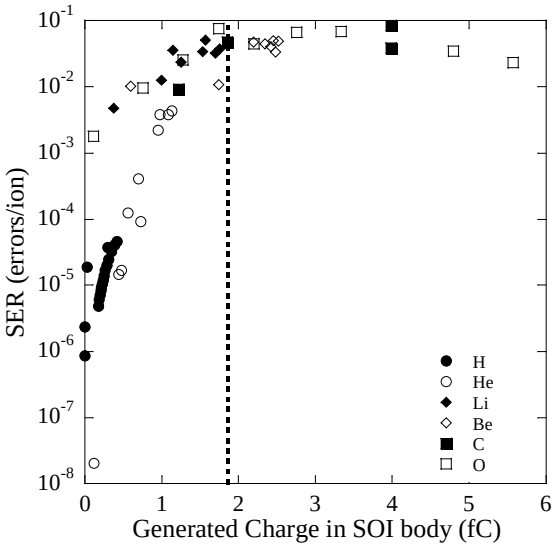

Fig. 4 SERs as a function of amount of generated charge in the SOI body by using H, He, Li, Be, C and O ion probes for 90 nm node PD SOI-SRAM. The vertical dotted line shows the critical charge of 1.8 fC.

References

[1] J. Ziegler, IBM J. RES. DEVELOP. VOL 40 NO. 1
JANUARY 1996.

[2] Satoshi Abo, Naoyuki Masuda, Fujio Wakaya, Shinobu Onoda, Takahiro Makino, Toshio Hirao,Takeshi Ohshima, Toshiaki Iwamatsu, Hidekazu Oda, and Mikio Takai, proceedings of the 9th International Workshop on Radiation Effects on Semiconductor Devices for Space Applications (9th RASEDA) (2010) 72.

[3] J. Ziegler, The Stopping and Range of Ions in Matter (SRIM2008) <http://www.srim.org>.

Applicability of redundant pairs of SOI transistors for analog circuits

A. Makihara[*1], T. Yokose[1], Y. Tsuchiya[1], K. Tani[1], T. Morimura[1], H. Abe[2], H. Shindou[3], T. Ebihara[3], A. Maru[3], K. Morikawa[3], S. Kuboyama[3], and T. Tamura[3]
1 High-Reliability Engineering & Components Corporation (HIREC), Japan
2 Japan Atomic Energy Agency (JAEA), Japan
3 Japan Aerospace Exploration Agency (JAXA), Japan
[*1]Email: makihara@hirec.co.jp
Keyword(s): SOI, Phase-Locked Loop, Radiation Hardness-By-Design

Abstract

Redundant pairs of SOI transistors have been utilized as a Radiation Hardening-By-Design technique and their applicability was subsequently extended for analog circuits. In this paper, the principle of the SET free inverter (SFI) operation is extended to analog circuits such as current mirror circuits and has been successfully demonstrated with a phase-locked loop circuit intended for use in ASICs, which includes some analog circuit blocks, such as the current mirror, differential amplifiers and so on.

1. Introduction

Single-event transient (SET) pulse in nanometer-scale integrated circuits, which is caused by high energy heavy ions and protons in space radiation, is a serious problem for electronic equipment intended to be operated in space. Much time has been spent extensively studying many mitigation techniques such as triple modular redundancy (TMR) [1].

The SET free inverter (SFI) circuit is one such mitigation technique and only applicable to SOI process technology [2]. However it has a unique ability to prevent SET pulse generation essentially via the circuit itself. Conversely, however, no other techniques can prevent the generation of SET pulses, meaning the pulses must be rejected or suppressed by additional voting or filtering circuits to eliminate their effects in this case and the additional timing penalty may impair the system operating frequency. A trade-off is thus needed between operating frequency and SEU immunity. The principle of the SFI circuit is easily extended to all other combinational and sequential logic circuits and successfully applied to application specific integrated circuits (ASICs) [3] including a micro-processor unit (MPU) for space applications.

In this paper, the principle of SFI operation is also extended to analog circuits such as current mirror circuits and has been demonstrated with a phase-locked loop circuit intended for use in ASICs, which includes some analog circuit blocks, such as the current mirror, differential amplifiers and so on.

2. Principle of the SET free inverter

The SFI circuit is obtained by replacing each transistor in a standard CMOS inverter with a pair of redundant transistors, i.e. each of the P- and N-channel transistors is replaced by a pair of P- and N-channel transistors connected in series as shown in Fig. 1(a). The supply current flow in its static condition is blocked by the redundant pair transistors and the potential of each node is divided by the transistors as shown in Fig. 1(b) in principle. Upon the incidence of high energy particles on one of the pair transistors, the voltage applied between the drain and source of the transistor is reduced, whereupon the voltage is transferred to another transistor in the pair and a very small amount of charge is displaced. It should be noted that the voltage transfer mechanism between the redundant pair of transistors only works as expected with SOI process technology because the transistors must be isolated by insulator instead of a reverse-biased p-n junction, as in bulk technology.

The worst case transient response is estimated by a circuit simulator such as SPICE, with a switch to short the drain and source [4]. For standard CMOS circuits, the series resistance and close time duration of the switch should be adjusted to simulate the response for the intended LET value of the incident ions. However, the switch can simply be closed with a low contact resistance to estimate the worst case response for SFI circuits. Even if the switch is closed, there is no DC power supply path. For the SFI circuit shown in Fig. 1(a), implemented by a 0.15 μm fully depleted SOI (FDSOI) from the LAPIS semiconductor (former OKI), the worst voltage disturbance at the output terminal is observed with an ion strike on M_{P2}. The peak level and full width at the half maximum (FWHM) of the output voltage disturbance are plotted as a function of switch resistance in Fig. 2. The supply voltage was a nominal specified voltage of 1.5 V. The peak level of the disturbance is less than 150 mV and declines in the higher switch resistance region. In contrast, FWHM is increased at the region, but remains less than 20 ps, even if the resistance is increased up to 10 kΩ. The collected charge (total charge passed through the switch) remained almost constant over the resistance range (0.56 fC ± 0.2 %) and much less than the

deposited charge from an incident ion; for example, an average of 27 fC for an ion with a LET of 68.9 MeV/(mg/cm^2), assuming top silicon thickness of 40 nm. Obviously the disturbance level is too small and cannot be propagated to the subsequent stage of the logic circuit. The very small collected charge is attributable to the loss of voltage applied to the transistor just after being struck. This loss means the deposited charge in the body region is diffused for both the drain and source regions of the transistor, and the net current flow is very small, which is a key feature of the redundant pair transistors in SOI process technology.

For the hardening technique with the redundant pair transistors, simple attention is required for their layout. To obtain the required SET immunity, spacing of the gates is the key parameter. For the SOI technology utilized in this study, a minimum of 0.35 μm is required to achieve SET immunity up to LET of 68.9 MeV/(mg/cm^2) and the immunity was demonstrated experimentally [2]. The area of the pair is less than twice that of the single transistor.

The simulation results with SPICE were compared to those obtained by the 3D device simulator, HyDeLEOS [5], which generally provided more rigorous results. As a result, with a LET of 68.9 MeV/(mg/cm^2), it was confirmed that the simulation with SPICE as described above was applicable to estimate the worst case response of circuits utilizing redundant pair transistors.

3. Application to analog circuits

Redundant pair transistors are also applicable to analog circuit blocks, such as current mirror circuits. The latter are generally utilized to generate a constant current to drive other circuit blocks and comprise a matched pair of transistors as shown in Fig. 3(a). Each of the transistors in the pair can be replaced by a redundant pair of transistors as shown in Fig. 3(b). In analog circuits such as current mirror circuits, the transistors in the circuits are operated in linear mode and there are steady current paths in its static condition. However the key feature of the redundant pair transistors, i.e. substantially reducing the collected charge at the struck transistor, remains workable.

If one of the transistors in the redundant pair is shorted out by the switch as the SFI circuit to simulate SET pulse generation, the steady state current level also changes. The total collected charge can be measured similarly as for SFI circuits (the integrated current passed through the switch just after switch closure to steady state). For the circuits shown in Fig. 3, implemented by the same fabrication process discussed in the previous section, the worst case disturbance was observed where M_{PL2} was struck. In this example, the output current was set to 100 nA with a nominal supply voltage of 1.5 V. The collected charge measured at the switch was also almost independent of the series resistance of the switch up to 10 kΩ and the values were around 2.5 fC. The collected charge gradually declined with increasing resistance beyond 1 kΩ and reduced to 2.0 fC at 100 kΩ. Therefore we can assume a worst case collected charge of around 2.5 fC. The peak current level passed through the switch and its FWHM (charge collection time) are plotted in Fig. 4. They were also almost independent of the series resistance of the switch up to 10 and 100 Ω and the values were around 360 ps and 6 μA, respectively. However, they increased or declined abruptly with switch resistance beyond 10 and 100 Ω.

Based on the above analysis, we can determine the switching condition to predict the worst case SET response, i.e. switch resistance of 10 kΩ and closure duration of 1 ns (around twice the FWHM). Fig. 5 shows the SET response for the current mirror circuits. For comparison, the SET response for a non-RHBD circuit is also indicated, which involved setting the switch resistance to 12.7 kΩ to adjust the collected charge to around 27 fC, i.e. a deposited charge for ions with LET of 68.9 MeV/(mg/cm^2) and a fixed switch closure duration of 1 ns. It is apparent that the SET response is greatly improved with the new RHBD technique, although the disturbance was not completely eliminated. It should also be noted that the result for the non-RHBD circuit is for ions with LET of 68.9 MeV/(mg/cm^2) and excludes any additional charge collection mechanism, such as bipolar amplification, meaning the result is not the worst case. In contrast, the result for circuits with a new RHBD technique is for the worst case with larger LET ions.

4. Verification with PLL circuits

4.1 PLL Circuit Design

Phase-Locked Loop (PLL) circuits comprise several functional circuit blocks as shown in Fig. 6. The programmable divider (DM/DN/DO) and phase detector (PFD) are digital circuits, which can be hardened using SFI and derivative basic logic circuits. The remaining analog circuit blocks are voltage-switching charge pump (VCP), voltage-controlled current source (VCCS), and VCO. In this study, all these circuits were hardened utilizing the redundant pair transistors.

In a previous study, it was proposed to utilize VCP to improve immunity to the SET pulse [6]. In our design, a further simplified VCP circuit was applied. The VCP circuit is essentially similar to SFI and although the gates of the P- and N-channel transistors are independently controlled, they are never opened simultaneously. Therefore its SET immunity is expected to be as SFI.

VCO comprised a 5-stage ring oscillator in our design. The oscillator itself is a digital circuit and easily

hardened by utilizing SFIs. However, its output signal is not at a normal logic level and should be restored by a level converter (LC) for the subsequent circuit block, i.e. DO. The LC comprised a differential amplifier with redundant pair transistors, followed by 3 stages of SFIs to boost the output current. To restore the signal level, the differential amplifier is operated in the saturation region, i.e. its expected output voltage is 0 or V_{DD} with a fast transition time. Accordingly, all transistors in the amplifier are operated as in the digital circuit and its SET immunity is expected to be as SFI.

VCCS is the most complicated analog circuit block in our PLL design and all the transistors are operated in linear mode. The circuit was also hardened using the redundant pair transistors. The circuit block comprised two current mirror circuits to boost the current supply capability to the VCO and gain control circuit. Its SET immunity was confirmed as described in the previous section.

The electrical performance of the PLL was evaluated with actual silicon. The power consumption was 2.4 mW at room temperature with power supply of 1.5 V. The cycle-to-cycle jitter was 70 ps rms at a VCO output frequency of 600 MHz.

4.2 Heavy Ion Testing

Heavy ions with LET of 3.4 to 68.9 MeV/(mg/cm^2) were used for the evaluation, the characteristics of which are listed in table II. These ions were irradiated normal to the chip surface and the supply voltage was set to a minimum of 1.35 V to obtain the worst case transient response. The input frequency was 10 MHz, VCO oscillated at an expected maximum operating frequency of 600 MHz, and the output frequency of PLL was set to 100 MHz for the experiments.

The cycle-to-cycle jitter was continuously monitored during irradiation by using 10Gs/s digital oscilloscope (TDS7104, Tektronix) with glitch detection trigger mode. The expected worst case cycle-to-cycle jitter (without irradiation) is an inherent characteristic of each PLL circuit and a function of operating time. For the irradiation test, the jitter attributable to the inherent characteristic should be excluded. In the actual test run, the prolonged or shortened cycles were defined as cycles with a deviation greater than |500ps| from the nominal cycle time. The jitter value is 7.1 and corresponds to the worst case jitter expected to be observed every 6 hours of PLL operation without irradiation.

The test data is shown in Fig. 7. For version A, erroneous output pulses (prolonged or shortened) for several contiguous cycles were observed. The saturated cross-section exceeded 10,000 μm^2. The output pulses are attributable to the non-RHBD VCCS. For version B, only single prolonged pulses were observed. The source of the error might be the non-RHBD LC. The observed saturated cross-section was around 20 μm^2 and in agreement with the area of LC as expected. Finally no erroneous pulse was observed up to LET of 68.9 MeV/(mg/cm^2) for version C.

5. Conclusions

In this paper, a new RHBD technique for analog circuits was proposed, which utilizes redundant pair transistors with SOI technology. The technique is very simple and incurs relatively little penalty in terms of power and area compared to TMR. Utilizing this technique, a PLL circuit with a maximum VCO frequency of 600 MHz was designed and fabricated with 0.15 μm Fully Depleted SOI technology. No erroneous pulse was observed up to a LET of 68.9 MeV/(mg/cm^2). The new RHBD technique was successfully demonstrated.

Acknowledgments

The authors gratefully acknowledge the technical support of the members of Ryoei Technica Corporation for the experiments and analysis. They also wish to thank the members of Soliton Technology Corp. for the detailed design of the PLL circuit used to demonstrate the new RHBD technique.

References

[10] F. L. Kastensmidt, IEEE NSREC Short Course Notebook, 2007.
[11] A. Makihara, et al., "Optimization for SEU/SET Immunity on 0.15 μm Fully Depleted CMOS/SOI Digital Logic Devices," IEEE Trans. Nucl. Sci., Vol. 53, No. 6, pp. 3422-3427 (2006).
[12] A. Makihara, in proceeding of IEEE RADECS, 2010.
[13] A. Makihara, et al., "New SET Characterization Technique Using SPICE for Fully Depleted CMOS/SOI Digital Circuitry," IEEE Trans. Nucl. Sci., Vol. 55, No. 6, pp. 2921-2927 (2008).
[14] HyDeLEOS : 3 dimensional device simulator (Hyper Device-Level Electrical Operation Simulator) Ver. 5.5, User's Manual from Semiconductor Leading Edge Technologies Inc., 2011.
[15] T. D. Loveless, et al., "A Hardened-by-Design Technique for RF Digital Phase-Locked Loops," IEEE Trans. Nucl. Sci., Vol. 53, No. 6, pp. 3432-3438 (2006).

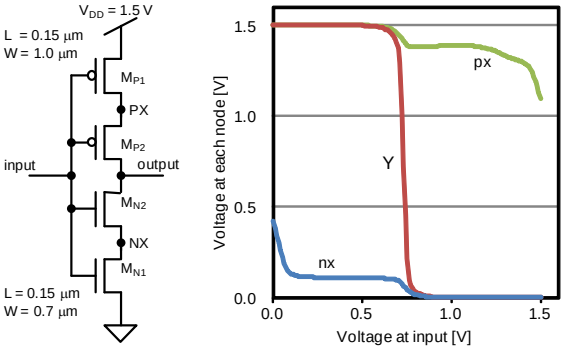

(a) (b)

Fig. 1. Schematic of SFI (a), and the Input-Output behavior of SFI (b).

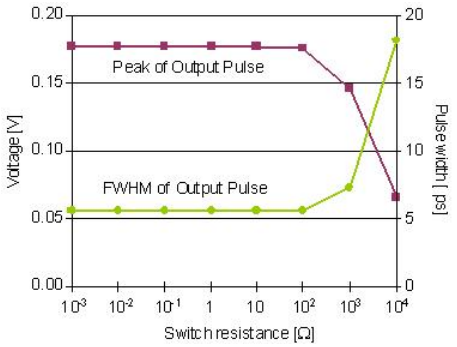

Fig. 2. Output voltage disturbance and as a function of switch resistance.

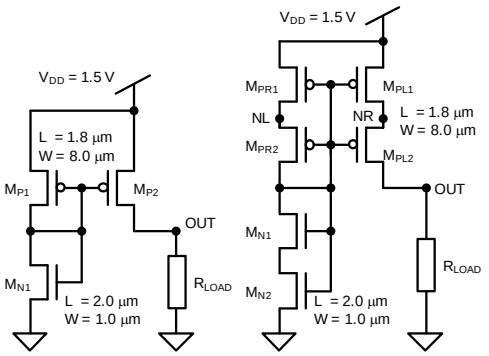

(a) (b)

Fig. 3. Current mirror circuit without RHBD (a), and Current mirror circuit with RHBD (b). Output current set to 100 nA for both circuits at V_{DD} = 1.5 V.

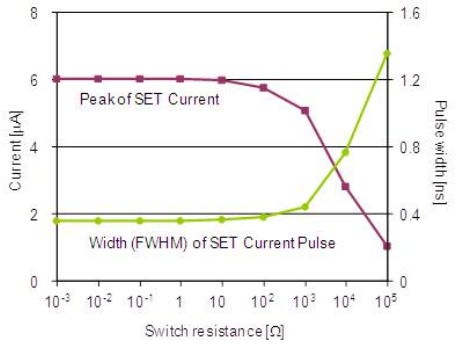

Fig. 4. Peak of the SET current pulse passed through the switch for the SET simulation and FWHM of the pulse as a function of the switch resistance.

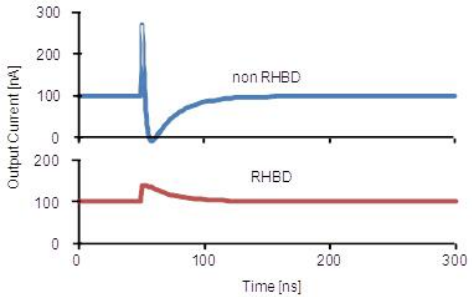

Fig. 5. SET response in the output current for RHBD and non-RHBD current mirror circuits.

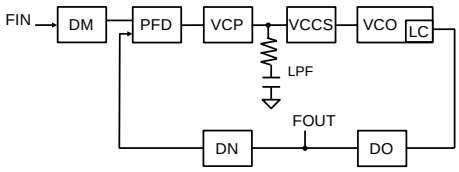

DM/DN/DO: Programmable Divider circuits
PFD : Phase-Frequency Detector
V-CP : Voltage-Switching Charge Pump
LPF: Low-Pass Filter
VCCS : Voltage Controlled Current Source
VCO: Voltage Controlled Oscillator
LC: Level Converter

Fig. 6. Block diagram of PLL to demonstrate the new RHBD technique.

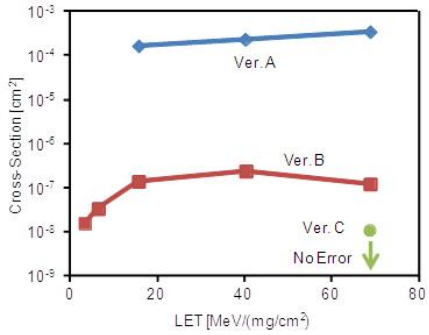

Fig. 7. Cross-section of erroneous output as a function of LET.

TABLE I
PLL DESIGN FOR SET IMMUNITY EVALUATION

Block	Version A	Version B	Version C
V-CP	RHBD	RHBD	RHBD
VCO	RHBD	RHBD	RHBD
LC	no	no	RHBD
VCCS	no	RHBD	RHBD
Digital Blocks	RHBD	RHBD	RHBD

TABLE II
CHARACTERISTICS OF IONS USED IN THIS STUDY

Ion Species	Energy [MeV]	LET [MeV/(mg/cm²)]	Range [µm]
N	53	3.6	49.1
Ne	70	6.5	38.9
Ar	137	15.8	36.1
Kr	289	40.3	37.3
Xe	398	68.9	35

Investigation of the SEE sensitivity of 90nm DICE based Flip-Flops using pulsed-laser testing methodology

H. Shindou*1, A. Maru[1], T. Ebihara[1], A. Makihara[2], S. Kuboyama[1] and T. Tamura[1]
1 Japan Aerospace Exploration Agency (JAXA), Japan
2 High-Reliability Engineering & Components Corporation (HIREC), Japan
*Email: shindou.hiroyuki@jaxa.jp
Keyword(s): 90nm, DICE, Single event transient, Charge sharing, Pulsed-laser testing

Abstract

This paper describes the evaluation result of the SEE sensitivity of 90nm DICE based flip-flops. Considering our past experimental results, modified DICE circuits were designed in order to minimize the charge sharing effect. The pulsed-laser SEE testing methodology was effectively utilized to identify the location of SEE sensitive areas. The comparison with the heavy ion irradiation test result were also discussed.

1. Introduction

Modern spacecrafts typically require a great variety of high-performance semiconductor devices to realize various types of space missions such as earth observations, telecommunications, planetary explorations, and so on. Recently, due to the requirements for higher density integration and device scaling, the logical circuits have been designed with <100nm design rule. Single-Event Upset (SEU) and Single-Event Transient (SET) phenomena are serious problems for those integrated circuits, because their supply voltage and the threshold to these events are also decreasing. In our past study[1,2], the effectiveness of Radiation Hardning by Design (RHBD) methodology for 90 nm CMOS process has been evaluated. Several types of Dual Interlocked Storage Cell (DICE) based Flip-flops have been designed and evaluated. As a result, by using the heavy ions AVF cyclotron, SEUs with relatively large cross-sections induced by the charge sharing[3-5] have been identified although normal angle irradiation test results showed excellent SEE tolerance.

In this study, modified DICE circuits were designed for 90nm CMOS process. The SEE sensitivity of these were also investigated. The pulsed-laser testing methodology was successfully utilized for the identification of potential vulnerabilities of test circuits.

2. Experimental

2.1 Descriptions of test circuits

The schematic diagram of DICE based flip-flop circuit evaluated in this study is shown in Fig.1. Considering our past experimental results[1-2], additional p-type transistors were inserted for each DICE elements to minimize the probability of multi-node SEUs caused by the penetration of ion particles with grazing angle. Filtering delay circuit was also applied in order to eliminate SET propagation on CLK signal line. Two types of circuit layout (Type A and Type B) were designed and tested as shown in Fig.2 (Because of the limitation of technology information disclosure, only the outline of layout was indicated in this figure). By using these element circuits, the memory block with a total size of 2k bit was constructed and installed to the test chip. Test chips were fublicated using Fujitsu's 90 nm bulk CMOS process.

2.2 Pulsed-laser test equipment

Usually SEE cross-sections are simply calculated from heavy ion irradiation test results by dividing a number of error bits by the total fluence. However this conventional method does not give us sufficient information to identify the location of SEE sensitive nodes. To overcome this issue, the pulsed-laser SEE test system, PULSYS-RAD made by PULSCAN (Bordeaux, FRANCE) was introduced and was used for this experiment (Fig.3). This was especially designed for the characterization of single-event effects in integrated circuits using picosecond laser pulses. The main characteristics of the light obtained from this equipment is shown in Table 1. In our experiment, DUT was mounted on the X-Y moving stage and scanned with 0.2 μm step width in order to identify the location of SEE sensitive area.

2.3 Sample preparation and test conditions

In general, modern semiconductor manufacturing processes use many metal layers to realize very large scaled integration circuits. In case of the laser testing, performing the irradiation from backside of the chip is indispensable to avoid the interfare of the laser penetration caused by metal layers. In our experiment, substrate of the test chip was thinned down to approximately 50 μm. After the thinning process, the chip was mounted to the small PWB board as shown in Fig.4.

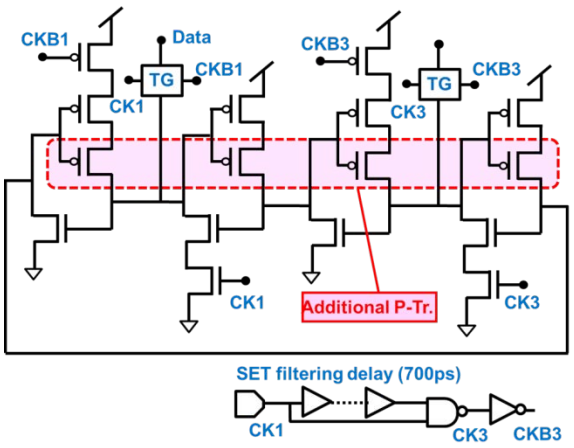

Fig.1. Schematic diagram of modified DICE.

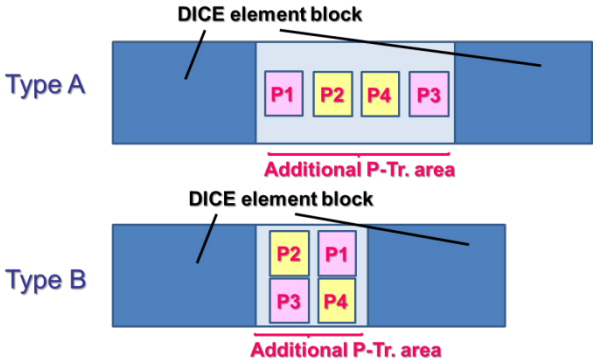

Fig.2. Outline of the circuit layout of modified DICE.

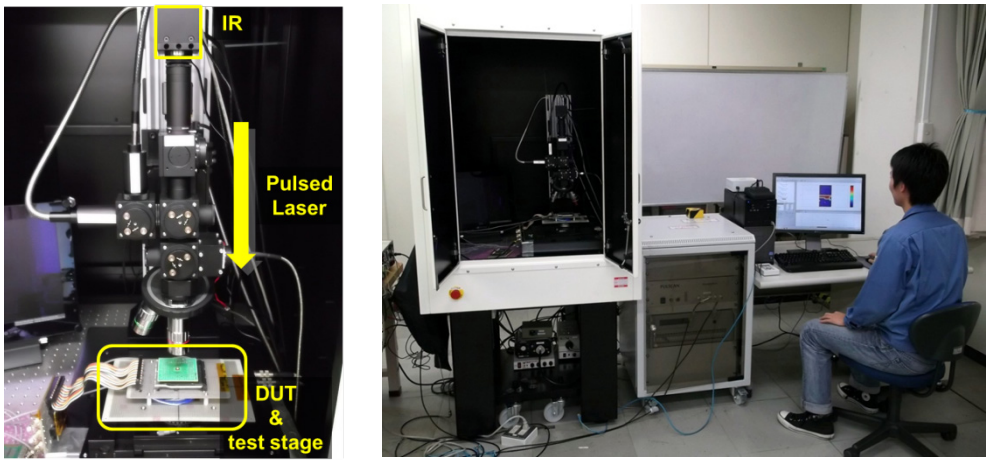

Fig.3. Pulsed-laser SEE test system. (@ JAXA Tsukuba Space Center.)

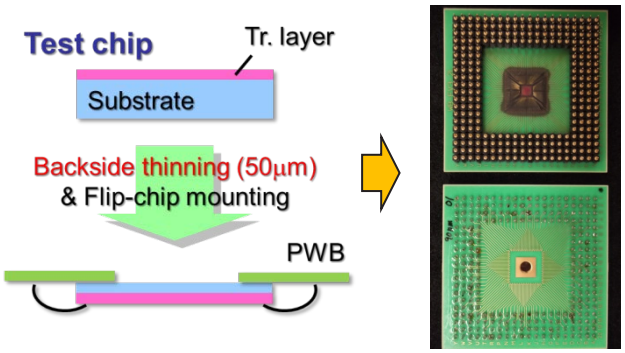

Fig.4. Procedure of the sample preparation used for the laser testing.

Table 1. Main profile of the pulsed-laser used in this study.

Parameters	Values
Laser Energy	up to 2,000 [pJ]
Wavelength	1,064 [nm]
Pulse duration	30 [ps]
Estimated spot diameter (@ $1/e^2$)	1.6 [μm]

3. Results and Discussion

At first the heavy ion irradiation was performed to check the SEE sensitivity of each test circuit. Specific Mono-energetic heavy ions were obtained from the Azimuthally Varying Frequency (AVF) cyclotron at Takasaki Radiation Chemistry Research Establishment of JAEA and the Heavy Ion Medical Accelerator synchrotron in Chiba (HIMAC), at the National Institute of Radiological Sciences (NIRS). As the result, unexpected SEUs were observed during the nomal angle (i.e. perpendicular to the chip surface) irradiation in addition to the angled irradiation test (Cross section characteristics are shown and discussed later compared with the pulsed-laser testing results.).

In order to clarify the location of sensitive nodes, pulsed-laser testing was performed. Fig.5 shows typical results of the error mapping obtained by the laser scanning. In the experiment of Type-A device, the error was observed only at F-state. This tendency agreed with the heavy ion irradiation test result previously mentioned. It was confirmed that the sensitive area was identified only in an additional P-Tr. area. It was also confirmed that the sensitive area was located on the center of an additional p-transistor area as shown in Fig.5(a). These facts suggest that SEUs were induced by a disturbance of electrical potential of a neighboring ON-state P-Tr. pair. With the Type-B device, SEUs were induced at both 0-state and F-state as shown in Fig.5(b). In this test case, memory cells were often permanently damaged during laser irradiation. It was thought that SEUs were induced by the same mechanism as Type-A device.

Cross section characteristics obtained by heavy ion irradiation and pulsed-laser test are shown in Fig. 6. Although further investigations about the relationship between the laser energy and the equivalent LET were needed, the cross-section determined from experiments showed good coincidence. Some investigations about the defining of a laser equivalent LET have already been reported[6-7]. Based on these studies it is roughly estimated that 100[pJ] (λ=1,064nm, sensitive volume depth d=1μm) is equivalent to the order of LET=10[MeV/(mg/cm^2)]. In case of our experiments, some elements which should be taken into consideration exist in calculating equivalent LET (For example, the limitation of the assumption of RPP model etc.). Additional experiments and numerical analysis are required to determine the laser equivalent LET in our test condition as the future work.

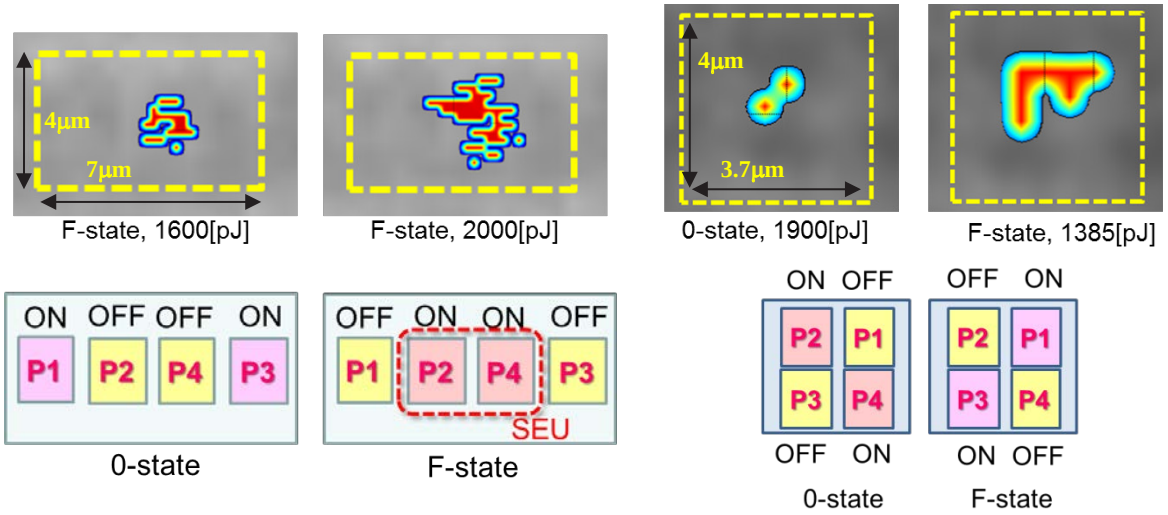

(a) Type-A (b) Type-B

Fig.5. Typical examples of the error mapping image obtained by the laser testing. The yellow dotted line shows additional p-transistor area described in Fig. 2.

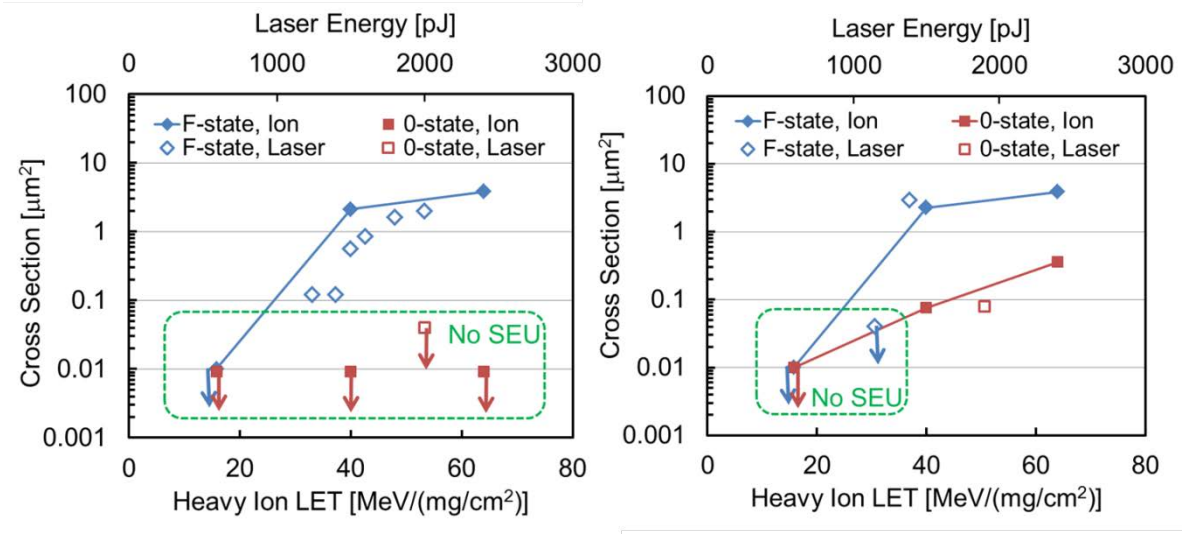

(a) Type-A (b) Type-B

Fig.6. Cross section characteristics obtained by heavy ion irradiation and pulsed-laser tests.
(Note: The relationship between the upper horizontal axis and the lower one is not calibrated.)

4. Conclusion

This paper described the evaluation result of the SEE sensitivity of 90nm DICE based flip-flops. Pulsed laser testing methodology was successfully utilized to the identification of SEU sensitive nodes. However some restrictions also exist in the laser testing (For example, the laser is unsuitable for angle irradiation because of the limitation of the penetration depth). It is said that the evaluation which combined heavy ion irradiation test and the pulsed laser testing is very effective way for shortening a period required for an optimization of rad-hard circuit designs. Charge sharing issue becomes major concerns for nano-scale devices due to the scaling trends such as reduced nodal charge and reduced area spacing. Careful design layout that took the separation of the sensitive transistor pairs into account is required. Based on the result obtained in this study, we would like to accelerate the construction of the RHBD library corresponding to nanoscale devices for space applications.

Acknowledgments

The authors gratefully acknowledge the support of the members of Ryoei Technica Corp. for the experiments and analysis. We also thank the members of JAEA for their helpful support.

References

[1] A. Maru et al., "DICE-based flip-flop with SET pulse discriminator on a 90 nm bulk CMOS process," IEEE Trans. Nucl. Sci., vol. 57, pp. 3602-3608 (2010).
[2] A. Maru et al., "DICE based Flip-Flop with SET pulse discriminator on a 90 nm bulk CMOS process," Proceedings of 9th RASEDA, pp.64-67(2010).
[3] A. Amusan et al., " Charge Collection and Charge Sharing in a 130 nm CMOS Technology," IEEE Trans. Nucl. Sci., vol. 53, pp. 3253-3258 (2006).
[4] A. Amusan et al., " Single Event Upsets in Deep-Submicrometer Technologies Due to Charge Sharing," IEEE Trans. Device and Materials Reliability, vol. 8, pp. 582-589 (2008).
[5] B.D.Olson et al., " Simultaneous single event charge sharing and parasitic bipolar conduction in a highly-scaled SRAM design," IEEE Trans. Nucl. Sci., vol. 52, pp. 2132-2136 (2005).
[6] V.Pouget et al., " Theoretical investigation of an equivalent laser LET," Microelectronics Reliability, vol.41, pp. 1513-1518 (2001).
[7] D.McMorrow et al., " Application of a pulsed laser for evaluation and optimization of SEU-hard designs," IEEE Trans. Nucl. Sci., vol. 47, pp. 559-565 (2000).

Suppression of Heavy-Ion induced Current in SOI Device

S. Ogura*[1], T. Komiyama[1], Y. Takahashi[1], T. Makino[2], S. Onoda[2], T. Hirao[2], and T. Oshima[2]
1 Nihon University, Japan
2 Japan Atomic Energy Agency (JAEA), Japan
*Email: cssu11011@g.nihon-u.ac.jp, ytaka@ecs.cst.nihon-u.ac.jp
Keyword(s): SET, SOI, SEE tolerance device, Displacement current

Abstract

We have investigated the transient current in a SOI p^+n junction diode induced by single heavy-ions. The amount of radiation induced total collected charge exceeds the generated charge in active SOI layer because some of generated charge in handle substrate is collected through a BOX layer by displacement current. The displacement current is caused by the charges collected at surface of handle substrate due to an electric field in depletion layer. In this paper, we show that the amount of collected charge can be suppressed by reducing the width of depletion layer at the surface of handle substrate.

1. Introduction

One of the most detrimental effects on semiconductor devices in radiation environment is single-event effects (SEE). When a high-energy heavy ion strikes the device, electron-hole pairs are generated along the ion-track and they can create sufficient transient current to cause an incorrect action such as single-event upset (SEU). Recently, silicon–on-insulator (SOI) devices have been developed for higher SEE tolerance device, because it has been believed that the charge collection is suppressed by the existence of a buried oxide (BOX) layer [1-2]. However, anomalous charge collection in the SOI device was reported [3-5]. That indicates some of generated charge in handle Si substrate is collected through a BOX layer. From the results of heavy-ion induced gate current in MOS structure, we have concluded that the radiation-induced current through an oxide layer is dominated by a displacement current [6].

In this paper, the transient current in p^+n junction diode on SOI substrate induced by single heavy-ion has been investigated. From the results of the transient current from each electrode in the device, we show the anomalous charge collection is caused by the displacement current through BOX layer. The displacement current is generated by the charges collected at surface of handle substrate due to an electric field in depletion layer. We also show the displacement current can be suppressed by reducing the width of depletion layer using SOI wafer with highly doped handle substrate.

2. Experiments

Two types of Al gate SOI-p^+n junction diodes, n/n and n/n^+ devices, with the junction area of 100 μm in diameter were used in this study. Figure 1 shows the device structure of these devices. The n/n device were fabricated on a SOI substrate in which active SOI layer and handle substrate layer are n-type and the donor concentration of both layers are about 10^{15} cm^{-3}. The n/n^+ device is fabricated on the wafer with highly doped handle substrate. In these devices, the thicknesses of active layer and BOX layer are 1.5 μm and 0.3 μm, respectively. The devices were fabricated at Micro Functional Device Research Center of the Nihon University.

The transient currents in these devices induced by 15 MeV Oxygen ions were measured. The LETs and project range of the ions are 6.5 MeV/(mg/cm^2) and 12.3 μm, respectively. Heavy-ion irradiation tests were carried out using the Single Ion hit (SIH) system in JAEA [7] and the transient current caused by the single ion was measured by Transient Ion Beam Induced Current (TIBIC) measurement system [8]. Figure 2 shows the experimental setup of the irradiation. The cathode and back contact electrode were connected to ground and the reverse

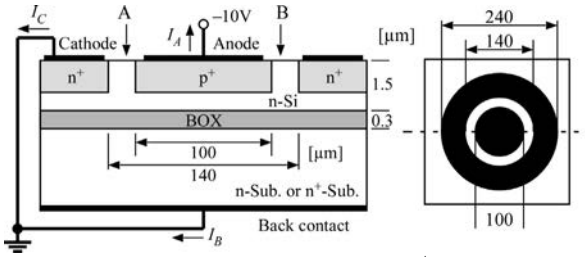

Fig. 1. Device structure of SOI p^+n diode

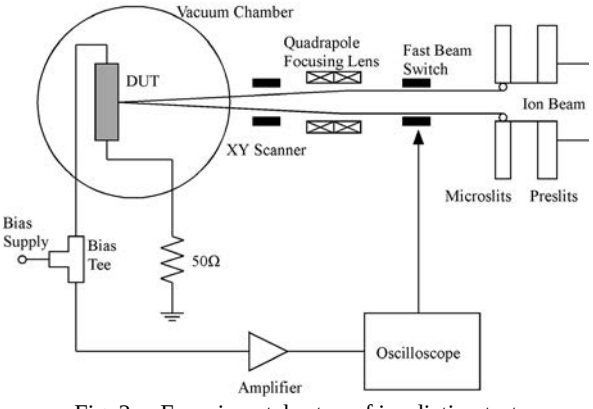

Fig. 2. Experimental setup of irradiation test

bias of 10V was applied to anode electrode during irradiation test. DC bias voltage is applied through a bias tee, and the transient current induced by heavy-ion irradiation is measured with a high-speed oscilloscope with a bandwidth of 3 GHz (Tektronix TDS 694C). In this system, the sample carrier is set on a high precision XYZ stage and the typical spot size of the focused ion beam is about 1 μm on DUT.

3. Results and Discussions

Figure 3 shows the peak of transient current and the amount of total collected charge from the anode electrode in n/n device as a function of the heavy-ion hitting location. The peak current depends on the location and larger current is observed when the heavy-ion hits to the edge of p^+ diffusion region. On the other hand, the amount of total collected charge is almost constant whenever the ion hits to the p^+ diffusion region. The charge generated in active layer due to irradiation is 100 fC and the measured collected charge is 2~3 times as much as the generated charge in active SOI layer.

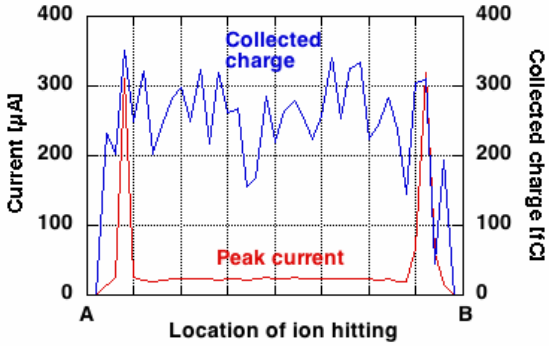

Fig. 3. Peak of transient current and total collected charge from anode electrode in n/n device as a function of the heavy ion hitting location

Figure 4 shows the transient current and the collected charge from each electrode (anode, cathode, and back contact electrodes) in n/n device when the ion hits to the center area of p^+ diffusion region. The collected charges by anode and back electrodes are almost same and the charge from cathode electrode is much smaller than that from other electrodes. These results indicate that the charges collected by anode electrode are mostly caused by the radiation induced generated charges in handle Si substrate and these charges were collected through the BOX layer.

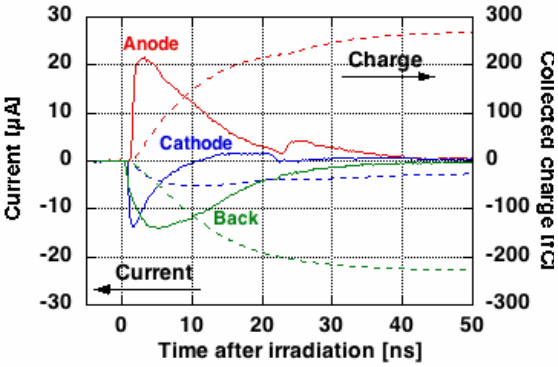

Fig. 4. Transient current and collected charge in n/n device when ion hits to the center area of p^+ region

Figure 5 shows the transient current and the collected charge in n/n device when the ion hit to the edge of p^+ diffusion region. The current peaks of anode and cathode electrodes are almost same and these are much higher than in case when the ion hits to the center area of p^+ region. When reverse bias is applied to the diode, lateral electric field is concentrated at the edge of p^+ region. The charges generated in active layer due to irradiation are collected quickly to anode and cathode electrodes by the electric field. It is considered that the quick charge collection causes the large current. The current form back electrode is much smaller than that from the other electrodes. However the current and collected charge are almost same as the result when the ion hits to the center of p^+ region, shown in Fig. 4. From these results, it is found that about half of collected charge by anode electrode is caused by the charges collected through the BOX layer.

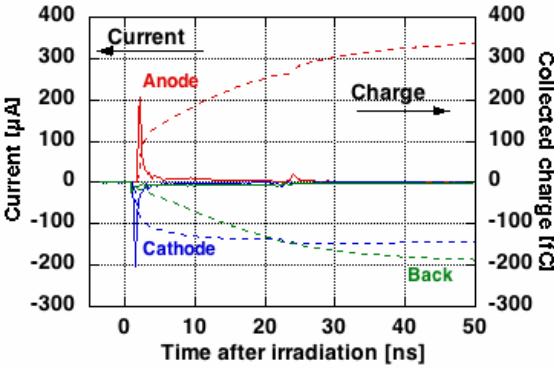

Fig. 5. Transient current and collected charge in n/n device when ion hit to the edge of p^+ region

In our present work, we concluded that the radiation-induced current through an oxide layer was dominated by a displacement current. So it is very important to suppress the displacement current through the BOX layer in order to improve radiation immunity of SOI devices. If the project range of irradiated heavy ion is much longer than the thickness of active SOI layer, electron-hole pairs are generated in handle substrate. In the case when the reverse bias is applied to the n/n device, depletion layer is formed at the surface of handle substrate under p^+ diffusion region. Some of generated electron-hole pairs escape from recombination and holes are accumulated to the surface by the electric field in depletion layer. The accumulated charges generate the displacement current through the BOX layer. So it is considered that the current can be suppressed by reducing of the width of depletion layer. The width changes with doping level of substrate and can be reduced using SOI substrate with highly doped substrate, n/n^+ device.

Figure 6 shows the peak of transient current and the amount of total collected charge form the anode electrode in n/n$^+$ device as a function of the heavy-ion hitting location. The transient current can be observed only when the ion hits to the edge of p$^+$ diffusion region. The peak current and collected charge in n/n$^+$ device are smaller than that of n/n device, and the amount of collected charge is about 100 fC which is same as the amount of generated charge in active SOI layer by irradiation.

Figure 7 shows the transient current and the collected charge from each electrode in n/n$^+$ device when the ion hits to the edge of p$^+$ diffusion region. The amounts of collected charge of anode and cathode electrodes are almost same and are less than 100 fC. The amount of collected charge by back electrode is about 20 fC that is much less than the result of n/n device. That indicates the collected charge by anode electrode is mainly caused by the radiation induced generated charge in active SOI layer.

From these results, it was confirmed that the heavy ion induced displacement current through the SOI layer could be suppressed using the device with highly doped handle substrate.

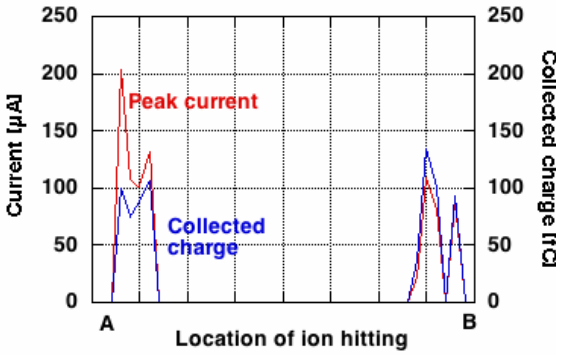

Fig. 6. Peak of transient current and total collected charge from anode electrode in n/n$^+$ device as a function of the heavy ion hitting location

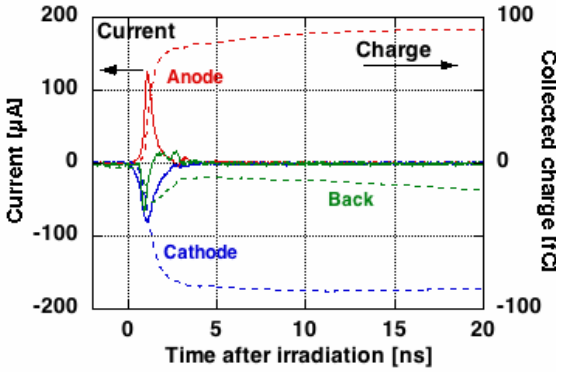

Fig. 7. Transient current and collected charge in n/n$^+$ device when ion hit to the edge of p$^+$ region

4. Conclusions

The heavy-ion induced transient current and collected charge in SOI p$^+$n diodes have been investigated. From the results of the device on n type SOI wafer, it was found that the amount of total collected charge by anode electrode exceeded the amount of radiation induced generated charge in active SOI layer and the anomalous charge collection is caused by displacement current through BOX layer. We also discussed the reduction of the displacement current by changing the width of depletion layer at surface of the handle substrate. By the experimental results, it was confirmed that the displacement current could be suppressed by decreasing the width of depletion layer, and the heavy-ion induced transient current and the total collected charge of SOI device can be reduced using the device with highly doped handle substrate.

Acknowledgments

This work was partially supported by the symbolic research project in college of science and technology, Nihon University.

References

[1] O. Musseau, "Single-Event Effects in SOI Technologies and Devices," IEEE Trans. Nucl. Sci., Vol. NS-43, No. 2, pp. 603-613 (1996).
[2] T. Hirao, T. Hamano, T. Sakai, and I. Nashiyama, "Studies of charge collection mechanisms in SOI devices using a heavy-ion microbeam," Nuclear Instruments and Methods in Physics Research, Vol. B-158, pp. 260-263 (1999).
[3] P.E. Dodd, et al., "SEU-Sensitive Volumes in Bulk and SOI SRAMs From First-Principles Calculations and Experiments, " IEEE Trans. Nucl. Sci., Vol. NS-48, No. 6, pp. 1893-1903 (2001).
[4] T. Hirao, et al., "Study of single-event current pulses induced in SOI diodes by collimated swift heavy-ions micro-beams," Nuclear Instruments and Methods in Physics Research, Vol. B-206, pp. 457-461 (2003).
[5] J.R. Schwank, P.E. Dodd, et al., "Charge Collection in SOI Capacitors and Cirsuits and its Effect on SEU Hardness," IEEE Trans. Nucl. Sci., Vol. NS-49, No. 6, pp. 2937-2947 (2002).
[6] Y. Takahashi, et al., "Heavy-ion induced current through an oxide layer," Nuclear Instruments and Methods in Physics Research, Vol. B-260, pp. 309-313 (2007).
[7] T. Sakai, T. Hamano, T. Suda, T. Hirao, and T. Kamiya, "Recent progress in JAERI single ion hit system," Nuclear Instruments and Methods in Physics Research, Vol. B-130, pp. 498-502 (1997).
[8] J.S. Laird, T. Hirao, H. Mori, S. Onoda, T. Kamiya, and H. Itoh, "The development of a new data collection system and chamber for microbeam and laser investigations of SEU phenomena," Nuclear Instruments and Methods in Physics Research, Vol. B-181, pp. 87-94 (2001).

Single Event Effects E – P2

Experimental study on radiation tolerance of SOI-PLLs

Eijiro Hoshino[*1], Daisuke Kobayashi[1,2], Takahiro Makino[3], Takeshi Ohshima[3], and Kazuyuki Hirose[1,2]
1 EE Dept., Graduate School of Eng.,University of Tokyo (UT), Japan
2 Institute of Space and Astronautical Sci., Japan Aerospace Exploration Agency (JAXA), Japan
3 Japan Atomic Energy Agency (JAEA), Japan
*Emails: e.hoshino@ac.jaxa.jp, hirose@isas.jaxa.jp,
Keywords:phase locked loops, heavy ion tests, and single event effects.

Abstract

Single event effects on phase locked loops (PLLs) are experimentally investigated. Test chips of the PLLs are fabricated in a 0.2-μm fully-depleted silicon-on-insulator technology. The PLL architecture is designed in conjunction with hardening techniques such as the triple modular redundancy and a stacked transistor design approach. A heavy-ion beam test confirms that the hardened PLL exhibits higher radiation tolerance than non-hardened one for 7.5-MeV Ne irradiation: The accelerated ions have the linear energy transfer of 7.3 MeV・cm^2/mg in Si.

1. Introduction

Phase locked loops (PLLs) are a circuit which supplies clocks to CPUs[1]. It generates an output-clock, accelerating a slow reference clock fed to the circuit. Its radiation tolerance needs to be high enough for the right work of CPUs under radiation environments; the output-waveform of the clock is distorted when a radiation particle hits the circuit[2-5]. We have designed a PLL the radiation tolerance of which is enhanced by using a 0.2-μm fully-depleted silicon-on-insulator (FD SOI) technology in conjunction with circuit design techniques such as a triple modular redundancy (TMR) technique [6] and a stacked transistor design [7].This work reports its experimental results; see simulation results in our previous paper [8].

2.Test vehicles

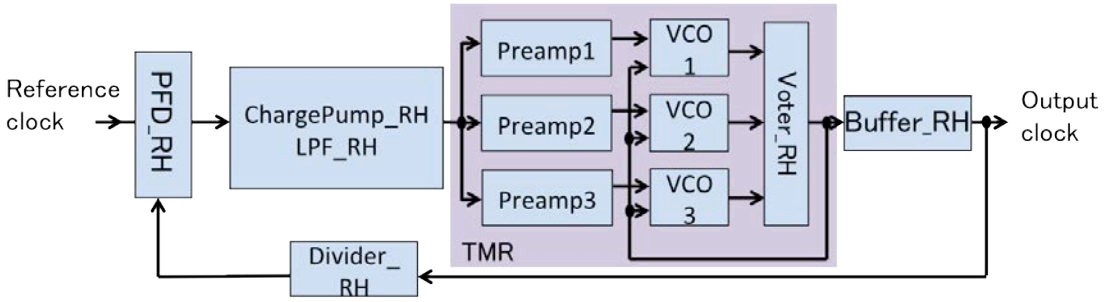

Fig.1 A block diagram of the designed SOI-PLL. PFD stands for phase frequency comparator.

Fig. 1 shows a block diagram of the tested SOI-PLL. TMR is applied to the voltage controlled oscillator (VCO) section. The stacked transistor design is applied to the all logic cells. To investigate effects of TMR, we have designed the PLL so that it can work with TMR deactivated: The power of one of the three VCO segments is kept off in this mode. In this paper, this operation mode is denoted as “non-TMR”. The other mode, where the three VCOs work harmoniously, is named “full-TMR”. The authors have fabricated test chips of the designed PLL with a radiation-hardened 0.2-μm FD SOI technology we developed [9]. To examine effects of the stacked transistor design, the chips have another “non-hardened” PLL, where neither TMR nor stacked transistor design is used.

3. Experimental tests

We have carried out a heavy-ion beam test in Takasaki Ion Accelerators for Advanced Radiation Application (TIARA) of JAEA. Ions such as 75-MeV $^{20}Ne^{4+}$ (its linear energy transfer or LET is 7.3MeV・cm^2/mg), 150-MeV $^{40}Ar^{8+}$ (15MeV・cm^2/mg), and 322-MeV $^{84}Kr^{17+}$ (40MeV・cm^2/mg) have been applied to the circuit in a vacuum chamber. The particle flux is about 5×10^3 count/cm^2/sec and the particle fluence is1×10^6count/cm^2,

which corresponds to an irradiation time of 200 sec. The circuit has been kept in operation during irradiation. The cycle length of the reference clock is fixed at 50 nsec, thus that of the output clock 10 nsec. This irradiation process has been carried out in the three various levels of mitigation technologies such as full-TMR, non-TMR, and non-hardened. During each irradiation time, to count the number of errors, we have used a trigger function of a high-speed single-shot oscilloscope(Wave Master 830Zi produced by LeCroy corporation).Errors are here defined as more than 10% changes in the cycle length of the output clock, which should be kept at 10nsec while the system works properly. Note that this measurement system is unable to detect events for 1μs after the trigger operation, i.e., the dead time is 1 μs, which is negligibly small compared to the event rates expected from the flux value. We have thus calculated the cross section according to Eq.1:

$$\text{Cross section } (\text{cm}^2) = \frac{\text{Number of errors (count)}}{\text{Flux (count/cm}^2\text{/s)} \times \text{Irradiation time (s)}}. \qquad \text{(Eq.1)}$$

These cross section measurements have been performed twice for each ion tests.

During the Ne and Kr tests, for more detailed analyses, we have recorded 50 waveforms for each irradiation time. Dynamic voltage evolution at the output is stored in each record of 5000 data points with a time resolution of 0.1nsec, thus a ±250-nsec system response is captured in total, where time "0" indicates the time at which the error is detected. From the stored waveform, to calculate the cycle lengths (T), we have read out clock edge time (t) because each cycle length is determined by the time between two adjacent clock edges. The defined clock edge time is the time when the voltage exceeds the threshold voltage (V_{th}), which is designed to be 0.25 volts. To ignore noises, ±0.05-volts margin is considered in this threshold operation (Fig. 2). Then we have drawn T - t graphs as shown in Fig.3: When a cycle length T_1 is sandwiched between two adjacent clock edges t_1 and t_2 (t_1 is earlier than t_2), we have plotted a point (t_1, T_1). This graph is representation helps us to understand cycle length modulations as a function of the elapsed time.

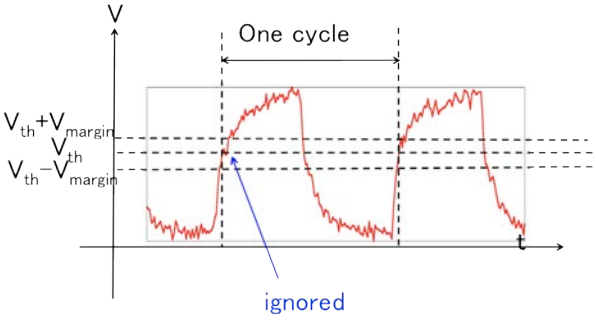

Fig .2 The define of one cycle.

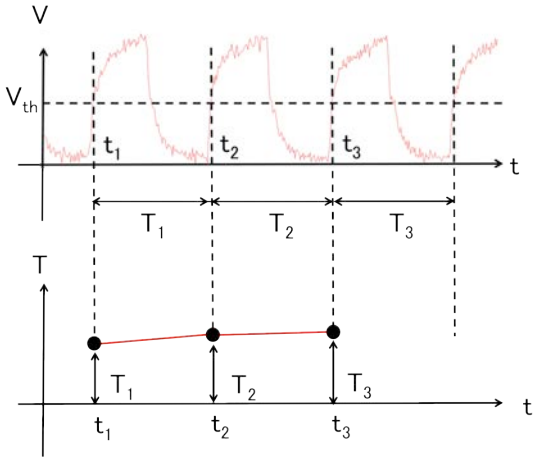

Fig.3 The way to plot the points (t,T)

4. Results

4.1cycle length modulations

Fig. 4 shows a result of cycle-length analyses. Represented by 50black lines, time-depended cycle-length modulations are extracted from 50waveforms under the Ne irradiation. The two red broken lines superimposed on the figures correspond to T = 9 nsec and 11 nsec. They represent the upper and lower boundaries of the acceptable margin. In the all circuit conditions (Fig. 4 a-c), it is observed that variations in T exceed the 10% acceptable margin at around t = 0. As the time elapses (around 100 nsec), these variations recover into the acceptable zone. These figures demonstrate that effects of a single-event transient (SET) on the PLLs continue seriously in a long time, although the original SET is as short as 100 psec [10]. The T-modulation of the non-hardened is lager and longer (Fig. 4(a)): Its max-min variance is 8.46 nsec and many of signals do not recover even after 250 nsec. Fig. 4(b) exhibits effects of the stacked transistor design (non-TMR): Its max-min variance is 5.40 nsec and most of the signals recovered at around 100 nsec. The stacked transistor design works effectively. The full-TMR exhibits the best results: Its max-min variance is 3.99 nsec and,

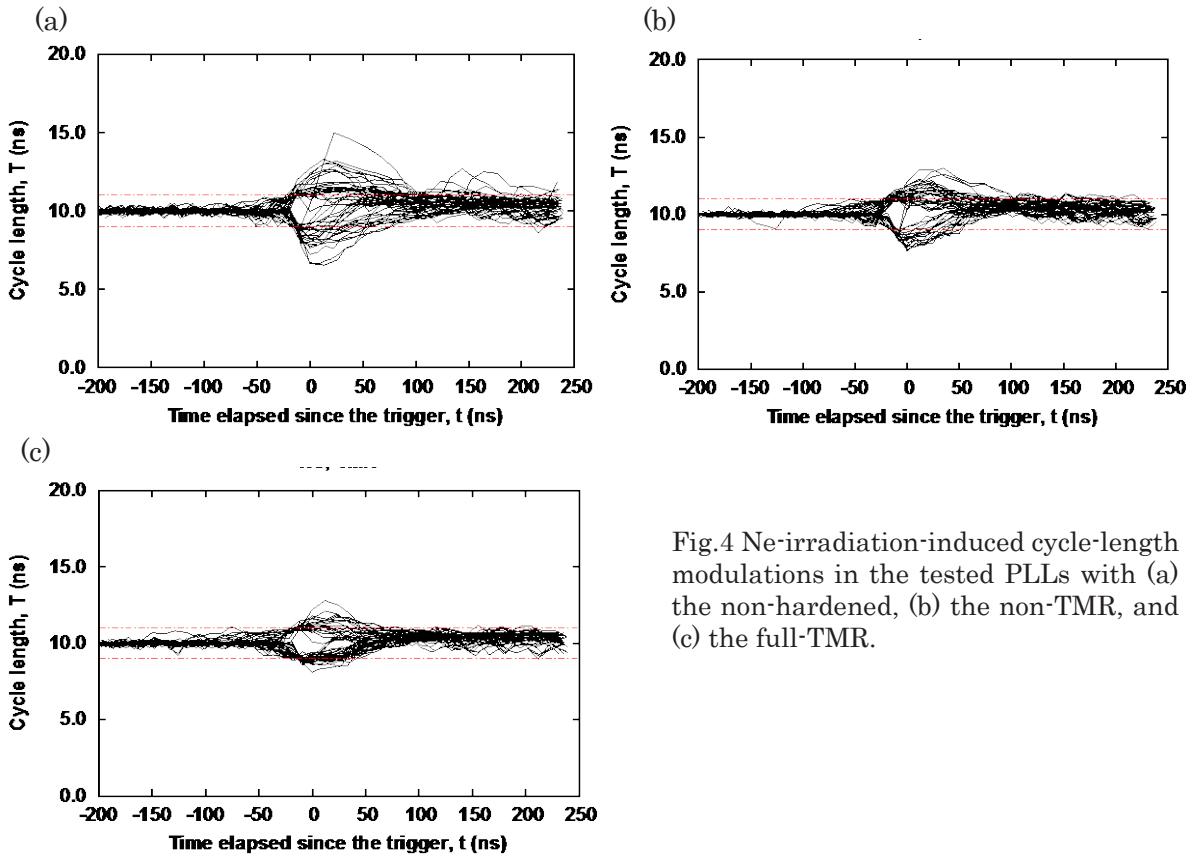

Fig.4 Ne-irradiation-induced cycle-length modulations in the tested PLLs with (a) the non-hardened, (b) the non-TMR, and (c) the full-TMR.

although a few signals are still in the error zone, almost all signals recover at around 50 nsec.

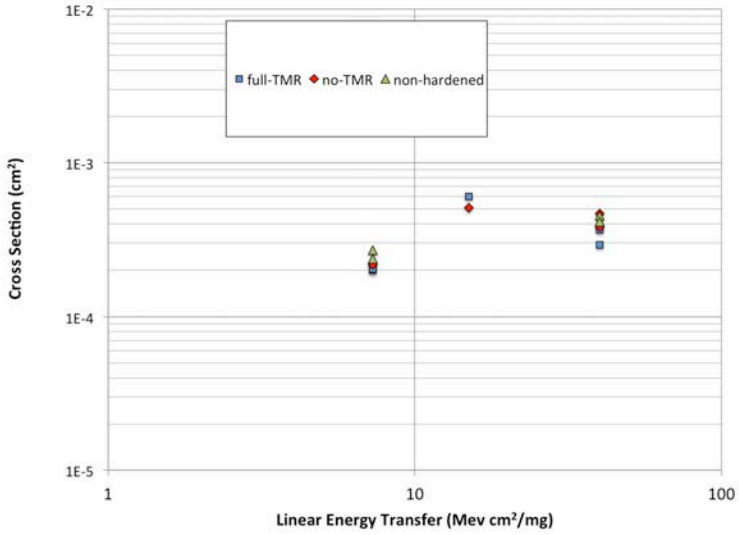

Fig. 5 The cross section-LET graph.

The TMR effectiveness is clearly observed. The Kr irradiation, on the other hand, does not exhibit this clear trend in the effectiveness of the hardening techniques, which needs further investigations.

4.2cross section

The resultant cross sections are shown in Fig.5 and summarize in Table 1. For both Ne and Kr irradiation tests, we can see the same trends as in the previous T-modulation tests.

The experimental cross sections are two orders of magnitude larger than simulation results [8]. The mitigation techniques may have some room to be improved, and there may be some circuit parts vulnerable to radiation attacks, that parts are not considered in the simulations.

Table 1 Cross sections.

Experiment	LET (MeV・cm^2/mg)	7.3(Ne)	15(Ar)	40(Kr)
	Cross section of full-TMR (cm^2)	2.0×10^{-4}	6.0×10^{-4}	3.7×10^{-4}
		2.0×10^{-4}	-	2.9×10^{-4}
	Cross section of non-TMR (cm^2)	2.2×10^{-4}	5.1×10^{-4}	4.7×10^{-4}
		2.2×10^{-4}	-	3.8×10^{-4}
	Cross section of non-hardened (cm^2)	2.7×10^{-4}	-	4.5×10^{-4}
		2.4×10^{-4}	-	4.1×10^{-4}

Simulation [8]	LET (MeV・cm^2/mg)	15	20	50	500
	Cross section of full-TMR (cm^2)	-	0.0	0.0	36.2×10^{-7}
	Cross section of non-hardened (cm^2)	3.5×10^{-7}	2.0×10^{-6}	2.1×10^{-6}	2.4×10^{-6}

5.Conclusion

We have examined radiation tolerance of PLLs that are protected by using a 0.2-μm fully-depleted SOI technology in conjunction with circuit design techniques such as a full-TMR technique for the voltage-controlled oscillator section and a stacked transistor design for the digital logic cells. The ion-irradiation results demonstrate that both techniques are effective, when LET is small, at least.

Acknowledgments

The authors would like to thank S. Ishii, D. Matsuura, and M. Kusano of Mitsubishi Heavy Industry, for developing the SOI-PLL test chips and giving supports to experiments and analyses.

References

[1] N. H. E. Weste, and D. Harris, “CMOS VLSI Design: A Circuits and Systems Perspective, Third Edition,” Addion Wesley (2005).
[2]Y. Boulghassoul, L. W. Massengill, A. L. Sternberg, and B. L. Bhuva, “Effects of Technology Scaling on the SET Sensitivity of RF CMOS Voltage-Controlled Oscillators,” *IEEE Trans. Nucl. Sci.*, vol. 52, no.6, pp. 2426-2432 (2005).
[3]Y. Boulghassoul, L. W. Massengill, A. L. Sternberg, B. L. Bhuva, and W. T. Holman, “Towards SET Mitigation in RF Digital PLLs: From Error Characterization to Radiation Hardening Consideration,”*IEEE Trans. Nucl. Sci.*, vol. 53, no.4, pp. 2047-2053 (2006).
[4]T. D. Loveless, L. W. Massengill, B. L. Bhuva, W. T. Holman, A. F. Witulski, and Y. Boulghassoul, “A Hardened-by-Design Technique for RF Digital Phase-Locked Loops,”*IEEE Trans. Nucl. Sci.*, vol. 53, no.6, pp. 3432-3438 (2006).
[5]T. D. Loveless,L. W. Massengill, B. L. Bhuva, W. T. Holman, R. A. Reed, D. McMorrow, J. S. Melinger, and P. Jenkins, “A single-Event-Hardened Phase-Locked Loop Fabricated in 130 nm CMOS,”*IEEE Trans. Nucl. Sci.*, vol. 54, no.6, pp. 2012-2020 (2007).
[6]T. D. Loveless, L. W. Massengill, B. L. Bhuva, W. T. Holman, M. C. Casey, R. A. Reed, S. A. Nation, D. McMorrow, and J. S. Melinger, “A Probabilistic AnalysisTechnique Applied to aRadiation-Hardened-by-Design Voltage-ControlledOscillator for Mixed-Signal Phase-Locked Loops”*IEEE Trans. Nucl. Sci.*, vol. 55, no. 6, pp.3447-3455 (2008).
[7] A. Makihara, M. Midorikawa, T. Yamaguchi, Y. Iide, T. Yokose, Y. Tsuchiya, T. Arimitsu, H. Asai, H. Shindou, S. Kuboyama, and S. Matsuda, “Hardness-by-Design Approach for 0.15 μm FullyDepleted CMOS/SOI Digital Logic DevicesWith Enhanced SEU/SET Immunity” *IEEE Trans. Nucl. Sci.*, vol. 52, no.6, pp. 2524-2530 (2005).
[8]D. Matsuura, K. Hirose, D. Kobayashi, S. Ishii, M. Kusano, Y. Kuroda, and H. Saito, "Radiation-Hardened Phase-Locked Loop Fabricated in 200 nm SOI-CMOS," in proceedings of *RADECS 2011*, Sevilla, Spain (2011).
[9]K. Hirose, H. Saito, Y. Kuroda, S. Ishii, Y. Fukuoka, and D. Takahashi, “SEU Resistance in Advanced SOI-SRAMs Fabricated by Commercial Technology Using a Rad-Hard Circuit Design,”*IEEE Trans. Nucl. Sci.*, vol. 49, no.6, pp. 2965-2968 (2002).
[10]T. Makino, D. Kobayashi, K. Hirose, Member, Y.Yanagawa, H. Saito, H. Ikeda, D. Takahashi, S. Ishii,M. Kusano, S. Onoda, T.Hirao, and T. Ohshima “LET Dependence of Single Event Transient Pulse-Widths in SOI Logic Cell,” *IEEE Trans. Nucl. Sci.*, vol. 56, no.1, pp. 202-207 (2009).

SEE Tests of the 4Gb and 8Gb Nand Flash

Pierre-Xiao Wang1, P-E Berthet1, L. Gouyet2, A. Rousset2, B. Vandevelde2
1 : 3D Plus , 408, rue Hélène Boucher, Buc, FRANCE
2: TRAD, 907 voie l'Occitane, Labège, France
Email :pwang@3d-plus.com
Keywords: Nand Flash, SEE, High Current Event, Function Failure

Abstract

This paper summarizes SEE test results on Micron 4Gb and Samsung 8Gb Nand Flash device focusing on High Current Events and Function Failure resulting from radiation events.

Introduction

NAND Flash uses floating-gate transistors, with the transistors connected in a structure resembling a NAND gate. Comparing to fault-free Nor Flash, Nand Flash also contains a limited number cell faults to maximize the storage capacity [1]. Both of these allow the Flash Nand to achieve very high density.
For space applications, many papers have been published on Nand Flash radiation characteristics. Most test results [2,3,5] show that Nand Flash is an acceptable solutionfor mass storage applications in space environments.
Meanwhile, as the process scaled down and the complicity of the control unit inside of the Nand Flash, some new phenomena, like High Current and Functional Failure, have been observed.
This paper characterizes Micron 4Gb and Samsung 8Gb Nand Flash SEE, not only SEL, SEU and SEFI but also High Current and Functional Failure. Moreover, this report is trying to summary an efficient test method to characterize different Single Event Effects and calculate their rates.

Description of Devices Under Test(DUT)

The tests performed at Catholic University of Louvain on May and December, 2011 and March 2012. Approximately forty delidded samples from Micron and Samsung were irradiated.

Table 1: SEE tests samples summary

Manufacture	Type	Density	Package	LDC	Sample Size
Micron	Nand SLC	4Gb	SOP48	1006	19
Samsung	Nand SLC	8Gb	SOP48	1031 1004	16

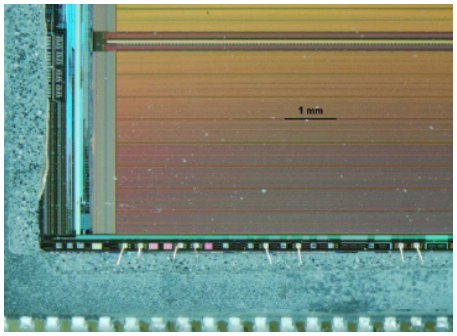

Figure1: Samsung 8GbNand Die

Experimental Procedure

Test facility: Catholic University of Louvain Cyclotron (U.C.L).

Table 2 Describes the availableions for the heavy ion SEE testing.
During the test, the power supply is monitored by a Protection circuit with a current threshold limiter. When an event occurs, the Protection circuit sends a trigger command to the oscilloscope to record this one, holds on the power supply during 1ms and cuts off during 7ms. Then, the power supply is applied again with the expected nominal current consumption. During the test current consumption is recorded with an ammeter at a sampling rate of one record every 150ms, and plotted for each run.
We performed runs up to a fluenceof 1.10^6 particles/cm^2

Table2 : Ions/Energys and LETs/Ranges

	Ion	DUT energy [MeV]	Range [µm Si]	LET [MeV/mg/cm²]
FORT LET	$^{124}Xe^{26+}$	420	37	67.7
	$^{84}Kr^{17+}$	305	39	40.4
	$^{40}Ar^{8+}$	151	40	15,9
	$^{20}Ne^{4+}$	78	45	6.4
	$^{15}N^{3+}$	60	59	3.3
FORT RANGE	$^{83}Kr^{25+}$	756	92	32,6
	$^{58}Ni^{18+}$	567	100	20.4
	$^{40}Ar^{12+}$	372	117	10,2
	$^{22}Ne^{7+}$	235	216	3
	$^{13}C4+^{+}$	131	292	1.1

for SEU, MBU, SEFI, while a fluence of 1.10^7 particles/cm^2 for the SEL, Functional Failureand High Current Events. During SEU, MBU and SEFI tests, a latchup monitoring was also done on the component's power supply in conjunction with the Protection circuit to eliminate destructive latchups.

Three test modes have been used:

- Static biased : SEL, SEU, MBU, SEFI, HCE, FF
- Dynamic Read Only: SEU, MBU, SEFI, HCE, FF
- Dynamic Erase/Write: SEU, MBU, SEFI, FF

* HCE: High Current Event, FF: Functional Failure

Current Threshold settings:

- SEL testing: High Current threshold guard to identify Real SEL form High Current Event;
- High Current Event (Standby + dynamic mode during irradiation): Low Current threshold guard to count the High Current trigger during irradiation, and also power cycle after the triggers;
- Functional Failure (Dynamic Read-only + Read-Write during irradiation): No current guard to identify all possible events, and also functional verification continually till events.

Results

1. SEL

No SEL observed for both Micron 4Gb and Samsung 8Gb samples during the tests until 67.7Mev.cm^2.mg^{-1} at 125C degree Static mode.

2. SEU, MBU & SEFI

SEUs and MBUs are defined by nondestructive single (SEU) or multiple (MBU) changes in the cell logic state from one to zero or vice-versa, and for which the cell logic state can be rewritten or reset. A SEFI is defined as a component state exhibiting a locked behavior requiring a complete reset of the system; in the context of this test, a SEFI is considered to be: at least half of a page of the flash memory exhibiting errors, or operational timeouts (the component performs operations with a period greater than device specifications).
Figure2 to Figure7 show the results from the tests in different test modes.

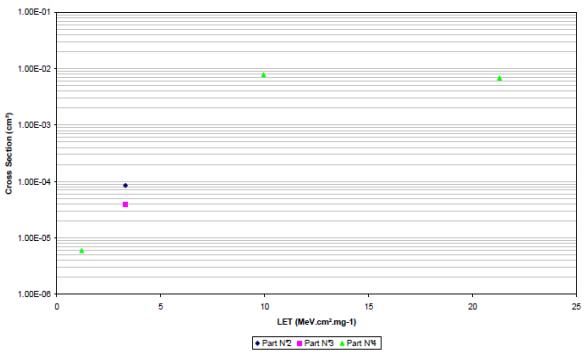

Figure 2: SEU Full static Mode cross section, Micron 4Gb Flash

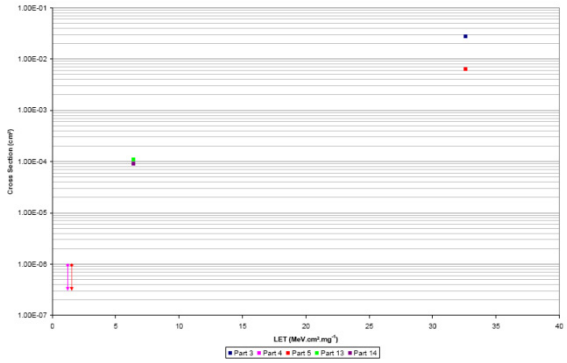

Figure 3: SEU Full static Mode cross section, Samsung 8Gb Flash

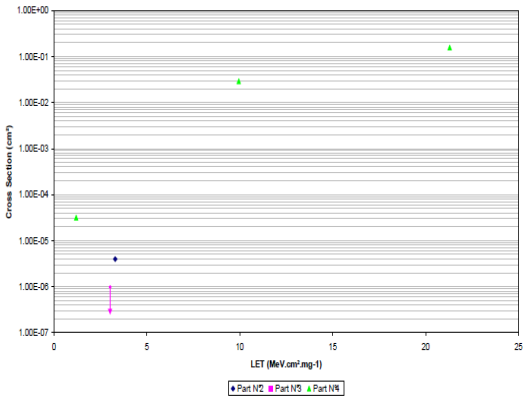

Figure 4: MBU Read only Mode cross section, Micron 4Gb Flash

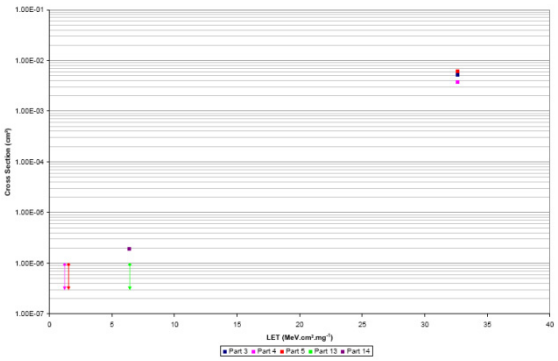

Figure 5: MBU Read only Mode cross section, Samsung 8Gb Flash

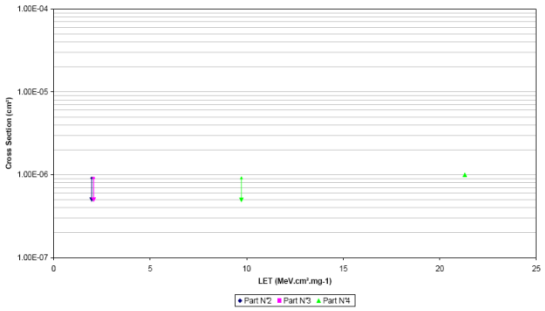

Figure 6: SEFI Erase/Write Mode cross section, Micron 4Gb

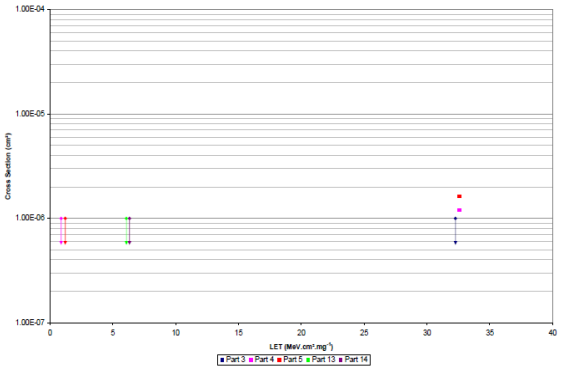

Figure 7: SEFI Read only Mode cross section, Samsung 8Gb

3. High Current Event

High Current Events, or High Current Spikes, have been observed and mentioned in previous studies [2,3,5], and researched in study [2] with a description of the High Current mechanism in study [4].

During our SEE testing, High Current Events observed from both Micron and Samsung, and the Micron current curve exhibited a much higher current peak. Figures 8 and 9 are examples of 4Gb Micron Nand Flash current curves during SEL (High Current threshold) and High Current Eventtest (low current threshold).

Although much higher current peak was recorded during Micron 4Gb Nand Flash test, no Functional Failure was found.

To evaluate the risk, we set 50mA as the current threshold to measure the High Current Event, and the results show in Table 3.

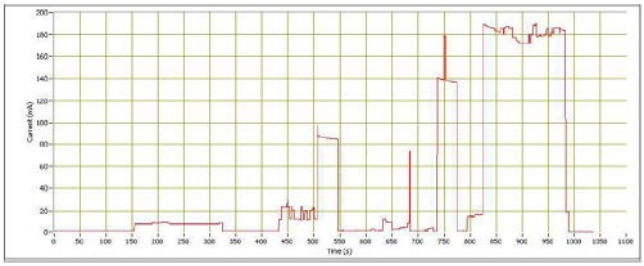

Figure 8: Current curve during SEL testing (no trigger) at LET=40.1Mev.cm^2.mg^{-1}

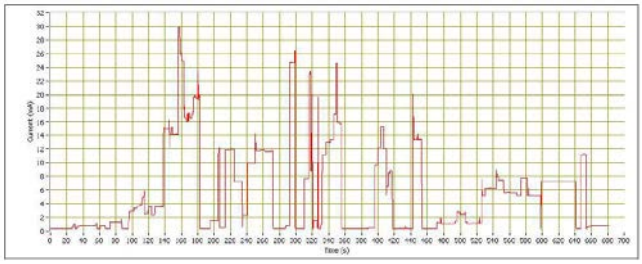

Figure 9: Current curve during High Current testing (low current threshold, triggers) with LET=40.1Mev.cm2.mg-1

Table3: Micron 4Gb HCE triggers Crosse Section

LET Eff [MeV/mg/cm²]	Cross Section (cm2)
40.1	6.00E-07
31	2.00E-07
21.3	2.00E-07

4. Functional Failure

During Samsung 8Gb SEL test, no SEL event was observed, and the current peak was much lower than Micron 4Gb, but some Functional Failures were observed in functional verification at High LET.

Additional tests with a fluenceof 1.10^6 particles/cm^2 have been performed at 25C degree for Read only mode and 125C degree for Erase/Write Mode, results are summarized in table4.

Only one fail at LET=59.86 MeV/mg/cm² has been observed at the end of the irradiation with the fluenceapproaching 1.10^6 particles/cm^2.

Table 4: Samsung 8Gb Functional Failure test result

LET Eff [MeV/mg/cm²]	Functional Mode During Irradiation					
	Read Only			Erase/Write		
	No2	No3	No 4	No2	No3	No 4
59.86	X	Pass	Fail	X	Pass	X
32.6	Pass	Pass	X	X	Pass	Pass
10.2	Pass	Pass	X	Pass	Pass	X

Discussion

There were very few surprises during SEU&SEFI tests, and the test results in general corresponded to previous studies. The approximate error rate calculated in an Adams 90 GEO orbit Environment for each component is summarized as follows:
Micron 4Gb Nand Flash Single bit Upset rate: 6.56E-15 error/bit/day, and SEFI rate: 3.1error/device/year;
Samsung 8Gb Nand Flash Single bit Upset rate: 3.46E-16 error/bit/day, and SEFI rate: 0.1error/device/year.
The data provided by the Die manufactures show that Micron 4Gb and Samsung 8Gb samples have similar Estimated Failure Rate (FIT), around 5 failure per 109 hours. From the High Current Event and Functional Failure results in the former chapter, we may calculate that the event rates are the same order of the FITin an Adams 90 GEO orbit Environment around 3 to 4E-3 error/device/10years.

However, the High Current Event and Functional Failure mechanisms may disturb the SEL test because the current threshold setting and Functional verification are sensitive in determining an SEL event.
As mentioned in this report, Micron 4Gb had much higher peak current but without Functional Failure comparing that Samsung 8Gb had Functional Failure but it did not show direct link to the current. In this case, the current threshold setting is critical.
After several evaluations, we set the current threshold at high level during SEL testing, and a relative low level during High Current Event testing with no threshold during Functional Failure testing. During testing nominal currents were variable between components, which make it difficult to establish a uniform definition of the current thresholds for each level which is supported by observations during testing and prior studies. We also did not see the direct link between the High Current Event and the test modes.
We noted that another factor impacted the accuracy of the result is the flux. To accelerate the test, normally the tester takes higher flux, which increases the risk of two particles striking at one transistor at a time. However in space, the ions flux is so low, it will be never happen. Meanwhile, the ground test result probably will completely change at same fluence but with lower flux.

Conclusion

We measured the Micron 4Gb and Samsung 8Gb SEE characteristics. Complex designs and small feature sizes of the Nand Flash samples in conjunction with High Current Events, Functional Failures and the flux complicated the test results and analysis.

After improvements in measurement procedures we established a comprehensive characterization routine for SEL, SEU, MBU, SEFI, High Current Event and Functional Failure testing and analysis. The results indicate the Micron 4Gb and Samsung 8Gb Nand Flash are ideal components for most of the space missions. In our evaluation new events were observed in High Current and Functional Failure areas, but the rates are very low (Same level of FIT as showed in previous chapter).

In summary this report has documented test methods and test results of Nand Flash SEE, including new events, and characterizes them in space environment.

References

[1] A. K. Sharma, “Advanced Semiconductor Memories”, IEEE , 2003.
[2] Timothy R. Oldham, Kenneth A. LaBel, etc.. “Investigation of Current Spike Phenomena During Heavy Ion Irradiation of NAND Flash Memories, NSREC 2011 – Oldham W-25
[3] H. Schmidt, D. Walter, F. Gliem, etc.. “TID and SEE Tests of an Advanced 8 GbitNAND-Flash Memory” July 1, 2008, Supported in part by the ESA / ESTEC.
[4] H. Shindou, S. Kuboyama, T. Hirao, and S. Matsuda “Local and Pseudo SELs Observed in Digital LSIs and Their Implication to SEL Test Method” IEEE TRANSACTIONS ON NUCLEAR SCIENCE, VOL. 52, NO. 6, DECEMBER 2005
[5] Irom. F, Nguyen,D.N. “Single Event Effect Characterization of High Density Commercial NAND and NOR Nonvolatile Flash Memories” Nuclear Science, IEEE Transactions on, 2007, Volume: 54 , Issue: 6 Page(s): 2547 - 2553

Single Event Effects E – P9

Consideration of Single-Event Gate Rupture Mechanism in Power MOSFET

S. Kuboyama[1], E. Mizuta[*1], N. Ikeda[1], H. Abe[2], T. Ohshima[2], and T. Tamura[1]
1 Japan Aerospace Exploration Agency (JAXA), Japan
2 Japan Atomic Energy Agency (JAEA), Japan
*Email: mizuta.eiichi@jaxa.jp
Keyword(s): Power MOSFETs, SEGR, Heavy ions, single-event effects, radiation damage

Abstract

The catastrophic failure mode caused by single-event gate rupture phenomenon observed in power MOSFETs still remains as a critical issue for those devices to be used in space radiation environments. Detailed analyses of the devices damaged by the phenomenon suggested a new possible mechanism. A preliminary model for the mechanism was proposed.

1. Introduction

Power MOSFETs are widely used for power handling portion of the electronic devices for space system as well as for ground-based commercial devices. However the catastrophic failure mode caused by single-event gate rupture (SEGR) in space radiation environments still remains as a critical issue for those devices.

The phenomenon of SEGR in power MOSFETs was reported for the first time in 1987 [1]. Over the past 20 years, the phenomenon was extensively characterized [2-9] and several models have been proposed to describe their mechanism [10-13]. In these studies, SEGRs are detected by abrupt increase of the gate and the drain current during heavy ion irradiation under the reverse bias condition, i.e. the device is in OFF state, according to the military specification [14]. Because the abrupt increase of the gate and the drain currents are usually observed simultaneously, it is assumed that the gate dielectric breakdown occurs between the gate and the drain. In addition to the in-situ observation, the increased gate current is measured to confirm the damage introduced by the irradiation as a post irradiation test. However, the drain terminal is tied to the source terminal for the measurement in general.

In the course of qualification test of power MOSFETs for space applications, a curious behavior was found that the leakage current introduced by SEGR phenomenon was not a simple current flowing through the damaged gate oxide area faced to the drain region on Si surface of the device die. Although the sample devices were manufactured by Fuji Electric (Tokyo, Japan) for the first observation, the same behavior was also confirmed with the devices from ST micro and IR.

To confirm the origin of the behavior, special test structures were fabricated with the manufacturing process for the p-channel power MOSFETs submitted for the qualification test. As a result of SEGR test on the test structures, it was found that the behavior was responsible to the specific structure of power MOSFETs.

In this paper, the curious behavior found in the course of the qualification test will be reviewed in detail. After the review, the results on the additional test structures will be discussed. Finally, a possible model for the mechanism of SEGRs will be proposed.

2. Review of Devices Damaged by SEGR

The irradiation test for SEGR phenomenon was carried out on the p-channel power MOSFETs for space applications manufactured by Fuji Electric. There were 2 rated voltage types, i.e. 100 and 200 V. Kr ions (768 MeV) from the cyclotron facility, RADEF, at Jyväskylä University in Finland were used for the experiments. Their LET at the device surface and range are calculated by using SRIM [15] as 32.4 MeV(mg/cm^2) and 94.1 μm, respectively. The range is sufficient to pass through the active layers of the power MOSFETs. A typical current monitor data during irradiation is shown in Fig. 1 for the device with 100 V of rated drain voltage. In this case, SEGR was observed just after V_{GS} switching from 12.5 V to 15 V. During the V_{GS} switching, the ion irradiation was interrupted. As the result of SEGR, I_{GS} and I_{DS} were abruptly increased to 2.86 mA and 690 μA, respectively. The current increases might suggest that the gate oxide was damaged and the current was injected from the gate, and flowing out to the drain and the source electrodes, because the current values were not identical. It was supposed that there were 2 current paths at least.

The electrical behavior of the damaged region introduced by SEGR has not been reported. It should be noted that the behavior cannot be explained by the model formerly proposed for SEGR mechanism [10]. According to those models, the maximum electric field is generated across the gate oxide on the drain region when an incident ion perpendicularly passes through the region. Therefore, the damaged gate oxide should be located on the drain region according to the model.

3. Experimental

To obtain additional information on the curious behavior, the test structures were fabricated with the manufacturing process for the p-channel power MOSFETs the behavior was found. Fig. 2 shows the cross-sectional views of the test structures. The structure A has a normal power MOSFET structure for reference. For the structure B, the source diffusion was omitted. Therefore many p-n diodes are formed between the drain and the source electrodes. For the structure C, the body diffusion was formed without masking. Therefore, a large p-n diode is formed on a chip. The structure D was fabricated with the same procedure for the structure C and the source diffusion was also omitted. These test structures were fabricated on the substrates both for 100 and 200 V devices, i.e. a total of 8 types of test structures. Those test structures will be identified as 100A, 100B, and so on, in this paper.

For these structures Kr ions (713 MeV) from the RIKEN Ring Cyclotron (RRC) at RIKEN in Japan were used for the experiments. Their LET at the device surface and range are calculated by using SRIM [15] as 33 MeV(mg/cm2) and 87 μm, respectively. The range is sufficient to pass through the active layers of the test structures.

As the experimental results, SEGRs were observed for the test structures A and B. For 100 V devices, SEGRs were observed at VDS = -100V and VGS = +12.5 V. For 200 V devices, SEGRs were observed at VDS = -200V and VGS = +7.5 to +10.0 V. In contrast, no SGER was observed for the test structures C and D at VGS = +15.0V and the rated drain voltages up to a fluence of 105 p/cm2. We can conclude that

(1) SEGRs are triggered regardless of the source diffusion,

(2) the existence of the body edge is a key to trigger SEGRs.

In addition to the p-channel power MOSFETs, n-channel power MOSFETs were examined for the electrical behavior, which were already damaged by SEGR tests and stored in our laboratory. The rated drain voltages of the devices were 100 and 130 V. For those devices, Kr ions (315 MeV) from the cyclotron facility, TIARA, at Japan Atomic Energy Agency (JAEA) in Japan were used for the SEGR tests. Their LET at the device surface and range are calculated by using SRIM [15] as 40.0 MeV(mg/cm2) and 40.1 μm, respectively. The range is also sufficient for the tests. Because of n-channel devices, the polarity of the voltage and the direction of the current were opposite, but the same behavior was observed.

Additional experiments for the test structures were performed with VDS = 0V. Kr ions from TIARA were also used for the experiments. SEGRs were observed at VGS of -38 to -44 V with average of 41.6 V regardless of the structure type and rated voltage. The value is predicted by an experimentally obtained fitting equation [5] as 45.6. The values are in good agreement. However, the electrical behaviors of the damaged devices were also very interesting. For the structure A and C, only leakage current path between the gate and source electrodes was confirmed. For the structures B and D, the same I-V characteristics as structures A and B were observed.

4. Discussion

4.1 Model of the current path to the drain after SEGR

The drain current pass through the body-drain junction where no damage was observed even after SEGR might be explained by minority carrier injection effect in an analogous way for bipolar transistors. In bipolar transistors, the minority carriers are injected from the emitter to the base region, and then they can be diffused into the collector region escaping recombination in the base region even if the base-collector junction is in reverse bias condition.

In the case of power MOSFETs damaged by SEGR, the minority carriers must be injected from the gate electrode to the body region through the damaged gate oxide. Fig. 3 shows the energy band diagram to explain the hole injection observed in the damaged p-channel MOSFETs. In this diagram, it was assumed that the current path inside the oxide was formed by the localized states or damage sites and conduction occurred by hole hopping between them [16], although exact conduction mechanism had not been identified. There are several possible mechanisms for hole conduction through the damaged oxide, for example [17]. To open the hole conduction path to the valence band of the body region, the applied gate voltage need to be larger than a certain threshold level as shown inset (b) in Fig 3.

It should be noted that there are also several possible mechanisms for electron conduction through the damaged oxide [17] to explain the I-V characteristics observed in n-channel power MOSFETs damaged by SEGR.

4.2 Location of SEGR damage

As mentioned in the section II, the damage region caused by SEGR had been considered to be located inside the oxide faced on the drain region where the drain bias was applied, because the highest electric field is generated by ions perpendicularly incident in the neck region (the region between body diffusions) [10]. In contrast, the damaged region experimentally observed was located inside the oxide faced on the body region. In addition to the fact, the body diffusions must have edge in the epitaxial layer (the drain region) as islands floating in the ocean.

According to the models for oxide breakdown [16], electrons injected into the oxide can be accelerated by the electric field applied across the oxide for impact ionization and trap creation mechanisms. This is the reason that the highest field region had been considered as the responsible region for SEGR. However the body diffusion is usually tied to the ground in normal applications of power MOSFETs. Therefore the electric field across the oxide between the gate and the body diffusion is basically separated from the electric field induced by the voltage applied to the drain and no destructively higher field is expected. However it might be possible in the power MOSFET structure to accelerate the electrons by the electric field across the body-drain junction and to inject them into the gate oxide as shown in Fig. 4. The oxide breakdown caused by hot carrier injection was studied and reported [18]. According to the study, the charge to breakdown, Q_{BD}, significantly depends on the energy of electrons injected and do not depend on the oxide field. As illustrated in Fig. 4, the electrons are generated along the ion track and accelerated by the electric field applied across the body-drain junction and injected into the gate oxide. The edge portion of the body diffusions might be more effective for the injection because of reduced thickness of the diffusions. More quantitative discussion will be made in the full paper for the mechanism.

For the cases with V_{DS} = 0V during irradiation, the electrical behaviors of the damaged devices of the structure B and D were exactly the same as the structures A and B with the rated V_{DS} was applied. The structures B and D had no source diffusion. Therefore, the electric field was applied only the gate oxide facing to the body diffusion and damage region must be introduced in the region. For the structures A and C, only the leakage current was observed between the gate and source electrode. From the behavior, it was supposed that the damaged region was located in the gate oxide facing to the source diffusion.

For n-channel power MOSFETs, hot holes can be injected into the oxide instead of hot electrons for p-channel devices. Unfortunately the hole fluence to breakdown, Qp, is not so sensitive to the energy of the injected holes according to the report [18]. There are possibilities that the drain voltage changes the injected hole fluence instead of the energy. The SEGR mechanism for n-channel device will be a future subject.

The electrical behavior observed with the power MOSFETs damaged by SEGR might be common to the devices from other manufacturers. Some of them were confirmed in our laboratory. The same behavior, i.e. I_{GS} was higher than I_{DS} at SEGR occurrence, was also found in the published paper [19].

5. Conclusion

The electrical characteristics of power MOSFETs damaged by SEGR were analyzed in detail. The analysis indicated a curious behavior and it was successfully explained by the minority carrier injection through the damaged gate oxide.

The behavior also requested a new SEGR mechanism to describe the phenomenon. The damaged spot inside the gate oxide introduced by SEGR was located on the body diffusion, where the electric field induced by incident ions had not to be so strong. The experiments with the test structures clearly indicated that the body diffusions in the epitaxial layer for the drain depletion region are responsible structure for SEGR. A possible mechanism of SEGR was proposed, where hot carriers were generated by the electric field across the body-drain junction and injected into the gate oxide. Additional work will be required to confirm the mechanism especially for n-channel MOSFETs.

Acknowledgments

The authors gratefully acknowledge the technical support of the members of Ryoei Technica Corporation for the experiments and analysis. They also thank the members of accelerator operation group at JAEA, Jyväskylä University and RIKEN and for their helpful support.

References

[1] T. A. Fischer et al., “Heavy-ion-induced, Gate-rupture in power MOSFETs,” IEEE Trans. Nucl. Sci., NS-34, No. 6, pp 1786-1791, Dec. 1987.

[2] C. F. Wheatley et al., "Single-event gate rupture in vertical power MOSFETs; an original empirical expression," IEEE Trans. Nucl. Sci., NS-41, No. 6, pp.2152-2159, Dec. 1994.

[3] I. Mouret et al., "Temperature and angular dependence of substrate response in SEGR [power MOSFET]," IEEE Trans. Nucl. Sci., NS-41, No. 6, pp. 2216-2221, Dec. 1994.

[4] D. K. Nichols et al., "Observations of single event failure in power MOSFETs," IEEE Radiation Effects Data Workshop, pp. 41- 54, 20 July 1994.

[5] J. L. Titus et al., "Impact of oxide thickness on SEGR failure in vertical power MOSFETs; development of a semi-empirical expression," IEEE Trans. Nucl. Sci., NS-42, No. 6, pp.1928-1934, Dec. 1995

[6] I. Mouret et al., "Experimental evidence of the temperature and angular dependence in SEGR [power MOSFET]," IEEE Trans. Nucl. Sci., NS-43, No. 3, pp.936-943, June 1996.

[7] J. L. Titus et al., "Effect of ion energy upon dielectric breakdown of the capacitor response in vertical power MOSFETs," IEEE Trans. Nucl. Sci., Nuclear Science, NS-45, No. 6, pp.2492-2499, Dec. 1998.

[8] L. E. Selva et al., "On the role of energy deposition in triggering SEGR in power MOSFETs," IEEE Trans. Nucl.

Sci., NS-46, No. 6, pp.1403-1409, Dec. 1999.
[9] J. L. Titus et al., "A study of ion energy and its effects upon an SEGR-hardened stripe-cell MOSFET technology [space-based systems]," IEEE Trans. Nucl. Sci., NS-48, No. 6, pp.1879-1884, Dec. 2001
[10] J. R. Brews et al., "A conceptual model of single-event gate rupture in power MOSFET's," IEEE Trans. Nucl. Sei., NS-40, pp. 1959-1966, Dec. 1993.
[11] J. L. Titus et al., "Simulation study of single-event gate rupture using radiation-hardened stripe cell power MOSFET structures," IEEE Trans. Nucl. Sci., NS-50, No. 6, pp. 2256- 2264, Dec. 2003.
[12] G. H. Johnson et al., "A physical interpretation for the single-event-gate-rupture cross-section of n-channel power MOSFETs," IEEE Trans. Nucl. Sci., NS-43, No. 6, pp.2932-2937, Dec. 1996.
[13] D. Peyre. Poivey et al., "SEGR Study on Power MOSFETs: Multiple Impacts Assumption," IEEE Trans. Nucl. Sci., NS-55, No. 4, pp.2181-2187, Aug. 2008.
[14] "Single-event burnout and single-event gate rupture," Method 1080 in "Test methods for semiconductor devices," Test method standard, MIL-STD-750E, Nov. 2006.
[15] J. F. Ziegler et al., "SRIM, the stopping and range of ions in matter," 2010 [Online].Available:http://www.srim.org
[16] D. J. DiMaria et al., "Impact ionization, trap creation, degradation, and breakdown in silicon dioxide films on silicon," J. Appl. Phys., Vol. 73, No.7, pp. 3367-3384, Apr. 1993.
[17] A. Cester et al., "A novel approach to quantum point contact for post soft breakdown conduction," Proc. IEEE-IEDM, pp. 305-308, 2001.
[18] Y. Kamakura et al., "Investigation of hot-carrier-induced breakdown of thin oxides," Proc. IEEE-IEDM, pp. 82-84, 1997.
[19] L. Scheick et al., "Sensitivity to LET and test conditions for SEE testing of power MOSFETs," IEEE Radiation Effects Data Workshop, 2009, pp.82-93, July 2009.

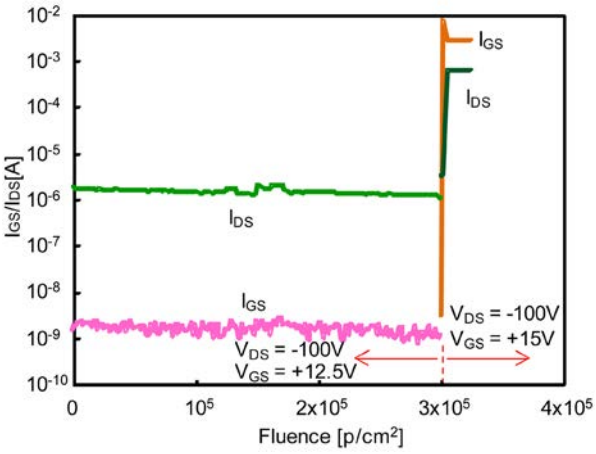

Fig. 1. Current monitor data during SEGR testing for p-channel power MOSFET with the rated drain voltage of 100 V.

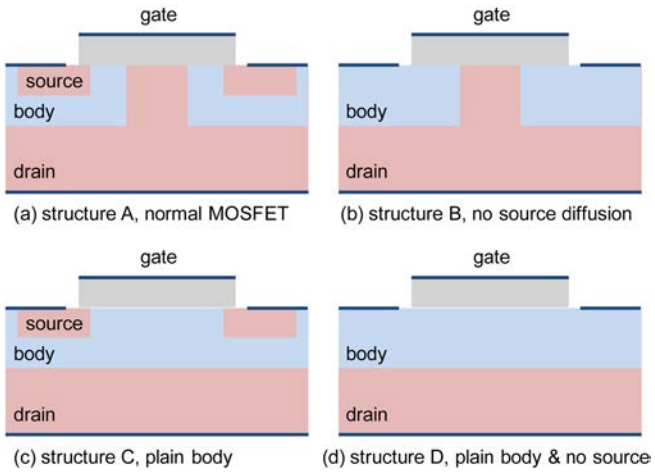

Fig. 2. Cross-sectional views of the test structures.

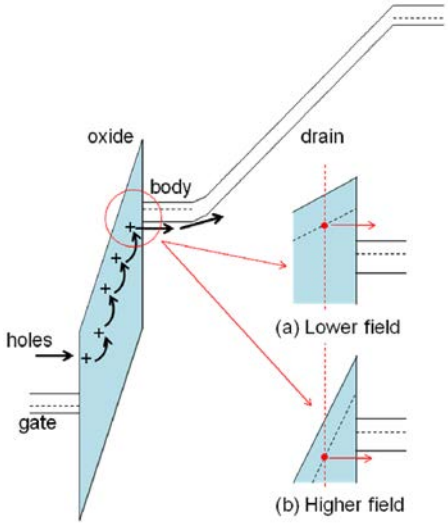

Fig. 3. Energy band diagram for p-channel power MOSFET damaged by SEGR.

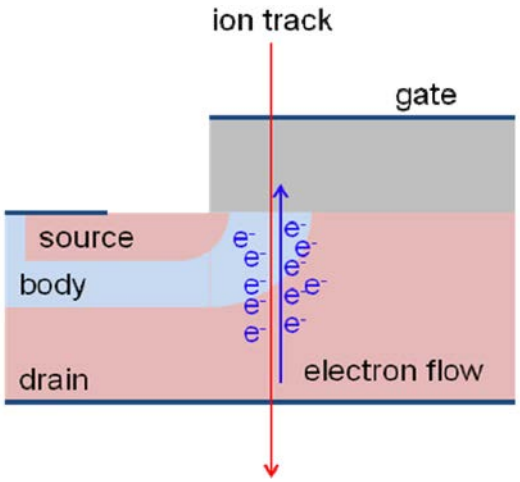

Fig. 4. Image of electron injection induced by ion strike in p-channel power MOSFETs.

Session F

Neutron Induced Single Events in Electrical Devices and Components

State-of-the-Art Study on Mitigation Techniques of Single Event Effects in Terrestrial Applications

Eishi Ibe[*1], Ken-ichi Shimbo[1], Tadanobu Toba[1], Hitoshi Taniguchi[1], Takumi Uezono[1], Koji Nishii[2], and Yoshio Taniguchi[3]

1Yokohama Research Laboratory, Hitachi, Ltd.

292 Yoshida, Totsuka, YokohamaKanagawa, 244-0817 Japan

2Telecommunication & Network System Division, Hitachi, Ltd.

Yokohama, Kanagawa, 244-8567 Japan

3Corporate Quality Assurance Division, Hitachi, Ltd.

Chiyoda,Tokyo, 101-8608 Japan

*E-mail: hidefumi.ibe.hf@hitachi.com

Keywords: terrestrial radiation, fault, soft-error, failure, network, stack layer, mitigation, DOUB, LABIR, TMR, MCBI, bipolar action

Abstract

***Abstract*—As semiconductor device scaling is on-going far below 100nm design rule, terrestrial neutron-induced soft-error typically in CMOS devices is predicted to be worsen furthermore. Moreover, novel failure modes that may be more serious than those in memory soft-error are recently being reported. Therefore, necessity of implementing mitigation techniques is rapidly growing at the design phase, together with development of advanced detection and quantification techniques. The most advanced such techniques are reviewed and discussed.**

I. INTRODUCTION

Scaling down of semiconductor devices to sub-100nm technology encounters a wide variety of technical challenges like V_{th} variation [1], Negative Bias Temperature Instability (NBTI)[2], short-channel effect[3], gate leakage[4] and so on. Terrestrial neutron-induced single event upset (SEU) is one of such key issues that can be a major setback in scaling. As scaling proceeds below 130nm, a number of new error modes are found to be emerging. Such errors, in principle, are originated from faults or charges produced in dual or triple well regions in CMOS devices. Fault does not always cause error, depending mainly on the location and the amount of charge collected to an active node. Similarly, error does not cause always a system failure, depending on a number of masking effects in the stack layers of manufacturing processes as illustrated in Fig.1. Some failures may be fatal when they take place in the *real-time system* like avionics control system and anti-lock brake in automobiles [5]. Some other failures are not necessarily taken care of as in entertainment applications. Soft-Error Rate (SER) has been regarded as one of major metrics in reliability of electronic devices and systems, but fatality /significance of failures must be considered in designing electronic systems since we have a number of error modes in electronic systems these days.

It is generally accepted from the very beginning of terrestrial neutron soft-error issues that mitigation techniques applied to only single stack layer cannot be effective and promising solution against system failures and collaboration among stack layers has been encouraged [6,7]. In reality, such collaboration is very difficult. It may be recognized that most engineers/researcher cannot expand their specialties beyond their stack layers. Novel strategies to overcome this situation are needed to be explored and being proposed. *Built-in* communication scheme among the stack layers is proposed by Ibe, *et al.* in their LABIR (inter Layer Built-In Reliability) concept [8]. Evans *et al.* are proposing the RIIF (Reliability Information Interchange Format) as common format or protocol to be used in system design among stack layers [9].

At present, a number of SEE (Single Event Effects) prediction/detection/prevention/recovery techniques have been proposed in each hierarchy or stack layer. Such techniques are overviewed in the present paper to explore overall mitigation techniques in electronic systems against terrestrial radiation induced system failures.

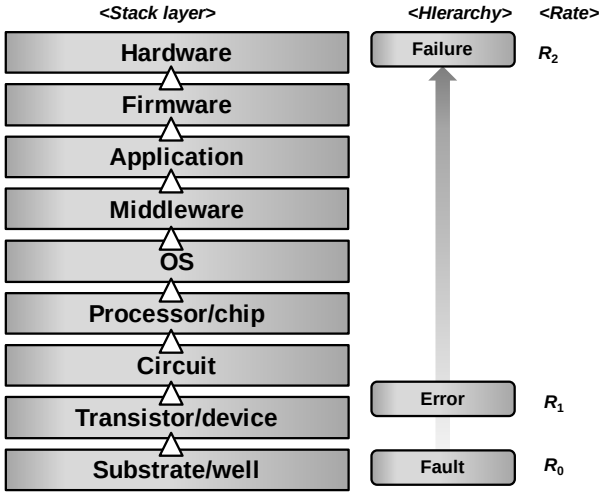

Fig. 1 Stack layers in manufacturing processes of electronic systems

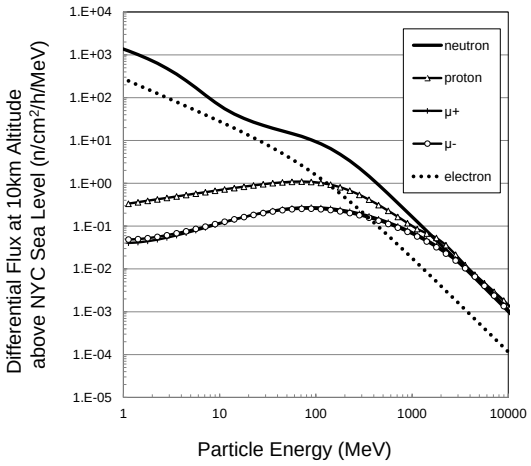

Fig. 2 Energy spectra of terrestrial radiation at NYC sea level

In addition, it is widely recognized that high-energy neutron is not unique source of terrestrial soft-error. Low energy neutron including thermal neutrons[10], protons[11], muons[12] and even electrons and photons could cause terrestrial soft-error as they are substantially present in terrestrial field as shown in Fig.2 [13]. The novel strategies must cover such global areas.

II. FALTY MODES IN EACH HIERARCHY

2.1 Fault modes

Figure 3 illustrates basic CMOS well structure. N-wells and p-wells are aligned in stripe pattern above p-substrate, and memory and logic devices are manufactured on the same well structure. As typically shown in Fig.4, charge collection mechanism take place when a charged particle pass through the storage node or bipolar action talks place when a charged particle pass through the p-n junction between the p-well and n-well. These phenomena in the well cause faults that may cause error in memory cells. The faults modes are summarized in Table 1 including stack-at fault and EMI (Electro-Magnetic Interaction).

Table 1 Fault modes and their property

Class	Definition	Name	Characteristics	In-situ detection method	In-situ recover/mitigation method
Transient/ noise	Transient in electric potential and/or current in a chip	SET[1]	Single transient due to charge collected to the diffusion layer in the chip. Pulse width is below a few nano second, and can long more than two clock pulses.	Time and/or space redundanbcy such as DMR[4], TMR[5]	None
		MNT[2]	Simultaneous SETs in more than two diffusion layers. Mainly, MNTs take place in a single well due to charge sharing or bipolar action. Space redundancy techniques such as DICE[6], TMR may not work against MNTs.	Monitoring the well potential and/or current	None
		EMI[3]	Electromagnetic noise including burst noise	Electro-magnetic probe	None
Defect	Lattice defects and or trap level in the oxides. They may cause leakage current and may disappear in time.	Vth shift	Cause of Vth shift in flash memory. They may cause stack at "0/1" error and can be permanent error.	Vth measurement	Annealing may work

1:Single Event Transient, 2:Multi-Node Transient, 3: Electro-Magnetic Interference,4: DoubleModule Redundancy, 5: Triple Module Redundancy, 6: Double Interconnect CEll

When fault take place in logic part, it is called as SET (Single Event Transient) that can cause SEU when the fault is captured in a memory element like a FF(Flip-Flop). Simple methods like parity in memory word are not effective to detect SET in logic circuit. Space redundancy

techniques such as DMR(Double Module Redundancy) or TMR (Triple Module Redundancy) can be applied to detect SET, but they have power and area penalties. Even if MNT (Multi-Node Transient) take place in the redundant nodes, the transient cannot be detected and may cause SDC (Silent Data Corruption).

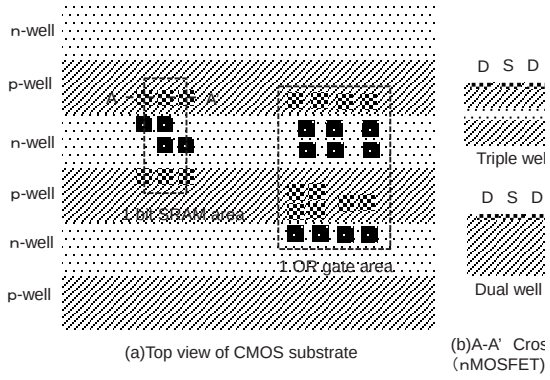

Fig. 3 Typical structure of CMOS dual/triple well and formation of a SRAM and an OR gate on the well

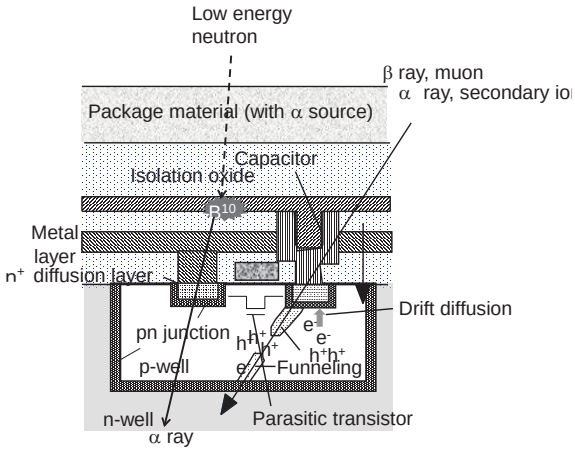

Fig. 4 Typical mechanisms of fault evolution

2.2 Error modes

Table 2 summarizes various error modes. Error modes can be classified into roughly three classes, such as soft-error or SEU(Single Event Upset), pseudo-hard error, and hard/permanent error. Soft error includes SBU(Single Bit Upset), MCU(Multi-Cell Upset), MBU (Multi-Bit Upset, MCU in the same word), MCBI (Multi-Coupled Bipolar Interaction) in memory element[14]. Direct hit on an FF by a charged particle may cause an SEU. They can be recovered by re-writing.

Table 2 Error modes of single event effects in semiconductor devices

Class	Definition	Mode name	Characteristics	In-situ Detection	In-situ recover method
SEU[1],Soft-error	Data cjhange in meomory elements such as SRAMs, Flip Flops by a single particle hit (event).	SBU[2]	Single bit error for one event.	Parity、ECC[16]	ECC
		MCU[3]	More than two bits fail in one event. Data in multiple FFs may be flipped by SET in clock line or SET/RESET lines.	Current / potential monitor	Interleave + ECC
		MBU[4]	MCU in the same word. They cannoy be corrected normal ECC.	Upper grade ECC	Upper grade ECC
		MCBI[5]	More than two bits fail locally due to potential disturbance in well by bipolar action.	Current / potential monitor	Interleave + ECC
Pseudo hard-error,PCSE[13]	Error that cannot be re-written They can mostly be activated by power cycling.	FBE[6]	Main error mode in SOI[12]. Body-tie may suppress this mode.	Parity、ECC	Power cycle
		SEL[7]	Re-writing does not work. Current continue to flow by parasitic cylyster effect. Power cycle can be applied to activate the chip.	Current / potential monitor	
		SEFI[8]	All in one definition of functional anormalities in logic circuits. Power ctcle or resetting ffs can activate the chip.SEFI in decoder in peripheral circuit of memory may cause wrong address.	FF parity/ECC	
		Firm Error	Error in configuration memory in SRAM based FPGA[14].	CRC[17]	Partial reconfiguration
Hard Error/Permanent error	Destructive and permanent error	SEGR[9]	Distruction of gate oxide in power devices mainly due to heavy ions. Flash memory can be failed by ythis mode as scaling extremely proceeds.	Anormalities in parts	Loading stand-by system
		SEB[10]	Distructive mode in power MOSFET such as IGBT[15]. SEB may take placer in IGBTs for trains and automobiles.	Anormalities in parts	Loading stand-by system

1:Sigle Event Upset, 2:Single Bit Upset, 3:Multicell upset,4:Multi-bit upset,5:Multi-Coupled Bipolar Interaction,6:Floating Body Effect, 7:Single Event Latchup, 8:Sigle Event Functional Interrupt, 9:Single Event Gate Rupture,10:Single Event Burnout, 11:Flip Flop, 12:System On Insulator, 13:Power Cycle Soft Error, 14: Field Programmable Gate Array, 15: Insulated Gate Bipolar Transistor, 16:Error Correction Code, 17: Cyric Redundancy Check

In particular, MCUs have been under close scrutiny and their ratio to the total SEU are drastically increasing [15-19]. Though MBUs can be avoided by a combination of ECC and the interleaving technique [19], MCUs that can be corrected by EDAC/ECC can still be problematic in high performance devices such as contents addressable memories (CAMs) [20] or registers used in network processors and routers. In the case of system design, it is therefore very important to evaluate MCUs as well as soft-error rates (SERs) of the device in design phase.

Pseudo hard-error cannot be recovered by re-writing but can be recovered by resetting FFs or power cycle.

Hard/permanent error cannot be recovered by any software and may cause fatal failure. Replacement or isolation of corrupted parts is only possible method to continue to use the system.

2.3 Failure modes

Failure is defined as observable faulty condition in an electronic system, which requires actions for solution. Faults and errors can be masked sometimes without any countermeasures. To establish solution, the root cause or physical mechanisms must be identified. Classification of failures is often applied to identify the root cause or root parts/chips in a system board.[21,22]

Table 3 shows an example of such classification of failures based on the fatality of the failure with two key factors such as latency in operation and duration for recovery. When SDCs take place in a large-scale super computer, simulation may give wrong results without any latency. This type of failure is called SLFL (SiLent FaiLure). If the SDCs suffer convergence of matrix calculation or frequent rollback due to error detection, significant time loss may take place in the computer system. We call it LTFL(LaTency FaiLure). If the system requires short-range outage to recover, we can the failure LHFL (Light Halt Failure). If the system requires long-range outage, we call the failure HHFL(Heavy Halt FaiLure). It the system is un-recoverable, we call the failure FTFL (FaTal FaiLure).

Table 3 Example for classification of failure modes

Class	Definition	Mode name	Characteristics	In-situ Detection	In-situ recover method
None-latency failure	Silent data corruption in data or address that cause wrong simulation results by super computer	SLFL[1]	Soft-error takes a major role.SDC[6] causes un-recognizable mis-calculation or mis-operation.	None	（If fault level detection works） Checkpointing+ Rollback
Latency failure	Performance of the electronic system is lowered due to over frequent rollback, for example.	LTFL[2]	In case time redundancy techniques are applied, this mode is commonly take place. Typically, rollback after fault detection by using double module redundancy technique	DMR[7] error flag, the number of retries.	Reboot
Light halt dailure	Electronic system can be recovered by short-time operation.	LHFL[3]	MBU, MNT、SEL can be the cause.	ECC、current/potential monitor	Reboot/power cycling
Heavy halt failure	Electronic system can be recovered by longt-time operation. Some logs and data may be lost.	HHFL[4]	Error in the configuration memory in FPGA, SEL can cause this mode.	CRC check	Partial reconfiguration/ power cycling
Unrecoverable (Fatal) failure	Distruction of power supply and/or power device. Power supply or overall electronic system maybe exchanged.	FTFL[5]	Distruction of IGBT、DC-DC converters due to SEB.	System down	None

1: Silent Failure, 2: Latency Failure, 3: Light Halt Failure, 4: Heavy Halt Failure, 5:Fatal Failure, 6:Silent Data Corruption, 7: Double Module Redundancy

III. VISUALIZATION AND MITIGATION OF SEE

In order to establish overall mitigation techniques in electronic systems, integration of four key technologies such as prediction, detection, prevention and in-situ/off-line recovery techniques is needed. Table 4 summarizes such techniques along with two axes, stack layers and the four key technologies.

Table 4 Visualization and mitigation techniques of SEE

Layer	Prediction/Estimation	Prevention	In-situ detection	In-situ recovery	Off-line recovery
Application	・Simulation based fault injection[r1]	・Probabilitistic calculation[r9]	・Anormally operation (e.g. SWAT[r18])	・Checkpointing-Rollback[r29]	
OS	・Log analysis		・detection mechanism in the kernel[r19]		・Reboot
PCB	・Full/partial board irradition [r2]	・DOUB（Design On Upper Bound)[r10]	・Watch-dog timer[r20]	・LABIR（inter-LAyer Built-In Reliability)[r30] ・Cross-Layer Reliability [r31]	・Reboot [r35]
Chip/Processor	・Simulation based fault injection ・Emulation based fault injection[r3] ・Irradiation test ・log analysis		・DMR（Double Module Redundancy)[r21] ・On-chip monitor [r22,r23] ・CRC[r24]	・TMR（Triple Module Redundancy)[r32] ・Chekpointing-Rollback ・Partial reconfiguration [r33]	・Reboot
Circuit	・Circuit simulation ・Logic masking simulation [r4,r5] ・Irradiation test	・Space/Time redundancy (DICE[r11], SEUT[r12], BISER[r13], SEILA[r14], LEAP[r15]),BCDMR[r16], RAZOR[r17]	・Parity for FFs[r25] ・BIST（Built-In Self Test) [r26]	BISR（Built-In Self Repair)[r34]	
Device	・SEE Monte-Carlo simulation [r6] ・TCAD Simulation[r7] ・Irradiation test	・Addition of resistor and/or capacitor ・Confinement of charge collection vollume ・Gate sizing	・ECC, parity	・ECC（SBU only） ・Data mirroing	
Substrate/well	・TCAD Simulation[r8]	・Enhancement of migration ・Optimization of well structure/size	・BICS（Built－In Current Sensor) [r27,r28] ・BIPS（Built-In Pulse Sensor）		

[r1] A. Evans, et al.(2012)
[r2] K. Shimbo, et al.(2011)
[r3] P. Roche(2010)
[r4] T. Takata, et al.(2010)
[r5] T. Talkata, et al.(2011)
[r6] E. Ibe, et al. (2001)
[r7] H. Yamaguchi, et al.()
[r8] E. Ibe, et al(2006)
[r9] R. Kumar(2011)
[r10] E.Ibe, et al.(2011)
[r11] T. Calin, et al.(1996)
[r12] N. Seifert, et al.2008()
[r13] S. Mitra, et al.(2007)
[r14] T. Uemura, et al(2010)
[r15] H.-H. Lee, et al.(2010)
[r16] J. Furuta, et al.(2010)
[r17] D. Ernst, et al.(2003)
[r18] M. Li, et al.(2008)
[r19] A. Pellegrini, et al.(2011)
[r20] P.C. Monferrer, et al.(2008)
[r21] J. Yao, et al.(2011)
[r22] K. Noguchi, et al.(2007)
[r23] K. Yoshikawa, et al.(2011)
[r24] S.-J. Wen, et al.(2008)
[r25] T. Uemura, private communication (2012)
[r26] A. Sanyal, et al.(2008)
[r27] T. Wang, et al.(2010)
[r28]S.A. Bota, et al.(2010)
[r29] D. Skalin, et al.(2009)
[r30] E. Ibe, et al.(2011)
[r31] J. Loncaric(2011)
[r32] H. Quinn, et al.(2007)
[r33] M. Abdelfattah (2012)
[r34] K.Z. Pekmestzi, et al.(2008)
[r35] K. Shimbo, et al.(2011)

The explanations on the following columns in Table 4 are skipped here because of space limitation.

3.1 Prediction/estimation techniques
3.2 Prevention Techniques
3.3 In-situ detection
3.4 In-situ recovery

3.5 DOUB (Design On Upper Bound) and LABIR (inter- LAyer Bulit-In Reliability)

In the Sections 3.2 and 3.4, stack layer (device, circuit, module/processor) level prevention/recovery techniques are reviewed and no single mitigation technique seems to fulfill simultaneously the reliability and performance requirements with minimum penalties and reasonable costs.

The authors, therefore, are working on the different and novel approach named (v) Design on Upper Bound (DOUB) by which the upper-bound failure rate can be estimated explicitly.

The equation (A), for example, gives the maximum upper-bound of chip-level SET because the equation does not include any masking effects. By modifying the maximum upper-bound with various physical limits determined by device structure/layout, circuit complexity, structure of logical layers, the realistic upper-bound failure rate free from the variations may be obtained. Figure 7 shows an example of such cumulative upper bounds of fault rates for various radiation sources calculated from the spectra in Fig. 2. If this upper-bound of a chip is low enough, the chip can be ignored for further analysis. If the upper-bound is of concern, mitigation techniques are applied from a simple and low cost method in design phase as shown in like:

By using soft-error Monte-Carlo simulator CORIMS, the author also tried to calculate upper-bound fault rates for various terrestrial radiation, and obtain some important conclusions:

(i) Exchange of weak logic gate/memory to robust logic gate/memory. DRAM is currently very robust device and can be substitute of SRAMSs where speed is not critical [33,34].

(ii) Minimization of active memory area

(iii) Limited and local use of space or time redundancy techniques in the circuit level, and so on.

The authors are proposing a novel method LABIR (Inter LAyer Built-In Reliability) as is illustrated in **Fig.8**. LABIR proposes interactive or communicative mitigation techniques in which a recovery action such as rollback to the checkpoint ignited when a layer finds any error symptom, not necessarily error or fault itself. BIST (Built –In Self Test) [47], Built-In Current (Pulse) Sensor (BICS[48], BIPS) can be used for such kind of technique for symptom detection. The symptom may

not appear so often so that power and area penalties can be minimized with minimum additional structure and circuits. By using BIPS, a pulse current propagated from an MCBI (Multi-Coupled Bipolar Interaction) zone in p-well can be detected in I_{dd} line as demonstrated in [14]. By capturing such a symptom by applying a sense amp between adjacent two p-wells, for example, errors or failures can be resumed by the rollback and replication operation in CPU level of the ULSI chip. Other sources of noises like EMI (Electro-Magnetic Interference) [35] propagate in wider area than soft-error over many wells so that they can be eliminated by the differential method between adjacent wells.

CONCLUSIONS

As semiconductor device scaling is on-going far below100nm design rule, terrestrial neutron-induced soft-error typically in SRAMs is predicted to be worsen furthermore.

Moreover, novel failure modes that may be more serious than those in memory soft-error are recently being reported. Therefore, necessity of implementing mitigation techniques with marginal penalties including power dissipation is rapidly growing at the design phase, together with development of advanced detection and quantification techniques. The most advanced such techniques are reviewed and discussed with proposal of novel mitigation strategies of the Design on Upper Bound (DOUB) and the inter LAyer Bulit-In Reliability (LABIR).

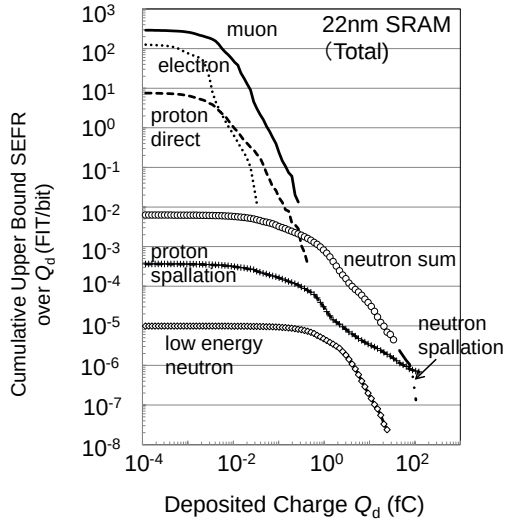

Fig. 7 Cumulative upper-bound fault rates due to various radiation sources at NYC sea level calculated by using CORIMS

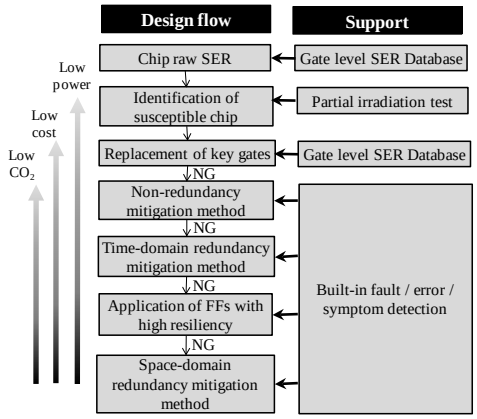

Fig. 8 General design flow of stepwise reduction in SER under the design on upper bound concept. Power consumption, cost, and global warming are key issues.

REFERENCES

[1] N. Sugii, R. Tsuchiya, T. Ishigaki, Y. Morita, H. Yoshimoto, K. Torii, and S. Kimura, *IEDM, San Francisco, Dec. 15-17,* pp. 249-253 (2008).
[2] S. Wen, R. Wong, and A. Silburt, *SELSE4, University of Texas at Austin, March, 26,27* (2008).
[3] D. Villanueva, A. Pouydebasque, E. Robilliart, T. Skotnicki, E. Fuchs, and H. Jaoue, *2003 IEDM, Washington, DC, December 7 - 10, 2003*, No.9.4 (2003).
[4] L.T. Clark, K.C. Moh, K.E. Holbert, X. Yao, J. Knudsen, and H. Shah, *TNS*, Vol.54, No.6, pp. 2028-2036 (2007).
[5] S. Hamdioui (Organizer), Special Session 4-Panel: "Reliability of Hard Real-time Systems in 32nm and Beyond: Who Will Solve the Challenges?," 2012 IEEE Int'l On-Line Testing Symposium (2012).
[6] C. Slayman, *2003IRPS, SER Panel Discussion, Dallas, Texas, April 2, 2003*, No.6 (2003).
[7] H. Quinn, *SELSE7, Champaign, Illinoi, March 29-30* (2011).
[8] E. Ibe, K. Shimbo, T. Toba, H. Taniguchi, and Y. Taniguchi, "LABIR: Inter-LAyer Built-In Reliability for Electronic Components and Systems," *SELSE7, Champaign, Illinoi, March 29-30* (2011).
[9] A. Evans, M.Nicolaidis, S.-J. Wen, D. Alexandrescu, and E. Costenaro, *IOLTS 2012, Sitges, Spain, June 27-29, 2012,* No.6.2 (2012).
[10] S. Wen, R. Wong, M. Romain, and N. Tam, *IRPS 2010, Anaheim, CA, May 2-6, 2010*, No.SE5.1, pp. 1036-1039(2010)..
[11] B.D. Sierawski, R.A. Reed, R.D. Schrimpf, R.A. Weller, M.H. Mendenhall, M.A. Xapsos, R.C. Baumann, and X. Deng, *NSREC, Quebac, Canada, July 20-24, 2009*, No.A-8 (2009)
[12] B.D. Sierawski, M.H. Mendenhall, R.A. Reed, M.A. Clemens, R.A. Welle, R.D. Schrimp, E.W. Blackmore, M. Trinczek,

B. Hitti, J.A. Pellish, R.C. Baumann, S.-J. Wen, R. Wong, N. Tam, *IEEE Trans.Nucl. Sci*, Vol.57, No.6, pp. 3273-3278 (2010).
[13] E. Ibe, T. Toba, K. Shimbo, and H. Taniguchi, *IOLTS 2012, Sitges, Spain, June 27-29, 2012*, No.3.2 (2012).
[14] E. Ibe, S. Chung, S. Wen, H. Yamaguchi, Y. Yahagi, H. Kameyama, S. Yamamoto, and T. Akioka, *2006 CICC, San Jose, CA., September 10 - 13, 2006*, pp. 437-444 (2006).
[15] E. Ibe, S. Chung, S. Wen, Y. Yahagi, H. Kameyama, and S. Yamamoto, *2007 NSREC, Ponte Vedra Beach, Florida, July 17-21, 2006*, No.PC-6 (2006).
[16] E. Ibe, S. Chung, S. Wen, S., Y. Yahagi, H. Kameyama, S. Yamamoto, T. Akioka, and H. Yamaguchi, *Workshop on Radiation Effects on Component and Systems (RADECS), Athens, Greece, September 27-29, 2006*, No.D-2 (2006).
[17] D. Radaelli, H. Puchner, P. Chia, S. Wong, and S. Daniel, *2005 NSREC, Seattle, Washington, July 11-15, 2005*, No.F-4 (2005).
[18] N. Seifert, and V. Zia, *SELSE3, Austin Texas, April 3, 4* (2007).
[19]T. Nakamura, M. Baba, E. Ibe, Y. Yahagi, and H. Kameyama, "Terrestrial Neutron-Induced Sift-Errors in Advanced Memory Devices," New Jersey, World Scientific (2008).
[20] K. Pagiamtzis, N. Azizi, and F. Najm, *2006 CICC, San Jose, CA., September 10 - 13, 2006*, pp. 301-304 (2006).
[21] C. Lopez-Ongil, M. Portela-Garcia, M.G. Valderas, A. Vaskova, Entrena,J. Rivas-Abalo, L. , A. Martin-Ortega, Oter,J. M, S.Rodriguez-Bustabad. , and I. Arruego, *IOLTS 2012, Sitges, Spain, June 27-29, 2012*, No.9.4, pp. 188-193 (2012)
[22] R. Baranowski, and H.-J. Wunderlich, *IOLTS2011, Athens, Greece, July 13-15, 2011*, No.13.3, pp. 278-283(2011).
[23] P. Roche, *IOLTS2010, Corfu Island, Greece, July 5-7*, Keynote 1, p. xv (2010).
[24] T. Takata, and Y. Matsunaga, *SELSE 2011, Champaign, Illinoi, March 29-30*, 2011
[25] T. Makino, D. Kobayash, K. Hirose, D. Takahashi, S. Ishii, M. Kusano, S. Onoda, and T. Hirao, and T. Ohshima, *TNS2009*, Vol.56, No.6, pp. 3180-3184 (2009).
[26] H. Nakamura, K. Tanaka, T. Uemura, K. Takeuchi, T. Fukuda, and S. Kumashiro, *IRPS, Anaheim, CA, May 2-6*, pp. 694-697 (2010).
[27] E.H. Cannon, and M. Cabanas-Holmen, *NSREC, Quebac, Canada, July 20-24, 2009,*, No.PI-3 (2009).
[28] JESD89A," *JEDEC STANDARD, JEDEC Sold State Technology Association*, No.89, pp. 1-85 (2006).
[29] E. Ibe, K. Shimbo, T. Toba, Y. Taniguchi and H. Taniguchi, *ICICDT2010, Grenoble, France, June, SER Session No.1 (2010)*
[30] E. Ibe, "Novel Features in SER Characteristics toward New Standards Special Session 1-Panel :SER standards: Where we are? What's next?," *IOLTS2010, Corfu Island, Greece, July 5-7* (2010).
[31] D. Alexandrescu, R. Baumann, A. Bougerol, E. Ibe, S. Rezgui, and C. Slayman, "Special Session 1-Panel: SER standards: Where are we? What's next?," *IOLTS2010, July5-7, 2010, Corfu Island, Greece* (2010).
[32] D.F. Heidel, K.P. Rodebell, P.W. Marshall, J.A. Pellish, K.A. LaBel, M.A. Xapsos, S.E. Hakey, M.C. Rauch,J.R. Schwank, P.E. Dodd, M.R. Shaneyfelt, M.D. Berg, M.R. Friendlich, A.D. Phan, and C.M. Seidleck, *NSREC, Quebac, Canada, July 20-24, 2009,*,, No.I-9 (2009).
[33] K. Shimbo, T. Toba, IEICE Technical report CPM2009-139, *Kochi, Dec. 2-4*, Vol.109, No.317,318, pp. 51-55 (2009)(In Japanese)
[34] K. Shimbo, T. Toba, K. Nishii, E. Ibe, Y. Taniguchi, and Y. Yahagi, *SELSE7 , Champaign, Illinoi, March 29-30* (2011).
[35] N. Kanekawa, E. Ibe, T. Suga, and Y. Uematsu, "Dependability in Electronic Systems-Mitigation of Hardware Failures, Soft Errors, and Electro-Magnetic Disturbances-," New York, Springer (2010).
[36] L. Borucki, G. Schindlbeck, and C. Slayman, *IRPS 2008, Phoenix, Arizona, April 27-May 1, Phoenix Convention Center*, No.5A.4 (2008).
[37] H. Ando, and S. Hatanaka, *IEEE Workshop on Silicon Errors in Logic - System Effects 3, Austin Texas, April 3, 4* (2007).
[38] M. Yoshimura, Y. Akamine, and Y. Matsunaga, *SELSE 2011, Champaign, Illinoi, March 29-30*, 2011
[39] T. Calin, M. Nicolaidis, and R. Velazco, *TNS*, Vol.43, No.6, pp.2874-2878 Dec.1996.
[40] M. Cabanas-Holmen, E. H. Cannon, A. Kleinosowski, J. Ballast, J. Killens, and J. Socha, *TNS*, Vol.56, No.6, pp.3505-3510 (2009).
[41] H.-H. K. Lee, K. Lilja, M. Bounasser, P. Relangi, I.R. Linscott, U.S. Inan, and S. Mitra , *idem.*, pp. 203- 212(2010).
[42] S. Mitra, M. Zhang, N. Seifert, T. Mak, and K.S. Kim, *ICICDT2007, Austin, Texas, May 18-20*, 2007, pp. 263-268 (2007).
[43] J. Furuta, K. Kobayashi, and H. Onodera, *IEICE Trans. on Electronics*, Vol.E93-C, No.3, pp. 340-346 (2010).
[44] J. Furuta, C. Hamanaka, K. Kobayashi, and H. Onodera, *VLSIC, Honolulu, HI, USA, June 16-18*, pp. 123-124 (2010).
[45] D. Ernst, N.S. Kim, S. Das, S. Pant, R. Rao, T. Pham, C. Ziesler, D. Blaauw, T. Austin, K. Flautner1, and T. Mudge, *MICRO-36*, 2003
[46] H. Quinn, K. Morgan, P. Graham, J. Krone, M. Caffrey, and K. Lundgren, *NSREC, Honolulu, Hawaii, July 23-27, 2007*, No.C-5 (2007)
[47] G. Theodorou, N. Kranitis, A. Paschalis, and D. Gizopoulos, *IOLTS2010, Corfu Island, Greece, July 5-7, 2010*, No.7.4, pp. 159-164 (2010).
[48] S.A. Bota, G. Torrens, B. Alorda, J. Verd, and J. Segura, *IOLTS2010, Corfu Island, Greece, July 5-7, 2010*, No.7.1, pp. 141-146 (2010).

Validation of Sensitive Volume Size based on a Multi-Scale Monte Carlo Simulation in Neutron-Induced Soft Error Analyses

Shin-ichiro Abe* and Yukinobu Watanabe
Department of Advanced Energy Engineering Science, Kyushu University, Japan
*Email: abe@aees.kyushu-u.ac.jp
Keyword(s): soft error, terrestrial neutron, PHITS, sensitive volume model,

Abstract

Neutron-induced soft errors in NMOSFETs from a 65 nm to a 25 nm technology are analyzed based on a simple sensitive volume (SV) model using the PHITS code, and the results are compared with those obtained by PHITS-HyENEXSS based on event-by-event TCAD simulation. The SERs calculated by PHITS-SV are in good agreement with the SERs obtained by PHITS-HyENEXSS by adjusting the SV size. Validation of the SV size is discussed on the basis of comparisons of the collected charge between TCAD simulation and SV model calculation for each single event.

1. Introduction

As semiconductor devices become increasingly sensitive to radiation, secondary cosmic-ray neutron induced soft errors have become a serious reliability problem for microelectronic devices at terrestrial altitudes. Since it is not easy to shield microelectronic devices from high-energy neutrons, it is required to take measures in semiconductor devices. Physics-based simulation of soft errors is helpful to take measures in the design of radiation-tolerant devices, because it can predict SERs in the design stage of devices and circuits.

Recently, we have developed a multi-scale Monte Carlo simulation code system "PHITS-HyENEXSS", and performed the analyses of soft error rates (SERs) based on event-by-event TCAD simulation [1, 2]. Although such physics-based simulation method is powerful and reliable, it is not necessarily suitable for quick estimation of SERs because TCAD simulation is time consuming. As a simple approach, a sensitive volume (SV) model [3, 4] has been commonly employed to estimate collected charges without TCAD simulation.

In the present work, the simple SV model with the shape of rectangular parallelepiped is employed instead of HyENEXSS, and the SV size is determined so as to reproduce the SERs obtained by PHITS-HyENEXSS. Moreover, the collected charges (Q_{coll}) calculated by PHITS-SV are compared with those obtained by PHITS-HyENEXSS for each single event.

2. Setup of soft error simulation using PHITS-SV

To compare with the results of [2], soft error simulations by PHITS-SV are performed in the same test device structure. Table I provides the parameters of NMOSFET for each technology, and Fig. 1 shows the test device structure for the 25 nm NMOSFET. An analysis volume with the size of 20 μm × 10 μm × 10.25 μm is placed on a 1.0 mm × 1.0 mm × 0.5 mm silicon substrate as two-dimensional grid. A silicon dioxide insulation layer 0.35 μm thick is placed on an analysis layer. A 3.0 μm metal layer consisting of copper and silicon dioxide is located on an insulation layer and a 0.5 mm silicon dioxide package layer is placed on a metal layer. Terrestrial neutrons with the energy distribution ranging from 1 MeV to 1 GeV given by the JEDEC standard [5] are incident vertically on the device.

In the SER analyses of [2], the single events responsible primarily for the soft errors were selected by imposing the following two conditions:

(i) If the charge deposited in the analysis volume is less than the critical charge (Q_c), the single event is rejected.

(ii) As shown in Fig. 1, the detection volume defined by the active area times the sensitive depth is placed in the analysis volume. If any secondary ions do not pass through the detection volume, the single event is also rejected.

Thus, these conditions are also applied in the soft error simulations by PHITS-SV.

In the simple SV model, it is assumed that all the charge generated in the SV is collected to the memory nodes. The soft error simulations by PHITS-SV are performed under different SV size. Figure 2 shows the 2-D cross section of SVs for each condition. In a condition A, the SV

Table I. Parameter of NMOSFET for each technology

Technology [nm]	65	45	32	25
Critical Charge [fC]	2.0	1.5	0.95	0.6
Bias voltage of drain [V]	1.2	1.1	1.0	0.9
Gate oxide thickness [nm]	2.2	2.0	1.7	1.5
Active area length [μm]	0.455	0.315	0.224	0.175
Active area width [μm]	0.248	0.172	0.120	0.098
STI depth [μm]	0.31	0.29	0.27	0.25

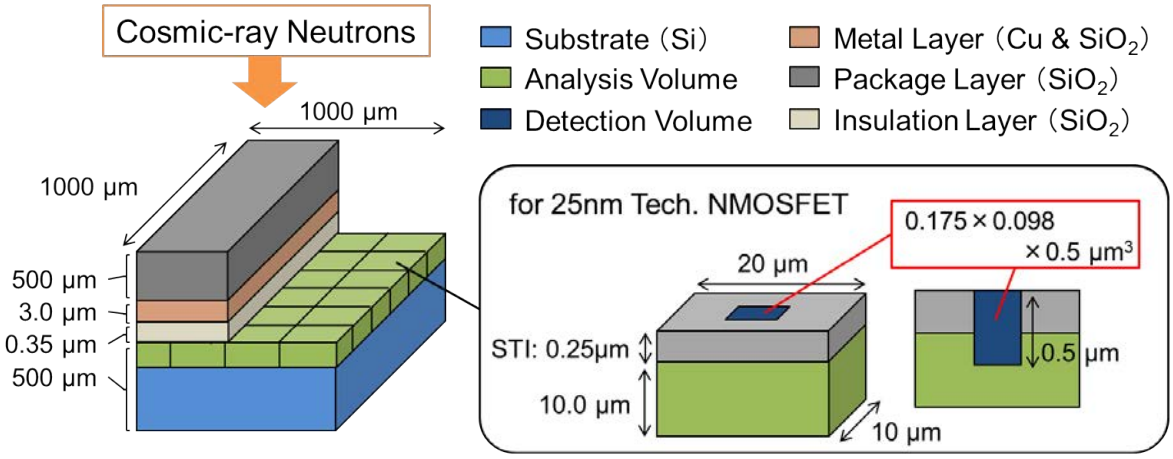

Fig. 1. Configuration of the test device structure for the 25 nm NMOSFET. The detection volume is defined by the active area (0.175 μm × 0.098 μm) and the sensitive depth (0.5 μm).

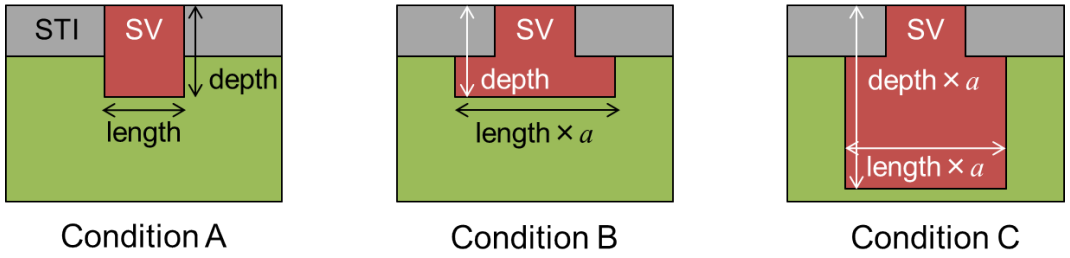

Fig. 2. 2-D cross section of sensitive volumes for each condition. *a* is a scaling factor, and the width is also expanded by a factor of *a*.

size is defined by the detection volume. In a condition B, the length and the width of SV are expanded by a factor of *a* based on the SV size of the condition A. In a condition C, the length, the width and the depth of SV are expanded by a factor of *a* based on the SV size of the condition A.

After the collected charge calculated, the number of event, $N(q)dq$, with the collected charge in $[q, q+dq]$ is obtained. The SER per bit is calculated as a function of the Q_c according to the following equation:

$$SER(Q_c) = \frac{F \times A}{N_{in} \times N_{bit}} \int_{Q_c}^{\infty} N(q)dq \qquad (1)$$

where F is the total neutron flux in units of $cm^{-2}s^{-1}$, A is the surface area of the test device, N_{in} is the number of incident neutrons in PHITS calculation, and N_{bit} is the number of bit cells placed in the device.

3. Results and discussion

3.1 Comparison of SERs for each technology NMOSFET

At first, the SER analyses using PHITS-SV are performed and the SERs are compared with those obtained by PHITS-HyENEXSS in order to confirm reproducibility of PHITS-SV. Figure 3 shows the comparison of SERs for each NMOSFET. The SERs per bit are calculated with A = 0.01 cm^2, $N_{in} = 4 \times 10^9$, N_{bit} = 5000, and $F = 5.94 \times 10^{-3}$ $cm^{-2}s^{-1}$ in Eq. 1. The scaling factor a used in the conditions B and C is adjusted so that the SER calculated by PHITS-SV agree with that obtained by PHITS-HyENEXSS for each NMOSFET at the Q_c given in Table I.

The SERs calculated by PHITS-SV under the condition A are about half the SERs obtained by PHITS-HyENEXSS at the Q_c given in Table I. Meanwhile, the SERs calculated by PHITS-SV under the condition B and C are in good agreement with those obtained by PHITS-HyENEXSS in the Q_c range below 2.0 fC. The scaling factor a decreases as the technology becomes smaller. This trend may be because the depletion layer becomes narrower with decreasing the bias voltage of drain. These results indicate that PHITS-SV with appropriate SV size can reproduce the SERs obtained by PHITS-HyENEXSS well.

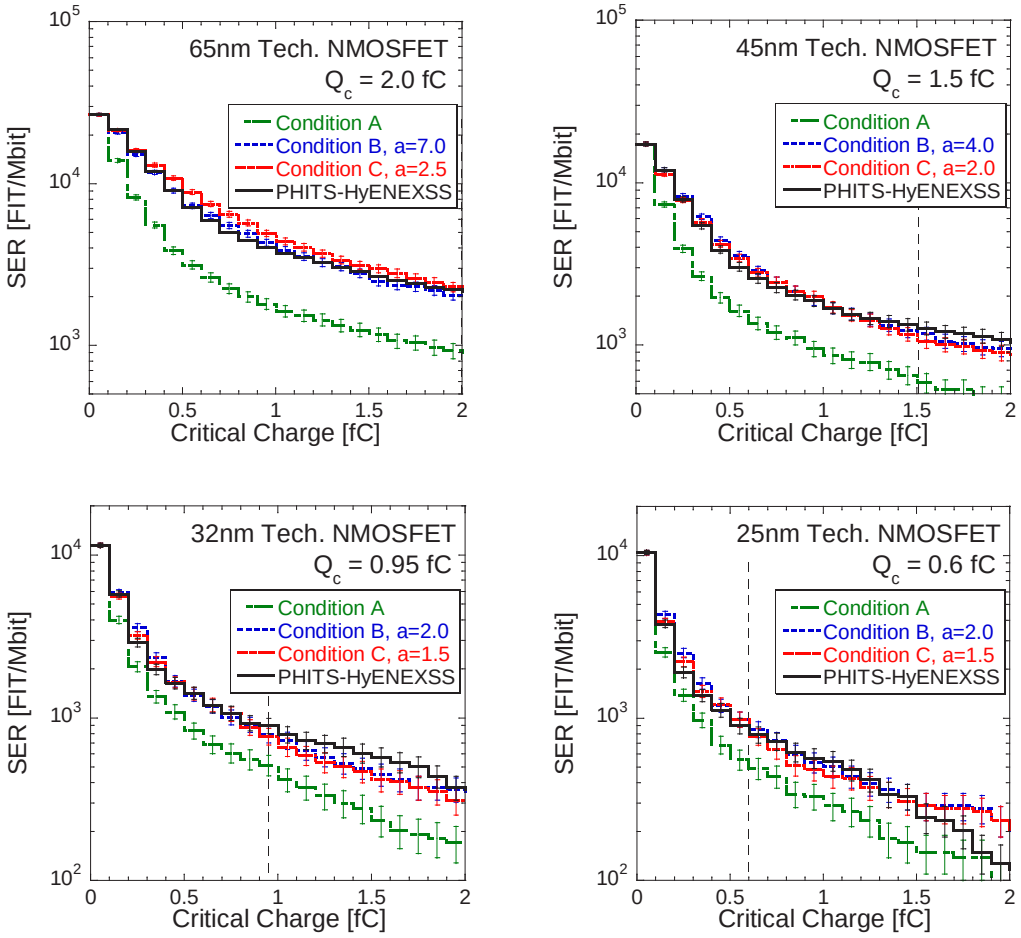

Fig. 3. Comparisons of SERs for 65 nm, 45 nm, 32 nm, and 25 nm NMOSFETs. The bar denotes the statistical errors.

3.2 Comparisons of collected charge for each single event

In order to examine which condition is better for soft error simulation based on the simple SV model, relative Q_{coll} (i.e., the ratio of the Q_{coll} calculated by PHITS-SV to the Q_{coll} obtained by PHITS-HyENEXSS) is calculated for each single event.

Figure 4 shows the mean value of relative Q_{coll} in each condition plotted as a function of design rule. For the 65 nm NMOSFET, the condition B is more suitable to describe Q_{coll} of each single event than the condition C. Meanwhile, the condition C is better to describe Q_{coll} of each single event than the condition B for the other technology NMOSFETs. From these results, it is found that the appropriate condition of SV size depends on the design rule.

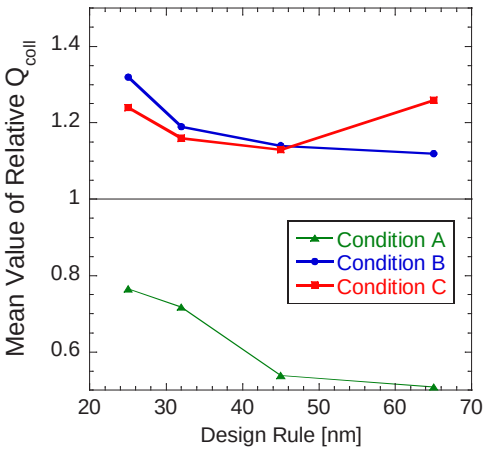

Fig. 4. Mean value of relative collected charge in each condition.

Figure 5 shows the event distribution of the relative Q_{coll} for the 65 nm and the 25 nm NMOSFETs. Here, the height of each histogram is normalized by the number of the total events to be analyzed. The dispersion of relative Q_{coll} around the mean value is seen for both NMOSFETs. One of the reasons for the dispersion may be due to the spatial dependence of charge collection efficiency. It cannot be considered by the present SV model. As one of the methods to estimate Q_{coll} considering charge collection efficiency, multiple SV models have been proposed and applied to calculate proton-induced SEU cross sections [6-8]. It is expected that the dispersion seen in Fig.5 would be reduced by using the multiple SV model.

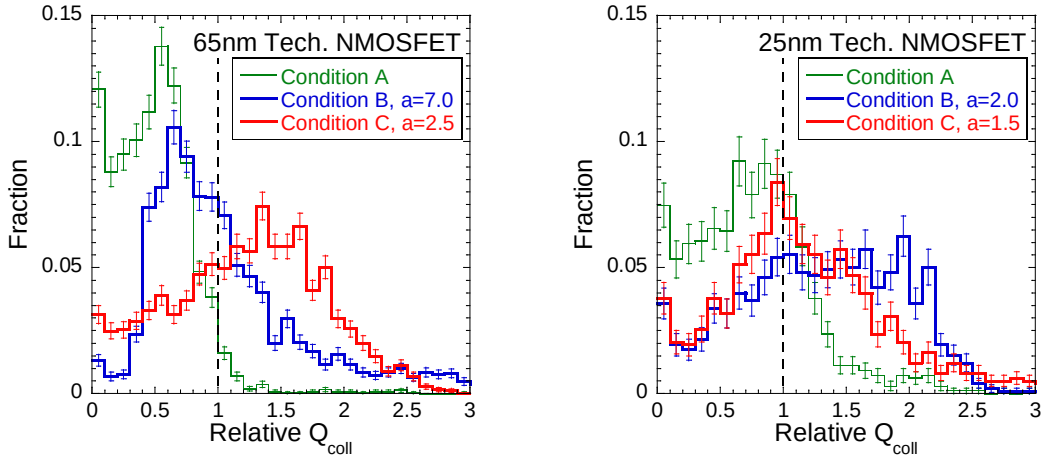

Fig. 5. Event distribution of relative collected charges for the 65 nm and the 25 nm NMOSFETs. The height of each histogram is normalized by the number of total analyzed event, and the bar denotes the statistical errors.

4. Conclusion

Neutron-induced soft errors in NMOSFETs from a 65 nm to a 25 nm technology are analyzed based on the simple sensitive volume (SV) model using the PHITS code and the results are compared with those obtained by PHITS-HyENEXSS based on event-by-event TCAD simulation.

The SERs calculated by PHITS-SV under the condition B and C are in good agreement with those obtained by PHITS-HyENEXSS for each technology NMOSFET by adjusting the scaling factor *a* of the SV. In order to validate which condition is better for soft error simulation based on the simple SV model, the relative Q_{coll} is calculated for each single event. From the comparison of the mean value of the relative Q_{coll} provided in each condition, it is likely that the suitable condition of SV size depends on the design rule.

The dispersion of the relative Q_{coll} around the mean value is observed for the 65 nm and the 25 nm NMOSFETs. This may be caused by the spatial dependence of charge collection efficiency because the simple SV model used in the present work cannot consider it. It is expected that the dispersion is reduced by the multiple SV models which can take into account the spatial dependence. In the future, we will extend the present work and aim at developing a reliable multiple SV model based on PHITS-HyENEXSS simulation results.

Acknowledgments

This work was supported by Grant-in-Aid for JSPS Fellows.

References

[1] S. Abe et al., "Multi-Scale Monte Carlo Simulation of Soft Errors using PHITS-HyENEXSS code system" IEEE Trans. on Nucl. Sci., vol. 59, pp. 965-970 (2012).

[2] S. Abe et al., "Neutron-Induced Soft Error Analysis in MOSFETs from a 65nm to a 25nm Design Rule using Multi-Scale Monte Carlo Simulation Method", IEEE Conference publications: in proceedings of International Reliability Physics Symposium 2012, pp. SE.3.1-SE.3.6 (2012).

[3] Y. Tosaka et al., “Simple Method for Estimating Neutron-Induced Soft Error Rates Based on Modified BGR Model” IEEE Electron Dev. Lett., vol. 20, pp. 89-91 (1999).

[4] K. M. Warren et al., “Application of RADSAFE to Model the Single Event Upset Response of a 0.25 μm CMOS SRAM”, IEEE Trans. on Nucl. Sci., vol. 54, pp. 898-903 (2007).

[5] Measurement and Reporting of Alpha Particle and Terrestrial Cosmic Ray-Induced Soft Errors in Semiconductor Devices, JEDEC Standard JESD89A, Oct. 2006 [Online]. Available: http://www.jedec.org

[6] A. V. Sannikov, “Single Event Upsets in Semiconductor Devices Induced by Highly Ionising Particles”, Rad. Protection Dosimetry, vol. 110, pp. 399-403 (2004).

[7] K. M. Warren et al., “Application of RADSAFE to Model the Single Event Upset Response of a 0.25μm CMOS SRAM”, IEEE Trans. on Nucl. Sci., vol. 54, pp. 898-903 (2007).

[8] C. Weulerse et al., “A Monte-Carlo Engineer Tool for the Prediction of SEU Proton Cross Section from Heavy Ion Data”, in proceedings of Radiation and Its Effects on Components and Systems (RADECS) 2011, Sevilla, Spain, September 19-23, 2011, pp. 376-383 (2011).

Measurement of Distance-dependent Multiple Upsets of Flip-Flops in 65nm CMOS Process

Jun FURUTA*1, Kazutoshi KOBAYASHI2, 3, and Hidetoshi ONODERA1, 3
1 Kyoto University, Japan
2 Kyoto Institute of Technology, Japan
3 JST CREST, Japan
*Email: furuta@vlsi.kuee.kyoto-u.ac.jp
Keyword(s): Multiple Cell Upset, Neutron irradiation, Flip-Flops

Abstract

We measured neutron-induced SEUs (Single Event Upsets) and MCUs (Multiple Cell Upsets) on FFs in a 65 nm bulk CMOS process. Measurement results show that maximum MCU / SEU ratio is 30.6% and is exponentially decreased by the distance between latches on FFs.

1. Introduction

As process scaling, MCU is becoming one of the most significant issues for LSI reliability since it cannot be removed by ECC [1], [2]. In a 65 nm process, MCUs are observed in FFs and increase soft-error rates of radiation-hardened FFs [3]. Since MCU rates depend on the cell-distance, redundant latches on radiation-hardened FFs are separated over 1.1μm for high error resilience in [4]. To increase soft-error resilience, it is necessary to measure characteristics of MCUs on FFs.

In this paper, we show measurement results of neutron-induced SEUs and MCUs on D-FFs in a 65 nm bulk CMOS process to evaluate the dependences of the distance of FFs.

2. Test Chip Structure

To measure neutron-induced MCU and SEU on FFs, three different shift registers are implemented as shown in Fig. 1. They have 0μm, 1μm, or 2μm horizontal displacements between odd rows and even rows. They are implemented in order to measure MCU rates by changing the distance between master latches or slave latches on FFs as shown in Fig. 2. They have tap-cells (well-contacts) which are inserted every 50 μm.

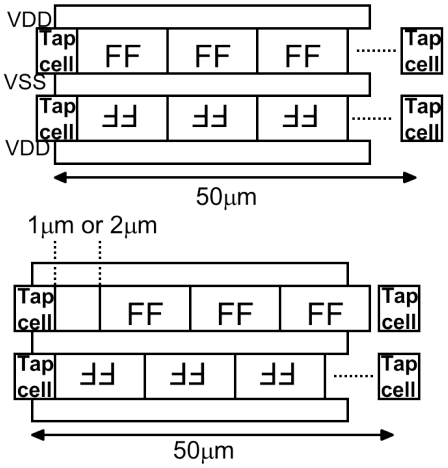

Fig. 1 Layout structures of shift registers.

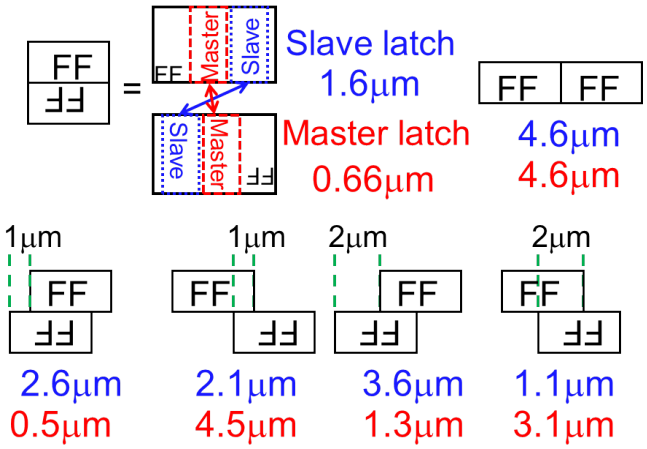

Fig. 2 Distance between master or salve latches on FFs.

3. Experimental Setup

Fig. 3 shows a chip micrograph fabricated in a 65 nm bulk CMOS process on a twin-well structure. Each shift register includes 10k FFs. The total area of four shift registers is 0.5 x 0.6 mm^2 on a 2 x 4 mm^2 die. Accelerated tests were carried out by spallation neutron irradiation at RCNP (Research Center for Nuclear Physics, Osaka University). The average acceleration factor is 3.8 x 10^8 compared with ground level of Tokyo. To increase soft error counts, 28 chips are measured simultaneously by using stacked DUT boards as shown in Fig. 4. During irradiation, clock signal is fixed to “1” or “0” to keep master or slave latches on FFs in the hold state. All stored values of the FFs were retrieved every 5 minutes.

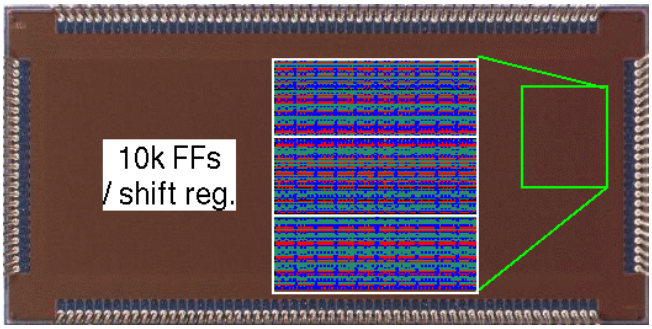

Fig. 3 Chip micrograph with floorplan.

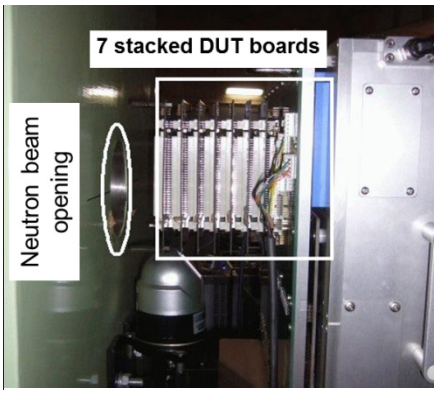

Fig. 4 Stacked DUT boards

4. Experimental Results

Table I shows the number of SEUs and MCUs of the shift registers as shown in Fig. 1. The maximum MCU / SEU ratio is 30.6% which is close to that on 65 nm SRAM cells [5]. These results clearly show that soft-error resilience of redundant FFs flipped by MCUs is only 4 times higher than non-redundant FFs and MCU mitigation design is necessary for redundant FF to improve soft error resilience. We observe more than 3-bit MCUs as shown in Fig. 5. We assume that 5 to 8-bit MCUs are caused by successive hits [6] since they spread in line.

Fig. 6 shows the distance-dependence of MCU / SEU ratios on FFs. MCU / SEU ratios are exponentially decreased according to $d^{1.68}$ (d is the distance between two latches) and fitting line shows that they can be 100% when $d \leq 30$ nm. To achieve 100x higher soft-error resilience in redundant FFs than in non-redundant FF, we must implement redundant FFs whose latches are separated by 4 μm from each other. However, it consumes huge area or complicated design procedures and these drawbacks cannot be reduced by the process scaling.

Table 1 The Number of SEUs and MCUs by neutron irradiation

	# of SEU	# of MCU	MCU/SEU ratio[%]
FF	507	110	21.6
FF with 1μm displacement	487	148	30.6
FF with 2μm displacement	567	91	16.2

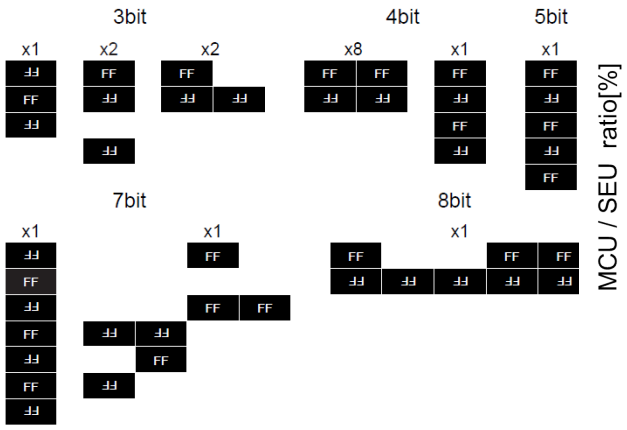

Fig. 5 MCU patterns with more than 3 FFs flipped

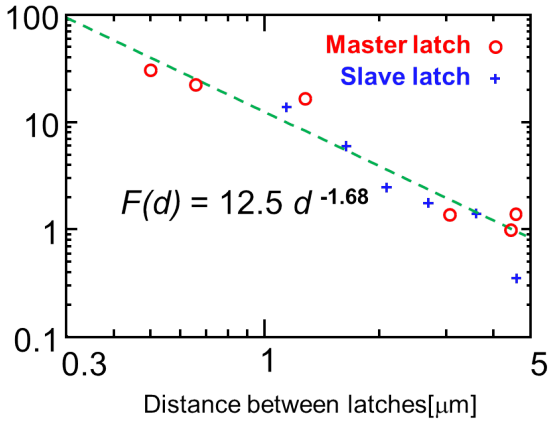

Fig. 6 Distance-dependence of MCU

5. Conclusion

We measured neutron-induced MCUs on FFs in a 65 nm CMOS process in order to evaluate their dependences on the distance of FFs. Accelerated test results show that the maximum MCU / SEU ratio is 30.6% and is exponentially decreased by the distance of latches. To achieve 100x higher soft-error resilience in redundant FFs than in non-redundant FF, we must implement redundant FFs whose latches are separated by 4 μm from each other.

Acknowledgments

The VLSI chip in this study has been fabricated in the chip fabrication program of VDEC, the University of Tokyo in collaboration with STARC, e-Shuttle, Inc., and Fujitsu Ltd. This work is partly supported by Grant-in-Aid for JSPS Fellows (24·7662).

References

[1] E. Ibe, S.S. Chung, S. Wen, H. Yamaguchi, Y. Yahagi, H. Kameyama, S. Yamamoto, and T. Akioka. "Spreading Diversity in Multi-cell Neutron-Induced Upsets with Device Scaling". In *IEEE Custom Integrated Circuits Conference*, pages 437 –444, September 2006.

[2] N. Seifert, B. Gill, K. Foley, and P. Relangi. "Multi-cell Upset Probabilities of 45nm High-k + Metal Gate SRAM Devices in Terrestrial and Space Environments". In *IEEE International Reliability Physics Symposium*, pages 181 –186, May 2008.

[3] R. Yamamoto, C. Hamanaka, J. Furuta, K. Kobayashi, and H. Onodera. "An Area-Efficient 65 nm Radiation-Hard Dual-Modular Flip-Flop to Avoid Multiple Cell Upsets". *IEEE Transactions on Nuclear Science*, vol. 58, No. 6, pp. 3053 –3059, December 2011.

[4] D. Krueger, E. Francom, and J. Langsdorf. "Circuit Design for Voltage Scaling and SER Immunity on a Quad-Core Itanium Processor". In *IEEE International Solid-State Circuits Conference*, pages 94 –95, February 2008.

[5] G. Gasiot, D. Giot, and P. Roche. "Multiple Cell Upsets as the Key Contribution to the Total SER of 65 nm CMOS SRAMs and Its Dependence on Well Engineering". *IEEE Transactions on Nuclear Science*, vol. 54, No. 6, pp. 2468 –2473, December 2007.

[6] T. Uemura, T. Kato, H. Matsuyama, K. Takahisa, M. Fukuda, and K. Hatanaka. "Investigation of Multi Cell Upset in Sequential Logic and Validity of Redundancy Technique". In *IEEE 17th International On-Line Testing Symposium (IOLTS)*, pages 7 –12, July 2011.

Evaluation of SiC Power Diodes against Terrestrial Neutron-Induced Failure at Ground Level

Hiroaki Asai[*1], Kenji Sugimoto[1], Isamu Nashiyama[1], Kensuke Shiba[1],
Mieko Matsuda[1], Tadaaki Morimura[1]
1 High-Reliability Engineering & Components Corporation (HIREC), Japan
*Email: asai@hirec.co.jp
Keyword(s): Silicon Carbide (SiC), Terrestrial Neutron, Single-Event Burnout (SEB),
RCNP, LANSCE/WNR

Abstract

Terrestrial neutrons cause single-event effects (SEEs) in semiconductor devices, which crucially affect the reliability of electronic systems used in the terrestrial environment. This paper presents evaluation results of high energy neutron-induced single-event burnout (SEB) in silicon carbide (SiC) power diodes and differences between SiC and silicon (Si) devices from the SEB standpoint.

1. Introduction

High energy neutrons, protons, pions and muons are produced in nuclear cascade showers created by nuclear reactions between cosmic rays and atmospheric nuclei. Charged particles are halted in a relatively short range, but neutrons produce a cascade of nuclear reactions (air shower) that eventually make terrestrial neutrons at the ground level. High energy neutron-induced single event effects (SEEs) in semiconductor devices, such as Power MOSFET, IGBT, silicon carbide (SiC) devices, SRAM and DRAM, crucially affect the reliability of electronic systems in the terrestrial environment [1-8]. Among them, single-event burnout (SEB) is one of the most serious problems causing fatal damage to electric systems. The SEB is initiated by energetic secondary ionizing atoms induced by neutrons within the semiconductor devices. In the high electric field region of a reversely-biased power device, the initial charge deposited by the secondary atoms is amplified through avalanche multiplication. As a consequence, power devices are short-circuited and broken down to be permanently damaged. In IGBTs and MOSFETs, the ion-induced massive carrier multiplication may result in the turn-on of parasitic bipolar transistors**,** which will also lead to permanent device failure [9-11].

SiC has been said to have far more suitable characteristics for high voltage and high temperature power device applications than silicon (Si), and SiC power devices are now in the phase of practical applications. However, their reliability against the terrestrial neutrons is not known yet and almost no information on SEB in SiC power devices is available at present.

We have been investigating neutron-induced SEB in high voltage power devices such as SiC diodes, Si diodes and IGBTs. To ensure world-wide consistency of the experimental data presented in this study, we have developed a transportable proton recoil detector (TPRD) to measure high flux and high energy neutron used for SEE testing, and measured neutron fluences at LANSCE/WNR (Los Alamos Neutron Science Center / Weapons Neutron Research) in the USA as well as RCNP (Research Center for Nuclear and Physics) in Japan [12].

This paper demonstrates that differences of device manufacturers and device structures have a strong influence on terrestrial neutron SEB susceptibility. We performed neutron-induced SEB testing in SiC and Si power diodes by using the spallation neutron beam at RCNP. The neutron SEB tolerance of SiC diodes is different by a manufacturer even though they have the same voltage ratings. Also, we discuss similarity between neutron-induced SEB and proton-induced SEB.

2. Experimental

The spallation neutron beam course has been recently developed at RCNP to simulate terrestrial neutrons for neutron-induced SEE testing [13]. Fig. 1 shows the neutron energy spectrum measured at RCNP by Japan Atomic Energy Agency (JAEA) research group in cooperation with RCNP and HIREC along with the spallation neutron spectrum of the WNR, the terrestrial neutron spectrum at sea level [14]. The RCNP neutron spectrum simulated by the Particle and Heavy Ion Transport code System [15] (PHITS) is also shown in Fig. 1. The spectrum of the RCNP spallation neutrons reproduces well the terrestrial neutron spectrum multiplied by 1.5x 10^8 in the energy range from 5 MeV to 300 MeV [16].

We used commercially available SiC Schottky diodes as test samples for neutron-induced SEB testing. To evaluate the variation in SEB tolerance, we applied two different SiC diodes with the same voltage rating (600 V) from different manufacturers (A and B) and Si diodes for the purpose of reference. SiC diode B and Si diode B are from the same manufacturer.

The neutron-induced SEB testing circuit in accordance with the MIL standard (MIL-STD-750E Method 1080: Single event burnout and single event gate rupture test) is shown in Fig. 2. Ten test samples of the Devices

Under Test (DUT) are connected in parallel on a DUT board and are reversely biased during neutron irradiation. When one of test samples is subjected to SEB by neutron irradiation, the fuse of the burnout sample blows out to disconnect the sample from the power line. Therefore, neutron-induced SEB testing is continuously performed until all test samples are burned out by neutron irradiation or until the preset time when the SEB testing is terminated, which is called type I (time-truncated) censoring [17]. Irradiation neutron flux was kept constant during the test. The reverse current of test samples is consistently monitored by a measurement system during neutron irradiation. SEB occurrence is judged when the reverse current increases abruptly to cause destructive permanent damage of test samples. Fig. 3 shows schematic experimental configuration. All the neutron irradiation was performed at normal incidence with almost uniform neutron beam. The test samples on the DUT board were placed in the neutron beam, and measurement systems and the high voltage power supply (HVPS) were remotely controlled by a personal computer (PC) in the measurement room. This measurement system detects an abrupt increase in reverse current of the test sample caused by SEB.

3. Experimental Results

Experimental results obtained at RCNP are shown in Fig. 4, which shows the dependence of the SEB cross section on applied voltage. The vertical axis indicates SEB cross section (reciprocal of the fluence at which SEB occurs), and the horizontal axis indicates applied voltage. SEB occurred by neutron irradiation at 600 V, 650 V and 700 V in all test samples. At 500 V and 550 V, SEB occurred only in SiC diode A (Manufacturer A).

Though the experimental data scatter widely by more than an order of magnitude, we could say that the SEB cross sections of SiC diode A (Manufacturer A) are about ten times higher than those of SiC diode B (Manufacturer B), indicating manufacturer difference affects strongly on neutron SEB tolerance of SiC diodes.

When the test results of SiC diode B (Manufacturer B) and Si diode B (Manufacturer B) are compared at 600 V (rating voltage), the SEB cross section difference is not clear because the SEB cross sections of Si diodes scatter in a very wide range of more than three orders of magnitude. This scattering is partly caused by the randomness of the neutron strike location in the diode, and also suggests that sample DUTs should be carefully selected to keep data consistency in the neutron SEB testing.

Fig. 5 shows the number of surviving devices normalized to the sample size as a function of fluence for SiC diode A. So, Fig. 5 indicates an experimental reliability function. The plots decrease monotonically and gradient increases with applied voltage. The plots are fitted by exponential curves. These curves reproduce the major part of the experimental data fairly well, indicating constant failure rate. It is worth of remark that initial failure and wear-out failure are suggested at higher bias voltages in Fig. 5.

The size of the burnout trace is about from 0.05 mm to 0.2 mm in diameter. The location of the burnout trace of the SiC diode and Si diode differs chip by chip spreading over the diode surface [13].

4. Discussion

Neutron burnout phenomena are considered to be random failure (Bernoulli trial) and have a constant failure rate. We performed neutron SEB testing by type I (time-truncated) censoring. In this case, the Maximum Likelihood Estimate (MLE) of failure rate, λ, at an applied voltage can be calculated by,

$$\lambda = \frac{r}{\sum_{i=1}^{r} t_i + (n-r)T}, \qquad (1)$$

where, t_i, T, r, and n are exact time when i'th failure occurs, censored time, total number of SEB occurrence, and sample size, respectively [17].

Fig. 6 shows the comparison between the present experimental results and those of reference [9], where the vertical axis is in estimated failure in time (FIT). The estimated FIT are calculated by,

$$FIT = \lambda \times \frac{\Phi_{terr}}{\Phi_n} \times 10^9, \qquad (2)$$

where, Φ_{terr} and Φ_n are the terrestrial neutron flux and the spallation neutron flux applied in SEB testing. The experimental data of SiC diode A in Fig. 6 show very weak dependence on an applied voltage (electric field). This suggests that crystalline defects in a SiC wafer have an influence on terrestrial neutron SEB susceptibility. Estimated FIT of the SiC diode A and SiC diode in reference [9] show fairly good agreement except at 600 V. Our experimental data of Si diode B link continuously to the Si diode in reference [9] in spite of the difference in the manufacturer. In reference [9], the SiC diode shows higher FIT than the Si diode up to the rated voltage (600 V), indicating the SiC diode is more vulnerable than the Si diode to neutron-induced SEB. Whereas, in our experiment, difference in FIT between the SiC diode A and the Si diode B is not clear at the rated voltage (600 V). It should be noted that the estimated FIT of SiC diode A is significantly higher than that of SiC diode B.

The mechanism of neutron-induced SEB is believed to be similar to that of proton-induced SEB as well as neutron-induced and proton-induced single-event upsets (SEUs) have similar upset mechanism [18]. In order to confirm this, we compare the present data of neutron-induced SEB with those of proton-induced SEB obtained

by Kuboyama *et al*. [10] for SiC power diodes from the same manufacture. Therefore, we applied the same method of analysis as used by Kuboyama et al. [10], [13]. Fig. 7 shows the median rank plots (symbols) where F_i *(i, n)* is plotted against the fluence when i'th failure occurs and fitting curves of the cumulative failure distribution function (lines) for SiC diode A. Fig. 7 also shows data plots and fitting curves from reference [10] for mono-energetic 70 MeV protons irradiation. As shown in Fig. 7, the entire test data are successfully fitted by the curves and a trend of the results agree with that of reference [10]. Therefore, similar to the proton-induced SEB, neutron SEB is caused by a single high energy neutron without cumulative effect, and triggered by the secondary particles generated by the nuclear reaction between terrestrial neutrons and the substrates of SiC and Si devices. It will be reasonable to assume that the neutrons produce the secondary particles that, in turn, trigger the SEBs. On the contrary to the 70 MeV proton irradiation results in reference [10], the median rank curve is not much affected by the bias voltage in the case of neutron irradiation. The reason is not clear yet, but may be related with the fact that neutrons have broad energy spectrum up to 392 MeV as shown in Fig. 1.

To evaluate the secondary particles generated by the nuclear reaction between terrestrial neutrons and the substrates of SiC and Si devices, we calculated about secondary particles by using PHITS simulation [13]. Through these PHITS simulation results, major difference between SiC device and Si device is secondary carbon atoms. Amount of the secondary carbon atoms in SiC device is much larger than that in Si device, and these energetic carbon atoms may increase SEB cross section, because they have higher energy and longer flight length than secondary energetic silicon atoms [13]. We will examine how these PHITS results have an influence on the mechanism analysis of the SEB occurrence in the future.

5. Summary

We performed testing of high energy neutron-induced SEB in SiC and Si power diodes by using the spallation neutron beam at RCNP. The neutron SEB tolerance of SiC diodes is different by a manufacturer by an order of magnitude even though they have the same voltage ratings. Some SiC diodes are burned out at very low voltages, showing no significant dependence on an applied voltage and that SEB threshold voltage may be strongly affected by crystalline defects in a SiC wafer. By comparing the neutron-induced SEB to the proton-induced SEB by using median rank method, the neutron SEB is triggered by the secondary particles generated by the nuclear reaction between terrestrial neutrons and the substrate of SiC. The PHITS Monte Carlo simulation indicates that secondarily generated energetic carbon nuclei may play important role in the SEB triggering mechanism in SiC power devices. We will examine how crystalline defects have an influence on the internal electric field and the mechanism of neutron-induced SEB in the future.

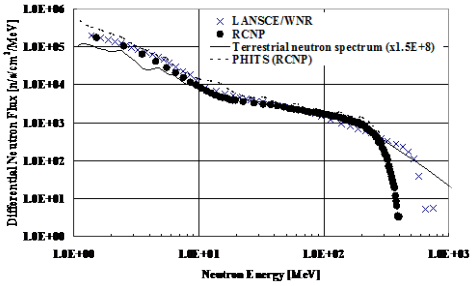

Fig. 1 Comparison of RCNP neutron energy spectrum with LANSCE/WNR neutron spectrum, the PHITS simulation spectrum for RCNP, and terrestrial neutron spectrum at sea level multiplied by 1.5 x 10^8 [13].

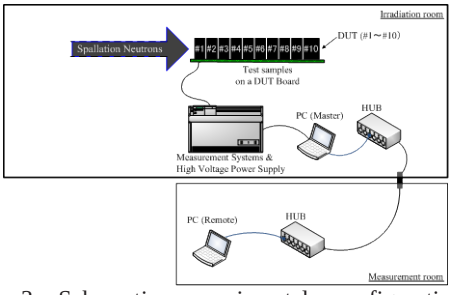

Fig. 3 Schematic experimental configuration of neutron-induced SEB testing. The test samples on the DUT board were placed at the center of the neutron beam, and the measurement systems and the HVPS were remotely controlled by a PC in the measurement room.

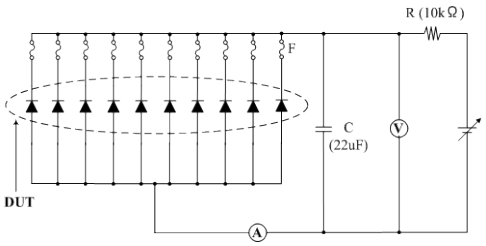

Fig. 2 Circuit diagram of neutron-induced SEB testing. Ten test samples of DUT are connected in parallel and are reversely biased during neutron irradiation.

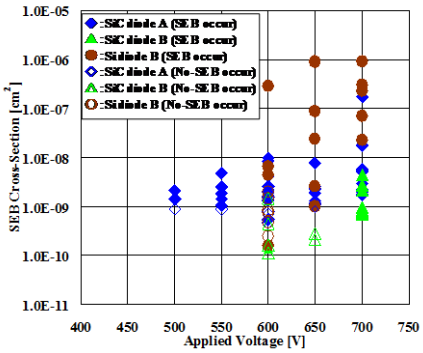

Fig. 4 Applied voltage dependent SEB cross-section of SiC diode A, SiC diode B, and Si diode B. The filled symbols are for SEB occurrence, and the open symbols are for no-SEB occurrence up to the fluence at which tests are terminated.

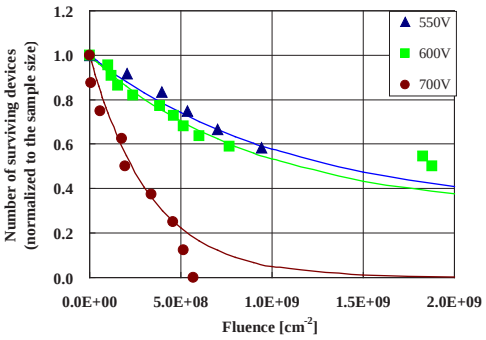

Fig. 5 Number of surviving devices versus neutron fluence for SiC diode A. The number of surviving devices is normalized to the sample size. Solid lines are exponential fitting curves to the experimental data plots.

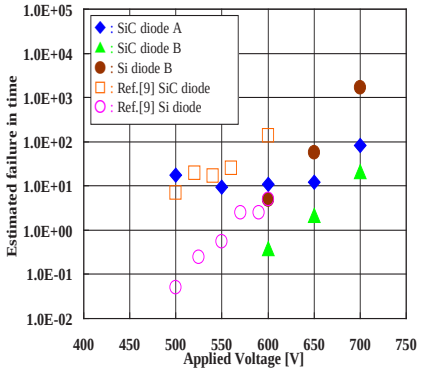

Fig. 6 Estimated failure in time (FIT) versus Applied Voltage. The experimental FIT and that of the reference [9] were compared.

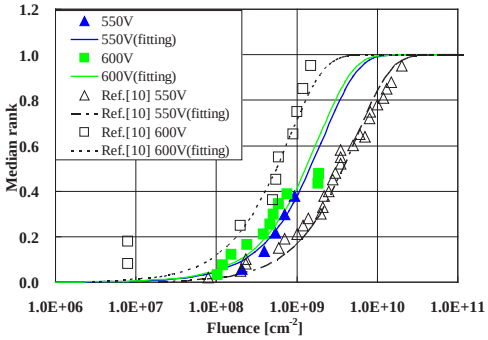

Fig. 7 Median rank plots (symbols) as a function of fluence and fitting curves of cumulative failure distribution functions (lines) for SiC diode A (neutron irradiation) and reference [10] (proton irradiation).

References

[1] H.R. Zeller, Microelectron. Reliab., vol. 37, No. 10/11, pp. 1711-1718, 1997.
[2] E. Normand et al., IEEE Trans. Nucl. Sci., vol. 44, pp. 2358-2366, 1997.
[3] D.L. Oberg et al., IEEE Trans. Nucl. Sci., vol. 43, pp. 2913-2920, 1996.
[4] Ch. Findeisen et al., International Foundation HFSJG, Activity Report, 1999/2000.
[5] Th. Stiasny, International Foundation HFSJG, Activity Report, 2005.
[6] S. Nishida et al., in proceedings of the 22th International Symposium on Power Semiconductor Devices & ICs, 2010.
[7] E. Normand, IEEE Trans. Nucl. Sci., vol. 43, pp. 2742-2750, 1996.
[8] H. Kobayashi, IEEE Proc. IRPS Symp., pp. 288-293, 2004.
[9] G. Soelkner, Materials Science Forum, vol. 556-557, pp. 851-856, 2007.
[10] S. Kuboyama et al., IEEE Trans. Nucl. Sci., vol. 54, pp. 2379-2383, 2007.
[11] L. Scheick, IEEE Radiation Effects Data Workshop, pp. 58-62, 2007.
[12] H. Asai et al., in proceedings of the 8th European Workshop on Radiation Effects on Components and Systems, 2008.
[13] H. Asai et al., IEEE Trans. Nucl. Sci., vol. 59, pp. 880-885, 2012.
[14] Y. Iwamoto et al., Nuclear Technology, vol. 173, pp. 210-217, 2011.
[15] H. Iwase et al., J. Nuci. Sci. Technol., 39, pp. 1142-1151, 2002
[16] K. Sugimoto et al., in proceedings of the 9th International Workshop on Radiation Effects on Semiconductor Devices for Space Applications, 2010
[17] NIST/SEMATEC e-Handbook of Statistical Methods, http://www.itl.nist.gov/div898/handbook/, June 2010.
[18] JEDEC Standard JESD89A, Oct. 2006

Session G

Total Ionizing Dose and Displacement Damage Effects

Total Ionizing Dose (TID) and Displacement Damage (DD) Effects in Integrated Circuits: Recent Results and the Implications for Emerging Technology

Leif Scheick[*1], Allan Johnston[1], Philippe Adell[1], Farokh Irom[1], and Steve McClure[1]
1 Jet Propulsion Laboratory, California Institute of Technology, USA
*Email: leif.z.scheick@jpl.nasa.gov
Keyword(s): ELDRS, NIEL, Total dose

Abstract

Over the last 50 years, the effects of cumulative radiation damage in microelectronics, and now nanoelectronics, have continually presented a design and assurance challenge to space flight missions. Feature sizes, that is, the size of the unit structure in microelectronics, has continually decreased, which has presented an added complexity to testing and assuring microelectronic devices. This paper outlines the paradigm shifts of total ionizing dose (TID) and displacement damage (DD) effects as device sizes have reduced and highlights some of the strategies developed to insert apply microelectronics into space. The current trends of the technology are analyzed in context of future JPL and NASA missions.

1. Introduction

With the recent deployment of the Mars Science Lander and Juno missions, the Jet Propulsion Laboratory (JPL) reaffirmed a long history of launching spacecraft to remote and harsh locales of the solar system. Of course the space radiation environment presents a unique assurance challenge to all spacecraft designs. The Juno mission, also called the Jupiter Polar Orbiter, will travel through the radiation belts of Jupiter and endure a severe radiation environment [1]. Such mission profiles to the moons of Jupiter or orbits toward the Sun, like Goddard Space Flight Center's Living with a Star (LWS) program are presenting ever-increasing requirements on radiation assurance. Total ionizing dose (TID) levels over 300 krad(Si) are expected for any mission to a Jovian moon [2], [3]. To enhance mission capabilities, the use of advanced technologies is in demand. However, it adds a layer of complexity when assuring the survivability of those devices in such environments.

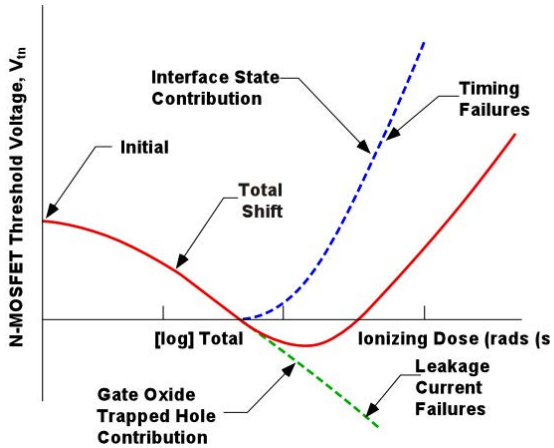

Fig. 1. Voltage threshold shift for an N-channel MOSFET with dose.

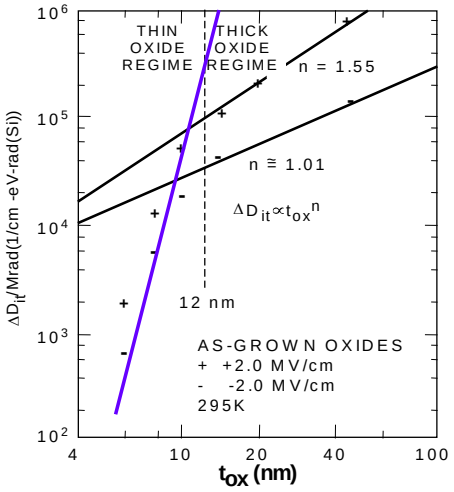

Fig. 2. Trapped charge per unit dose for various oxide thicknesses. Gate oxides are much thinner in modern devices.

2. CMOS radiation effects

2.1 Historical Trends in Radiation Effect as Devices Scale Down

The trend of scaling and increased performance due to reduction in feature size has been governed by and large by Moore's law [4]. Moore's law has stated that in microelectronic devices, especially in CPUs,

transistor count doubles and the feature size reduces by 30% every 2 years. Twenty two nanometers gate length is the current feature size in modern devices. This feature size and the design rules that follow determine the density of memories, which is critical to the space science and communication community as the data and bandwidth needs have driven the need for highly scaled memories and data processors for space missions.

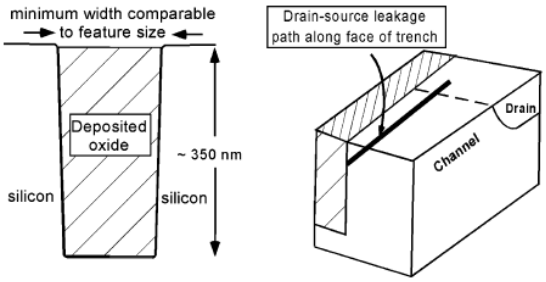

Fig. 3. Side-wall leakage path in a STI structure. The interface between silicon and silicon dioxide always presents a perspective leakage path.

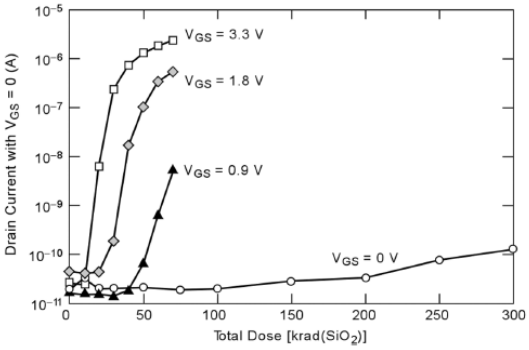

Fig. 4. Inversion measurements for 180 nm test structures irradiated under different bias conditions.

The main effect of TID on microelectronics is the effect liberated charge has on the insulating silicon dioxide (SiO_2). Fig. 1 shows the typical response of trapped charge in the oxide of an N-channel metal oxide silicon (MOS) structure. The polarity of the charge liberated in an oxide is trapped according to the nature of the local silicon. In an N-channel device, the charged trapped at the interface is negative, that is electrons, and the bulk oxide that is away from the interface, is holes. The relative trapping rate of charge in the interface versus the bulk determines the overall response of the devices. All N-channel devices, if irradiated long enough, will show the behavior in Fig. 1. The dose level at which one type of charge out numbers another depends on many factors, such as dose rate, gate bias, oxide thickness and temperature. A P-channel device, on the other hand, will have only trapped holes, so the effect is a solely negative threshold shift on the MOS structure. As the gate oxides of advanced CMOS technologies scale to thinner dimensions, the threat of shifts in DC parameters due to oxide trapped charge (N_{ot}) buildup in the gate oxide is reduced as shown in Fig. 2.

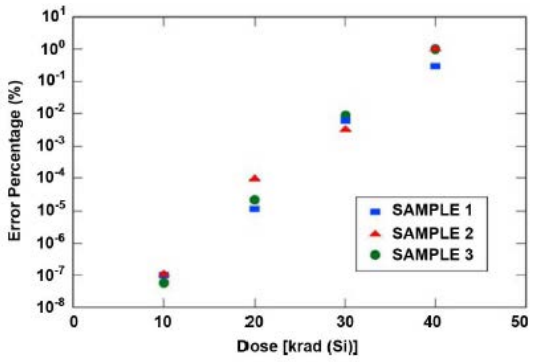

Fig. 5. Percentage of data errors versus dose for 8 Gb MLC Samsung NAND flash for sequential pattern in No Refresh Mode.

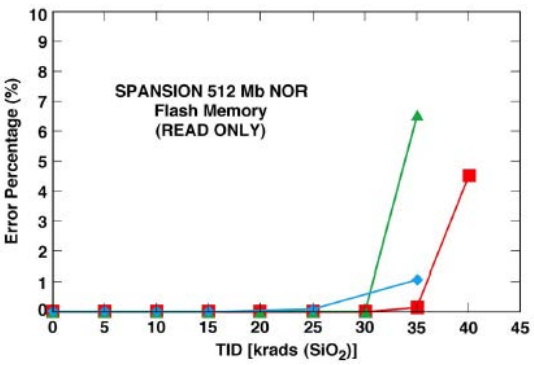

Fig. 6. Percentage of bit errors versus dose for three samples of Spansion 512Mb NOR flash memory in No Refresh Mode.

These results would indicate that as features size reduces, the TID hardness of a device will increase. If only the gate oxide is considered, then one could expect that TID effects will disappear [5]. Instead, as devices shrink, radiation-induced charge buildup in field oxides has become to dominate the degradation and induces leakage currents. Indeed, the structure of a highly scaled modern device consists of several isolation oxide structures with thicknesses (~300 nm) order of magnitude higher than the gate oxide. The field oxide is more prone to traps that, when charged, present a voltage shift to the channel or surrounding silicon [6]. This results in MOSFET threshold shifts or a parasitic leakage path through the local silicon. Processing changes like shallow trench isolation (STI) or devices constructed on silicon on insulator (SOI)

processes have been proposed to reduce these effects, but STI suffers from side-wall leakage paths and SOI suffers from back channel leakage [7].

2.2 Radiation Effect is Advanced MOS Structures and Devices

Recent studies at JPL have addressed many of these issues for TID. JPL's goal for a Jovian moon mission would be 1 Mrad(Si) hard microelectronic devices, and even after one inch of aluminum shielding the expected dose level is 300 krad(Si). So considerable thoughts at JPL have been expended to develop strategies to assure proper device operations to these dose levels. Johnston et al have done considerable work in recent years about the radiation hardness of CMOS structures. For example, Fig. 3 shows the simplified STI structure along with the suspected drain-to-source parasitic leakage path possible if the STI oxide traps enough charge [8]. The effect is modulated by the distance of the oxide from the channel of the MOSFET and the length of the parasitic path, which implies that the proper architecture for a CMOS device can vastly mitigate field oxide or STI leakage. The irradiation bias is an ever present problem for CMOS as Fig. 4 shows. The same structure as Fig. 3 is shown modeled to a 180 nm process and the damage is noticeably worse at higher bias, which is an inescapable fact of CMOS TID effects.

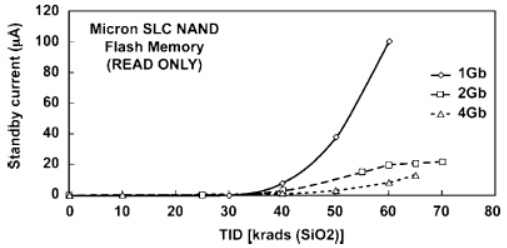

Fig. 7. Standby current results versus dose for Micron Technology 1, 2 and 4 Gb SLC NAND flash memory in No Refresh Mode.

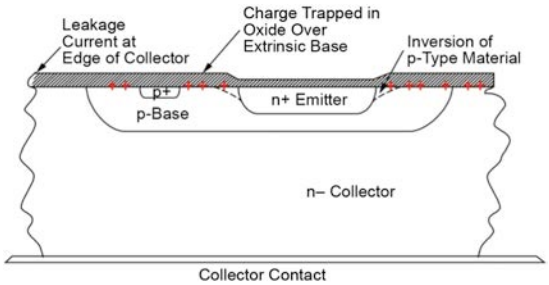

Fig. 8. Charge trapping effect in a PNP bipolar transistor. The reduction in gain due the increase recombination causes bipolar device failure.

The driving requirement for more bandwidth and data depth in space missions, especially for JPL, has driven the use of commercial off the shelf (COTS) solutions. Among other, memories with high capacity are in demand and for instance, the only current high density non-volatile memory (NVM) option is the floating gate based flash memory. Both NAND and NOR based flash memories are used and are heavily tested to find uniquely robust devices. Densities of flash memories are currently at 32 Gbit and multiple bits of information can now be stored on a single cell. The erasure of a flash device by TID has been known for some time; however, the primary TID failure mechanism of flash memory currently lies in the charge pump of the device. Fig. 5 shows the number of errors in a multi-level cell (MCL) NAND flash due to the degradation of the charge pump [9]. Bagatin et al showed for modern flash memories the output of the charge pump drops immediately with dose and eventually cannot support programming or erasing the device around 50 krad(Si) [10]. A similar response was seen for NOR flash in Fig. 6 where the errors grow exponentially with doses [11]. Both NAND and NOR flash memories exhibit 100% error coverage around 50 krad(Si) and is considered to coincide with the charge pump failure. The support circuitry for flash memory, however, has seen the benefits from the decrease in feature size, so the effects of TID on the leakage paths of the control circuitry has been seen to decrease for more dense devices as shown in Fig. 7 [12]. Since memory retention TID effects and charge pump degradation can be mitigation, the TID effects on control circuitry with remain an issue for flash memory.

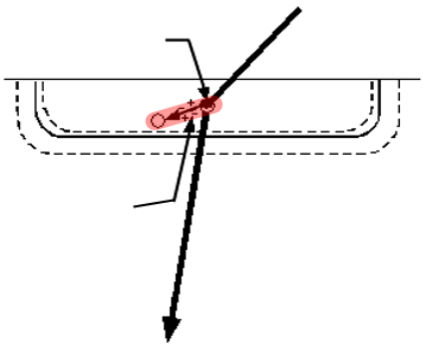

Fig. 9. Atomic iteration of a particle in a depletion region. This is the core interaction of DDD damage.

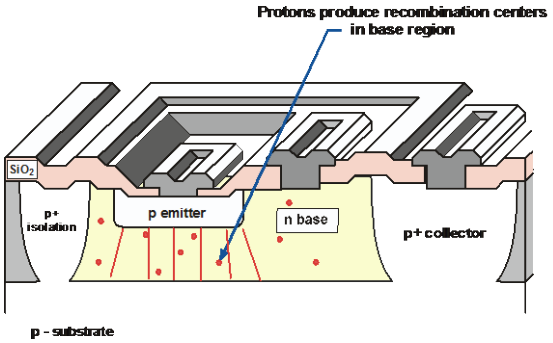

Fig. 10. DDD accrual in the transistor region of a PNP device.

3. Bipolar Radiation Effects

3.1 Radiation Effect in Modern Bipolar Devices

Bipolar devices, unlike CMOS, have evolved toward greater precision and efficiency in recent years. This is mainly because bipolar technologies are predominantly used in measurement and telemetry applications, which by and large do not require a significant density to function in a space system. Bipolar ICs that have been designed in the context of Moore's law have received some of the benefit in modern devices; however, the effects of these are seen in the size or density of newer devices. At the core of dose effects on bipolar ICs is the effect of radiation on the bipolar junction transistor (BJT). Fig. 8 shows how the oxide that that exists near the transistor region of the device is affected by TID. The trapped charge in the oxide increases the recombination in the base-emitter region by influencing the depletion region of the device. The result of this increase in recombination is a decrease in the gain of the transistor. Both PNP and NPN have a similar drop in gain, but the magnitude of the drop depends on the irradiation conditions and architecture of the device. Recombination of the bipolar device will also increase if the minority carrier lifetime decreases. Atomic dislocations from irradiation, called displacement damage (DD or DDD for displacement damage dose), reduce minority carrier lifetime as shown in Fig. 9. Fig. 10 shows how the displacement damage in a bipolar transistor reduces the gain. In both cases of TID and DDD irradiation, the damage to the bipolar transistor, which is the primary constituent device of a bipolar IC, will affect any parameter of the IC that depends on the integrity of the transistor. As the parameters of the constituent device on a bipolar IC degrade, the performance of the device will degrade. Matched transistors in an operational amplifier will induce more offset voltage as the damage increases. Finally, as the forced gain requirements of the device are not met, the device will exhibit functional failure.

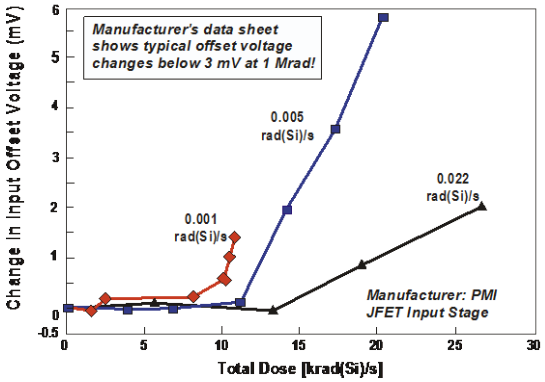

Fig. 9. ELDRS effect in JFET input stage OPAMP.

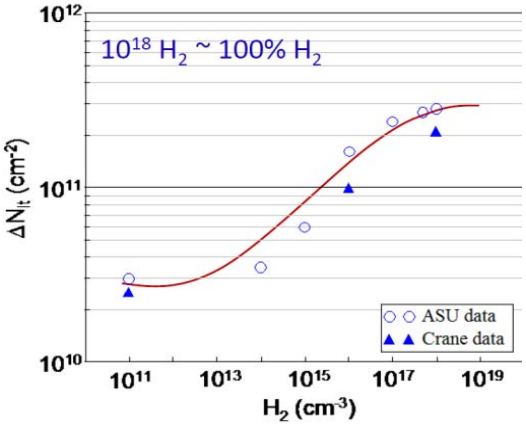

Fig. 10. Enhancement of the ELDRS effect as a function of hydrogen.

Bipolar devices are unique in TID sensitive devices in that the rate at which the bipolar IC is irradiated affects the magnitude of the damage. The effect has been named Enhanced Low Dose Rate Sensitivity (ELDRS) but should be noted that since it is seen to occur that dose rates over 0.01 rad(Si)/s or 300 krad(Si)/year, it is actually more of an artifact of the laboratory high dose rate testing. It this vein ELDRS should be called Reduced High Dose Rate Sensitivity. The ELDRS basic process is due from the self-interaction of injected charge in the oxide near the passivation layer that reduces trapping by increasing recombination and charge transport. Fig. 9 presents the archetypical ELDRS response in a bipolar device. Many bipolar ICs have saturated ELDRS response at 0.01 rad(Si)/s, but as Fig. 9 shows, some devices show continued ELDRS response at lower dose rates.

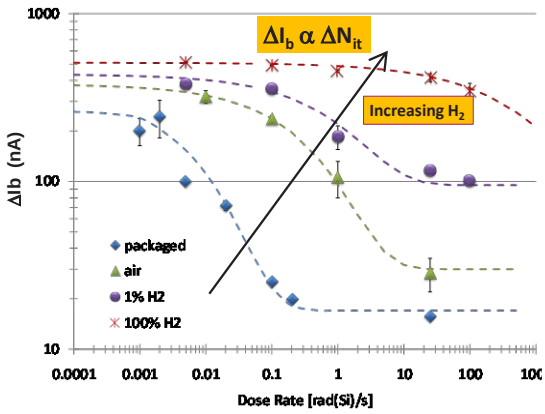

Fig. 11. Enhancement of the ELDRS effect as a function of dose rate for various H_2 levels.

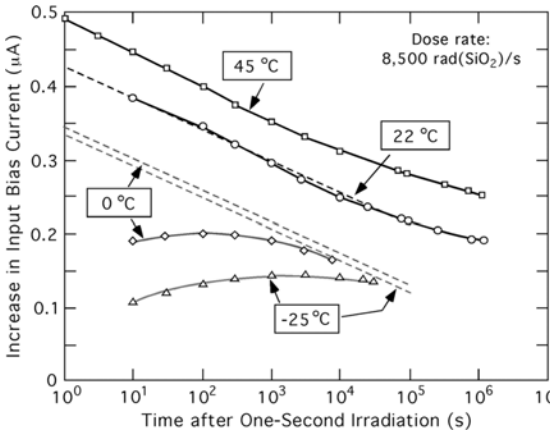

Fig. 12. Effect of temperature on annealing.

3.2 Recent Bipolar IC Radiation Test Results

The lion's share of recent research at JPL into the ELDRS has focused on understanding the dynamics of the effect. The presence of hydrogen in or near the passivation layer of the device was postulated to aggravate the effect. Taken from [15], Fig. 10 shows the effect of hydrogen concentration in a device. The amount of hydrogen does two things: 1) it increases the degradation at LDR; i.e. the saturated ELDRS effect by a factor of up to 10; 2) it increases the dose rates region where the transition from high dose rate (HDR) to low dose rate (LDR) enhancement occurs. Fig. 11 shows the continuation of the research for various dose rates and hydrogen concentrations [16]. The presence of hydrogen near the passivation results in more ionic hydrogen attaching to dangling bonds at the passivation/oxide interface and this condition results in more trapping sites. It is important to note that the ELDRS effect is present even when the hydrogen concentration is zero.

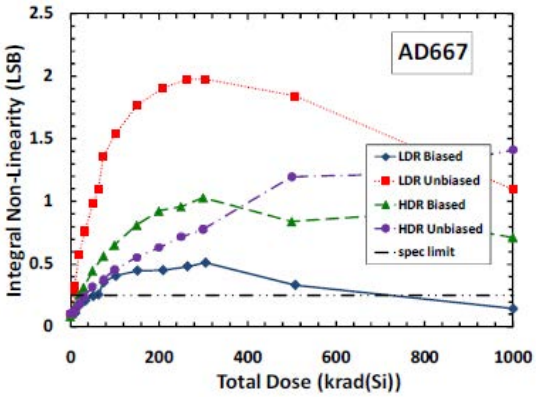

Fig. 13. AD667 Integral Non-Linearity degradation at high dose LDR irradiation.

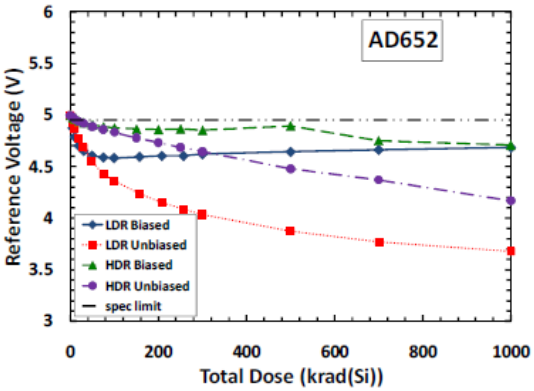

Fig. 14. AD652 Reference Voltage degradation at high dose LDR irradiation.

Other EDLRS studies sought to understand the nature of charge migration in irradiated bipolar devices. Fig. 12 shows the effect of irradiating a bipolar device at various temperatures to study the charge transport effects [17]. The lower temperature irradiations resulted in less measured shift. The results were correlated to a continuous random walk (CTRW) model to explain the observed ELDRS effect.

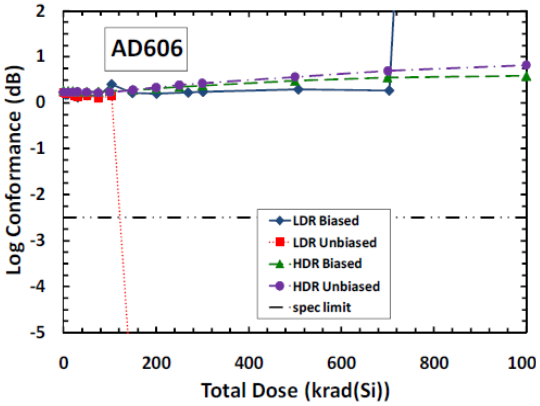

Fig. 15. Sudden device failure of a bipolar IC under high dose LDR irradiation.

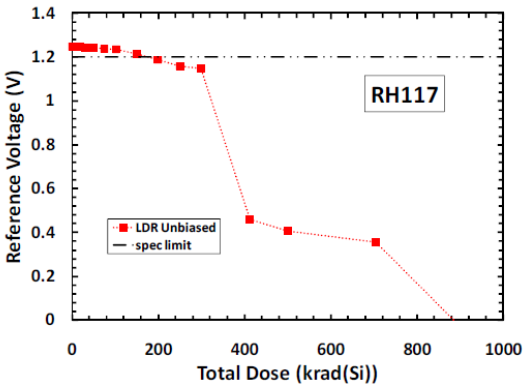

Fig. 16. Eventually functional failure of a radhard voltage regulator under continual LDR irradiation.

Since the target goals of various JPL missions reflect TID levels between 300 and 1000 krad(Si), the effects of these dose levels at LDR is of great interest. Since the difference between HDR and LDR will affect results in each constituent device of the IC differently, the overall response of a complex bipolar IC to LDR at high dose levels is hard to predict. Recent testing at JPL has shown this to be true [18]. Fig. 13 and Fig. 14 show LDR tests to 1 Mrad(Si) for two COTS devices. As expected the LDR in the unbiased condition is the worst case, however the effect saturated and seem to rebound in the case shown in Fig 13. This effect was postulated to be due to the competing degradation of devices in the IC. In both cases, the LDR biased condition was the least responsive. Both of these cases show the HDR testing was not able to predict the final LDR response. HDR testing was also not able to predict device failure, as seen in Fig. 15, where the LDR testing of a device resulted in functional failure not seen in the HDR testing. Finally, Fig. 16 shows the inevitable functional failure of a voltage regulator at high enough dose in LDR testing.

4. Conclusion

CMOS technology has continually increased in capability and density. And in these changes, TID effects have evolved with the device. Gate leakage and shifts have been replaced by similar effects due to side-wall leakage in STI, back channel leakage in SOI and side-channel leakage for field oxides. These effects however have been able to be addressed in many rad-hard designs. The primary limit to CMOS and bipolar ICs is the underlying silicon. Silicon is at its efficiency and bandwidth limit, and therefore presents a mass, speed and power limitation to both very large and very small JPL missions. Some exotic silicon structures like FINFET or FOXFET allow for devices to advance, but the fundamental limits are the same. Proposed technologies like graphene based ICs offer much lower power for the same speed allowing for very small space missions, which allow for unprecedented mission flexibility. Alternate device materials, like SiC or GaN, offer speed and power options to space applications.

A. Acknowledgments

The authors would like to thanks Bernard Rax and Dennis Thorbourn of JPL for their tireless efforts in taking much of the data presented in this work. The research was carried out at the Jet Propulsion Laboratory, California Institute of Technology, under a contract with the National Aeronautics and Space Administration. Copyright statement must be added until copyright is transferred to publisher. Copyright 2012 California Institute of Technology. Government sponsorship acknowledged. Partial support by the NASA Electronic Parts and Packaging Program (NEPP) is acknowledged.

B. References

[1] Kayali, S.; McAlpine, W.; Becker, H.; Scheick, L., "Juno radiation design and implementation," Aerospace Conference, 2012 IEEE, pp.1-7, 3-10 March 2012

[2] Johnston, A.; "Space radiation effects and reliability considerations for the proposed Jupiter Europa Orbiter," Reliability Physics Symposium (IRPS), 2011 IEEE International, vol. ??, no., pp.2G.1.1-2G.1.6, 10-14 April 2011.

[3] Jupiter Europa Mission Study 2008: Final Report, Feb. 12, 2009 (available on line through the NASA website).

[4] Kuhn, K.J., "Moore's Law Past 32nm: Future Challenges in Device Scaling," Computational Electronics, 2009. IWCE '09. 13th International Workshop on, vol.??, no.??, pp.1-6, 27-29 May 2009

[5] Dodd, P.E.; Shaneyfelt, M.R.; Schwank, J.R.; Felix, J.A., "Current and Future Challenges in Radiation Effects on CMOS Electronics," Nuclear Science, IEEE Transactions on, vol.57, no.4, pp.1747-1763, Aug. 2010
[6] Shaneyfelt, M.R.; Dodd, P.E.; Draper, B.L.; Flores, R.S., "Challenges in hardening technologies using shallow-trench isolation," Nuclear Science, IEEE Transactions on, vol.45, no.6, pp.2584-2592, Dec 1998
[7] Rezzak, N.; En Xia Zhang; Alles, M.L.; Schrimpf, R.D.; Hughes, H., "Total-ionizing-dose radiation response of partially-depleted SOI devices," SOI Conference (SOI), 2010 IEEE International, vol., no., pp.1-2, 11-14 Oct. 2010
[8] Johnston, A.H.; Swimm, R.T.; Allen, G.R.; Miyahira, T.F.; "Total Dose Effects in CMOS Trench Isolation Regions," Nuclear Science, IEEE Transactions on, vol.56, no.4, pp.1941-1949, Aug. 2009
[9] Irom, F.; Nguyen, D.N.; Harboe-Sorensen, R.; Virtanen, A., "Evaluation of Mechanisms in TID Degradation and SEE Susceptibility of Single- and Multi-Level High Density NAND Flash Memories," Nuclear Science, IEEE Transactions on, vol.58, no.5, pp.2477-2482, Oct. 2011
[10] Bagatin, M.; Cellere, G.; Gerardin, S.; Paccagnella, A.; Visconti, A.; Beltrami, S.; "TID Sensitivity of NAND Flash Memory Building Blocks," Nuclear Science, IEEE Transactions on, vol.56, no.4, pp.1909-1913, Aug. 2009
[11] Irom, F.; Nguyen, D.N., "SEE and TID Response of Spansion 512Mb NOR Flash Memory," Radiation Effects Data Workshop (REDW), 2011 IEEE, pp.1-4, 25-29 July 2011
[12] Irom, F.; Nguyen, D.N.; Underwood, M.L.; Virtanen, A., "Effects of Scaling in SEE and TID Response of High Density NAND Flash Memories," Nuclear Science, IEEE Transactions on, vol.57, no.6, pp.3329-3335, Dec. 2010
[12] Esqueda, I.S.; Barnaby, H.J.; Adell, P.C.; Rax, B.G.; Hjalmarson, H.P.; McLain, M.L.; Pease, R.L.;, "Modeling Low Dose Rate Effects in Shallow Trench Isolation Oxides," Nuclear Science, IEEE Transactions on, vol.58, no.6, pp.2945-2952, Dec. 2011
[13] Kruckmeyer, K.; Prater, J.S.; Brown, B.; Trinh, T.;, "Analysis of Low Dose Rate Effects on Parasitic Bipolar Structures in CMOS Processes for Mixed-Signal Integrated Circuits," Nuclear Science, IEEE Transactions on, vol.58, no.3, pp.1023-1031, June 2011
[14] Zebrev, G.I.; Gorbunov, M.S.;, "Modeling of Radiation-Induced Leakage and Low Dose-Rate Effects in Thick Edge Isolation of Modern MOSFETs," Nuclear Science, IEEE Transactions on, vol.56, no.4, pp.2230-2236, Aug. 2009
[15] Pease, R.L.; Adell, P.C.; Rax, B.G.; Xiao Jie Chen; Barnaby, H.J.; Holbert, K.E.; Hjalmarson, H.P.;, "The Effects of Hydrogen on the Enhanced Low Dose Rate Sensitivity (ELDRS) of Bipolar Linear Circuits," Nuclear Science, IEEE Transactions on, vol.55, no.6, pp.3169-3173, Dec. 2008
[16] Philippe Adell, Ivan Sanchez, Hugh Barnaby; Modeling the Effects of Hydrogen and Dose Rate Sensitivity in CMOS and Bipolar Technologies Jet Propulsion Laboratory California Institute of Technology JPL Publication 11-17 12/11
[17] Johnston, A.; Swimm, R.; Harris, R.D.; Thorbourn, D.; , "Dose Rate Effects in Linear Bipolar Transistors," Nuclear Science, IEEE Transactions on , vol.58, no.6, pp.2816-2823, Dec. 2011
[18] Harris, R.D.; McClure, S.S.; Rax, B.G.; Thornbourn, D.O.; Kenna, A.J.; Clark, K.B.; Tsun-Yee Yan; , "ELDRS Characterization for a Very High Dose Mission," Radiation Effects Data Workshop (REDW), 2010 IEEE , vol., no., pp.7, 20-23 July 2010

Verification of Enhanced Low Dose Rate Sensitivity (ELDRS) Accelerated Test Method

Marc Poizat [1)], Michael Wind [2)], Peter Beck [2)], Marcin Latocha [2)], Laurent Dusseau [3)], Jerome Boch [3)], Fréderic Saigné [3)], Ali Zadeh [1)].
[1)] ESA/ESTEC, TEC-QEC, 2200 AG Noordwijk, The Netherlands
[2)] AIT Austrian Institute of Technology GmbH, A-1220 Vienna, Austria
[3)] UM2 Université Montpellier 2, IES – UMR UM2 / CNRS 5214, F-34095 cedex 5, France

Abstract
Low dose rate testing was performed at AIT using the accelerated switching test method developed at Université de Montpellier 2. Experiments were aiming at trying to validate the accelerated low dose rate test method for the selected parts.

Introduction
The enhanced degradation exhibited at low dose rates by many bipolar technology components is a major reliability issue for spacecraft electronics. As an accelerated ELDRS test method, an approach has been suggested that makes use of sequenced high dose rate and low dose rate exposures, the so called accelerated switching test method, developed at the University of Montpellier II [1] - [5]. It is based on the important observation that the degradation rate of device parameters after a high dose rate exposure is equal to the degradation rate recorded at low dose rate, independent at what total dose level the dose rate is switched from high to low. The dose level at which the dose rate is switched is called dose switch. Thus a high dose rate step can be used to reach a certain degradation level. With a subsequent low dose rate exposure the characteristics of the low dose rate degradation from this degradation level on can be measured. However, a shift in the (low dose rate) degradation curve is observed. This shift may be assigned to degrading species (holes and protons) that are not contributing to the degradation process during the high dose rate exposure. It is assumed, that these species are lost after the high dose rate exposure and do not affect the subsequent low dose rate irradiation. Consequently, the high dose rate degradation curve has no effect on the shape of the following low-dose-rate degradation curve [1], [2]. By using multiple switches several points on the low dose rate degradation curve can be reached. Thus it is possible to measure several segments of the low dose rate characteristics in parallel which in turn leads to a significant reduction of testing time. Finally, a prediction curve of the low dose rate degradation characteristic is constructed from the various measured segments by shifting them to the left (in terms of total dose) until an overlap of the segments is achieved (for details see [4] and Fig. 1).

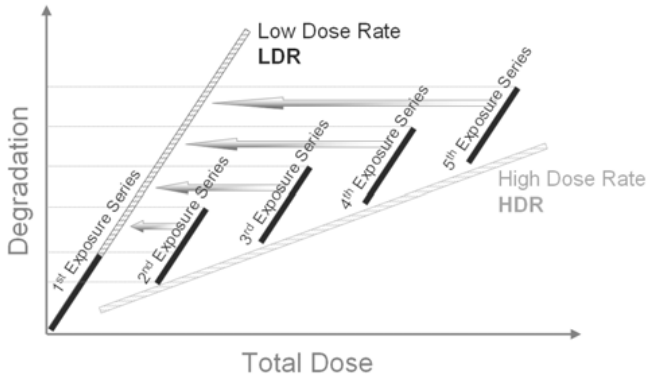

Figure. 1. schematic illustration of the switching test method to predict LDR degradation of bipolar devices. The five dark lines (denoted with 1st to 5th exposure series) correspond to data obtained from LDR measurements performed at the same time. The 1st exposure series is irradiated without a dose switch, all other using a dose switch. LDR prediction curves are obtained by shifting the data of the 2nd to 5th exposure series until an overlap is achieved (Figure is taken from [4]).

In this paper we will report on the results of an extensive study [6] that investigates the applicability of this test method to several linear integrated circuits.

Objectives of the study

The main objective of the study is to validate the applicability of the accelerated switching test method by applying it to characterize the low dose rate degradation of an extensive set of parameters of many bipolar microcircuits.

Method

The structure of the workflow is presented in Figure 2. At first all units that are used for the experiments are electrically characterized and faulty parts are rejected. The low dose rate degradation is determined with the switching test method and in addition with a reference measurement. The switching test method makes use of combining exposures at high dose rate (HDR-S) and low dose rate (LDR-S) and a subsequent data analysis to determine the estimate for the low dose rate degradation. The reference measurement makes use of a single low dose rate exposure (LDR-C) that serves to validate the results of the switching test method. Nine microcircuits are selected for testing: five operational amplifiers, three comparators, and a voltage reference (see Table 1). The electrical parameters that are selected for validating the accelerated switching test method with operational amplifiers and comparators are the offset voltage (VOS), the positive and negative supply currents (IS+ and IS-), the bias currents (Ib, Ib+, Ib-, and IOS), the open loop gain (AVO), the common mode rejection ratio (CMRR), the positive and negative power supply rejection ratio (PSRR and PSRR-), the positive and negative output voltage swing (V0+ and V0-), the positive and negative short circuit current (ISC+ and ISC-), and the slew rate (SR). The parameter selected for validating the accelerated switching test method with the voltage reference is the output voltage (VOUT).

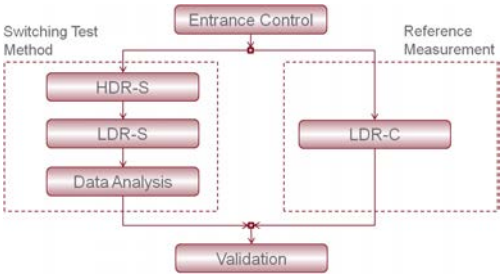

Figure 2: Workflow to verify the applicability of the accelerated switching test method.

Table 1: Microcircuits selected for testing.

Microcircuit	Description	LOT #
LM324AN	Operational Amplifier	CZ8P1667D019
LM158AJ	Operational Amplifier	C6X405476
LM339AN	Comparator	EM8V3371G019
LM311N	Comparator	EM8V7541K019
HS-OP470ARH	Operational Amplifier	DCEVVJA
HS9-139RH	Comparator	DTCJCDD
OP470	Operational Amplifier	E163778.3 (biased units) E165098.3 (unbiased units)
OP177GS	Operational Amplifier	AE37195.17
LM336-2.5	Voltage Reference	CZAT2047E019

Tests are conducted in biased and unbiased configuration. In the unbiased configuration all terminals of the microcircuits are held at ground potential. When exposing the microcircuits in biased condition the devices are driven in a typical operational condition. Operational amplifiers are biased in a non inverting DC gain configuration, comparators are exposed in a basic comparator configuration, and the voltage reference is operated as a 2.5 V Zener diode. The switching experiment makes use of four dose switches that are set at 20 krad(Si), 40 krad(Si), 60 krad(Si), and 80 krad(Si). For the experiments the exposed units are grouped in so-called exposure series that are composed of five units each (also denoted as “sample size: 5”). All the units of one exposure series are treated identically. Sample size 5 is used to assure a good statistics of the test results. The 1st exposure series is only exposed at LDR-S, the 2nd to 5th exposure series are exposed at HDR-S. Hereby the 2nd exposure series is irradiated to a dose level of 20 krad(Si), the 3rd to a dose level of 40 krad(Si), the 4th to a dose level of 60 krad(Si), and the 5th to a dose level of 80 krad(Si). Subsequent to the HDR-S all exposure series are exposed at LDR-S (for details of the switching test method see [1] - [5]). The exposure is performed according to ESCC specification No. 22900 [8] at a dose rate of approximately 1.2 rad(Si)/s, the low dose rate exposure LDR-S is performed at 10 mrad(Si)/s. The radiation source is 60Co gamma point source. To ensure charged particle equilibrium at the position of the DUTs during exposure a build up plate is used that is made from PMMA with a thickness of 3 mm.

Results

The low dose rate degradation of 256 parameters – exposure of nine microcircuits exposed in two biasing conditions – are characterized using the switching test method. From the comparison of switching data with reference data it can be seen for each individual parameter of every microcircuit whether the accelerated switching test method can be applied or not. Figures 3(a) and 3(b) show for the slew rate of the LM158AJ how the data from the various exposure series are shifted to the left (in terms of total dose) until an overlap is achieved. The reference measurement obtained from continuous low dose rate data (LDR-C) is shown as well.
In the following figures, the analysed data is superimposed with the results of the reference measurements denoted in the graphs as LDR-C Reference (black symbols).

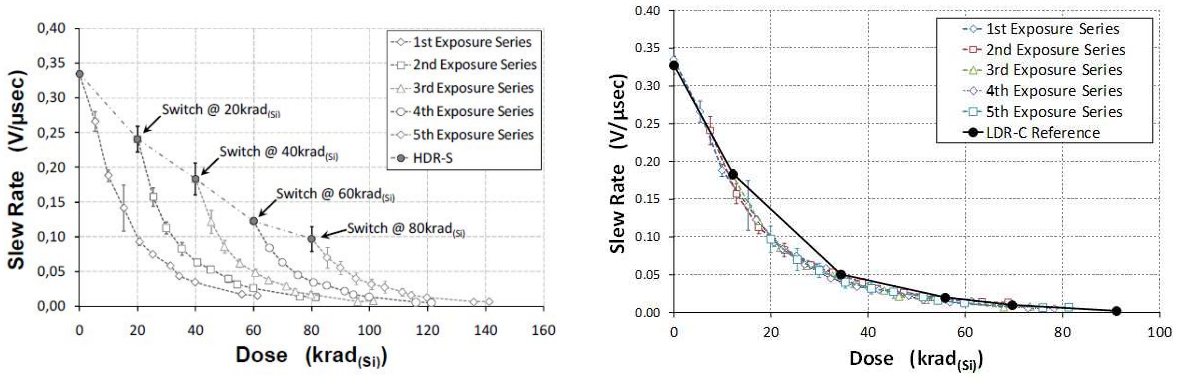

(a) (b)

Figure 3: Results of the experimental method to determine the low-dose-rate degradation curve of the LM158AJ microcircuit's slew rate. (a) degradation derived from the HDR-S / LRD-S measurements of all five exposure series using dose switches at 20, 40, 60 and 80 krad(Si). (b) The low dose rate prediction curve with superimposed the LDR-C reference curve.

Fig. 4 and Fig. 5 present four prediction curves of the low-dose- rate degradation for the LM158AJ microcircuit when exposed in biased and unbiased configuration, respectively. Prediction curves are presented for the parameters: positive supply current (IS+), the input bias current at the non-inverting input (Ib-), the open loop gain (AVO), and the common mode rejection ratio (CMRR).
Fig. 6 and Fig. 7 present four prediction curves for the low-dose-rate degradation for the LM339AN microcircuit when exposed in biased and unbiased configuration, respectively. Prediction curves are presented for the parameters: positive supply current (IS+), the input bias current at the inverting input (Ib-), the negative short circuit current (ISC-), and the slew rate (SR).
In all the presented cases, the low dose rate prediction curves generated by switching test method are in good agreement with the LDR-C reference measurement even for devices that are designed to be radiation hard.

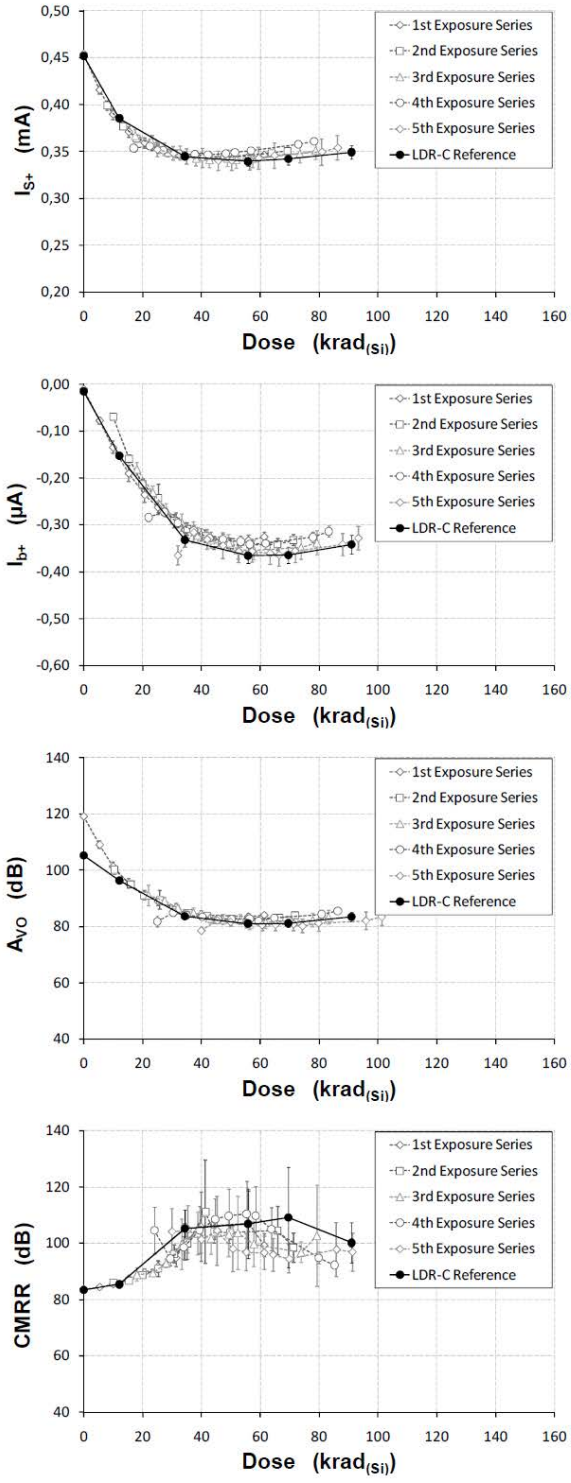

Figure 4: Results obtained with the switching test method to determine the low-dose-rate degradation curves of the LM158AJ microcircuit when exposed in biased configuration. Presented are the low-dose-rate prediction curves of four parameters (hollow symbols) with superimposed the LDR-C reference curves (full symbols). (Figure from [6])

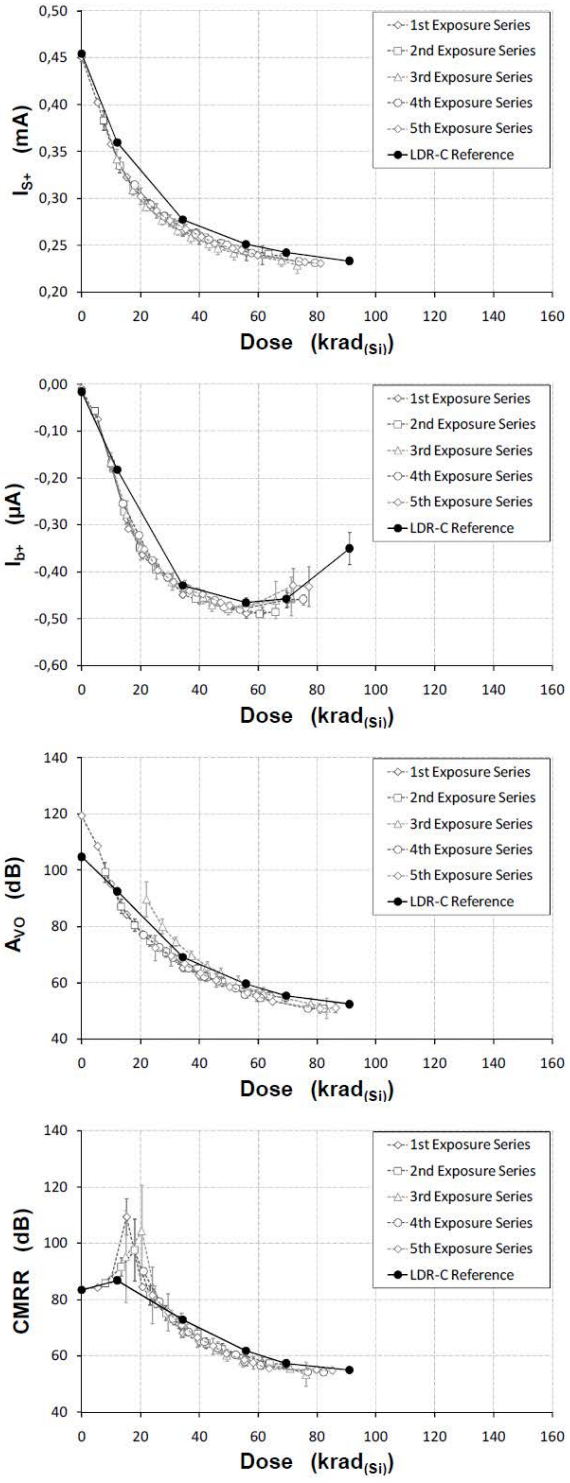

Figure 5: Results obtained with the switching test method to determine the low-dose-rate degradation curves of the LM158AJ microcircuit when exposed in unbiased configuration. Presented are the low dose rate prediction curves of four parameters (hollow symbols) with superimposed the LDR-C reference curves (full symbols). (Figure from [6])

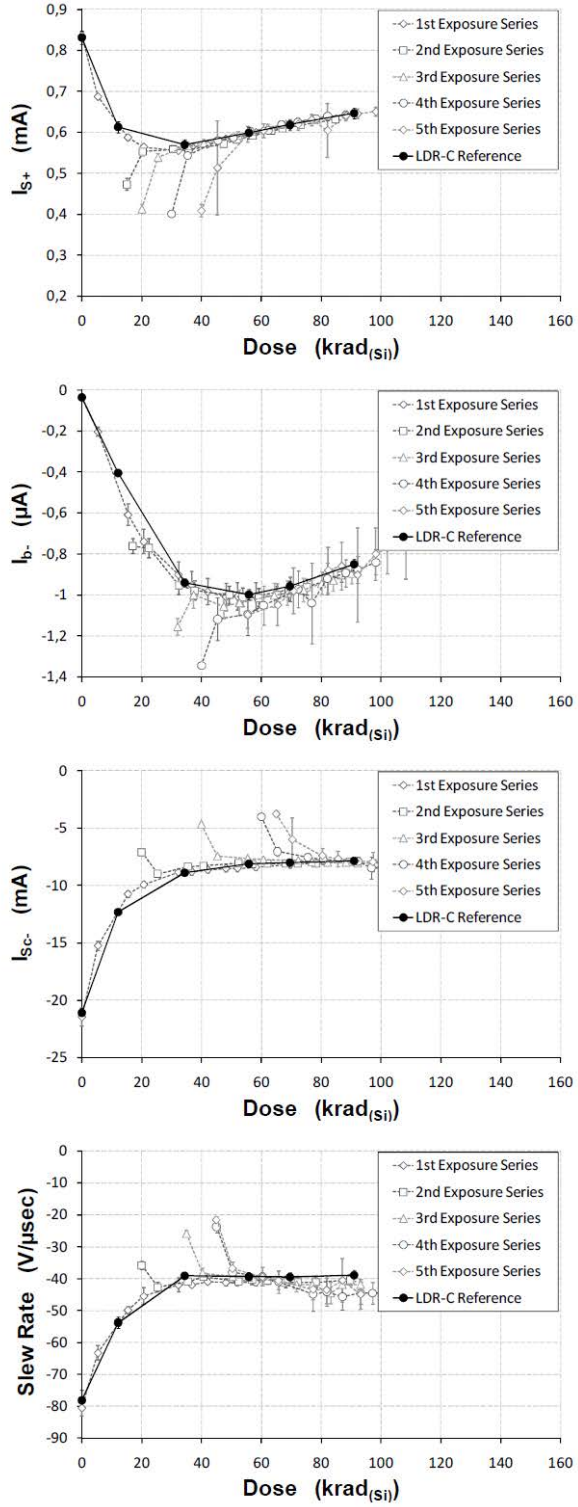

Figure 6: Results obtained with the switching test method to determine the low-dose-rate degradation curves of the LM339AN microcircuit when exposed in biased configuration. Presented are the low-dose-rate prediction curves of four parameters (hollow symbols) with superimposed the LDR-C reference curves (full symbols). (Figure from [6])

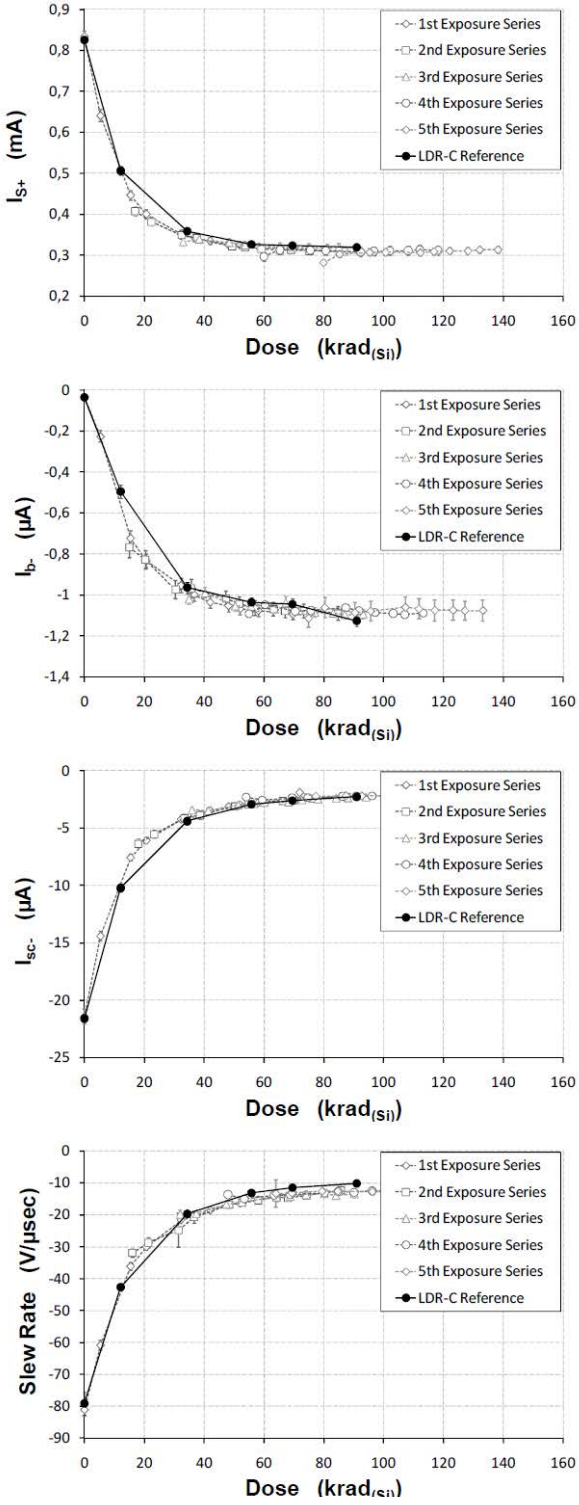

Figure 7: Results obtained with the switching test method to determine the low-dose-rate degradation curves of the LM339AN microcircuit when exposed in unbiased configuration. Presented are the low-dose-rate prediction curves (hollow symbols) of four parameters with superimposed the LDR-C reference curves (full symbols). (Figure from [6])

Summary and Conclusion

The present work covers investigation on low dose rate degradation of 256 parameters of nine bipolar microcircuits in biased and unbiased configurations. Experiments are performed using the accelerated switching test method and a continuous low dose rate irradiation as reference measurement. In total more than 100,000 data points are assessed. The method works fairly well for the investigated microcircuits and parameters. However, an acceptable fit is not observed for all measured parameters, care should therefore be taken in the implementation of this test method. Additionally, in the frame of this study, for each device type, 70 samples were used which can represent significant added costs in the case of high reliability components. The complexity associated with the practical implementation of the method (large samples size, switching dose rates at various time intervals), should not be underestimated either. It seems therefore premature to implement this test method in the European ESCC22900 TID test guidelines [8]. To improve the results, further investigations with larger dose rate applied during HDR-S are suggested in the literature. Statistical methods could potentially be used to limit the number of test samples while still maintaining an acceptable confidence level.

Acknowledgements

The project was carried out under the ESA GSTP program, supported by the Austrian Ministry of Traffic, Innovation and Technology, coordinated by the Austrian Space Agency and Research Promotion Agency (FFG). The support of National Semiconductor, Intersil, and Analog Devices, Tyndall National Institute is very much acknowledged.

References

[1] J. Boch et al, Effect of Switching From High to Low Dose Rate on Linear Bipolar Technology Radiation Response, IEEE-TNS, vol. 51(5), p. 2896, October 2004

[2] J. Boch et al, Estimation of Low-Dose-Rate Degradation on Bipolar Linear Integrated Circuits Using Switching Experiments, IEEE-TNS, vol. 52 (6), p. 2616, December 2005

[3] J. Boch et al, Dose-Rate Effects in Bipolar Oxides: Competition between Trap Filling and Recombination, Appl. Phys. Letters, vol. 88, pp. 232113, 2006

[4] J. Boch, Y. et al, “The Use of Dose-Rate Switching Experiments to Characterize Bipolar Devices”, IEEE-TNS, vol. 56, pp. 3347 – 3353, 2009

[5] L. Dusseau, et al , Review and Analysis of the Radiation Induced Degradation Observed for the Input-Bias Current of Linear Integrated Circuits, IEEE-TNS, vol. 55(6), p. 3174, December 2008

[6] M. Wind, P. Beck, J. Boch, L. Dusseau, M. Latocha, M. Poizat, A. Zadeh, Applicability of the Accelerated Switching Test Method – A Comprehensive Survey, Radiation Effects Data Workshop (REDW), 2011

[7] J. Boch, et al, “ELDRS: Optimization Tool for the Switched Dose Rate Technique”, IEEETNS 2011

[8] ESCC Basic Specification No. 22900, Total Dose Steady-State Irradiation Test Method

Built-In Self-Test Circuit for Total Ionizing Dose Radiation Effects in Analog-to-Digital Converters

Esko O. Mikkola*[1], Viraj S. Pandit[2], Byoung Uk Kim[1], and Andrew Levy[1]

[1] Ridgetop Group, Inc., USA
[2] Novellus Systems, Inc., USA
*Email: Esko.Mikkola@RidgetopGroup.com

Keywords: Built-in self-test (BIST), Total ionizing dose (TID), Radiation Effects, Analog-to-Digital Converter (ADC)

Abstract

Innovative Built-In Self-Test (BIST) circuit for monitoring Total Ionizing Dose (TID) radiation effects in Analog-to-Digital Converters (ADC) is presented.

Introduction

Total ionizing dose (TID) effects remain a significant problem in analog-to-digital converter (ADC) design, despite the trend of improving TID hardness of deep submicron CMOS technologies. High-resolution ADCs require high-gain analog components, such as operational transconductance amplifiers (OTA). The high open loop voltage gain in these amplifiers is normally achieved by stacking several transistors on top of each other in cascodes, which requires the use of analog power supply voltages higher than the thin gate oxides of standard deep submicron nanotechnology CMOS transistors can withstand. Moreover, it is preferable to use higher power supply voltages in order to maximize the converter signal-to-noise ratio (SNR) in the presence of thermal noise. Hence, older CMOS technologies or thick-oxide I/O transistors available in newer technologies are still commonly used for ADC designs, thus TID remains a problem.

One of the main challenges has been the TID-induced offset errors in analog and mixed-signal circuits, such as amplifiers and comparators. These offset errors can be caused by TID-induced threshold voltage (V_T) shifts and/or leakage currents [1]. Systems containing these building blocks, such as ADCs, have been shown to be particularly “soft” for TID in numerous studies and tests. Several types of failures, such as missing codes [1], [2], increased non-linearity [1-6], increased power supply current [3-5], degraded internal reference voltage [4-6], and increased gain error [7] have been shown to occur in ADCs after only 5 to 60 krads of TID.

This paper describes an innovative BIST system that can be used to monitor TID-induced performance degradation effects in ADCs, such as increased differential non-linearity (DNL), integral non-linearity (INL), gain error, offset error, and missing codes. The BIST system is designed in a commercial 0.25 μm CMOS process. The digital and mixed-signal circuit blocks have been simulated and verified through VHDL, VHDL-AMS, and SPICE simulations in the Dolphin SMASH® simulation environment. Radiation effect simulations were performed in VHDL-AMS to prove the effectiveness of the BIST circuit in capturing the TID-induced parameter drifts in a commercial 8-bit ADC.

Total Ionizing Dose Radiation Effects

The TID damage pertains to a cumulative charge collection and trapping in semiconductor oxides caused by ionizing radiation over the exposition time. It is measured in rads, and can cause slow gradual degradation in IC performance. Trapped charge in the gate oxide of an NMOS device causes a V_T shift, which further can cause an offset in an analog circuit that the transistor is used in. The TID-induced V_T shift does not seem to be a concern for CMOS generations of 180 nm and smaller [9]. It is assumed that this increase in TID hardness is caused by the reduction of the gate oxide thickness below the intrinsic tunneling length of SiO_2.

The other TID effect type is the leakage current that is caused by inversion of the silicon adjacent to insulation trench oxides that contain trapped charge. The severity of this effect has been significantly reduced in modern nano-CMOS fabrication processes. This is thought to be caused by several factors, one of which is the increased STI sidewall doping in the modern processes [10]. The TID-induced leakage current is still a concern for CMOS fabrication processes commonly used to design analog and mixed-signal circuits (0.18 to 1.0 μm), such as ADCs, and for I/O transistors of modern deca-nanometer processes [10].[1] The severity of the TID problem in ADC circuits can be seen in studies where top-of-the-line commercial ADCs were shown to manifest parameter drifts

[1] The TSMC 0.25 μm CMOS process, used for the designs in this paper, has been shown to have a severe leakage problem and a minor V_T shift problem in radiation environments that are comparable to the environment of the Earth orbiting satellites [9].

that render them useless after only 5 to 60 krads of TID [2-7]. It is obvious that there is a need for BIST circuits that can monitor changes in most critical ADC parameters in radiation environments.

BIST Design Overview

We have designed a BIST system that can be used to accurately self-test TID effects in different types of ADCs. The ADC performance metrics that can be tested with this BIST system are missing codes, offset error, gain error, differential non-linearity (DNL) and integral non-linearity (INL). A block diagram of the developed BIST system is shown in Fig. 1. This particular BIST design is optimized for monitoring TID effects in ADCs with resolutions up to 10 bits. Our test ADC is a commercially available 8-bit, 20 megasamples per second (MS/s), sub-ranging two-step converter [11]. For testing higher ADC resolutions, the basic circuit topology remains the same but the resolution of the delta-sigma digital-to-analog converter (DAC) in the system needs to be increased. For accurate BIST operation, the DAC resolution should be 2 to 4 bits higher than the resolution of the tested ADC. Since the conversion speed of the DAC is not critical in this BIST design, the resolution of the delta-sigma DAC can be increased by increasing the oversampling ratio (OSR). DAC resolutions up to 18 bits can be achieved, which allows self-testing of ADCs with up to 16 bits of resolution with this technique.

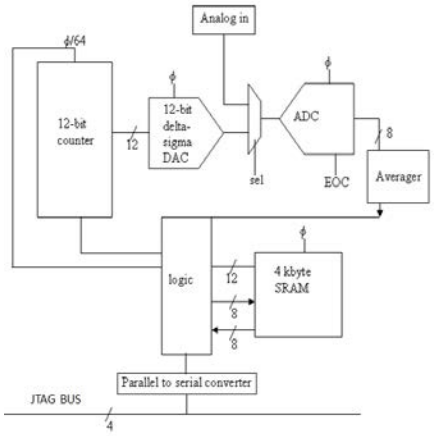

Fig. 1. The BIST system block diagram.

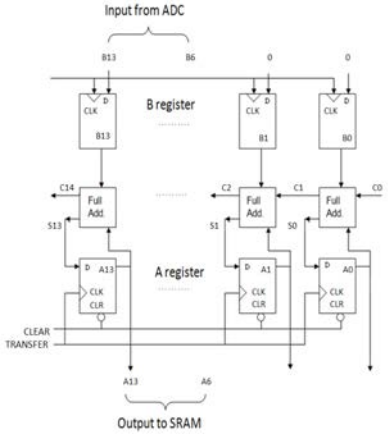

Fig. 2. Averager block diagram.

The operation of the BIST circuit in Fig. 1 is discussed next. A 12-bit counter creates the digital code input for a 12-bit delta-sigma DAC that outputs a highly linear analog voltage ramp that is used as the test bias of the 8-bit ADC. An analog multiplexer (MUX) at the input terminal of the ADC selects between the normal ADC input (shown as “Analog in” in Fig. 1) and a test bias used during a BIST cycle. A BIST cycle can be executed any time during normal operation. During a BIST cycle, the ADC samples the test signal at its nominal sampling rate, which in this case is 16 MS/s. Since the tested ADC is much faster than the high-OSR DAC, a large number of digital data for every voltage step in the input ramp will be created. These data may be stored in an off-chip memory.

Our application requires an area-intensive on-chip radiation-hardened memory, thus a special data averaging subcircuit was created to reduce the amount of data that needed to be stored. This subcircuit is called Averager in Fig. 1. The Averager computes the arithmetic average of 64 consequent ADC conversion results, and stores this average into an on-chip 4 kilobyte radiation-hardened SRAM memory. The Averager consists of digital full adders and shift registers. Its block diagram is shown in Fig. 2. Without this subcomponent, a much larger 320 kbyte on-chip memory would be needed. The control interface to the BIST circuit is a JTAG bus, which requires a serial data stream from the BIST. Thus, a component that converts the SRAM 8-bit parallel output into serial form is needed. An 8-bit parallel-to-serial converter was designed for this purpose. The last designed subcircuit is a control logic block that communicates between different subcircuits in the BIST system.

Due to area constraints, the BIST system does not contain on-chip logic that directly calculates TID-induced ADC parameter changes, such as changes in DNL and INL. The data stored in the SRAM can be accessed via the JTAG connection and the TID effect characterization will be performed off-chip. The format of the data stored in the memory is optimized for a characterization technique called “ramp histogram method” that can be used for missing code, gain error, offset error, DNL and INL characterization [2], [12]. All the parts in the BIST system have to be hardened against TID and tolerant to single-event effects (SEE). This can be done by using standard radiation-hardened-by-design (RHBD) techniques, such as the enclosed gate layout technique, guard rings, DICE cells, and triple modular redundancy. The fact that the operation frequency of the BIST circuit is

slow makes the implementation of these techniques easier.[2]

Tested ADC

The 8-bit, sub-ranging, two-step ADC used as the test device is designed [11] and manufactured by Ridgetop Group, Inc. located in Tucson, Arizona. The SPICE net list for the circuit, provided by Ridgetop, was used as a basis for the VHDL-AMS model design in this project. The 8-bit ADC consists of two flash-type 4-bit sub-ADCs. The voltage range between positive and negative reference voltages (REF+, REF-) is divided into several "internal" reference voltage values with a resistor ladder. These node voltages are connected to the reference voltage nodes of an array of comparators. The comparator array compares the input signal voltage to these reference values and outputs digital thermometer code. The thermometer code is then converted to the ADC digital output with decoder logic. An N-bit full-flash ADC has 2^N-1 comparators. Thus, a 4-bit flash has 15 comparators.

Ridgetop's 8-bit sub-ranging, two-step ADC consists of two of the above-described 4-bit flash-ADC components and control logic. The first 4-bit sub-ADC is used for extracting the four most significant bits (MSB) and the second sub-ADC extracts the remaining four least significant bits (LSB). The resistor ladder consists of 16 "large" resistors, each of which is actually formed by 16 "small" resistors connected in series. The 16 "large" resistors provide the reference voltages for the MSB converter. The MSB converter provides the four MSB bits and also controls the sub-ranging process for the LSB converter. The LSB comparator array connects to a "small-resistor" sub-range when the MSB conversion is done, and then performs the LSB conversion. The location of the sub-range, which the LSB converter connects to, is based on the MSB conversion output. The MSB and LSB bits are stored in the output registers.

Radiation Effect Simulation

The effectiveness of the BIST circuit in monitoring TID effects in ADCs was demonstrated by HDL simulations. The TID effects in the ADC circuit were modeled with a VHDL-AMS-based method that has been previously developed and published by the authors [1], [14]. In this method, TID-induced leakage currents are modeled with parasitic transistor models in SPICE simulations for basic circuit blocks, such as voltage comparators. Then these simulation results are used to construct accurate behavioral simulation models for larger circuits and systems, such as ADCs.

A VHDL-AMS simulation result for the 8-bit ADC which includes 500 krad TID models is shown in Fig. 3. The VHDL-AMS simulator was SMASH® by Dolphin Integration [15]. When this figure was created, the output of the ADC was converted back to analog format with an ideal DAC to make the radiation effect observations easier for the reader. The input to the ADC in this transient simulation is the high-linearity slowly increasing analog voltage ramp created with the 12-bit DAC in the BIST system. It's clearly seen that the radiation-induced offsets in the 8-bit ADC circuit cause severe distortions (missing codes) in the output. These missing codes are caused by voltage offsets generated in the comparators of the MSB flash ADC. These offsets cause the LSB comparator to get momentarily connected to a wrong sub-range, causing a 4-bit decrease in the resolution of the full converter, which can be clearly seen in the ADC output curve in Fig. 3.

To prove the functionality of the BIST circuit, the data stored in the 4-k SRAM block after a simulated self-test cycle are plotted (shown in Fig. 4; note that the digital code is converted to analog format with an ideal DAC again to make the radiation effect observations easier for the reader) and compared to the data directly measured at the ADC output (Fig. 3). As can be seen, the two curves are (almost) identical. After more in-depth evaluation, it was found that the data stored in the memory during the BIST cycle are an accurate representation of the distorted signal directly measured at the ADC output. This proves the functionality and effectiveness of the BIST design.

[2] The authors have previously published an innovative technique that can be used to harden the comparator in the delta-sigma DAC against single-event transients [13].

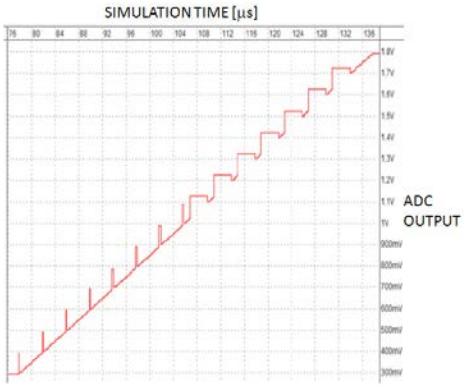

Fig. 3. Simulation with TID models show that the ADC output is severely distorted by missing codes after 500 krads of TID stress.

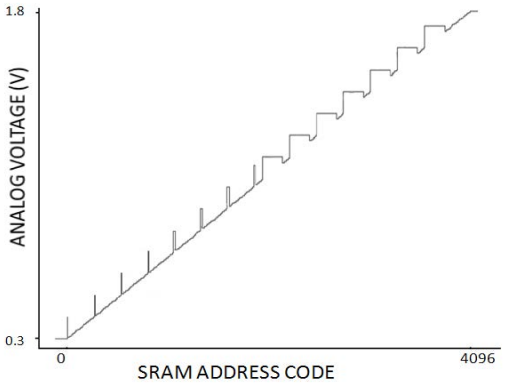

Fig. 4. The codes stored in the SRAM during the BIST cycle show exactly the same distortion effects as observed in the output of the ADC, proving the functionality of the BIST system.

Summary

An innovative built-in self-test (BIST) circuit for TID effects in analog-to-digital converters is presented in this paper. The BIST circuit can be used to monitor TID-induced performance degradation effects in ADCs, such as missing codes, increased DNL and INL, and increased gain error and offset error. Functionality of the designed BIST circuits and the effectiveness of the system in monitoring TID effects in a commercial ADC were verified through rigorous electrical and radiation effect simulations in SPICE and VHDL-AMS.

Acknowledgments

The authors wish to thank Sara Nation from NAVSEA/Crane and Ridgetop Group, Inc. for sponsorship of this work. In addition, the authors wish to thank A. Vaddigiri, E. Grubbs and U. Padmanabhan from the Electrical and Computer Engineering Department at The University of Arizona, Tucson, AZ, USA; B. Vermeire from Arizona State University, Tempe, AZ, USA; and Lucile Rey de Nardo from Dolphin Integration, Meylan, France.

References

E.O. Mikkola, B. Vermeire, H.G. Parks, R. Graves, "VHDL-AMS modeling of total ionizing dose radiation effects on CMOS mixed signal circuits," *IEEE Trans. Nucl. Sci.*, vol. 54, no. 4, part 2, pp. 929 – 934, Aug. 2007.

Sharma, A.K., et al., "Evaluation of high performance converters under low dose rate total ionizing dose (TID) testing for NASA programs," Radiation Effects Data Workshop, IEEE 1998, Page(s): 142 – 147.

Black, J.D., et al., "Total dose evaluation of state-of-the-art commercial analog to digital converters for space-based imaging applications," Radiation Effects Data Workshop, IEEE 1998, Page(s): 121 – 126.

C.I. Lee and A.H. Johnston , "Comparison of total dose responses on high resolution analog-to-digital converter technologies," *IEEE Trans. Nucl. Sci.*, vol. 45, no. 3**,** Jun. 1998.

Tomasch, G., et al., "Co-60 total dose test of 14- and 16-bit ADCs,"Radiation Effects Data Workshop, 2000, Page(s): 26 – 31.

Layton, P., et al., TID performance degradation of high precision, 16-bit analog-to-digital converters Radiation Effects Data Workshop, 20, IEEE , Page(s): 6 – 10.

H. Nakajima, et al., "Performance of an Analog ASIC Developed for X-ray CCD Camera Readout System Onboard Astronomical Satellite, " IEEE Transactions on Nuclear Science, Vol. 56, No. 3, June 2009.

M. Shadfar, Z. Navabi, "BIST modeling and its application in design verification", eda.org VIUF Proc, pp. 4.17-4.21, 1995.

R.C. Lacoe, "Improving integrated circuit performance through the application of hardness-by-design methodology," *IEEE Trans. Nucl. Sci.*, vol. 55, no. 4, Aug. 2008.

M. McLain, H.J. Barnaby, K.E. Holbert, R.D. Schrimpf, H. Shah, A. Amort, M. Baze, and J. Wert, ''Enhanced TID susceptibility in sub-100 nm bulk CMOS I/O transistors and circuits,'' *IEEE Trans. Nucl. Sci.*, vol. 54, no. 6, Dec. 2007.

InstaCell ADC-8-100 Analog to Digital Data Converter IP Data Manual, Ridgetop Group Inc., Tucson, AZ: 2005. Available: http://www.ridgetopgroup.com

S. Cherubal, A. Chatterjee, "Optimal INL/DNL testing of A/D converters using linear model", *ITC Int. Test Conf.*., IEEE 2000.

E.O. Mikkola, B. Vermeire, H.J. Barnaby, H.G. Parks, and K. Borhani, "SET tolerant CMOS comparator," *IEEE Trans. Nucl. Sci.*, Dec. 2004.

E.O. Mikkola, B. Vermeire, T. Chiu, H.J. Barnaby, H.G. Parks, "Total dose radiation effect simulations on a high-precision data acquisition system", *IEEE Trans. Nucl. Sci.*, RADECS 2007 Special Issue, Aug. 2008. (Submitted for publication)

SMASH Mixed-Signal Simulator, http://www.dolphin.fr/medal/smash/smash_overview.php

Study of radiation damage caused by 23MeV protons on Multi-Pixel Photon Counter (MPPC)

Zhengwei Li[*1,2], Yupeng Xu[1], Congzhan Liu[1],Yudong Gu[1], Xu Zhou[1,2], Xuefeng Lu[1], Xufang Li[1], Shuo Zhang[1,2], Zhenling Xu[1], Yifei Zhang[1] and Jianling Zhao[1]

1 Key Laboratory of Particle Astrophysics, Institute of High Energy Physics, Chinese Academy of Sciences, Beijing, China

2 University of Chinese Academy of Sciences, Beijing, China

*Email: lizw@ihep.ac.cn

Keyword(s): Radiation damage, MPPC, SiPM, HXMT

Abstract

The automatic gain control system (AGC) is designed to continuously monitor and automatically control the gain of the phoswich detectors of the Hard X-ray Modulation Telescope (HXMT). It consists of a ^{241}Am radioactive source distributed within a plastic scintillator (BC408) viewed by Multi-Pixel Photon Counter (MPPC). To verify the feasibility of application in space experiments, four MPPCs (S10362-33-050C) from Hamamatsu were irradiated using a beam of 23 MeV protons with flux 1.0×10^{8}pcm^{-2}, 2.0×10^{8}pcm^{-2}, 4.0×10^{8}pcm^{-2} and 1.0×10^{10}pcm^{-2}. The leakage current of irradiated MPPC samples is found to increase linearly with total dose due to radiation damage. The device has completely lost its photon-counting capability when irradiated up to 13.6Gy. The pulse-height resolution has deteriorated hardly after irradiation and couldn't work with more than 450Gy, where the measured sample has been illuminated with a few hundred photons by the ^{241}Am radioactive source.

1. Introduction

The Hard X-ray Modulation Telescope (HXMT) is an X-ray satellite working in 1-250 keV band, consisting of three collimated instruments: the High Energy X-ray telescope (HE, 20-250 keV), the Medium Energy X-ray telescope (ME, 5-30keV) and the Low Energy X-ray telescope (LE, 1-15keV) [1,2]. HXMT will perform an all-sky scan survey with high sensitivity and high angular resolution in 20-250keV by using the Direct Demodulation (DD) image reconstruction method [3,4]. It will also carry out pointing observations to investigate the temporal and spectral properties of compact objects such as black hole and neutron star binaries.

HE is composed of 18 modules. Each module has a collimator, a phoswich scintillation detector, and readout electronics. The gain of the detectors are continuously monitored and automatically controlled by the automatic gain control system (AGC). The AGC placed in front of the detection plane of phoswich detector consists of a ^{241}Am radioactive source distributed within a plastic scintillator (BC408) viewed by a MPPCs (Hamamatsu S10362-33-050C).

The Multi-Pixel Photon Counter (MPPC), developed by Hamamatsu, consists of an array of Avalanche Photodiodes (APDs) working in the Geiger mode which biased above the breakdown voltage (V_{BD}) with quenching resistor in serial and connected in parallel. Their insensitivity to magnetic field and low operating voltage (<100 V) and sensitivity to a small number of photo-electrons make them good light detectors for the plastic scintillators of AGC. AGC will be operated in harsh radiation environments such as cosmic protons, electrons which produce damage in silicon detectors. As shown by many investigators, parameters of MPPC such as leakage current, dark count rate, gain, and photon detection efficiency may change during irradiation [5-8]. How these parameters change during irradiation when operating in orbit becomes one of the most important questions for the application of the MPPC on board the HXMT satellite. The total dose for one HXMT lifetime in the proximity of the AGC photo-detector is expected to be approximately 3.4 Gy. To verify the feasibility of application in space experiments, four MPPCs (S10362-33-050C) with 3×3 mm^2 active area from Hamamatsu were irradiated using a beam of 23MeV protons.

2. Experiment setup

The radiation studies were carried out at China Institute of Atomic Energy (CIAE) using the HI-I3 accelerator. The fluence delivered on target was measured directly during irradiation using CsI detector which calibrated by an Au-Si surface barrier detector. The four MPPCs were mounted on printed circuit board as an 2×2 array in a vacuum dark box. The MPPCs were biased at 72V during radiation with a Keithley 6487 picometer. The current delivered to the MPPCs were monitored during irradiation.

The performances of the MPPC samples were checked before irradiation, such as current-voltage (I-V) curve and dark noise pulse height spectrum and the alpha spectrum of a ^{241}Am radioactive source distributed within the plastic scintillator. These performances are to be compared with that after irradiation. And the leakage current was monitored from the moment that the beam was switched on to about 10 minutes after the proton beam off. The proton beam flux irradiated (φ_p) was 4.0×10^{4}pcm^{-2}s^{-1} for Sample 4847, 1.0×10^{5}pcm^{-2}s^{-1} for Sample 4848 and 4849 and 1.0×10^{7}pcm^{-2}s^{-1} for Sample 4851. For Sample 4849, it was irradiated twice, thereby the estimated proton fluence (Ψ_p) is 4.0×10^{8}pcm^{-2} in total. The beam flux and total fluence for each sample are summarized in

Table I.
Table III Summary of proton irradiation for MPPCs

Irradiation	φ_p ($cm^{-2}s^{-1}$)	Ψ_p(cm^{-2})	D(Gy)
Sample 4847	4.0×10^4	1.0×10^8	4.5
Sample 4848	1.0×10^5	2.0×10^8	9.1
Sample 4849	1.0×10^5	3.0×10^8	13.6
Smaple 4851	1.0×10^7	1.0×10^{10}	450

The total dose (D) due to the proton irradiation can be estimated from the proton fluence Ψ_p by taking the stopping power of 23 MeV protons in silicon into account. The estimated total dose was 4.5 Gy for Sample 4847, 9.1Gy for Sample 4848, 13.6Gy for Sample 4849 and 450Gy for Sample 4851 respectively.

3. Result

3.1Variations of the leakage current

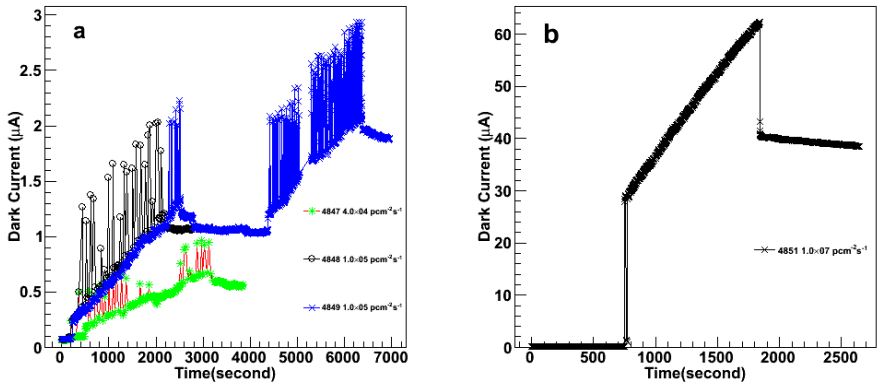

Fig. 1 Variations of the leak current for the four Samples. The fixed operating voltages, 72.0V for the samples, were applied to the samples with the voltage source during irradiation. (a) Sample 4847, 4848, 4849 (b) Sample 4851

Fig. 1 shows the variations of leakage current of Sample 4847, 4848, 4849 and 4851. The measurement of the leakage current was started before the irradiation. The current sometimes increased largely and then decreased in a short time during radiation as shown in Fig.1 (a). This is caused by the beam spot uniformity which worked in scan mode with average intensities uniform in a long time. To avoid this, the Sample 4851 was irradiated in the spread mode which the beam was pointed to Sample 4851 with $4.5\times4.5cm^2$ beam spot and was located in the center of the beam spot. The step-like changes during the irradiation as in the case of Sample 4848 disappeared as shown in Fig.1 (b). Step-like changes of leakage current at the beginning and ending of the irradiation would be caused by free carriers generated due to the ionizing processes of the beam protons traversing in silicon. And the offset change of leakage current of Sample 4851 is about 30μA. Considering the uniformity of the beam, the leakage current almost linearly increased with time due to radiation damage. The increasing rate of Sample 4848 and 4849 during irradiation was the same as the same irradiation intensity. Compared with the Sample 4848, the increasing rate of Sample 4851 was high because of higher irradiation intensity. After the beam stopped, the leakage current gradually decreased with time. This indicates recovery phenomenon from the radiation damage, although the recovery was not completed to the original conditions.

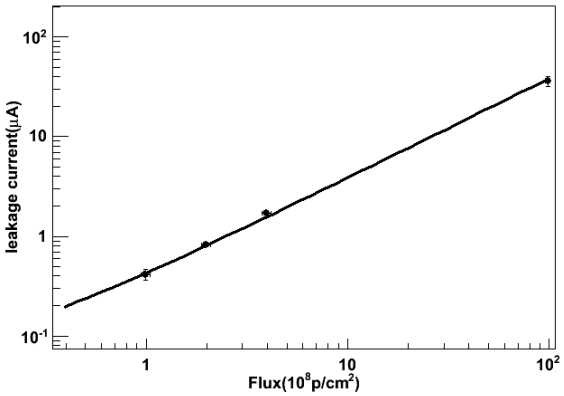

Fig. 2 Plots of the leakage current under the operating voltage measured for 5 days after irradiation as a function of 23MeV proton fluence, the black line shows the linear

Five days after the irradiation, the leakage current of the four MPPCs at operating voltage was measured and compared with the leakage current before the irradiation. Fig. 2 shows the increased leakage current of the four samples as a function of the 23MeV proton fluence Ψ_p. The leakage current increases linearly with the fluence as shown in Fig. 2. The black line in the figure shows the linear function fitted to the data of four samples, which indicates the relation between the leakage current and the irradiation fluence with a slop parameter $a=0.38\times10^{-8}$[μA /pcm^{-2}].

The I-V curves were measured before and after the irradiation. The results are shown in Fig. 3. From these plots, the leakage currents have rapidly increased with reverse voltages after the irradiation in comparison with that before the irradiation. This tendency is more significant for higher dose. As shown in these plots, the breakdown voltage (V_{BD}) of the four samples keeps unchanged after irradiation.

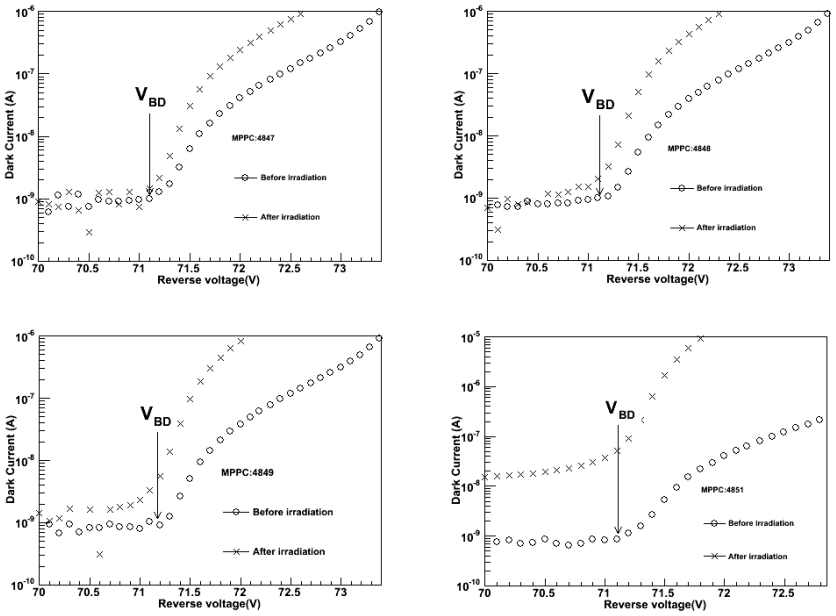

Fig. 3 I-V curves of samples for different radiation doses. The symbol V_{BD} denotes the breakdown voltage of each sample measured before the irradiation.

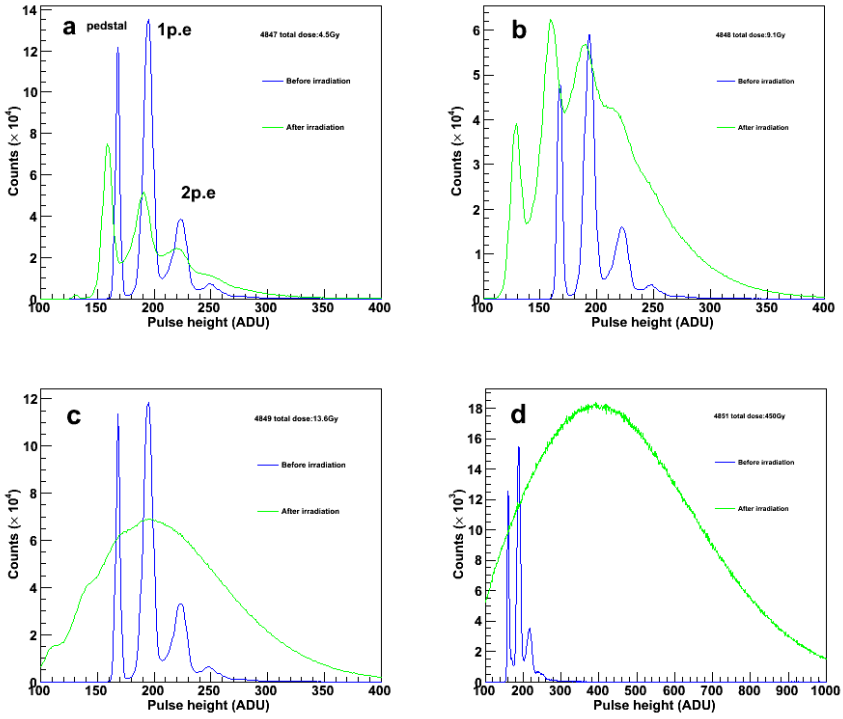

Fig. 4 Noise distributions for four MPPCs with different total dose before and after irradiation, integrated with the same time. (a) 4847 with 4.5Gy (b) 4848 with 9.1Gy (c) 4849 with 13.6Gy (d) 4851 with 450Gy

3.2 Pulse height resolution

The pulse-height resolution of MPPC as photo-detector is one of the most important properties in the case of measuring the incident alpha particles of AGC. In order to check whether the radiation damage could affect the pulse-height distributions of the MPPC, we measured the pulse-height distributions of the irradiated samples in a dark box without light sources. Fig. 4 shows the distributions for different irradiated dose. Before the irradiation the distributions for different samples all show the structure with clear discrete peaks, which includes a pedestal peak, single equivalent photon peaks, and those peaks are well separated with each other. The position of the pedestal peak shifts slightly toward lower channels because of the baseline shift coming from high dark counting rates after irradiation. The dark counting rate of MPPC increases after the irradiation, which is the main reason for the increase in the leakage current. This is because production of the lattice defects duo to radiation damage with higher probability of thermal carrier generation [9]. As the radiation damage on individual microcell pixels

is different, the gain uniformity of MPPCs deteriorated after irradiation. The single equivalent photon electron peaks of dark noise pulse-height distribution would be broadened result from this uniformity [9], as shown in Fig.4. For these reasons, the discrete peak structure has completely disappeared for the total dose of more than 13.6 Gy. This means that the MPPC has completely lost its capacity of the photon-counting by measuring pulse-height spectra due to the radiation damage.

And then Another pulse-height distribution of the 4849 and 4851 were taken by illuminating them by the ^{241}Am radioactive source dotted in the plastic scintillator, as shown in Fig. 5. Compared to that of the Sample 4849 and Sample 4851 before irradiation, it could tell whether the MPPCs should also be able to detect the alpha particles as a photo-detector of the AGC when the MPPC lost its capacity of single photon-counting. It was found that the Sample 4851 with 450Gy could not detect the alpha particles by measuring pulse-height spectra while the Sample 4849 could still work with high dark count rate. In the pulse-height distribution of Sample 4851, there was only one peak including the dark noise and the alpha signals, shown in Fig. 5 (b). And the dark count rate is much higher than that before irradiation. This would deteriorate the performance of the AGC by causing much more dead time of the associated electronics.

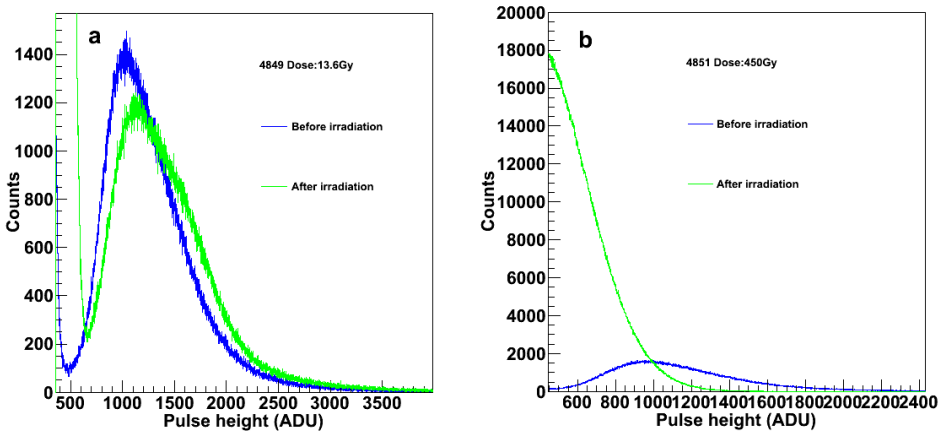

Fig. 5 Alpha pulse spectrums which integrated in the same time before and after irradiation (a) 4849 13.6Gy (b) 4851 450Gy

4. Summary

The effects on the performance of the MPPCs mainly leakage current and pulse-height resolution, caused by proton irradiation, has been discussed as a photo-detector in space environment. The four MPPC samples were irradiated by 23MeV protons with different fluence to investigate the effects of radiation damage. It is found that the leakage current increase linearly with time during irradiation. And the increment in leakage current is increase with the total beam fluence. From the measurement of pulse-height distribution in a dark box without any light sources, it indicates that the MPPCs completely lost its capacity of single photon-counting after more than 13.6Gy absorption dose. But the MPPCs as a photo-detector to detect the alpha particles from the ^{241}Am radioactive source by measuring pulse-height spectra still works, until irradiated by more than 13.6Gy.

References

[1] Li T P, Zhang S N, Lu F J., "Hard X-ray modulation telescope (HXMT) mission", Chin J Space Sci., vol. 26(Suppl), pp. 30-49 (2006).
[2]Lu F J., “The Hard X-ray Modulation Telescope (HXMT): Mission and Its Current Status”, AAPPS, vol. 19, pp. 36-38 (2009).
[3] Li T P, Wu M. “A direct restoration method for spectral and image analysis”, Astrophys Space Sci, vol. 206, pp. 91-102 (1993).
[4]Li T P, Wu M. “Reconstruction of objects by direct demodulation”, Astrophys Space Sci, vol. 215, pp. 213-227 (1994).
[5]P. Bohn et al., “Radiation damage studies of silicon photomultipliers”, Nucl. Instr. And Meth. A, vol.598, pp. 722-736 (2009).
[6]M. Angelone et al., “Silicon photo-multiplier radiation hardness tests with a beam controlled neutron source”, Nucl. Instr. And Meth. A, vol. 623, pp. 921-926 (2010).
[7]Y. Musienko et al., “Radiation damage studies of multipixel Geiger-mode avalanche photodiodes”, Nucl. Instr. And Meth. A, vol. 581, pp. 433-437 (2007).
[8]S. Sanchez et al., “Noise and radiation damage in silicon photomultipliers exposed to electromagnetic and hadronic radiation”, Nucl. Instr and Meth. A, vol. 602, pp. 506-510 (2009).
[9]T. Matsumura et al., “Effects of radiation damage caused by proton irradiation on Multi-Pixel Photon Counters (MPPCs)”, Nucl. Instr and Meth. A, vol. 603, pp. 301-308 (2009).

Total Ionizing Dose and Displacement Damage Effects G – P2

Difference of radiation tolerance with p- and n-type JFETs

K. Takakura[*1], S. Sakiyama[1], I. Tsunoda[1], M. Yoneoka[1], T. Nakashima[2, 3]
1 Kumamoto National College of Technology, 2659-2 Suya, Koshi, Kumamoto, Japan
2 Chuo Denshi Kogyo Co. Ltd., 3400 Kohoyama, Matsubase, Uki, Kumamoto, Japan
3 University of Miyazaki, 1-1, Gakuen Kibanadai-nishi, Miyazaki, Japan
*Email: takakura@kumamoto-nct.ac.jp
Keyword(s): COTS device, electron irradiation degradation, junction field effect transistor, electrical

Abstract

The radiation tolerance by 2 MeV electrons irradiated to the commercial-off-the-shelf (COTS) p- and n-JFETs was studied. For the situation of p-JFET, the drain current (I_D) of the input characteristics decreased by electron irradiation. The I_D decreasing attributed to the increase of channel resistance by electron irradiation. In contrast, for n-JFET, the I_D decreases at the fluence lower than $1x10^{15}$ e/cm^2, then the I_D increases at the fluence higher than $5x10^{15}$ e/cm^2. The anomalous I_D behavior of n-JFET could be explained by considering extending and narrowing of the n-channel.

1. Introduction

In electronic devices such as various sensors and attitude control used in satellites and space stations, a number of semiconductor devices are used. Semiconductor devices have highly sensitive to radiation, such as in nuclear power industries and in space. It is difficult to replace semiconductor devices in radiation environments. Therefore, very high reliability and radiation tolerance are required to the semiconductor devices used in radiation environments. However, development of the integration of semiconductor devises for space application needs high cost. Cost reduction of electronic devices and high integration could be realized alternating to the commercial semiconductor. An important segment of the aerospace/military integrated circuit market is taken by radiation-hard devices, with and increasing importance for space applications. The optimization of the overall reliability performance is becoming of key importance as the space community is more using the commercial-off-the-shelf (COTS) approach and is thereby also greatly interested in the feasibility of the use of more advanced materials and components. Therefore, it is important to accumurate information the radiation torelance for various COTS devides. We had been studied on radiation tollerance of semiconductor devices such as InGaAs photodiodes [1], SiC MESFET [2], SiGe MOSFET [3], and so on. The junction field effect transistor (JFET) is important device used in the electrical circuit for amplification the audio frequency signal. Also, JFET used in radiation environments, because it has high radiation hardness. For MOSFETs, degradation of the input characteristics by irradiation complicated, because some defects (interface defects at oxide and semiconductor, oxide defects, *etc*) correspond to the degradation. For the JFETs, the degradation became mainly causes from increasing channel resistance by irradiation, because of the JFET channel thicker than that of MOSFET. Therefore, the JFET used about Rad-Hard device for front end device [4] in radiation ambient and radiation detector [5]. However, detailed of the degradation mechanism of JFETs in radiation did not cleared, because it have few reports about radiation irradiation effects for electrical properties [6 - 8]. These studies discussed about gamma-ray or neutron irradiation effects/degradation of the JFETs, and there are few reports on the results of electron irradiation to the JFETs. It is important that the evaluation of electron irradiation effects of semiconductor devices for use in space. In this study, electron irradiation degradation of electrical properties for commercial p- and n-type JFET are evaluated.

2. Experimental

The Si p- (2SJ103 TOSHIBA) and n-JFETs (2SK117) were evaluated for samples. Both devices were normally applied for low noise audio amplifier. Devices without applied bias voltage were irradiated at room temperature by 2-MeV electrons in the acceleration reactor at the Takasaki Japan Atomic Energy Agency (JAEA). The electron fluence was varied from $1x10^{13}$ to $1x10^{16}$ e/cm^2. Before and after electron irradiation, the electrical performance has been evaluated by the input (I_D-V_G) characteristic with a drain voltage (V_D) at 10 V and gate voltages (V_G) ranging from 0 to 1.4 V for p-JFET and -0.5 to 0 V for n-JFET, respectively, using a semiconductor parameter analyser (HP-4156C). The threshold voltage (V_{TH}) was extracted from linear extrapolation of the input characteristics. Also, capacitance/voltage (C/V) characteristic between the source/drain and gate electrodes is studied using Agilent DL8000. From the C/V characteristic, depletion widths at the p- and n-JFET channel are studied.

3. Results and discussion

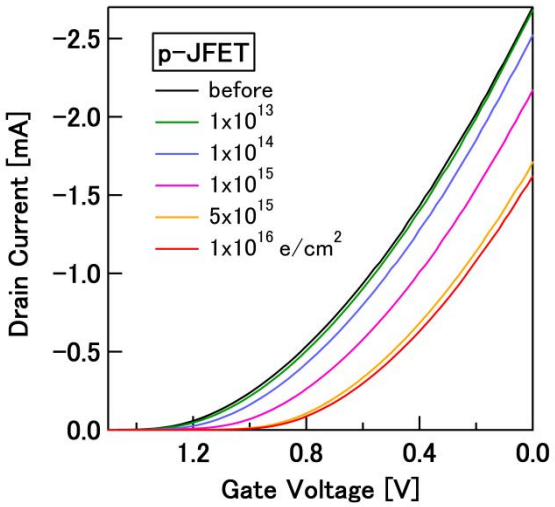

Fig. 1. Input characteristics of the p-JFETs before and after the electron irradiation.

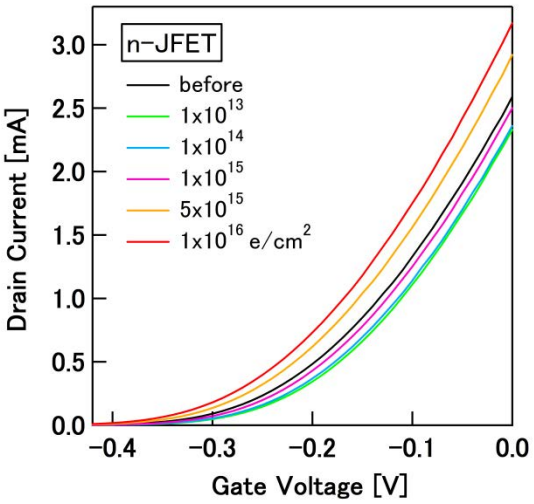

Fig. 2. Input characteristics of the n-JFETs before and after the electron irradiation.

Figure 1 shows the input characteristics of p-JFET for different electron fluences. It could be observed that I_D decreases by electron irradiation. On the other hand, I_D decreases at the fluence lower than $1x10^{15}$ e/cm^2, then I_D increases at the fluence higher than $5x10^{15}$ e/cm^2 in n-JFET, as shown in Fig. 2. It seems the channel resistance for n-JFET increases at the fluence lower than $1x10^{15}$ e/cm^2, then the channel resistance decreases at the fluence higher than $5x10^{15}$ e/cm^2. To consider the channel resistance of JFETs, the swing at subthreshold region determined by eq. (1) is estimated. The swing means the required gate voltage for one decade increasing I_D.

$$\text{Swing} = \frac{dV_G}{d\log_{10}(I_D)} \qquad \text{(eq. 1)}$$

The swings determined by input characteristics for p- and n-type JFETs are shown in Fig. 3. The swing for p- and n-JFET increased with increasing electron fluence, but the values are different with the conduction type. This result could be said that resistance of p-JFET larger increased by electron irradiation. From the result, the increasing of I_D for p-JFET by electron irradiation could not explain using the change of channel resistance.

Figure 4 shows the V_{TH} shifts of the p- and n-JFET before and after the electron irradiation. The I_D change inferred by V_{TH}. For p-JFET, the V_{TH} shifts toward positive. It corresponds to channel narrowing by the electron irradiation. However, the V_{TH} shift for n-JFET changes negative to positive with increasing electron fluence. This result indicates that the channel width extended by the electron irradiation. Therefore, it could be said that the channel width extending leads I_D increasing.

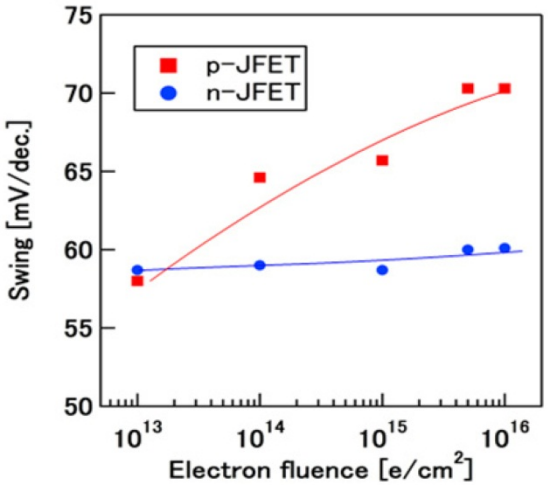

Fig. 3. The swings determined by input characteristics of the p- and n-JFETs.

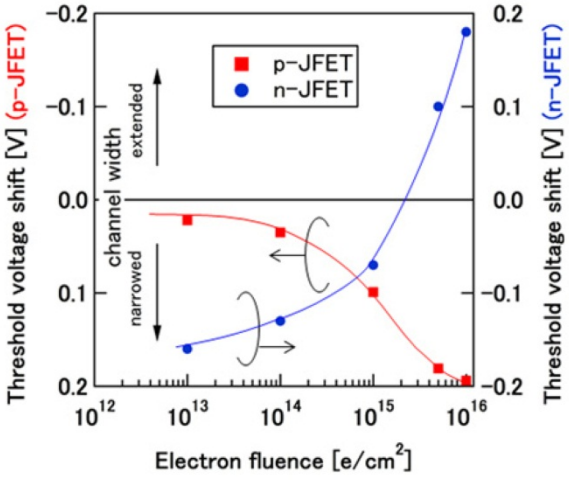

Fig. 4. Shift of V_{TH} by electron irradiation for p- and n-JFETs.

The depletion width inferred with carrier density of the p- and n-region. Therefore, the carrier density of p- and n-channel estimated from C/V characteristic of source/drain and gate electrodes. Unfortunately, the area of pn junction at the gate had not been known. Therefore, change ratio of carrier density before and after the electron irradiation determined damage factor D_C as eq. (2).

$$D_C = \frac{n_{after}}{n_{before}} \quad \text{(eq. 2)}$$

where, n_{after} and n_{before} are carrier density after and before the electron irradiation. Figure 5 shows D_C at the channel of p- and n-type JFET. As shown in Fig. 5, although, the carrier density at the p-channel has decreased by electron irradiation, there is little decrease of carrier density at the n-channel. Generally, phosphorous or arsenic atom is used as donor and boron atom is used as acceptor in Si. Accordingly, the number of knock-on atom by electron irradiation of phosphorous or arsenic atom smaller than that of boron atom. The knock–on atom deactivate as an acceptor or a donor. Under these assumptions, depletion layer at the pn junction easily extended to the p-region by electron irradiation. The depletion width of n-JFET became narrowed by the irradiation caused by deactivation of acceptor. It could be considered the n-channel extended by electron irradiation.

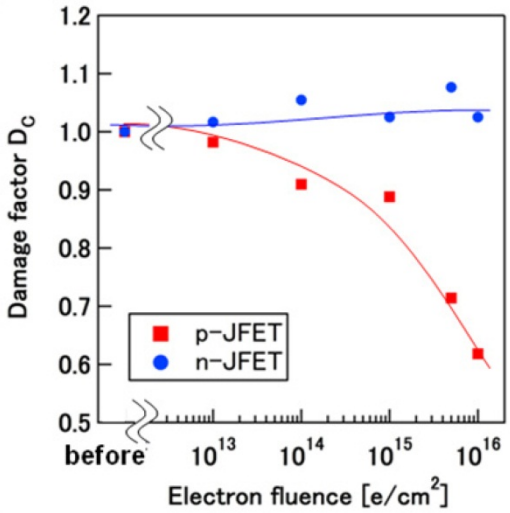

Fig. 5. The damage factor of carrier density (D_C) for the p- and n-channel after the electron irradiation.

4. Conclusion

To purpose of accumulate the information of radiation tolerance the COTS devices. Electrical properties of electron irradiated p- and n-JFETs were studied. For p-JFET, decreasing the I_D corresponds to the increasing channel resistance by electron irradiation. It could be confirmed by subthreshold swing increasing. In contrast, the I_D decreases at the fluence lower than $1x10^{15}$ e/cm^2, then I_D increases at the fluence higher than $5x10^{15}$ e/cm^2 in n-JFET. Also, the threshold voltage shift changes negative to positive with increasing electron fluence. These behaviors corresponds to the considering the difference the number of knock-on atoms (acceptor and donor) by electron irradiation. It could be confirmed from the C/V characteristics, the amount of deactivated acceptor larger than donor. Therefore, the channel width extended by electron irradiation because deactivation of acceptor at p-type gate and the depletion layer narrowed.

Acknowledgments

Part of this work was supported by Grant-in-Aid for Scientific Research (No. 12009 and No. 12064) from the Japanese Ministry of Education for Science, by Inter-University Laboratory for the Joint Use of JAEA Facilities.

References

[1] H. Ohyama, K. Kobayashi, J. Vanhellemont, E. Simoen, C. Claeys, K. Takakura, T. Hirao, S. Onoda, “Induced lattice defects in InGaAs photodiodes by high-temperature electron irradiation,” Physica B, vol. 340-342 pp. 337-340 (2003).
[2] H. Ohyama, K. Takakura, M. Yoneoka, K. Uemura, M. Motoki, K. Matsuo, M. Arai, S. Kuboyama, E. Simoen, C. Claeys, “Effect of gate interface on performance degradation of irradiated SiC-MESFET,” Physica B, vol. 401-402 pp. 37-40 (2007).
[3] T. Nakashima, T. Idemoto, I. Tsunoda, K. Takakura, M. Yoneoka, H. Ohyama, K. Yoshino, M.B. Gonzalez, E.

Simoen, C. Claeys, “Radiation damage of $Si_{1-x}Ge_x$ S/D p-type metal oxide semiconductor field effect transistor with different Ge concentrations,” Thin Solid Films, vol 520 pp. 3337-3340 (2012).
[4] M. Citterio, J. Kierstead, S. Rescia, V. Radeka, “Radiation effects on Si-JFET front-end electronics,” IEEE Trans. Nucl. Sci., vol 43 pp. 1576-1584 (1996).
[5] J.C. Lund, F. Olschner, “Junction field effect transistors as radiation detectors,” IEEE Nucl. Sci. Symp. And Med. Imag. Conf., Conference Record of the 1992 vol .1 pp. 47-49 (1992).
[6] W. Shedd, B. Buchanan, R. Doian, “Radiation Effects on Junction Field Effect Transistors,” IEEE Trans. Nucl. Sci., vol 16 pp. 87-95 (1969).
[7] J. Assaf, “High gamma dose induced damage on two types of discrete JFET transistors,” Physica B, vol. 404 pp. 73-78 (2009).
[8] J. Assaf, “Recovering behavior of JFET transistors after gamma ray irradiation,” Radiation Physics and Chemistry, vol. 80 pp. 491-495 (2011).

Innovating Energy Technology

Through our pursuit of innovation
in electric and thermal energy technology,
we lead to a responsible and sustainable society.

High Reliability Power MOSFET for Space Use

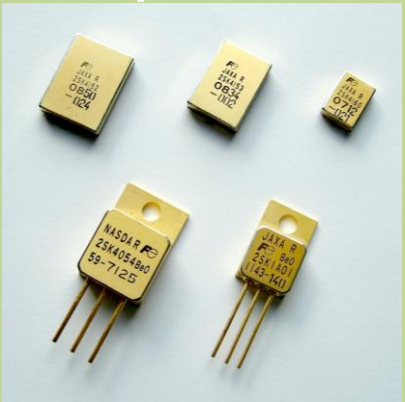

Part Number	Polarity	VDS(V)	ID(A)	Ron(Ω)	Package
JAXA R 2SK4048	n	100	42	0.018	TO-254
JAXA R 2SK4049	n	100	42	0.033	TO-254
JAXA R 2SK4050	n	100	15	0.069	TO-254
JAXA R 2SK4217	n	100	42	0.013	SMD2
JAXA R 2SK4218	n	100	42	0.028	SMD1
JAXA R 2SK4219	n	100	15	0.064	SMD0.5
JAXA R 2SK4214	n	130	42	0.024	TO-254
JAXA R 2SK4215	n	130	35	0.046	TO-254
JAXA R 2SK4216	n	130	15	0.096	TO-254
JAXA R 2SK4152	n	130	42	0.017	SMD2
JAXA R 2SK4153	n	130	39	0.039	SMD1
JAXA R 2SK4154	n	130	15	0.089	SMD0.5
JAXA R 2SK4051	n	200	42	0.033	TO-254
JAXA R 2SK4052	n	200	33	0.069	TO-254
JAXA R 2SK4053	n	200	14	0.155	TO-254
JAXA R 2SK4155	n	200	42	0.026	SMD2
JAXA R 2SK4156	n	200	32	0.062	SMD1
JAXA R 2SK4157	n	200	14	0.148	SMD0.5
JAXA R 2SK4054	n	250	42	0.045	TO-254
JAXA R 2SK4055	n	250	27	0.098	TO-254
JAXA R 2SK4056	n	250	12	0.23	TO-254
JAXA R 2SK4158	n	250	42	0.038	SMD2

Part Number	Polarity	VDS(V)	ID(A)	Ron(Ω)	Package
JAXA R 2SK4159	n	250	26	0.091	SMD1
JAXA R 2SK4160	n	250	12	0.223	SMD0.5
JAXA R 2SK4185	n	500	23	0.18	TO-254
JAXA R 2SK4186	n	500	10	0.48	TO-254
JAXA R 2SK4187	n	500	4.5	1.15	TO-254
JAXA R 2SK4188	n	500	23	0.18	SMD2
JAXA R 2SK4189	n	500	10	0.48	SMD1
JAXA R 2SK4190	n	500	4.5	1.15	SMD0.5
JAXA R 2SK1A01	n	600	3.9	1.9	TO-257
JAXA R 2SJ1A01	p	-100	-42	0.045	TO-254
JAXA R 2SJ1A02	p	-100	-25	0.097	TO-254
JAXA R 2SJ1A03	p	-100	-11	0.226	TO-254
JAXA R 2SJ1A04	p	-100	-42	0.038	SMD-2
JAXA R 2SJ1A05	p	-100	-29	0.09	SMD-1
JAXA R 2SJ1A06	p	-100	-13	0.219	SMD-0.5
JAXA R 2SJ1A07	p	-200	-35	0.091	TO-254
JAXA R 2SJ1A08	p	-200	-16	0.21	TO-254
JAXA R 2SJ1A09	p	-200	-7.5	0.487	TO-254
JAXA R 2SJ1A10	p	-200	-37	0.084	SMD-2
JAXA R 2SJ1A11	p	-200	-18	0.203	SMD-1
JAXA R 2SJ1A12	p	-200	-8.5	0.48	SMD-0.5

Fuji Electric

Ryoei Technica Corporation

Provides the following services to development of semiconductor devices using radiation test facilities.

Radiation Testing Services:

1. Comprehensive testing and analysis on Integrated Circuits in radiation environments.
2. Evaluation of the radiation tolerance of Commercial –off- the-shelf (COTS) parts and subsystems.
3. Total Ionizing Dose (TID), Displacement Damage (DD), and Single Event Effects (SEE) tests on new and advanced, high performance technologies.

We have experienced in a wide range of device types to include:
Microprocessors, Memories, Analog-ICs, FPGAs, Transistors, etc.

And we will

- Assist you with test circuit designs and interpretation of radiation test data
- Guide you in the selection of application appropriate devices
- Help you select radiation hardened device vendors
- Provide you with the best radiation tolerant IC solutions and data

Radiation Facilities & Radiation Verification Tests

JAEA

BNL

CNL

Total Service Provider
Ryoei Technica Corporation
325 Kamimachiya, Kamakura Kanagawa, 247-8520 Japan
Phone : +81-467-44-1400 URL : http//www.ryoei.co.jp

HIREC's goal is to contribute to our client's success by providing the EEE parts and engineering supports.

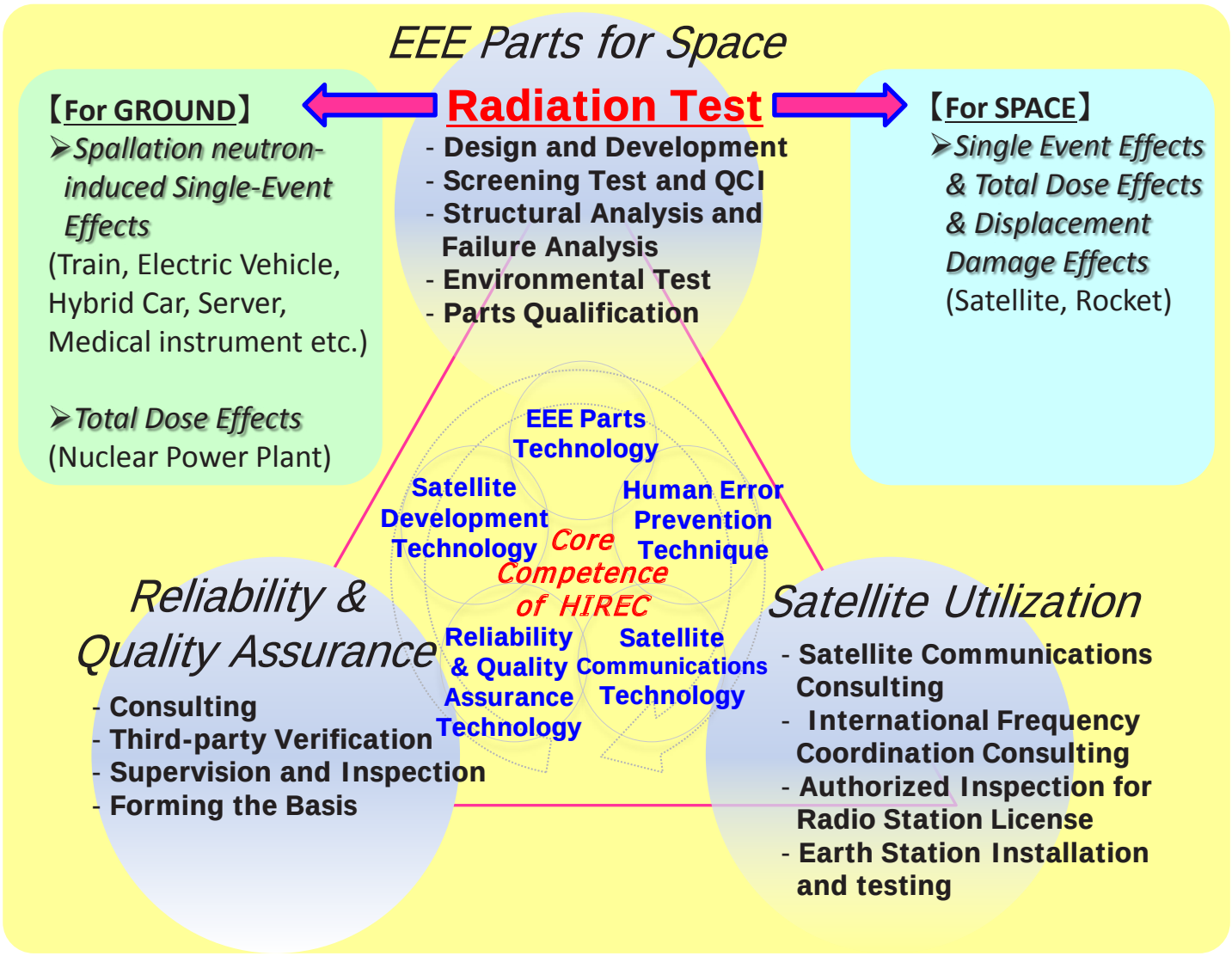

We will held the **2nd RADIATION SCHOOL of Radiation Effects on semiconductor devices for Students, Beginner etc.**

Please feel free to come and join us!!

■Date : March 1, 2013
■Venue : Surugadai Campus, College of Science and Technology, Nihon University (Tokyo)
■Attendance fee : **FREE!**
■Agenda : "Basic Mechanism of Radiation Effects" , "Status for JAXA EEE parts Development" and "Required & Selection of EEE parts from satellites" etc.
■Contact : rad_meeting@hirec.co.jp, TEL: +81-29-868-6770

HIREC
High-Reliability Engineering & Components Corporation

High-Reliability Engineering & Components Corporation

8-1, Higashi-Arai, Tsukuba-Shi, Ibaraki, 305-0033, Japan
TEL: +81-29-868-6770, FAX: +81-29-868-6771
URL: http://www.hirec.co.jp